Polymer Self-Assembly and Thin Film Deposition in Supercritical Fluids

by

Nastaran Yousefi

M.Sc., University of Western Ontario, 2014

B.Sc., Islamic Azad University, 2009

Thesis Submitted in Partial Fulfillment of the
Requirements for the Degree of
Doctor of Philosophy

in the
Department of Chemistry
Faculty of Science

SIMON FRASER UNIVERSITY

Spring 2021

Declaration of Committee

Name:	**Nastaran Yousefi**
Degree:	**Doctor of Philosophy (Chemistry)**
Thesis title:	**Polymer Self-Assembly and Thin Film Deposition in Supercritical Fluids**
Committee:	**Chair:** Corina Andreoiu Associate Professor, Chemistry
	Loren Kaake Supervisor Associate Professor, Chemistry
	Paul Percival Committee Member Professor Emeritus, Chemistry
	Vance Williams Committee Member Professor, Chemistry
	Neil Branda Examiner Professor, Chemistry
	James Watkins External Examiner Professor Polymer Science and Engineering University of Massachusetts Amherst

Abstract

Patterning of flexible electronic devices using large-area printing techniques is the focus of intense research due to their promise of producing low-cost, light-weight, and flexible devices. The successful integration of advanced materials like semiconductor nanocrystals, carbon nanotubes and polymer semiconductors into microscale electronic devices requires deposition techniques that are robust, scalable, and enable fine patterning. To this end, we have established a deposition technique that leverages the unique solubility properties of supercritical fluids. The technique is the solution-phase analog of physical vapour deposition and allows thin films of a semiconducting polymer to be grown without the need for in-situ chemical reactions. To demonstrate the flexibility of the technique, we demonstrated precise control over the location of material deposition using a combination of photolithography and resistive heating. The versatility of the technique is demonstrated by creating a patterned film on the concave interior of a silicone hemisphere, a substrate that cannot be patterned via any other technique. More generally, the ability to control the deposition of solution processed materials with lithographic accuracy provides the long sought-after bridge between top-down and bottom-up self-assembly.

In addition, we investigated the self-assembly of polymers in supercritical fluids by depositing thin films and studying their morphology using polarized optical microscopy and grazing incidence wide angle x-ray scattering. We summarized our observations with a two-step model for film formation. The first step is pre-aggregation in solution whereby the local crystalline order is established, and the solution turbulence can easily disrupt the solution-phase self-assembly. The second step to film formation is the longer length scale organization that is influenced by the chain mobility on the surface. We identified pressure and solvent additive as two powerful tools to facilitate the local crystalline order and longer length scale organization. The work demonstrated key insights necessary to optimizing thin-film morphologies and principles for understanding self-assembly in supercritical fluids that could be applied to self-assembly of materials in other contexts. Finally, we developed a simple empirical model based on classical thermodynamics that highlights the interplay of intermolecular interactions and solvent entropy and describes both the temperature and pressure dependence of polymer solubility in supercritical fluids.

Keywords: supercritical fluids; self-assembly; semiconducting polymers; organic semiconductors; thin film deposition; thin film morphology

To my brother, Pedram, for sacrificing his own happiness for mine and our family.

Acknowledgements

I would like to extend my sincerest appreciation to my supervisor, Dr. Loren Kaake, for providing me with every opportunity to thrive, and more importantly, paved my way to become a competent scientist. I will always appreciate his insatiable curiosity for science, his willingness to be unconventional, and his boldness when it comes to scientific ideas and pushing barriers.

I would like to thank the members of my supervisory committee, Dr. Percival, and Dr. Williams for their constant support and guidance throughout my PhD studies and providing me with constructive feedbacks during annual committee meetings.

To my academic family at Simon Fraser University and particularly the Department of Chemistry, you made my journey one full of wonderful memories and I will cherish those memories forever. Thanks for supporting me through tough times with insurmountable amount of chocolate, hugs, and words of encouragement. I consider myself lucky to be surrounded by such intelligent and thoughtful people.

To my fiancé, Dr. Michael Meanwell, thank you for your love, constant encouragement, and above all your genuine kindness. I am forever grateful for having you by my side during the most challenging years of my life and I will not forget how you empowered me in different ways every day. Indeed, there is no better feeling than having a person like you by my side to celebrate my accomplishments with and hold me when I fail miserably.

To my family and friends, this thesis would have not been completed without your unconditional love, collective kindness, and unwavering support. You all managed to amazingly show up and support me in the most difficult moments of my life and lifting my spirits.

Lastly, to my brother Pedram, I am forever in your debt for always making me a priority in your life, listening to my challenges patiently, imparting your wisdom gracefully whenever possible, and above all always being there for me.

Table of Contents

List of Figures

List of Acronyms and Symbols

∇T	Temperature Gradient
2D	Two Dimensional
4D LABS	4D Laboratories
A	Absorbance
a.u.	Arbitrary Units
AFM	Atomic Force Microscopy
AWG	American Wire Gauge
BeCu	Beryllium Copper
BT	Benzothiadiazole
CCD	Charge-Coupled Device
CDT	Cyclopentadithiophene
CF	Chloroform
CFD	Computational Fluid Dynamics
CN	Chloronaphthalene
CTRW	Continuous Time Random Walk
DNA	Deoxyribonucleic Acid
DPP	Diketopyrrolopyrrole
e	Electric Charge
E	Electric Field
EMI	Electromagnetic Interference
EoS	Equation of State
ES	Efros-Shklovskii
E_T	Mean Energy of The Trap States
ε	Energy Associated with the Intermolecular Forces
$\boldsymbol{\varepsilon}$	Molar Absorptivity
F8BT	Poly(9,9-dioctylfluorene-*alt*-Benzothiadiazole)
FET	Field-Effect Transistor
G	Gibbs Free Energy

G_{ex}	Excess Gibbs Free Energy
GIWAXS	Grazing-Incidence Wide-Angle X-Ray Scattering
GIXS	Grazing Incidence X-Ray Scattering
Gr	Grashof Number
H	Enthalpy
HL	Halogen Light
HMDS	Hexamethyldisilazane
HOMO	Highest Occupied Molecular Orbital
HXMA	Hard X-Ray Micro-Analysis
I	Light Intensity
IDT	Indacenodithiophene
iPP	Isotactic Polypropylene
ITO	Indium Tin Oxide
J	Current Density
K	Solubility Coefficient
k	Wavevector
L	Length
LAC	Library and Archives Canada
L_C	Counter Length
LCST	Lower Critical Solution Temperature
LED	Light Emitting Diode
L_P	Persistence Length
LUMO	Lowest Unoccupied Molecular Orbital
*m**	Effective Mass
m_e	Electron Mass
ML	Monolayer
M_n	Number Average Molecular Weight
MOF	Metal−Organic Framework
MTR	Multiple Trap and Release

M_W	Weight Average Molecular Weight
M_{WD}	Molecular Weight Distribution
n	Refractive Index
NDI	Naphtalenediimide
NEXAFS	Near Edge X-Ray Absorption Fine Structure
NIST	National Institute of Standards and Technology
NLO	Nonlinear Optical
$\emptyset$	Lattice Volume Fraction
OECT	Organic Electrochemical Transistor
OFET	Organic Field-Effect Transistor
OPVC	Organic Photovoltaic Cell
OSC	Organic Semiconductors
P	Pressure
P(NDI2OD-T2)	Poly(([N,N'-bis(2-octyldodecyl)naphthalene-1,4,5,8-bis(dicarboximide)-2,6-diyl]-Alt-5,5'-(2,2'-bithiophene))
P3HT	Poly(3-hexylthiophene)
PBTTT	Poly[2,5-bis(3-tetradecylthiophen-2-yl)thieno[3,2-b]thiophene]
PC-SAFT	Perturbed Chain-Statistical Associating Fluid Theory
PDI	Polydispersity Index
PDMS	Poly(dimethylsiloxane)
PDTTT	Poly(2,5-di(thiophen-2-yl)thieno[3,2-b]thiophene)
PEDOT	Poly(3,4-ethylenedioxythiophene)
PID	Proportional–Integral–Derivative
PMMA	Poly(methyl methacrylate)
POM	Polarized Optical Microscopy
Pr	Prandtl Number
P_r	Critical Pressure
PSS	Polystyrene Sulfonate

PTAA	Poly[bis(4-phenyl)(2,4,6-trimethylphenyl)amine]
PTI	Industrial Pressure Transducers
q	Scattering Vector
R	Differential Retardation
Ra	Rayleigh Number
Re	Reynolds Number
RFID	Radio-Frequency Identification
r_{hop}	Average Hopping Length
RIE	Reactive Ion Etching
R_{ij}	Hopping Space Range
RR	Regioregular
RRa	Regiorandom
S	Entropy
SAFT	Statistical Associating Fluid Theory
SAM	Self-Assembled Monolayers
SC	Supercritical
sccm	Standard Cubic Centimeter Per Minute
$ScCO_2$	Supercritical Carbon Dioxide
SCF	Supercritical Fluid
SEM	Scanning Electron Microscopy
SFU	Simon Fraser University
Si	Silicon
SEC	Size Exclusion Chromatography
T	Temperature
TCB	Trichlorobenzene
TCB	Trichlorobenzene
TER	Total External Reflection
TIPS	6,13-bis(triisopropylsilylethinyl)
T_r	Critical Temperature

UCST	Upper Critical Solution Temperature
UV-vis	Ultraviolet–Visible
vdW	Van Der Waals
VLE	Vapor-Liquid Equilibrium
VRH	Variable Range Hopping
X	Mole Fraction
Z	Compressibility Factor
α	Alpha
α_c	Total External Reflection Angle
β	Beta
γ	Gamma
ΔF	Change in Helmholtz Energy
ΔG	Change in Gibbs Free Energy
ΔH	Change in Enthalpy
Δn	Birefringence
ΔP	Change in Pressure
ΔS_C	Change in Configurational Entropy
ΔS_P	Change in Entropy of Pure Solvent
ΔT	Temperature Gradient (K)
ΔU	Change in Internal Energy
ΔV	Change in Volume
λ	Wavelength
Λ	Transition Energy
μ	Charge Carrier Mobility
v	Average Velocity
v_d	Drift Velocity
ξ_0	Localization Length at Zero Magnetic Field
π	(Pi) Bonding Orbital(s)
π*	(Pi-Star) Antibonding Orbital(s)

ρ	Density
P	Momentum
σ	Electrical Conductivity
τ	Scattering Time
χ	Interaction Parameter
ω	Acentric Factor
ν	Fluid Kinematic Viscosity

Chapter 1. Introduction

1.1. Past, Present, and Future of Organic Semiconductors

The beginnings of the modern-day organic semiconductor started over more than a century ago. Key discoveries contributing to its development include the first studies of photoconductivity of anthracene crystals (early 20th century) and the discovery of electroluminescence in the 1960s. These early investigations on organic small molecules helped scientists understand the fundamental processes involved in optical excitation and charge carrier transport.[1,2] While most of the prospective advantages of organic electronics were proposed decades ago, organic electroluminescent diodes are the only organic electronic application to have successfully entered the commercial market, whose display market in smartphones (Samsung, Apple) and televisions (LG) will grow above US$300 billion by 2025.[3,4]

In 1977, Shirakawa, MacDiarmid and Heeger reported the first use of an organic polymer, polyacetylene, as a conducting material. This landmark discovery soon led to several applications of polyacetylene-based materials including uses as organic photoconductors, conductive coatings, and photoreceptors in electrophotography.[5,6] The field has since evolved from these first generation polymers toward more complex polymers such as soluble poly(alkylthiophenes) and poly(2,5-di(thiophen-2-yl)thieno[3,2-b]thiophene) (PDTTT). More recently, there has been significant focus on donor-acceptor co-polymers which are comprised of monomeric building blocks based on indacenodithiophene (IDT), diketopyrrolopyrrole (DPP), naphtalenediimide (NDI), cyclopentadithiophene (CDT), benzothiadiazole (BT), thiophene or isoindigo.[7]

Commercialization efforts for organic semiconductors are driven by their many unique properties which distinguish them from crystalline materials (i.e. silicon or gallium arsenide) and allows for the tuning of their physical mechanics. The seminal work on undoped small-molecule organic semiconductors goes back to 1980s. Notably, during this time, Tang demonstrated the use of an organic heterojunction consisting of p- and n-conducting materials in a photovoltaic cell.[8] Furthermore, Tsumura, Burroughes, and Horowitz independently showed the successful fabrication of thin film transistors from conjugated polymers and oligomers.[9-11] An important breakthrough came from the

demonstration of high-performance electroluminescent diodes from molecular films[12] and conjugated polymers.[13] Subsequently, as a result of these discoveries, the first commercial products were developed incorporating organic light-emitting device displays and lighting. Other applications of organic semiconductors are in organic photovoltaic cells (OPVCs) and organic field-effect transistors (OFETs). While not destined to replace silicon-based technologies, organic semiconductors promise the advent of flexible solar cells, low-cost printed integrated circuits, and large area, flexible light sources and displays.

The electronic performance of devices based on organic semiconductors depends largely on the rate with which charge carriers move within the π-conjugated materials. The charge carrier mobility of semiconducting polymers has been dramatically increased over the years and has achieved performances exceeding that of amorphous silicon (>1 $cm^2 V^{-1} s^{-1}$),[14-18] reaching mobilities comparable with commercial metal–oxide transistors (10–30 $cm^2 V^{-1} s^{-1}$) (Figure 1.1).[19] This steady improvement in polymer mobility is primarily due to significant advances in molecular design and processing techniques.

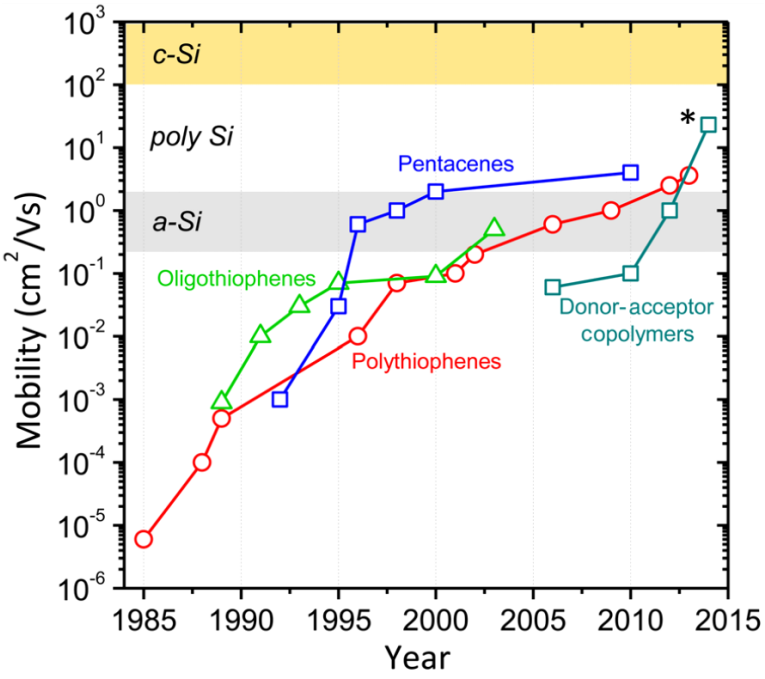

Figure 1.1. The advancement of semiconducting polymer mobility. State-of-the-art polymer mobilities have improved by over six orders of magnitude in the last 30 years. The asterisk indicates materials aligned using a special technique. Reprinted with permission from reference 20.

The commercialization of semiconducting polymers is very promising owing to advancements in their electronic performance, combined with their low-temperature solution processing, easy deposition, and mechanical flexibility. Nonetheless, the continuous growth of the field will be dependent on the simultaneous effort to design new molecules, understand the fundamentals governing the structure-property relationships, and explore new areas for commercialization. The development of synthetic methodologies for semiconducting polymers has mainly focused on developing synthetic routes that allow for control over chain length, chain length distribution, and regioregularity – features that greatly affect intra- or inter-chain packing and hence charge transport. Moreover, the synthetic approaches must be scalable and show reliable solution processability while avoiding toxic reagents and by-products.

Additional progress has come from studies on charge transport physics focusing on how chain conformations, doping, and ion incorporation can impact charge transport characteristics of semiconducting polymers. For instance, transport studies have shed light on how different polymer film morphologies demonstrate different optoelectronic performance, thus suggesting new processing design strategies are critical for further performance improvement.[7,21] In recent years, semiconducting polymers have received much attention (owing to their flexibility/stretchability, biocompatibility, and some cases biodegradability) in bioelectronic applications such as biosensors,[22,23] actuators for drug release,[24,25] and neural photostimulation.[26-28] The basic unit for the majority of these devices is an organic electrochemical transistor (OECT) consisting of p-type poly(3-hexylthiophene) (P3HT) and poly(3,4-ethylenedioxythiophene) polystyrene sulfonate (PEDOT:PSS) polymers.[29,30] The continued development of these bioelectronics holds great promise for next-generation medical technology.

1.2. Research Motivation

As mentioned in the previous section, advances in processing strategies play a crucial role in continuing to push the performance further for the organic optoelectronic devices. For this reason, more attention has been paid to further performance improvements based on processing techniques and achieving optimal morphology. Additionally, research efforts have became more focused on establishing new strategies that do not merely enable the control of morphology, but also facilitate process scale-up for large scale production.

The crucial building blocks in any electronic devices consist of thin films (100-300 nm) deposited on a substrate. Based on the application of the device, this layer can be composed of either a single or a blend of two or more materials. In general, it is essential for the device performance that the deposition is homogeneous over a large area and that the layer thickness is well-controlled. There are significant differences in deposition methods for the two classes of organic semiconductors (e.g. small molecules and polymers) with their advantages and disadvantages. Figure 1.2 demonstrates some of the methods which have been employed to form thin organic films.

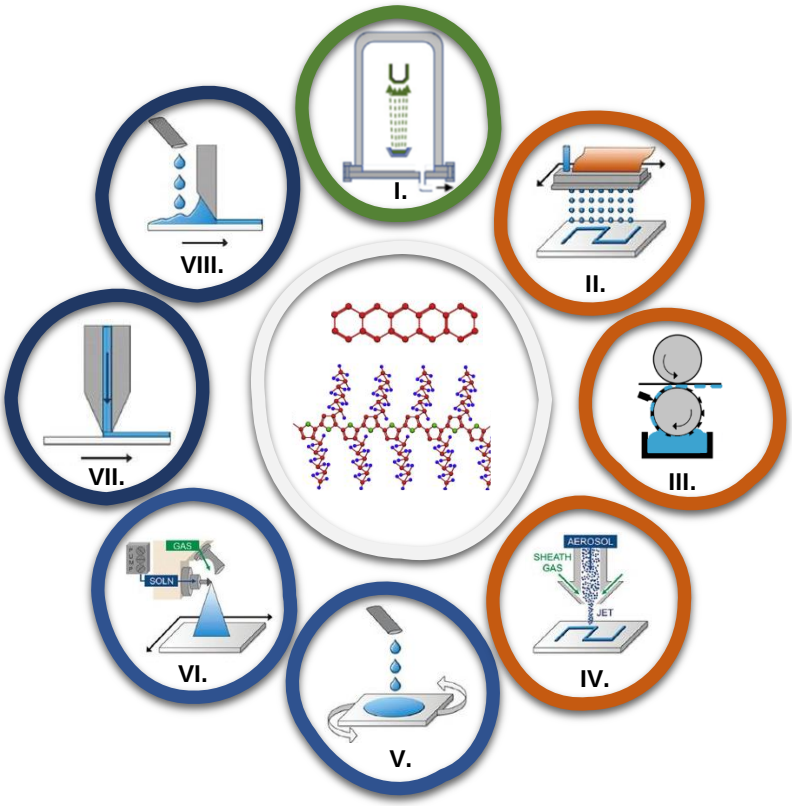

Figure 1.2. Several deposition methods for growing thin films of organic semiconductors. I. Vacuum deposition, II. Inkjet printing, III. Gravure printing, IV. Aerosol jet printing, V. Spin-coating, VI. Spray-coating, VII. Slot casting, VIII. Doctor blade.

Small molecules are processed mainly via vacuum thermal evaporation and are entirely solvent-free. The vacuum deposition offers a comparatively easy path for the preparation of a well-defined films (high resolution) and high purity films for multi-layer systems. In contrast, semiconducting polymers are mainly processed from solution since they would otherwise decompose into smaller molecules during this high-temperature sublimation process. There are two deposition categories for solution-soluble

semiconducting polymers: deposition of a soluble precursor from a solution and subsequent conversion to the final film, and direct deposition from solution. Spin-coating is one of the most popular examples of direct solution deposition, often used for polymers such as poly(3-hexylthiophene) (P3HT).

As mentioned, the properties of the thin film are not merely dictated by the nature of the constituent materials as the film nanostructure strongly affects device performance. For instance, in thin film transistors, the morphology of the thin film plays a major role in switching, processing, and transmitting electronic information. Wang et al.[31] used three deposition methods (spin-coating, drop-casting, and dip-coating) for the fabrication of regioregular P3HT film in organic thin film transistor structures and discovered dip-coating ultrathin films show significantly higher mobility due to the improved structural order of the semiconducting molecules at the interface. In the same manner, the control over the mesoscopic order in polymers can be carried out via different complementary approaches such as post-deposition thermal annealing,[32,33] solvent additive processing,[34,35] strain-aligning,[36,37] and modification of the substrate.[38-40] These strategies have been shown to improve mobility while also leading to a higher degree of crystalline order observed in the polymer thin films. Thus, the development of organic electronic devices goes hand in hand with nano-engineering of organic thin films via manipulation of the supramolecular organization.

Although spin-coating is the commonly used approach to fabricate high efficiency organic thin films, it is not suitable for the large-scale deposition of organic semiconductors in electronics. The main criteria for a process to be deemed efficient for electronics requires moderate temperature, high rate, continuity, and a small number of simple process steps. As a result, printing techniques such as flexographic, gravure, screen and ink-jet printing have attracted much interest as promising technologies for the successful realization of organic electronics. Despite the remarkable performance reported in literature for organic-based integrated circuits,[41] RFID-tags,[42,43] and displays,[44,45] the adaptation of mass-printing methods for the fabrication of these electronic devices is complicated and requires significant modifications in processes and materials.

1.3. Thesis Overview

Although there are several deposition techniques for the fabrication of thin film organic semiconductors, due to specific limitation of each techniques, new solution processing methods are actively being investigated. The motivation behind the research comprising this thesis is to develop a novel deposition technique using supercritical fluids. Supercritical fluids (SCFs) are exceptional solvents for triggering the precipitation of organic molecules. For instance, $ScCO_2$ has been utilized as an antisolvent to control the precipitation of C_{60} crystals from the solution. Additionally, manipulating temperature and pressure of SCFs can alter solvent properties drastically, making SCFs a great tool in controlling the morphology of organic semiconductor films. The process discussed in this thesis is related to a method for depositing metal films from organometallic precursors, called cold wall deposition.

- **Chapter 2:** The purpose of this chapter is to provide a set of relevant background concepts for the research presented thereafter in this thesis. This chapter mainly focuses on explaining the basic physical and electronic properties of organic semiconductors and the theories describing the charge transport in them. Furthermore, the thermodynamic of polymer solutions using different models, supercritical fluid properties, and fluid dynamics are reviewed.

- **Chapter 3:** This chapter describes the experimental setup for film deposition and solubility measurements. It also includes the relevant details regarding the custom-made supercritical fluid chamber, in-situ UV-vis spectroscopy set up, materials and other technical equipment used during research.

- **Chapter 4:** This chapter discusses our initial steps towards developing a novel deposition technique including the solubility study of a selected semiconducting polymer, poly[2,5-bis(3-tetradecylthiophen-2-yl)thieno[3,2-b]thiophene] (PBTTT-C_{14}), in n-pentane at different temperatures and pressures. Additionally, the technological relevance of this technique is exhibited by depositing finely patterned features onto flat, curved, and flexible substrates.

- **Chapter 5:** In this chapter, the self-assembly of isotactic polypropylene films from supercritical n-pentane is investigated to gain a deeper understanding of the polymer self-assembly in SCFs. Additionally, a simple thermodynamic model is proposed to predict both the temperature and pressure dependency of the polymer solubility. Further, the morphology of the deposited films is investigated to establish a relationship with pressure.

- **Chapter 6:** This chapter examines the effect of solvent additive on solubility and self-assembly of polymers in supercritical fluids using isotactic polypropylene in n-pentane:acetone solution as the model system. The morphology of the deposited films in different solution systems is compared and a film formation model is proposed that can be applied to self-assembly of materials in other contexts.

- **Chapter 7:** This chapter provides a summary of the key results presented in this thesis and how these findings are relevant to further performance improvements of the organic optoelectronic devices. In addition, this chapter provides some future directions for further improvement of supercritical fluid deposition technique as a sustainable processing technique and achieving optimal morphology.

Chapter 2. Background

2.1. Organic Semiconductors

Organic semiconductors (OSCs) are a class of molecules and polymers with solid-state properties typically associated with semiconducting materials. For example, their lowest energy electronic absorption is in the visible or near infrared frequency range, they are insulating in their undoped state, and can be used in a variety of devices like light emitting diodes, field effect transistors, and solar cells.

Organic semiconductors have sp^2-hybridization, giving rise to π (bonding) or π* (anti-bonding) orbitals. As a result, the molecule planarizes and allows the π/π* state to be delocalized over several carbon atoms. This process is known as conjugation and the delocalization of electron density between neighbouring carbon atoms stabilizes this electronic configuration in the (π) configuration.[46] As the conjugation length increases, the energy difference between the highest occupied molecular orbital (HOMO) and lowest unoccupied molecular orbital (LUMO) decreases. The energy gap between LUMO and HOMO is analogous to the bandgap in a crystalline material such as silicon.[47] Therefore, such conjugated systems can act as semiconductors. For instance, the polymerization of ethylene can reduce the band gap energy from 6.7 eV for the monomer to almost 1.5 eV for stretch-oriented polyacetylene as shown in Figure 2.1.

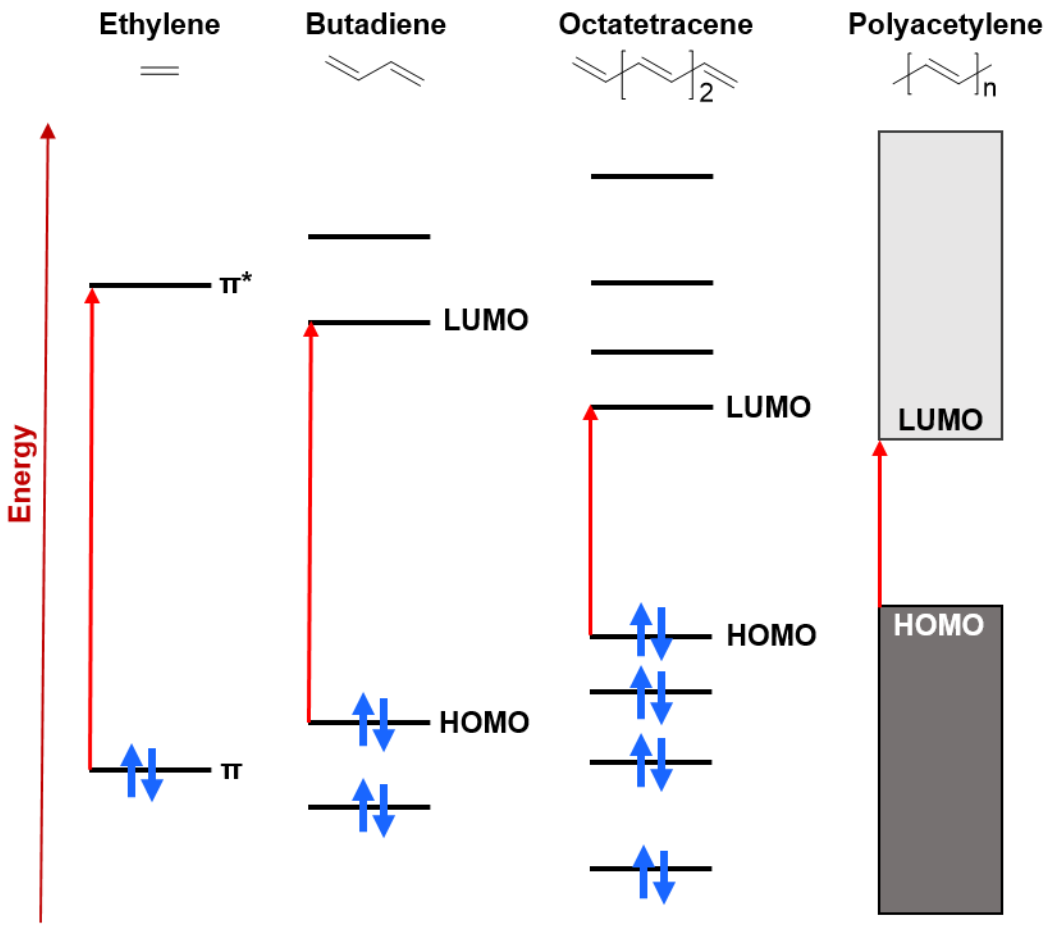

Figure 2.1. Schematic of energy-level splitting in alkenes with increasing conjugation length and the resultant decrease in bandgap.

Organic semiconductors can be divided into two different classes — small molecules (molecular crystals or thin films) and polymers. As illustrated in Figure 2.2, semiconducting small molecules are usually derivatives of flat, large, aromatic molecules such as polyarenes. In the case of semiconducting polymers, the polymer backbone is formed by a carbon chain with alternating single and double bonds or (hetero)aromatic rings.[48] Early examples of conjugated polymers include polyaniline, polythiophene, and polyphenylene vinylene. However, these polymers suffer from poor solubility, making them difficult to use in sophisticated devices. This challenge was addressed by the addition of side chains which improved polymer solubility in organic solvents.[49] However, it is now known that they can also play a significant role in polymer packing during thin film processing by altering electronic interactions.[50-52] The classic example of side chain impact on polymer semiconductor properties is the regiorandom versus regioregular poly(3-hexylthiophene) as will be discussed in more details in section 2.2.4.

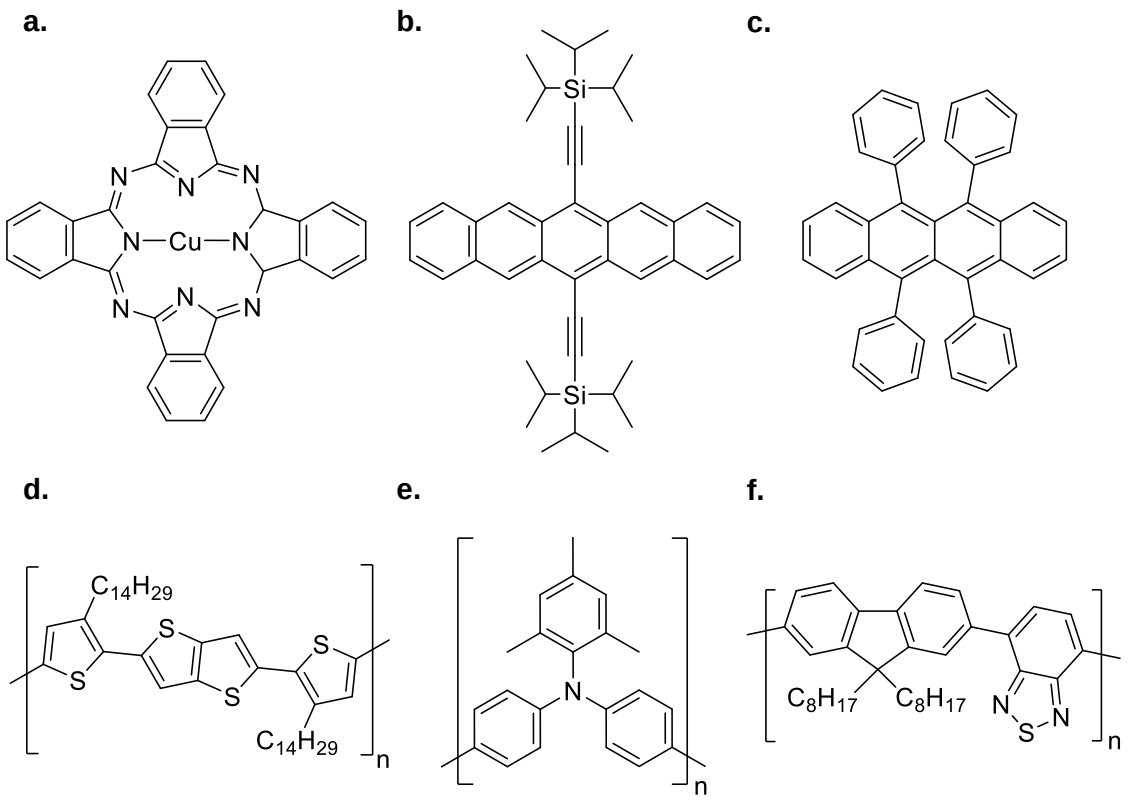

Figure 2.2. Chemical structures of some of the commonly used semiconducting small molecules and polymers: (a) Copper phthalocyanine, (b) 6,13-bis(triisopropylsilylethinyl) pentacene or TIPS-pentacene, (c) Rubrene, (d) Poly[2,5-bis(3-tetradecylthiophen-2-yl)thieno[3,2-*b*]thiophene] or PBTTT-C_{14}, (e) Poly(triaryl amine), Poly[bis(4-phenyl)(2,4,6-trimethylphenyl)amine] or PTAA, (f) Poly(9,9-dioctylfluorene-*alt*-benzothiadiazole) or F8BT.

2.1.1. Doping of Semiconducting Polymers

Semiconducting polymers lack intrinsic charge carriers (holes, or electrons); thus, charge carriers must be introduced into their system via doping in order to possess electronic functionality.[53] Different methods of doping of semiconducting polymers are summarized in Figure 2.3. The two primary methods of doping semiconducting polymers are chemical or electrochemical doping.

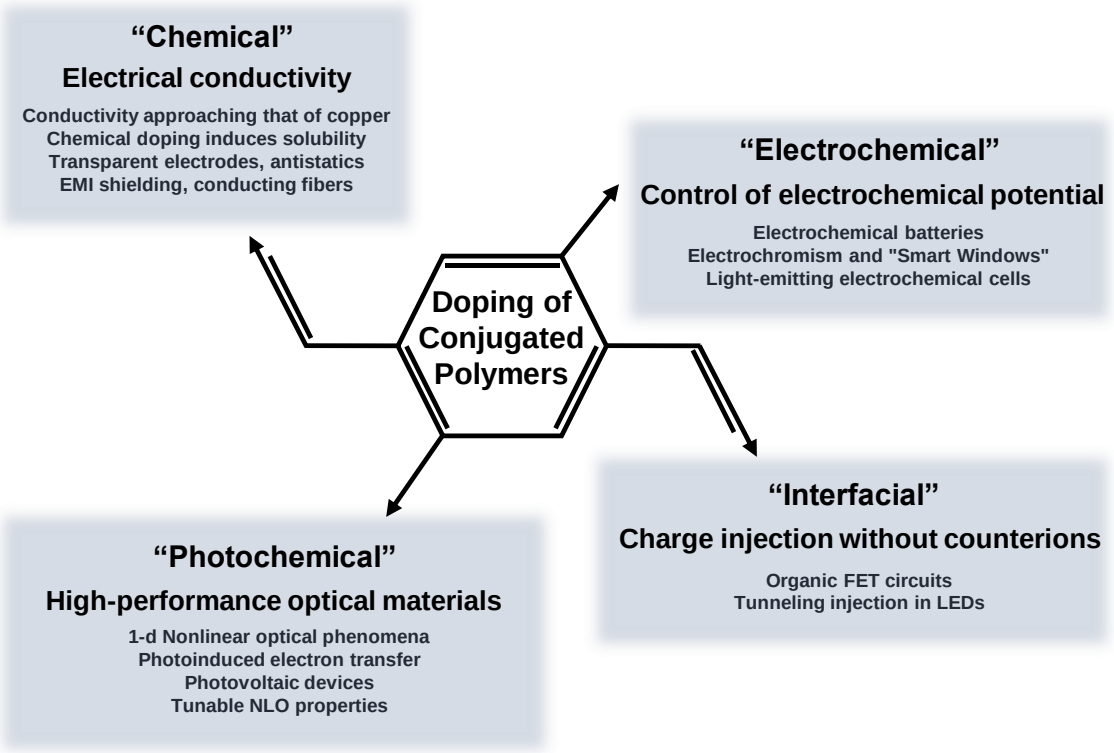

Figure 2.3. Doping mechanisms in semiconducting polymers and their application. Reprinted with permission from reference 54.

One of the methods of doping in organic semiconductors is analogous to inorganic materials and is illustrated in Figure 2.4. The generation of extra mobile charge is achieved by the addition of electron donors or acceptors to the material, a process known as chemical doping. In chemical doping, a polymer is exposed either to an oxidant (p-type doping) or reductant (n-type doping) where a direct charge transfer initiates the doping process.[55-57] Here is the example of chemical p-type doping where iodine is used as an oxidant and creat holes

$$(SC\ polymer)_n + \frac{3}{2}ny\ (I_2) \rightarrow [(SC\ polymer)^{+y}(I_3^-)_y]_n \quad (2.1)$$

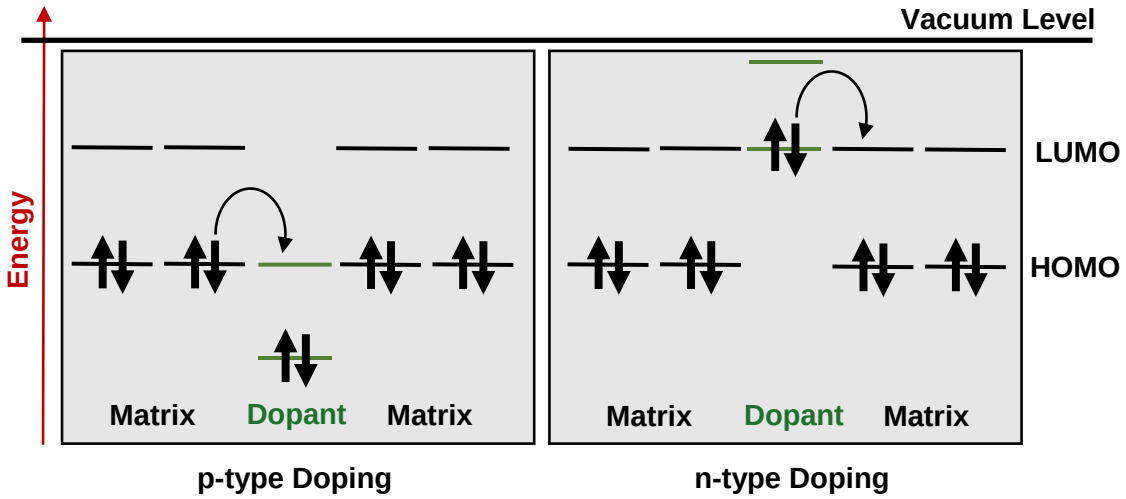

Figure 2.4. To achieve n-type doping in organics the dopant has to donate electrons to the LUMO states while p-type dopants obtain electrons from the HOMO states and create holes.

In contrast, the electrochemical doping process can take place in an electrolyte solution where the polymer-coated working electrode is submerged, and the doping level can be easily tuned by the applied voltage between electrodes. As a result of the created electrical potential difference, charges (electrons or holes) are delivered to the conducting polymer, while counter ions from the electrolyte diffuse into (or out of) the polymer. An example of an electrochemical p-type doping is illustrated here where lithium tetrafluoroborate is served as an electrolyte

$$(SC\ polymer)_n + [Li^+(BF_4^-)]_{solution} \rightarrow [(SC\ polymer)^{+y}(BF_4^-)_y]_n + Li_{electrode} \quad (2.2)$$

In Eq. 2.2 lithium is shown as being reduced at the counter electrode to maintain charge neutrality of the expression. This is not always necessary. The counter electrode itself can become charged in a manner similar to a capacitor to effect charge neutrality.

Additionally, charge carriers can be created in semiconducting polymers by photon absorption and charge separation of the photoexcited species. In contrast to chemical and electrochemical doping, where the induced electrical conductivity is permanent, the conductivity following photoexcitation and charge separation lasts only until the excitations are either trapped or decay back to the ground state.[54]

In the case of interfacial doping, the polymer is in contact with a metallic surface and charge injection happens from the metallic contacts, at the interface, by either adding electrons to the π* band or removing an electron from π band of the semiconducting polymer based on the voltage biased applied. Although the semiconducting polymer is oxidized or reduced during the process of interfacial doping, the doping mechanism is in contrast with chemical and electrochemical doping since it does not involve the introduction of any redox agent in the process. By introducing charges via an applied voltage, the semiconducting polymer can be used as the active layer in thin film diodes[58] and field effect transistors (FETs).[10,59,60] The development of polymer based light-emitting diodes (LEDs) are the result of dual carrier (electrons and holes) injection in metal-polymer-metal structures.[61]

2.2. Charge Transport Mechanism in Semiconductors

The electrical conductivity of a material is a measure of the amount of electric current it can carry under the influence of an applied electric potential and is denoted by the symbol (σ). The electrical conductivity is dependent on both external parameters such as electric field strength and temperature, as well as intrinsic material properties and the number of charge carriers. The conductivity can be expressed as the product of charge carrier concentrations (n), their electric charge (q), and charge carrier mobility (μ):

$$\sigma = nq\mu \tag{2.3}$$

As discussed previously charge carrier concentration in conjugated polymers can be changed by a variety of means. The relationship of mobility to temperature, electric field strengths, charge carrier density, molecular properties, and material properties such as thin film morphology can be quite complex. To develop a molecular-level description of carrier motion, it is common to express the mobility in terms of drift velocity, defined as the average velocity (v), and electric field strength (E):

$$v = \mu E \tag{2.4}$$

The Drude model is a simple model describing the factors that contribute to the conductivity of charges in materials by applying Boltzmann kinetic theory. Essentially, Drude model treats the free electrons in a metal like an ideal gas that move against a background of heavy fixed ions and is scattered randomly by nuclei. Though the Drude

model is limited, it can provide some insight into the types of processes that influence electrical conductivity. Based on Ohm's law, a constant electric force will result in a constant electrical current. On the other hand, electrons experience a force under the application of a constant electric field and accelerate according to Newton's laws. Therefore, it is essential to consider some kind of resistance to electron movement to be able to bridge these two theories. The Drude theory makes assumptions that electrons scatter with the probability of $\frac{dt}{\tau}$ at the dt time interval and that electrons stop upon scattering and return to zero momentum ($\overrightarrow{p'} = 0$). The average time between collisions is the scattering time (τ) and the distance travelled between collisions is known as the mean free path (l). After a collision, the electron velocity is randomly directed and therefore the average velocity is zero. However, electrons can still respond to external forces in between scattering events. The applied force can be due to applied electric (or magnetic) field that couples to the electron's charge, similar to the Lorentz force. The electron mobility can be quantified based on the electron velocity before the collision takes place by setting the Lorentz force equation equal to Newton's equation of motion and integrating from zero to the scattering time (τ).[62-64]

$$\mu = \frac{q\tau}{m_e} \tag{2.5}$$

where m_e is the electron mass. In the free electron gas model, an electron has the mass of m_e. Upon the application of an electric field, the average velocity of all electrons would reach their maximum value (known as drift velocity v_d). As a result, the current density for n mobile electrons per unit volume can be achieved by

$$J = \sigma E = -nqv_d \tag{2.6}$$

where n is the density of electrons and q is the electron charge. In order to make drift velocity (v_d) independent of applied electric field (E), the conductivity (σ) can be defined as a product of μ , where μ is the mobility equal to $\frac{v_d}{E}$.

2.2.1. Band Theory in Inorganic Semiconductors

In a single atom, electrons reside in distinct energy states in orbits and when many atoms are brought together to form a solid, the energy states mix to form a continuous set

of states (energy bands). There are 3 general forms of band structures in solids that is categorized solids into metals, semiconductors, and insulators. As shown in Figure 2.5, the valence band is consists of fully occupied energy states, while the conduction band is mainly unoccupied energy states. In metals, there is an overlap between the conduction and valence bands, resulting in the conduction energy bands being to some degree filled by electrons at any temperature, while the semiconductors and the insulators have fully filled valence bands separated by the band gap from the empty conduction bands at T = 0 K.[63] Band gap is the energy difference between the valence band maximum and conduction band minimum. As illustrated in Figure 2.5, the band gap is much narrower in semiconductors compared to insulators, allowing electrons that are thermally excited to contribute to conductivity by moving above the Fermi level. Fermi level in band theory represents the maximum energy state that electrons can populate at T = 0 K.

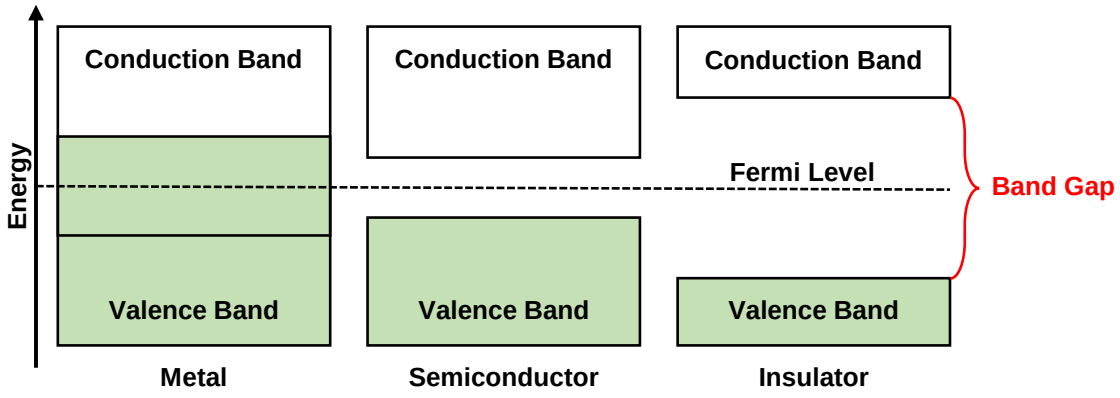

Figure 2.5. Schematic of band structures in metal, semiconductor, and insulator.

Figure 2.5 is an essential schematic for conceptualizing the band theory, however, it lacks meaningful information when it comes to describing the optical and electrical properties of metals and semiconductors. As a result, the real band structure in three dimensions is illustrated by $E(Energy) - k\,(wavevector)$ diagram (i.e. band structure diagram) to describe the relationship between the energy and wavevector of quantum mechanical states for electrons in the material. As shown in Figure 2.6, the $E - k$ diagram has a parabolic shape, either concave up or down, which is like the dispersion relation for free electrons quantum mechanically, where E is directly proportional to k^2.

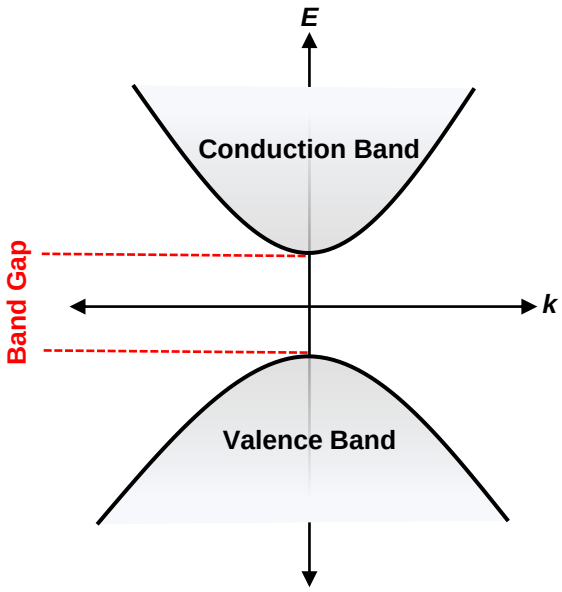

Figure 2.6. The reduced E-K diagram for a semiconducting material illustrating valence and conduction bands.

The electron in a periodic potential is accelerated relative to the lattice in an applied electric field such that its mass is equal to an effective mass (denoted m^*).

$$E = \frac{\hbar^2 k^2}{2m^*} \tag{2.7}$$

Based on Eq. 2.7, the m^* is not a fundamental constant and its value is dependent on the shape of the band. Specifically, the effective mass depends on the steepness of the parabola around the conduction band minimum or the valence band maximum.

$$m^* = \frac{\hbar^2}{\frac{\partial^2 E}{\partial k^2}} \tag{2.8}$$

Using equation (2.8), the effective mass for an electron in the conduction band or a hole in the valence band can be calculated.

In a perfectly crystalline network of atoms, such as silicon crystal, the charge carriers can move as plane waves (Bloch waves) with very high velocity. In other words, Bloch electrons possess wavefunctions delocalized over the entire crystalline lattice.[63,65] However, scattering of electron wavefunctions from phonons and defects in the crystal can reduce the mean free path of a charge carrier, lowering its charge carrier velocity.[66] Since the number of phonons increases at higher temperatures, the mean drift velocity

decreases with increasing temperature.[67] This is the hallmark of conduction via a band mechanism.

2.2.2. Charge Transport Mechanisms in Organic Semiconductors

The basic solid-state properties of organic semiconductors differ considerably from their inorganic counterparts. In organic semiconductors, every molecule is attracted to the neighboring molecule via the weak van der Waals interaction. As a result of weak intermolecular interaction in organic semiconductors, the charge carrier (electron and hole) mobility values are typically much lower than observed mobilities in their inorganic counterparts (typically less than 10 $cm^2 V^{-1} s^{-1}$, except for rubrene).[47,68]

Additionally, small changes in molecular packing can result in drastically different electronic properties and mobilities in organic semiconductors. A classic example exhibiting the impact of molecular packing is the comparison between tetracene and rubrene. Figure 2.7 displays the chemical structures of tetracene and rubrene accompanied with their molecular packing motifs. Rubrene chemical structure consists of a tetracene backbone with four phenyl rings attached to the two central fused rings (Figure 2.7.b) and has hole mobility as high as 40 $cm^2 V^{-1} s^{-1}$, while tetracene mobility reaches values of 2.4 $cm^2 V^{-1} s^{-1}$. [69,70] The origin of this outstanding transport property for rubrene is due to the presence of conduction band structure.[71-73] In rubrene, the strong intermolecular electronic couplings due to the slipped-cofacial packing of the π-conjugated tetracene backbones[74,75] results in electronic bands whose dispersion behavior associates closely with the band-like transport mechanism. In contrast, tetracene exhibits a flat band structure, indicating a very large effective mass, meaning that the charges are localized. This is an example of how molecular structure changes can impact the molecular packing and ultimately the charge transport. Hence, in addition to the chemical structure, other elements such as the relative positions of the molecules in the crystals can also readily influence molecular packing and result in drastic changes in electronic properties. Based on these, it is challenging to establish a general charge transport mechanism in organic semiconductors by applying the conventional charge transport descriptions.

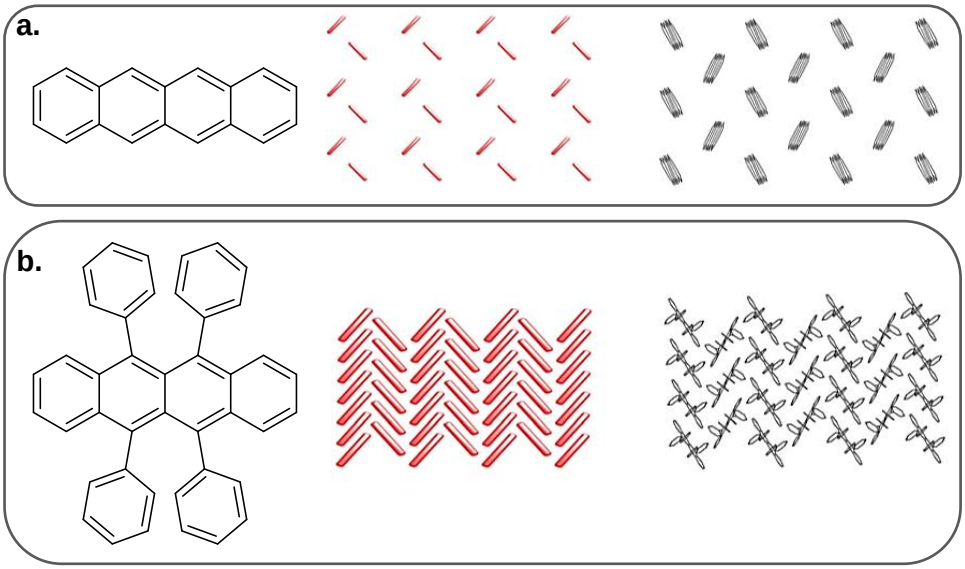

Figure 2.7. Molecular packing motifs in (a) tetracene with herringbone structure packing motif and (b) rubrene with slipped-cofacial packing of the π-conjugated tetracene backbones. All the hydrogen atoms are omitted for clarity. Adapted with permission from reference 76.

Thus far, there is not a universally accepted, general model describing charge transport in organic semiconductors. Nevertheless, a great deal is understood about the nature of charge transport in organic semiconductors with the most common models are band transport, polaronic transport, and disorder-based transport. The applicability of a model to a particular material (crystals as well as molecular and polymeric materials) depends on number of factors including the strength of electronic coupling, and the thin film structure.

Band-Like Transport

As discussed previously, the large values of charge carrier mobility in highly crystalline molecules such as rubrene[77] and TIPS-pentacene[78,79] indicates a transport mechanism similar to inorganic semiconductors where the charges move as highly delocalized plane waves in a conduction band with a mean free path that is larger than the nearest neighbor distance.[2] However, in contrast to the classical description of band transport which implies charge carriers are delocalized over a large distance compared to lattice spacing, the delocalization of electrons in organic semiconductors is limited to few molecules and in fact is not spatially fully extended to Bloch electrons.[80] Thus, the band-like mechanism occurs mainly in crystals featuring delocalized charge carriers.[81] However, not all molecules exhibit this behavior, and other mechanisms must be used for different

classes of organic semiconductors.[82,83] The band-like transport mechanism is mainly realized in highly ordered organic materials, whereas the more disordered the materials are, the more relevant hopping transport becomes.

Marcus Charge Transfer

In semiconducting polymers, Marcus theory is often invoked as a rational for charge transport. The basic Marcus theory is the proper model for redox reactions in polar environments, where low-frequency rotational vibrations and other solvent modes are treated classically. According to the Marcus theory, electron transfer can occur without breaking or making any bonds, through a sequence of transfers (jumps) over energy barriers. In Figure 2.8, the Marcus electron transfer path is indicated by a solid red line, where λ corresponds to the reorganization energy. Hence, the rate of electron transfer in Marcus theory can be expressed by the free energy barrier (ΔG) using the below equation

$$k_{\mathrm{CT}} = A \exp\left[-\frac{(\Delta G+\lambda)^2}{4\lambda k_{\mathrm{B}} T}\right] \tag{2.9}$$

where A is proportional to the electronic coupling between the initial and final state of the charge transfer. Based on Eq. 2.9, maximum charge transfer rate is achieved under conditions of $-\Delta G = \lambda$, when the transfer is barrierless, meaning the acceptor parabola crosses the donor state energy minimum. However, the more common scenario is that $\Delta G = 0$, making the reorganization energy the primary barrier to transport.

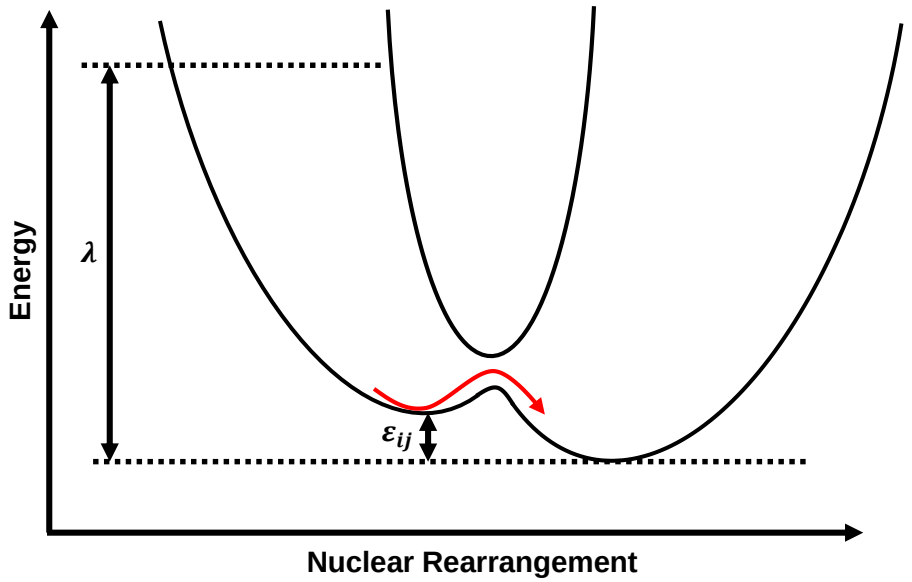

Figure 2.8. A schematic representing electron transfer in a biased double quantum well. λ is the reorganization energy, ε_{ij} is the difference in minimum of the potential energy wells. The Marcus hopping path is indicated by the solid-red arrow.

Marcus theory was first used by Brédas et al. to describe the charge transport in organic semiconductors.[84] Later on, Heeger presented the fundamental principles for charge transport in organic and polymeric semiconductors using Marcus theory.[54] In the case of semiconducting polymers, charge transport can be described as an electron transfer (hop) from a charged oligomer to an adjacent neutral oligomer. In the hopping regime, the fast charge transfer processes entail large transfer integrals and a weak coupling of the charges to the vibrations of the oligomer backbones. Therefore, Marcus charge transfer model is appropriate when the intermolecular transfer integrals are much smaller than the charge reorganization energy. However, the calculated mobility values are often underestimated in Marcus theory, especially when charge delocalization is present. For instance, a theoretical hole mobility calculated by Marcus theory for pentacene resulted in values ranging from 6 to 15 $cm^2 V^{-1} s^{-1}$,[85] while the experimental values for single crystal field-effect transistor reached mobilities of 15 to 40 $cm^2 V^{-1} s^{-1}$.[86]

Polaronic Transport

The term “polaron” was first introduced by Lev Landau to describe an electron that is moving in a dielectric crystal where the atoms shift from equilibrium to screen the electron charge.[87] During the early years of research in organic materials, the notion of polaron was adapted to describe the localization of charge carriers in molecular crystals

due to the interaction of charge carriers with the surrounding electrons and nuclei in the lattice attributed.[1] Depending on the interplay between the intra and intermolecular electron–lattice interactions, one can describe transport mechanism in different categories. For instance, in single-crystal pentacene, when the relative strength of the localization energy (E_1) is comparable to the electronic intermolecular interaction (J), the transport moves away from hopping to a polaronic transport. Although, the polaron becomes unstable for intermolecular interaction strength above 120 meV and transport becomes band-like (typically when $J >> E_1$).[88]

In the polaronic band model the delocalization of carrier wavefunction happens over many molecules and propagates with a small deformation of the lattice (Figure 2.9.a). In organic materials, the polaron movement is usually treated in terms of the small-polaron model introduced by Holstein and Friedman, where the carrier wavefunction is localized on one molecular site, as illustrated in Figure 2.9.b, in contrast to polaronic band model.[89,90] Later, the mechanism of the small-polaron hopping was verified by L. B. Schein et al. based on their observation in molecularly doped polymers.[91] The polaron transport was also reported in molecularly doped polymers by Parris et al. via combining the experimental observation and the Marcus rate model.[92] Recent experiments carried out by Blom et al. indicate that polaron hopping is an important mechanism in the conduction of charges in polymer films.[93]

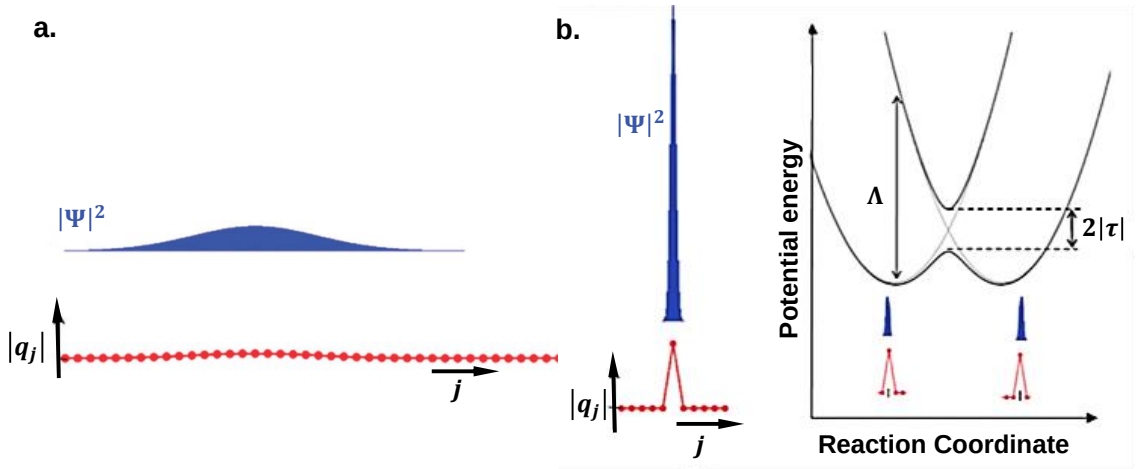

Figure 2.9. Schematic of (a) polaronic band model and (b) small-polaron hopping model. The hopping process to the neighbouring site is dependent on the reorganization energy (Λ) corresponding to the vertical transition energy between the two potential energy curves and the electronic coupling between the localized molecular orbitals (τ). Adapted with permission from reference 94.

2.2.3. Disordered-Based Transport in Organic Semiconductors

Because organic semiconductor thin films are disordered, charge carrier transport is often described in terms of disordered semiconductor theory. Much of the original theory was developed to describe the transport of charges in lightly doped semiconductors, which was later extended to polycrystalline and amorphous inorganic semiconductors. This section will review a few of the most important charge transport mechanisms in disordered semiconductor theory.

Nearest Neighbor Hopping

In disordered semiconductors, charge carrier transport at sufficiently low temperatures becomes dominated by hopping mechanism between localized state relatively close to the Fermi level. The probability distribution function of hopping is dependent on both the spatial and energetic separation of hoping sites. The hop to the nearest neighboring site is often the most dominant hop due to the exponential character of the hopping probabilities:

$$P_{ij} \approx \exp\left(-2\alpha R_{ij} - \frac{E_j - E_i}{k_B T}\right),\ E_j > E_i \tag{2.10}$$

$$P_{ij} \approx \exp\left(-2\alpha R_{ij}\right),\ E_j \leq E_i \tag{2.11}$$

where P_{ij} is the probability of a carrier tunneling from a localized state i (E_i) to an empty state j (E_j), α reflects the potential landscape surrounding the hopping sites, and R_{ij} is the hopping space range. Hopping conduction follows the simple Arrhenius-like law as

$$\sigma = \acute{\sigma} \exp[-\frac{\Delta E}{k_B T}] \tag{2.12}$$

$$\Delta E \sim \frac{1}{N E_F a^3} \tag{2.13}$$

where $\acute{\sigma}$ is a constant, ΔE is the activation energy, k_B is the Boltzmann constant, T is the absolute temperature, and a is the distance between nearest neighbours.

Variable Range Hopping (Mott and Efros–Shklovskii)

Variable range hopping (VRH) has been one of the widely used models to describe the charge transport in crystalline and non-crystalline materials including amorphous

conducting polymers.[95-97] Mott noted the hopping conductivity can be expressed in terms of the tunneling between localized wave functions and thermal activation

$$\sigma \propto \exp[-\frac{2r_{\mathrm{hop}}}{\xi_0} - \frac{\Delta E}{k_{\mathrm{B}}T}] \tag{2.14}$$

where r_{hop} is the temperature-dependent average hopping length, ξ_0 is the localization length at zero magnetic field, ΔE is the width of the energy interval near the Fermi level where hopping happens, and $k_{\mathrm{B}}T$ is the thermal energy. The transport is dominated by thermally activated nearest neighbor hopping in the high-temperature limit resulting in Arrhenius-like conductivity. On the other hand, at lower temperatures, the hopping is more energetically favorable to occur over distances that on average are larger than the nearest-neighboring distance.[98] As a result, the conductivity can be expressed based on the Mott's law of VRH

$$\sigma(T) \propto \exp[-(T_0/T)^S] \tag{2.15}$$

where S is defined based on the system dimensions and is equal to $1/(d+1)$. Another VRH-based conduction model is the Efros-Shklovskii (ES) which accounts for a vanishing density of localized electron states near the Fermi level as a result of electron-electron interactions.[99] This leads to the variable range hopping conductivity which redefines the exponent S in Equation (2.15) to a constant value of 0.5 regardless of dimensions.[99,100] At the extreme low temperature regime, the conduction occurs by field-assisted hoping, where the average hopping length follows an electric field dependence, resulting in the field-driven, highly non-linear, and temperature-independent transport. [101-103]

Multiple Trap and Release (MTR)

The multiple trap and release (MTR) model was introduced to depict the effect of shallow traps on the conductivity. Defects in a semiconducting material create localized electronic states in the band gap. Among all the mid-gap states, shallow traps are the most important one in the MTR model. There are two types of traps categorized based on their position to the mobility edge: shallow and deep traps. The mobility edge is defined as the energy level that separates the extended states from the localized ones in disordered materials. The shallow traps are located within a few $k_{\mathrm{B}}T$ of the mobility edge and can influence the charge transport. Thus, if a charge is trapped in one of the shallow

traps, it can be thermally activated and released to the band after a fixed trapping time (τ_{tr}) where it travels as a Bloch wave. Based on the MTR model, transport happens through a sequence of trapping events and thermal releases.[104,105] The MTR model has been successfully used to describe the temperature dependent and gate voltage dependent transport of OFETs using the below equation[106-108]

$$\sigma(T) \propto \sigma_0 \, \alpha \exp[-\frac{E_T}{k_B T}] \tag{2.16}$$

where σ_0 is the intrinsic trap-free conductivity, α reflects the ratio between the effective density of states near the transport band and the density of traps, and E_T is the mean energy of the trap state.

Figure 2.10 summarizes the band-like transport and the most common transport models discussed for disordered semiconductors, accompanied with the calculated mobility and temperature relationships predicted from these models. In these calculations, only the essential factors for the mobility–temperature relationship were varied, while keeping other parameters constant. In the band-like model (Figure 2.10.a), *α* corresponds to the scattering factor, indicating that as the temperature increases, the mobility drops sharper at lower scattering factor values. In the case of VRH model (Figure 2.10.b), T_1 is proportional to the size of the localized states and as it increases, the mobility decreases. However, at higher T_1 values, mobility becomes more temperature dependent. In the MTR model (Figure 2.10.c), E_T corresponds to varying mean energy of the trap states. The MTR model result highlights the impact of E_T on mobility to be more significant at lower temperatures. Overall, the MTR model predicts a decrease in mobility with an increase in energy of the trap states.

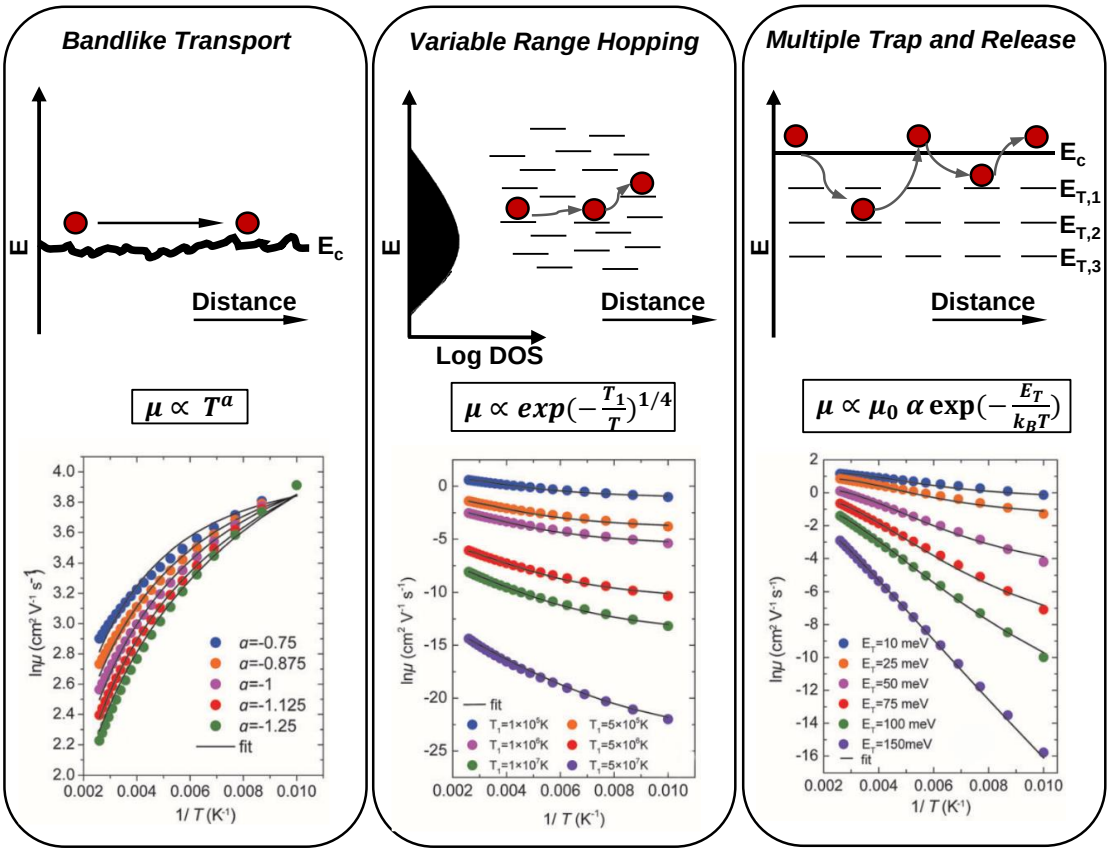

Figure 2.10. Schematic representation of main transport mechanisms in organic semiconductors with the temperature dependence of the mobility calculated by different transport models. Adapted with permission from reference 109.

2.2.4. The Influence of Microstructure on Charge Transport in Semiconducting Polymers

In the previous section, the charge transport physics of organic semiconductors and different transport mechanisms were discussed in detail. In this section, the attention is focused on the structural parameters influencing the charge transport in organic semiconductors. Understanding the structure-property relationship in organic semiconductors is essential for charge carrier mobility enhancement by improving the ability to control the microstructures.

The macroscopic electronic properties of organic semiconductors are not only influenced by the molecular structure and the chemical nature, but also the solid-state assembly of the components (polymers or molecules).[110-112] Because the length scales of polymer semiconductor devices are typically larger than the chain length the effective transport of charges in a semiconductor device requires that the charges be able to move

both rapidly along the chain and easily pass from chain to chain.[113] Thus, charge transport in conjugated polymers averages local properties, developing at the nanometer scale, over distances orders of magnitude larger. This highlights how vital it is to investigate processes across multiple length scales when studying charge transport in conjugated polymers.

There are many different morphologies that semiconducting polymers can adopt. The earliest systems were largely amorphous and exhibited low charge carrier mobilities. Later with the advent of solubilizing side chains, polymers which adopted more crystalline structure were created, most notably, regioregular P3HT. This system possesses considerably high charge carrier mobility and as such has become an important benchmark for discussing the relationship between thin film morphology and charge transport. Figure 2.11 shows some important considerations for describing the thin-film morphology of regioregular P3HT.

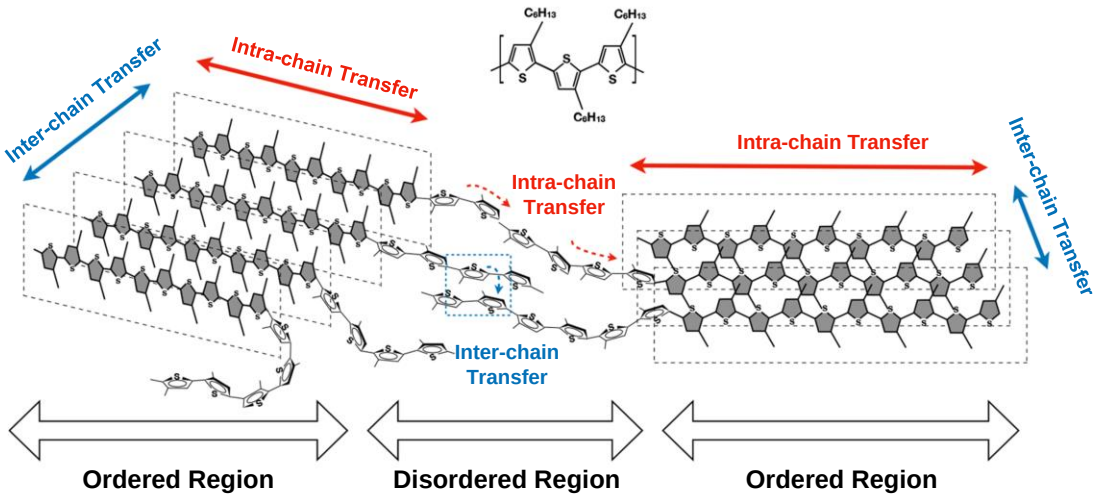

Figure 2.11. Charge transport processes and disorder at different length scales in a two-dimensional sheet of edge-on regioregular P3HT. Reprinted with permission from reference 114.

Semiconducting polymers, with semicrystalline nature, form thin films with ordered regions (crystallites) distributed throughout a disordered (amorphous) matrix. As illustrated in Figure 2.11, the charge transport in ordered regions of polymer thin films is governed by an intra-chain pathway along the π-conjugated backbone and an inter-chain pathway along the π-π overlaps between the face-to-face π-π stacked backbones.[115,116]

However, the charge transport can also take place between the adjacent ordered regions. For example, long polymer chains, known as polymer tie chains, link crystallites in proximity to each other.[117,118] As expected, the mobility on the same chain is orders of magnitude larger than that measured over macroscopic distances.[119] For example, the mobility of charges along isolated ladder-type polymer chains is reported to be as high as 600 $cm^2 V^{-1} s^{-1}$ whereas the intra-chain mobility is found to be 30 $cm^2 V^{-1} s^{-1}$.[120] Thus, charge transport is limited by the most difficult (longest time scale) transport processes and is therefore dominated by the transport between crystallites.[113] As mentioned previously, transport between crystallites is mainly through the polymer tie chains taking either a direct tie line path between two crystallites, or a path requiring inter-chain hopping. Based on Monte Carlo simulations, the slow interchain hopping is predicted to be the dominant path at low fraction crystallinity, whereas at higher fraction crystallinity, the on-chain mobility limits transport.[118]

Given the significant impact of microstructure on charge transport in polymer semiconductors, the processing condition is as influential parameter as the chemical structure in the charge transport processes.[121] The local packing of polymer chains can dramatically change conduction pathways on longer length scales and result in different mobility values. The challenge is that the local packing is highly dependent on different parameters such as the monomer structure (regioregularity), polymer molecular weight (*Mw*) and molecular weight distribution (M_{WD}),[122] the degree of alignment of polymer backbones (chain rigidity),[123] side-chain length,[124] and processing conditions, making it difficult to predict the morphologies on such multiple length scales.

The Role of Regioregularity

It has been demonstrated that the regioregularity (the percentage of head-to-tail linkages between monomer units in the polymer backbone)[125] affects the kinetics and thermodynamics of polymer self-assembly and consequently film morphologies. As shown in Figure 2.12.a, when alkyl chains are introduced in the thiophene dimers, there are three possible configurations based on the arrangement of alkyl chains: head-to-head (HH), head-to-tail (HT), and tail-to-tail (TT). Subsequently, there are four different regioisomeric thiophene triads (HH–TT, HT–HH, HT–HT, and TT–HT, Figure 2.12.b). As the number of monomer units increases in the polymer chain, the side chains can be arranged in a repeating pattern of $(HT\text{-}HT)_n$ and form a regioregular isomer (Figure 2.12.c). On the other

hand, in the regiorandom isomer, there is no established pattern for the arrangements of side chains and the placement of side chains is arbitrary (···HT-TH-HT-HT-TT-TH···).

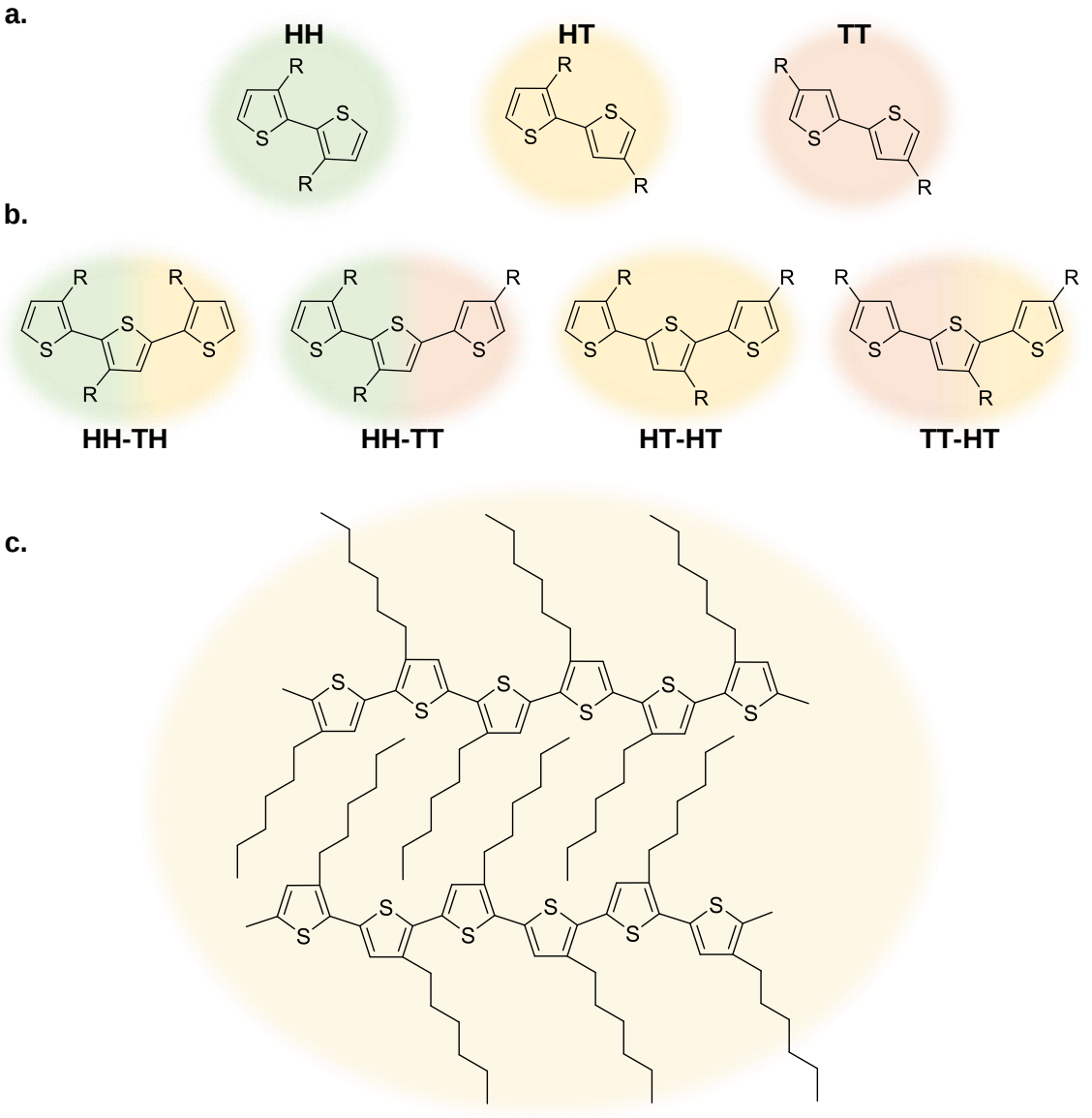

Figure 2.12. The specific relative arrangement of the side chains in a chain defines different configurations. (a) Structures of possible couplings in the dimers of 3-alkylthiophene rings (H:head, T:tail). (b) Structures of possible regioisomeric triads (HH–TT, HT–HH, HT–HT, and TT–HT), of which HT–HT is the regioregular isomer and displays better solid-state packing of the polymer. (C) The solid-state packing efficiency of HT-coupled P3HT.

In the case of P3HT, the regiorandom version has a twisted chain conformation with poor packing and low crystallinity.[126] On the other hand, the polymers in the regioregular fashion possess planar conformation, assembling into more crystalline

structures with lamella packing and better π-stacking.[126-128] When the alkyl chains are introduced in the thiophene units in regioregular fashion, head-to-tail (Figure 2.12), the alkyl chains trigger their interdigitation which in turn forces the polymer chains to assemble into lamellae. The regioregular frame has shown to increase the charge carrier mobility several order of magnitude due to the delocalization of polarons over several molecules.[129,130] Additionally, a comparison study showed that regioregular P3HT (>91% of HT attachment) formed lamellae with edge-on orientation with respect to the substrate, whereas less regioregular P3HT (~80%) exhibited face-on orientation and mobilities several orders of magnitude lower.[38,113]

The Role of Molecular Weight

Molecular weight of a semiconducting polymer can have a profound effect on its thin film structure and consequently, its charge carrier mobility. It is typically observed that low molecular weight polymers have higher crystallinity than their high molecular weight counterparts, with crystallinity being correlated with higher charge carrier mobility in the case of regioregular vs. regiorandom P3HT. However, it has been reported for several conjugated polymers that despite the morphology analysis showing higher degree of crystallinity in low-M_W polymer films, higher charge carrier mobilities is usually achieved by higher MWs.[131-133] This behavior is due to an increase of polymer chains content that are long enough to bridge between crystalline domains and enable electrically connective pathways (Figure 2.13).[134-136] For instance, the mobility in P3HT-FETs increases from 10^{-5} to 0.1 $cm^2 V^{-1} s^{-1}$ within a relatively narrow range of molecular weights (2–50 $kg.mol^{-1}$) and then saturates. Furthermore, higher charge carrier mobility in high-*Mw* P3HT has been attributed to the reduction of hopping events and ensuring good electrical connectivity. This is due to the longer chains allowing charge carriers to travel longer distances on a chain rather than hopping to another chain.[137,138]

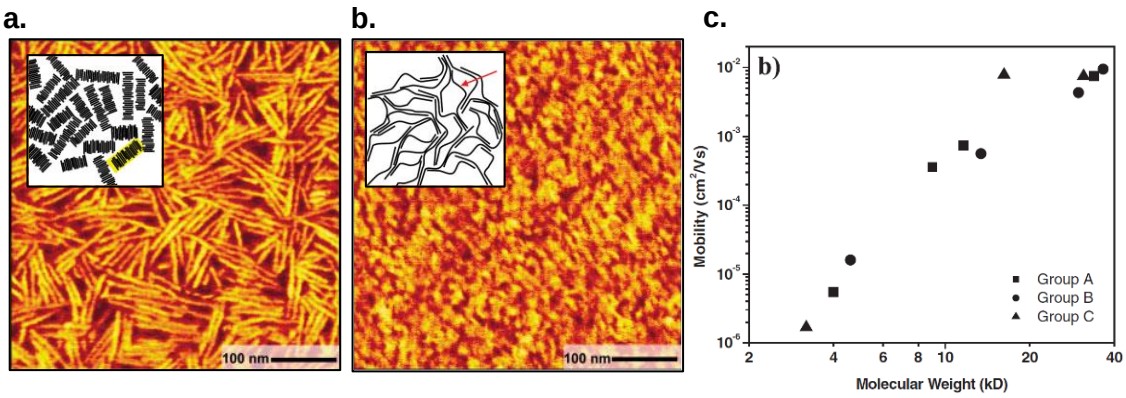

Figure 2.13. P3HT films morphology as evidenced by AFM. (a) Crystalline rod-like morphology of M_n = 3.2 kD and (b) nodule structure for M_n = 31 kD. (c). Plot of field-effect mobility versus the number average molecular weight. Group A and B refer to the bromine-terminated polymers modified by different routes and group C is the methythiophene-terminated polymers. Reprinted with permission from reference 134. Schematics are transport models in low and high-*Mw* films. Charge carriers are trapped on nanorods (highlighted in yellow) in the low *Mw* case, while long chains in high-*Mw* films bridge the ordered regions and soften the boundaries (marked with red arrow). Reprinted with permission from reference 135.

The Role of Chain Rigidity and Side-chain Unit

The rigidity of polymer chain is computed by its persistence length (L_P), the length of chain over which the chain orientation remains similar. Persistence length defines the regimes across which theoretical treatments of chain conformations vary.[139] The polymer behaves like a flexible chain if the contour length (L_C, the length of a chain at its maximum physical extension) is significantly larger than L_P and is considered a rigid rod when L_C of a chain is considerably smaller than L_P. In the intermediate regime when L_C is comparable to L_P, the semiflexible chain is described by a worm-like chain.[139,140]

Most semiconducting polymers are classified as rod-polymers due to their stiff and rigid backbones.[141,142] In particular, the fairly rigid thienothiophene units planarize the backbone which enhances the π–π stacking and promote intra- and intermolecular order and efficient charge transport.[143] FETs based on PBTTT can reach mobilities of up to 0.72 $cm^2\ V^{-1}\ s^{-1}$ after annealing into the mesophase, while high performance donor-acceptor polymers has demonstrated mobilities as high as 3.6 $cm^2\ V^{-1}\ s^{-1}$ due to their higher persistence length.[115,144,145] The higher persistence length also facilitate the connectivity between polymer chains, which critically control structural parameters, including the fraction and size of ordered regions and the distance between them.[117,146]

Due to the challenges correlated with the solubility and processability, often the alkyl functionalities are required for very rigid and high M_W polymers. However, the chain rigidity of conjugated polymers is very sensitive to the addition of alkyl chains and ultimately alters the microstructure of the material in the solid state.[147] The side chains separate the conjugated backbones and as a result the intermolecular overlap decreases.[148] Thus, the challenge is to find a side-chain chemistry that achieves polymer solubility without any detrimental effect on packing and mobilities.[149,150] For instance, in cyclopentadithiophene-benzothiadiazole copolymers, the π-stacking distance decreases from 3.8 to 3.5 Å by moving the branch point further away from the conjugated backbone and as a result the mobility values span from 10^{-4} to 0.41 $cm^2 V^{-1} s^{-1}$,reaching their highest value when the branch point is furthest from the polymer backbone.[151]

The Role of Processing Conditions

The control of thin film morphology is not only dependent on the intrinsic molecular parameters to achieve a self-assembly of the polymers into a certain degree of macroscopic ordered regions. But also, extrinsic parameters such as device architecture optimization and material processing conditions strongly affect the morphology.[110] Indeed, different processing techniques offer control over macroscopic self-assembly to the level that power conversion efficiency,[152-154] carrier mobility,[35,155] and conductivity in polymer electronic devices vary several orders of magnitude based on the morphology.[156,157]

Processing parameters acting as the primary handles for greatly influencing morphology of semiconducting polymers in thin films are solvent,[158-160] solvent additives,[153,161,162] deposition methods,[113,155,163-165] postdeposition treatments,[166-168] and surface treatments of the substrates.[169,170]

The impact of processing condition on thin film morphology is illustrated in Figure 2.14, which shows AFM images of P3HT films cast by three different methods under identical conditions. In the case of dip-coating and spin-coating, chloroform was used as the solvent and drop-cast films were obtained from a solvent mixture of chloroform and tetrahydrofuran (14:3, v/v). While there are rod-like structures in spin-coated films from low molecular weight samples, the films are almost featureless at high M_n. In comparison, the slow solvent evaporation by dip-coating results in well-defined nanostructures that are consistent in the wide range of molecular weight.[155] Furthermore, the studies of charge transport in ultrathin dip-coated films (thickness of a few nanometers) proved the impact

of such slow solvent evaporation by exhibiting mobilities as high as 0.2 $cm^2 V^{-1} s^{-1}$.[31] In P3HT spin-coated layers, the microcrystalline order can be significantly improved by using high boiling point solvents such as trichlorobenzene (TCB), as evidenced by X-ray diffraction and AFM.[159] This also causes a significant enhancement of the charge carrier mobility compared to layers cast from chloroform.

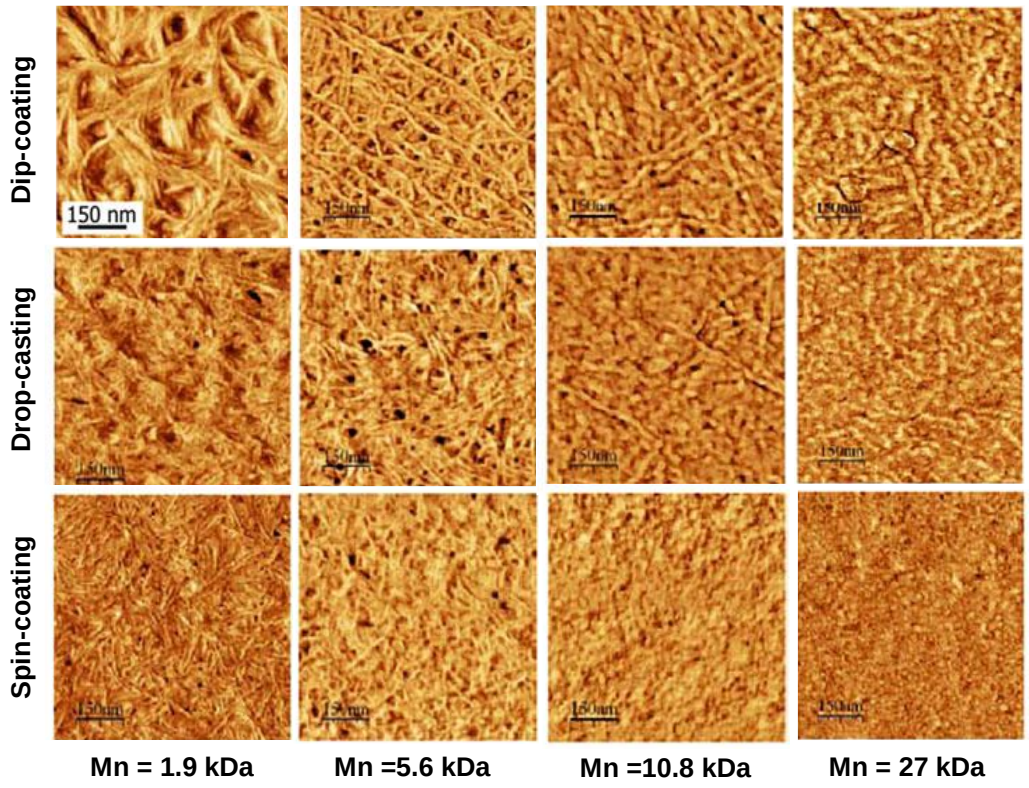

Figure 2.14. AFM phase images of thin RR-P3HT films of different molecular weight achieved by three different casting techniques. Adapted with permission from reference 155.

It is intriguing that even the level of molecular pre-aggregation in solution prior to deposition can impact the deposited film morphology.[171-173] For instance, thin films of P(NDI2OD-T2) deposited via spin-coating using acetonitrile as the solvent do not reveal any significant features when imaged using a polarized light microscope and also the topography does not reveal any evident texture. In contrast, the same deposition using dichlorobenzene results in 10–20 nm wide fibrillar-like supramolecular structures visible in film topography images (Figure 2.15). Despite the strong directional coherence within bundles (in the order of hundreds of nanometers long),[174] there is no order present between bundles which explains the lack of any features when imaged via optical polarized microscope. The highest degree of aggregation in solution is prompted by

solvents such as toluene or mesitylene, exhibiting marked birefringence, with continuous features extending to millimeters. Regarding the film topography, fibrils are observed similar to DCB case, however directionality is preserved on much wider scales which is the basis of the observed birefringence (Figure 2.15).

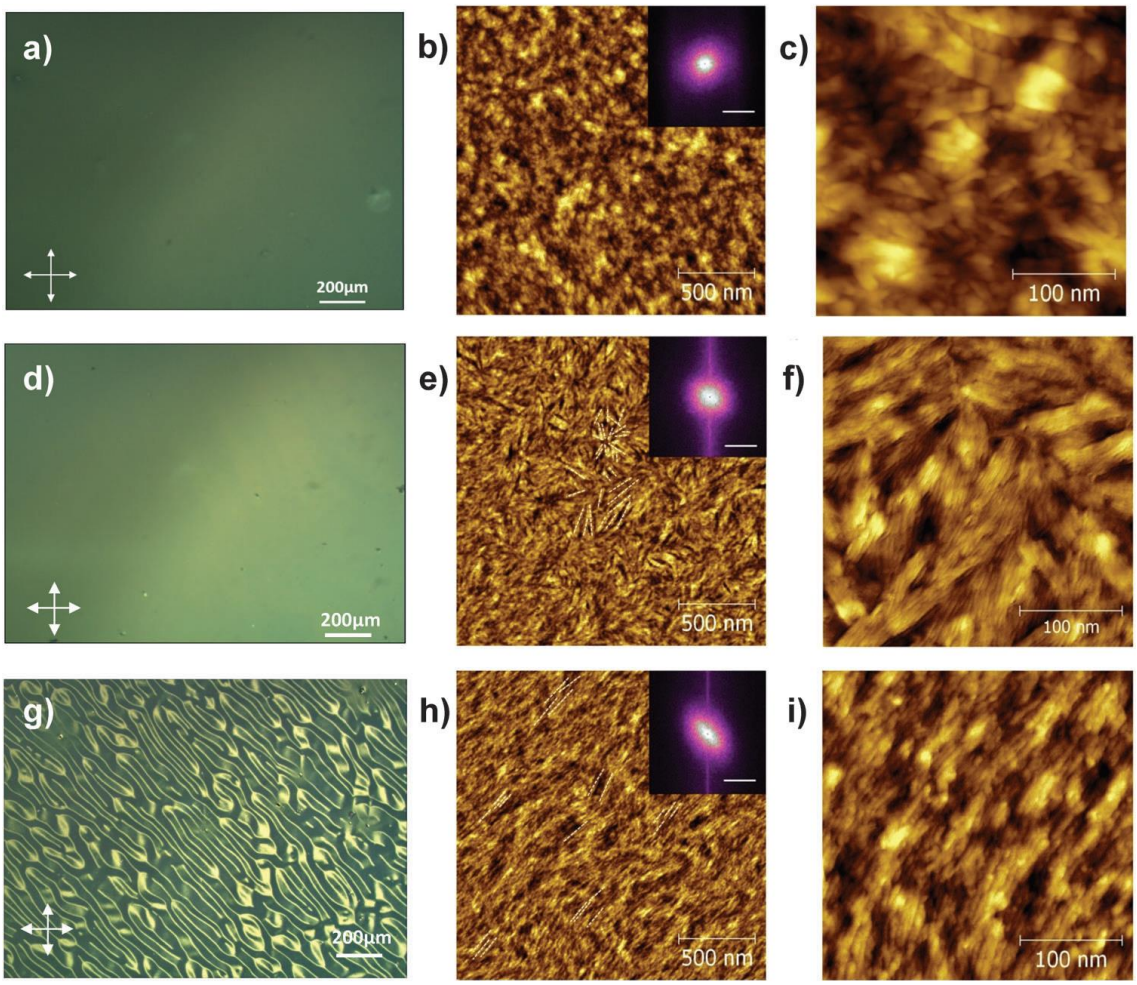

Figure 2.15. Thin films of P(NDI2OD-T2) deposited by spincoating from solutions CN:CF (a, b, c), DCB (d, e, f), and toluene (g, h, i). Cross-polarized optical microscope images (a, d, g) and AFM topography images (b, c, e, f, h, i). Reprinted with permission from reference 175.

The link between charge transport and crystalline texture (the out-of-plane orientation of crystallites with respect to the substrate) was first demonstrated in a TFT showing three orders of magnitude higher mobilities because of P3HT films containing edge-on oriented crystallites (Figure 2.16.a) rather than face-on textured crystallites (Figure 2.16.b) by altering the regioregularity of P3HT and the casting method.[113] However, it was later proven that P3HT regioregularity in the 90–97% range affects the

overall crystallinity of the film but has little impact on the texture.[176] Further studies with X-ray absorption near edge structure (NEXAFS) in highly regioregular P3HT films prove that plane-on orientation is preferred at fast spin speed due to the rapid drying of the film.[177] Thus, it is likely that texture is controlled by a combination of regioregularity and film-formation kinetics.

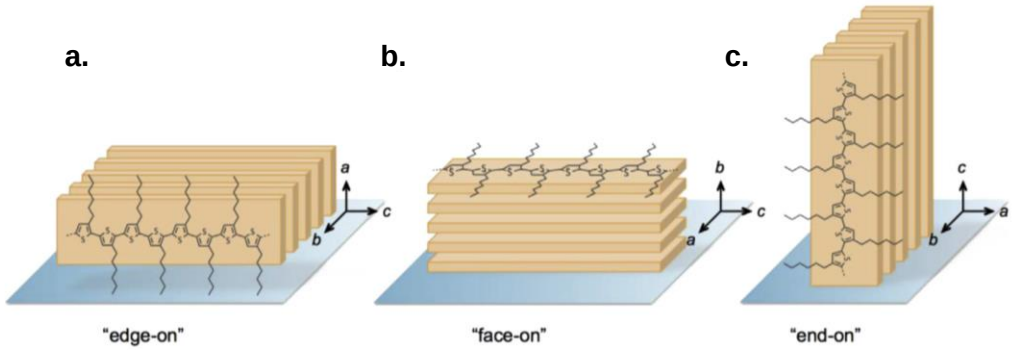

Figure 2.16. Molecular orientation of P3HT in thin layers with respect to the substrate surface. (a) edge-on, (b) face-on, (c) end-on. Reprinted with permission from reference 178.

Charge transport is extremely sensitive to the nature of the surface on which the molecules self-assemble as it can significantly influence the film texture. For instance, substrate functionalization with self-assembled monolayers (SAMs) such as hexamethyldisilazane, octadecyltrichlorosilane, and γ-aminopropyltriethoxysilane directs the preferential polymer backbone orientation relative to the substrate and results in an edge-on texture.[122, 179-181] On the other hand, substrates treated with octyltrichlorosilane leads to the formation of a face-on oriented P3HT monolayer (ML).[180,181] As illustrated in Figure 2.17, depending on the surface properties obtained by SAMs of different end-group functionalization, the P3HT chains in the monolayer films can adopt two different conformations (edge-on and face-on).

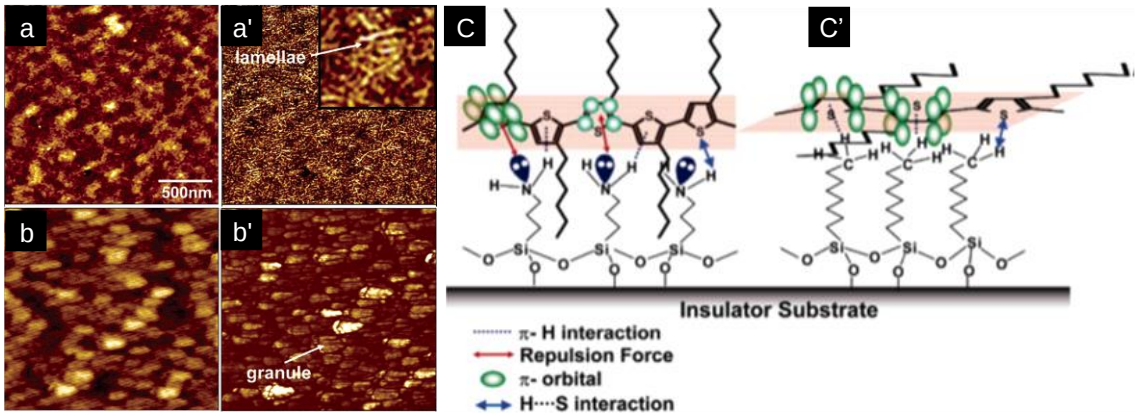

Figure 2.17. Molecular orientation of P3HT on different surfaces. Tapping mode scanning force microscope images of a regioregular P3HT ML_NH_2 film [(a) topography and (a') phase], and of a P3HT ML_CH_3 film [(b) topography and (b') phase]. Schematic representation of the different conformations [(c) edge-on and (c') face-on] according to interfacial characteristics. Adapted with permission from reference 180.

To summarize, to achieve the maximum charge carrier mobilities of organic semiconductors, it is essential to ensure that charges are able to move from molecule to molecule (chain to chain) without experiencing scattering or electronic trapping. A broad investigation of the conditions that influence charge carrier mobilities have been carried out, indicating many factors such as molecular weight, regioregularity, and processing conditions. In particular, the plethora of parameters that can be tailored using different processing conditions offers a unique opportunity to control the macroscopic electronic properties of organic semiconductors.

2.3. Fluid Mechanics

The self-assembly process that controls polymer film morphology occurs in solution during film formation. This statement also holds true for polymer self-assembly in supercritical fluids. As such, a rudimentary understanding of important concepts in fluid mechanics is important to understanding physical supercritical fluid deposition.

Fluid mechanics describes the effects of forces and energy exerted on fluids (liquids, gases, and plasmas) and is divided into fluid statics (fluid at rest) and fluid dynamics (fluid in motion). Fluid mechanics is a key part of chemical engineering and is used to design reactors and processes for large scale chemical manufacturing. In the context of organic semiconductors, fluid mechanics governs the process of spin coating

and is an important consideration when designing inks for printed electronics. As will be demonstrated later, the fluid mechanics operating in a supercritical fluid vessel can exert an important influence on the self-assembly of thin films.

The fluid movement is described by the known laws of physics for mass, momentum, and energy conservation as embodied by the Navier–Stokes equations. However, solutions of the Navier–Stokes equations are quite difficult, and only a small number of analytical solutions have been obtained and are typically limited to reduced dimensions and smooth flow. In general, chaos and turbulence have prevented the development of analytical solutions, and researchers frequently employ computational fluid dynamics to design everything from airplanes to underwater bridge supports.

2.3.1. Laminar and Turbulent Flow

Determining whether flow is laminar or turbulent is a vital first step to understanding the fluid dynamics at play in each context. Streamlines describe the path followed by a parcel of fluid as it traverses the region of interest with closely spaced streamlines associated with faster flow. Laminar flow is described by smooth streamlines, describing well-defined paths of fluid movement. In addition, a laminar flow can be distinguished as either steady or unsteady. The flow is considered steady when its properties (e.g., temperature, pressure, velocity, and density) at different points are independent of time. In contrast, the flow parameters are a function of time in an unsteady flow. It is important to note that steady flow does not necessarily mean fluid is flowing at a constant acceleration or velocity as their properties might be a function of space. For instance, the steady flow in a curved pipe experience acceleration through moving to a different spatial position.

On the other hand, turbulent flow is described by irregular fluctuations of streamlines and unstable flow. Intuitively, one expects smooth flow at low speeds. As the flow speed increases, so does the propensity for turbulence, and eventually, the streamlines become complicated, the flow becomes turbulent and instabilities occur (Figure 2.18). In addition, smooth flow is favored in viscous liquids which resist the influence of rapidly changing forces. The transition from laminar to turbulent flow is dependent on other parameters like density, pressure, and temperature. These influences can be combined into a dimensionless number called the Reynolds number (Re)

$$Re = \frac{\upsilon L}{\nu} \tag{2.17}$$

where ν is the fluid kinematic viscosity ($m^2\ s^{-1}$), υ is the flow speed ($m\ s^{-1}$), and L is the length of the sheer layer (m).

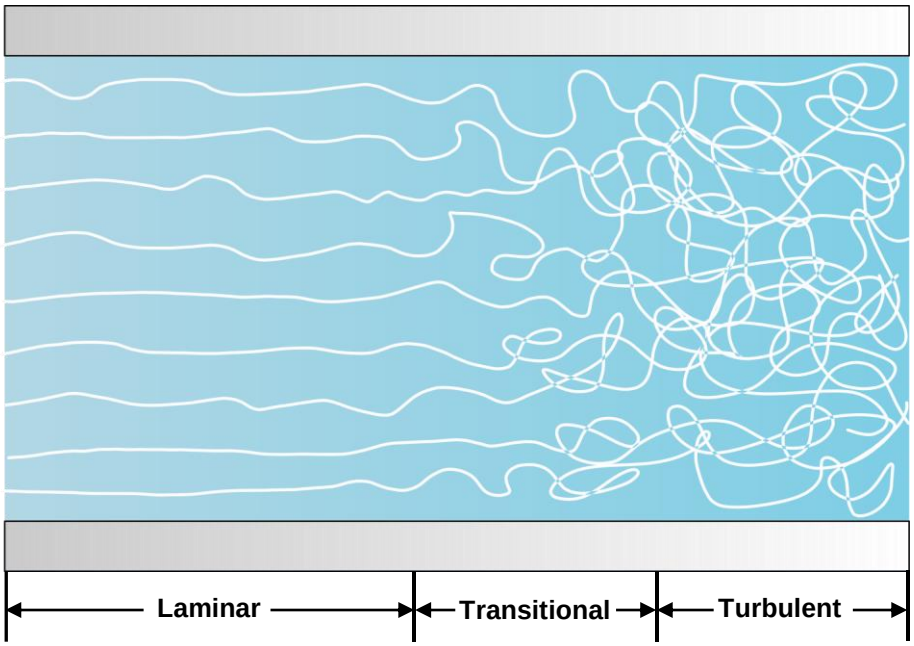

Figure 2.18. The three regimes of flow demonstrating the transition from laminar flow at low Reynolds number to turbulent flow at high Reynolds number.

2.3.2. Heat Transfer via Convection or Conduction

The research described in this thesis deals with heat transfer in supercritical fluids. It is therefore useful to describe a few general aspects of heat transfer not typically discussed within the traditional chemistry curriculum. Heat transfer is classified into three main mechanisms: conduction, convection, and radiation, which will be discussed briefly in this section.

Conduction (or diffusion)

In the absence of any material flow, conductive heat flow involves the transfer of heat from one location to another by transferring molecular agitation, often in the form of acoustic phonons for electrically insulating materials. The principle of thermal conduction (Fourier's law) connects the rate of heat transfer to the temperature gradient and the area through which the heat flows. The differential form of Fourier's law of thermal conduction

is provided in Equation (2.18), where $\vec{q}$ is the local heat flux density (W m^{-2}), k is the materials conductivity (W m^{-1} K^{-1}), and $\vec{\nabla}T$ is the temperature gradient (K m^{-1}).

$$\vec{q} = -k\vec{\nabla}T \tag{2.18}$$

It should be noted that a material's thermal conductivity changes with temperature. However, for many materials the variation can be ignored over a range of useful temperatures.

Convection

Convection is a heat transfer mode via the motion of fluid (matter) due to the temperature (density) gradient within the material. These fluid motions are called convection currents, and the convective movement of fluid persists until there is no temperature gradient present between regions. If the convective heat transfer is a result of buoyancy forces, it is considered natural convection. The buoyancy forces result from density differences due to variations of temperature in the fluid. On the other hand, forced convection involves driving the fluid transfer from one location to another by use of external mechanical means, such as a pump or fan.

Radiation

Radiative heat transfer occurs when matter emits thermal energy via photons as electromagnetic waves. In the absence of a medium, thermal radiation can be propagated through a vacuum and its release rate is proportional to its temperature to the fourth power ($\propto T^4$). Temperature also affects the frequency and the wavelength of the radiated waves that constitute an emission spectrum.

Table 2.1. Fundamental modes of heat transfer and their differences.

Conduction	Convection	Radiation
Occurs between media by direct contact	Occurs within the medium	Occurs through electromagnetic waves
Can occur in static object	requires fluid motion	can occur across a vacuum
Fourier's law of thermal diffusion	Navier Stokes equation	Blackbody radiation

Table 2.1 summarizes different modes of heat transfer and their properties. In a situation where both conduction and convection mechanisms are feasible for heat transfer, the dominant mode is predicted by the Rayleigh number.

2.3.3. Rayleigh Number

The Rayleigh number (Ra) is a parameter that measures the relative importance between the effects of the buoyancy forces and the effects of the viscosity forces and thermal conduction. The interplay between the gravitational force pulling the cooler fluid down and the viscous damping force in the fluid is expressed by a non-dimensional factor, Rayleigh number, specified as

$$Ra = \frac{g\beta\Delta T L^3}{\nu\alpha} = Gr \times Pr \tag{2.19}$$

where g is acceleration due to gravity, β is coefficient of thermal expansion of the fluid, ΔT is temperature difference, L is length, ν is kinematic viscosity and α is thermal diffusivity of the fluid. The Grashof Number (Gr) represents the ratio of the buoyancy force due to the spatial variation in fluid density to viscous force acting on a fluid in the boundary layer. The Prandtl Number (Pr) describes the relationship between momentum diffusivity and thermal diffusivity.

The magnitude of the Rayleigh number can be used for both characterizing the fluid's flow regime and predicting convectional instabilities. As shown in Figure 2.19, the turbulent flow regime corresponds to the higher range for the Rayleigh number (Figure 2.19.c), while the lower range Rayleigh number is related to laminar flow (Figure 2.19.b). Below a certain value of Rayleigh number, there is no motion in the fluid and heat transfer is purely via conduction (Figure 2.19.a) and when it passes a critical value heat transfer happens by natural convection. There is typically no convective motion at values lower than the critical value of Rayleigh number, Ra < 1700.[182]

Additionally, the Rayleigh number can be used as a criterion to predict convectional instabilities and convection cell appearance. In the case of spatially periodic flow, commonly observed at lower values of Rayleigh number, the convection cells look identical and closely pack. Most frequently, the idealised convection cells are categorized into two-dimensional rolls (Figure 2.19.d), square cells (superpositions of two sets of mutually perpendicular rolls), and hexagonal cells (Figure 2.19.e, superpositions of three sets of rolls rotated by an angle of 2π/3 to one another). However, as the Rayleigh number value increases and the turbulent convection becomes dominant, the thermal boundary layer thickness decreases linearly and results in a sharp drop in temperature near the boundary layers.

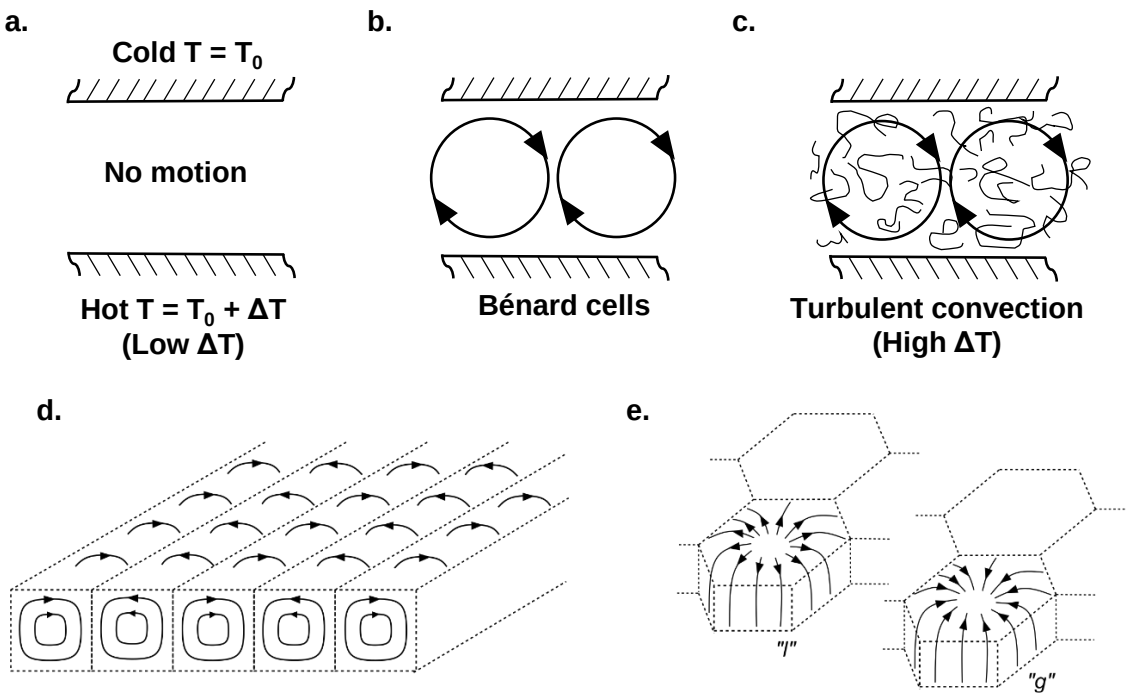

Figure 2.19. A case showing fluid being held between two flat, parallel plates. (a) At low temperature gradients, the fluid is stable. (b) As the temperature gradient increases, natural convection sets in the form of regular convection cell. (c) At high ΔT, the fluid reach the state of turbulent convection. Schematic of convection cells: (d) two-dimentional rolls and (e) hexagonal convection cells; *l* and *g* indicates different ciculation dirrection.

2.3.4. Rayleigh-Bénard convection

Rayleigh-Bénard convection is driven by a non-uniform temperature distribution across the horizontally extended boundaries of a fluid's layer. This induces a turbulent convective fluid motion at high temperature gradients (Ra > critical value), creating convection in alternating patterns of upward and downward motion.[183] If the temperature gradient in the sealed container exceeds a threshold value, a pattern of convention cells starts to appear. This is based on the buoyant forces pushing the less-dense fluid up towards the cooler end of the container while the cooler and denser fluid at the top sinks and displaces the warmer fluid (Figure 2.20.a). Due to the continuous density gradient, the resultant cyclical motion creates a honeycomb pattern called Bénard convection cells (Figure 2.19.b).[184] Rayleigh-Bénard convection is considered a prototype for nonlinear systems exhibiting pattern forming in chaotic dynamics and fully developed turbulence.[185] However, when the Rayleigh number increases several times the critical value, these patterns become unstable, oscillatory patterns arise, and convection becomes chaotic.

a.

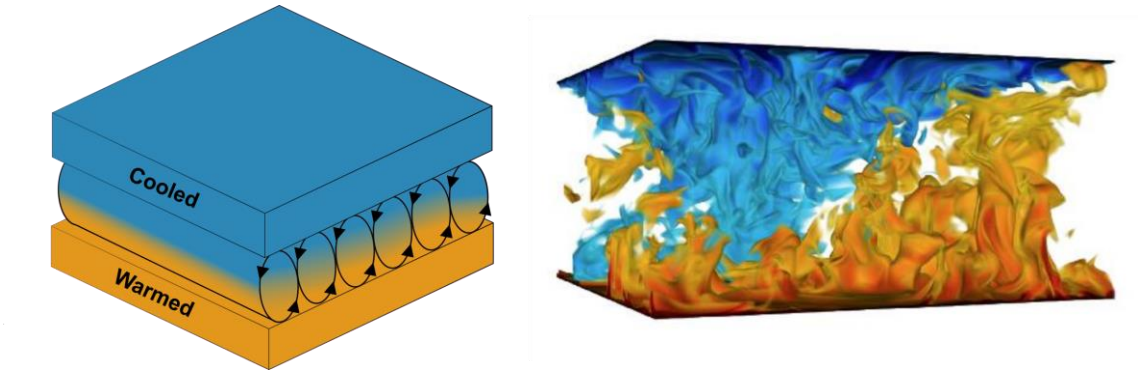

b.

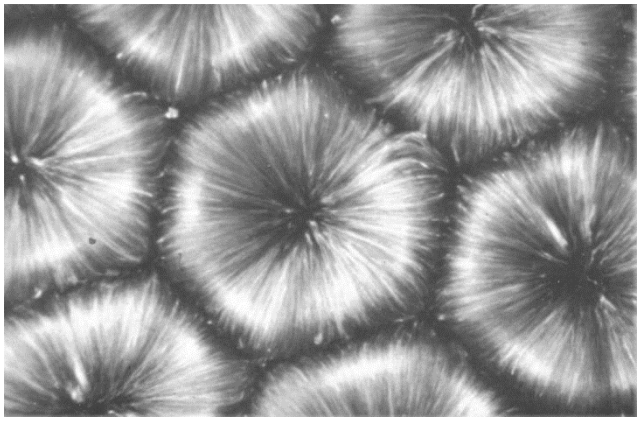

Figure 2.20. Rayleigh-Bénard convection. (a) Schematic of the cyclical motion creating Rayleigh-Bénard convection cells (Left drawing). A snapshot taken from a movie based on data from a Rayleigh-Bénard convection simulation is provided on the right side where red and blue indicate hot and cold fluid. Photo credit: Physics of Fluids Group, University of Twente, 2018. (b) Time-lapse photograph of hexagonal Rayleigh-Bénard convective cells. Flow lines are manifested by aluminum fakes and 10-second exposure. Photo credit: M. Van Dyke, 1982, *An Album of Fluid Motion*.

2.4. Solubility and Thermodynamics

The method of depositing polymers from supercritical solvents relies on the saturation concentration of polymer solutions. It is therefore vital to understand solvation thermodynamics. The discussion will begin with a general statement of the process in terms of the Gibbs free energy before proceeding to models of liquid-liquid mixtures based on statistical thermodynamics. With the basic terminology outlined, a discussion of Flory-Huggins theory of polymer solutions will then take place.

The spontaneity of a chemical process at constant pressure is governed by the change in the Gibbs free energy (ΔG), with negative values of ΔG indicating a

thermodynamically favorable process. The free energy of mixing is thermodynamically favored at constant temperature and pressure if the Gibbs free energy change is negative. In Equation (2.20), entropy and enthalpy of mixing are denoted by ΔS_m and ΔH_m respectively.

$$\Delta G_m = \Delta H_m - T\Delta S_m \tag{2.20}$$

2.4.1. The Lattice Model of Solutions

Liquid-liquid solutions are a convenient starting place for describing mixing thermodynamics, as liquids are well approximated as incompressible and possessing short-range order. The lattice model of solutions assumes that both solvent and solute occupy similar volumes with molecules being randomly packed together in a regular lattice (Figure 2.21). While the molecules are presumed to be positioned in a box, they can still move by swapping places. If N_1 is the number of solvent molecules and N_2 is the number of solute molecules, for the simple square lattice shown in Figure 2.21, the lattice would contain $N_0 = N_1 + N_2$ lattice sites.

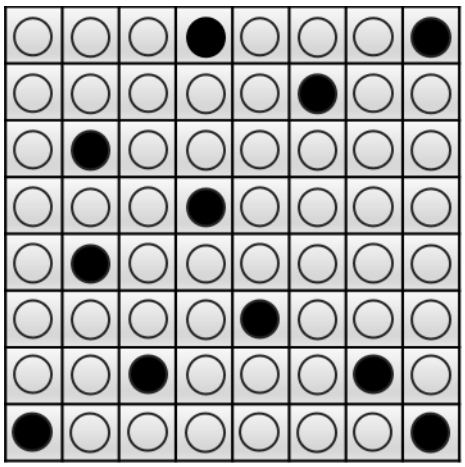

Figure 2.21. A two-dimensional square-lattice example of the lattice model of solutions. The filled circles portray solute molecules and open circles represent solvent molecules.

Since it is considered that the lattice does not change size upon solute introduction, there can be neither a change in pressure nor a change in volume, meaning that pressure-volume work is zero, making enthalpy and internal energy equal. This has the additional consequence of making the Gibbs free energy equal to the Helmholtz energy in this model.

The internal energy of mixing can be approximated by the van Laar equation which parameterizes the intermolecular interactions between the two solution components. This provides an accurate estimate even for solutions containing polymers where the size of solvent and solute particles is not comparable.

$$\Delta U_m = zN_1\phi_2\Delta\varepsilon \tag{2.21}$$

$$\Delta\varepsilon \approx \varepsilon_{12} - \frac{1}{2}(\varepsilon_{11} + \varepsilon_{22}) \tag{2.22}$$

In Equation 2.21, z is the coordination number of the lattice, for example the number of nearest neighbor lattice sites, and ϕ_2 is the volume fraction of the solute. In Equation 2.22, the parameter ε_{11} is the energy associated with the intermolecular forces between nearest neighbor solvent molecules, ε_{22} is the energy associated with the forces between nearest neighbor solute molecules, and ε_{12} is the energy associated with the forces between a solute-solvent pair which are nearest neighbors to each other. Typically, ε_{11} and ε_{22} represent a more stable interaction than ε_{12}, making the internal energy almost always a positive contribution to the Helmholtz energy of mixing. In other words, the internal energy typically does not favor mixing.

The entropy of a solution can be readily calculated in terms of the number of possible microstates using the Boltzmann equation. Assuming N_0 site lattice containing N_1 molecules of solvent and N_2 molecules of solute, the entropy can be written as

$$S = k_\mathrm{B}\,(\ln N_0! - \ln N_1! - \ln N_2!) \tag{2.23}$$

Before mixing, the system only possesses a single microstate, making the entropy of the original segregated arrangement zero and therefore $\Delta S_m = S_c$, where S_c is configurational entropy. Using Stirling's approximation for factorials and the relationship of $N_0 = N_1 + N_2$, the solution entropy can be rewritten as

$$\Delta S_m = -k_\mathrm{B}\,(N_1 \ln X_1 + N_2 \ln X_2) \tag{2.24}$$

In the above equation, X_1 and X_2 are the mole fractions of solvent and solute, respectively. By rewriting the solution entropy based on their relative concentrations, Equation 2.24 can be expressed as

$$\frac{\Delta S_m}{N k_B} = -x \ln x - (1-x)\ln(1-x) \tag{2.25}$$

where $x = N_1/N$ and $1 - x = N_2/N$. In an ideal solution the ΔS_m is always positive and $\Delta U_m = 0$, as result the ΔF_m has a negative value and favors mixing. Therefore, ΔF_m for an ideal solution is

$$\frac{\Delta F_m}{N k_B T} = -x \ln x - (1-x)\ln(1-x) \tag{2.26}$$

In contrast to ideal solutions, $\Delta U_m = 0$ does not hold anymore for regular solutions, and the mixing involves the energies of solution. The model describing regular solution was first introduced by Hildebrand, showing that beside the entropy of solution driving the solvation, regular solutions are driven also by the energy of the mean-field form. However, there are still systems that are even more complicated than regular solution model, for instance polymer solutions where solute and solvent are not comparable in size.

2.4.2. Flory-Huggins Theory

Flory-Huggins Theory applies the lattice model of liquid-liquid mixtures to polymer solutions, providing a good estimate of the free energy of polymer solutions mixing and is based on the lattice approach with a mean-field estimate. The system is defined similar to a lattice consisting of N sites with equal volume v_0. In dealing with polymers, the degree of polymerization (x_i) should be considered when calculating the volume fraction. However, the assumption is made that the monomer volume (v_i) is equal to the volume of a lattice site (v_0) and therefore the total volume for species i (V_i) is given as

$$V_i = n_i x_i v_0 \tag{2.27}$$

where n_i is the number of molecules. Based on this, the lattice volume fraction (ϕ_i) occupied either by a solvent molecule or polymer can be defined as

$$\phi_i = \frac{n_i x_i}{n_1 x_1 + n_2 x_2} = \frac{n_i x_i}{N} \tag{2.28}$$

In the case of ideal polymer chains, the change in the conformational entropy of polymer chains is insignificant when transitioning from free polymers in solid form to

polymers in solution. Hence, the entropy associated with mixing polymers should be mainly from translational motion. The entire chain is considered a large molecule that gains more translational entropy by having more available locations to place its center of mass, just as in ideal solutions. Consequently, the entropy per molecule can be written as

$$S_i = k_{\mathrm{B}} \ln V_i \tag{2.29}$$

Therefore, the change in the entropy of mixing can be written as

$$\Delta S_m = (n_1 S_1)_M + (n_2 S_2)_M - (n_1 S_1)_P - (n_2 S_2)_P \tag{2.30}$$

where "P" and "M" denote pure and mixed states, respectively. The rearrangement of Equation (2.30) results in a similar form of entropy discussed for the regular solution theory in the previous section. The only difference is that mole fraction is replaced by volume fraction (ϕ) and the degree of polymerization is in the pre-factor as shown below:

$$\frac{\Delta S_m}{N} = -k_{\mathrm{B}}[\frac{\phi_1}{x_1} \ln \phi_1 + \frac{\phi_2}{x_2} \ln \phi_2 \,] \tag{2.31}$$

The enthalpy of mixing for polymers can either be positive (disfavoring mixing) or negative, favoring mixing, the less common scenario. The energy of polymer mixing can be derived the same way as in the regular solution theory, taking into account for all interactions between solvent-solvent (ε_{11}), monomer-monomer (ε_{22}), and monomer-solvent (ε_{12}):

$$\Delta\varepsilon = \varepsilon_{12} - \frac{1}{2}(\varepsilon_{11} + \varepsilon_{22}) \tag{2.32}$$

Upon mixing, the probability of adjacent site being occupied by either monomer or solvent can be used to calculate the energy of the mixed state:

$$\Delta U_m = \frac{N_1 N_2}{N_0} z \Delta\varepsilon \tag{2.33}$$

where z is the number of neighbours in the lattice site. The energy of mixing per lattice site can be rewritten by substituting the mole fractions with volume fractions ϕ_1 and ϕ_2

$$\frac{\Delta U_m}{N k_{\mathrm{B}} T} = \chi \phi_1 \phi_2 \tag{2.34}$$

The χ parameter is the interaction parameter derived by using a mean-field approximation and is defined as

$$\chi = \frac{z}{k_B T}(\varepsilon_{12} - \frac{\varepsilon_{11}+\varepsilon_{22}}{2}) \tag{2.35}$$

where the ε corresponds to the molecular interactions between monomers and solvent molecules. The combination of Equations (2.31) and (2.34) results in the Helmholtz free energy of mixing for polymer solutions

$$\Delta F_m = \Delta U_m - T\Delta S_m \tag{2.36}$$

$$\frac{\Delta F_m}{N k_B T} = \chi \phi_1 \phi_2 + \frac{\phi_1}{x_1} \ln \phi_1 + \frac{\phi_2}{x_2} \ln \phi_2 \tag{2.37}$$

In the case of solvent-polymer mixture ($x_1 = 1$ and $x_2 =$ large) and polymer-polymer mixture ($x_1 =$ large and $x_2 =$ large), the asymmetric free energies are dictated by the degrees of polymerization. Additionally, the favorable entropy of mixing decreases as the degree of polymerization of either or both species increases.

The derived Flory-Huggins Theory for the Gibbs free energy of polymer solution mixing has shown that χ is inversely proportional to temperature and thus the energy of mixing will vary with temperature. This indicates that polymer solubility can change significantly over small ranges of temperatures. To calculate the miscibility/phase separation conditions for a polymer solution, a phase diagram can be constructed. To construct the phase diagram, the Gibbs energy of the homogeneous solution with the Gibbs energy of two coexisting phases should be compared. Rearranging the Flory-Huggins Equation (2.37), ΔF_m can be rewritten as

$$\frac{\Delta F_m}{N k_B T} = \frac{\phi_A}{N_A} \ln \phi_A + \frac{\phi_B}{N_B} \ln \phi_B + \chi \phi_A \phi_B \tag{2.38}$$

where the term N denotes the degree of polymerization of the species and ΔF_m is the free energy of mixing per site. The first two terms in Equation (2.38) represent the ideal or combinatorial part of the entropy of mixing. Although the combinatorial entropy of mixing is much smaller for polymers than for low molar mass compounds, the entropy still favors mixing. However, the third term in Equation (2.38) is related to the non-zero enthalpy of

mixing and promotes phase separation. Based on Equation (2.35), the temperature dependency of the χ parameter can be parameterized as

$$\chi(T) = \alpha + \frac{\beta}{T} \tag{2.39}$$

This approach implies that $\chi \propto \frac{1}{T}$, if the influence of α is considered insignificant, and hence χ^{-1} can be considered as an analog of T. The temperature dependency of the interaction parameter results in different type of polymer phase diagrams as illustrated in Figure 2.22. The temperature-composition diagram displayed in Figure 2.22 show the binodal curves (or coexistence curves) separating the one-phase region from the two-phase region. In Figure 2.22.a**,** the upper critical solution temperature (UCST) corresponds to a temperature above which the mixture components are miscible in all proportions and below which it will phase separate. It is the interactions between the components that causes an enthalpically driven ($\Delta H_m > 0$) phase separation. In contrast to UCST, the lower critical solution temperature (LCST) behavior is observed when there is an entropic driving force for phase separation. As shown in Figure 2.22.b, above the lower critical solution temperature, the solution separates into two phases and below it exists as one homogeneous phase. Additionally, it is possible for a polymer solution system to have both UCST and LCST (Figure 2.22.c and d) or neither (Figure 2.22.e). For instance, in Figure 2.22.c, the system is miscible in all proportion for temperatures between the LCST and the UCST but becomes thermodynamically unstable at higher and lower temperatures.

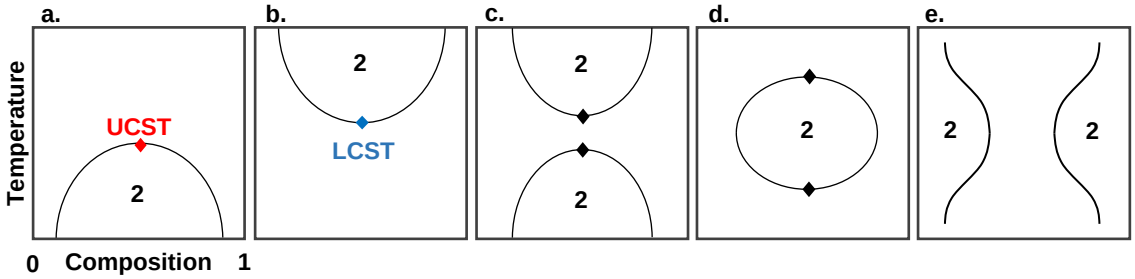

Figure 2.22. Different type of polymer phase diagram and miscibility gaps. The two-phase region is denoted by "2" on the phase diagram.

2.5. Supercritical Fluids

The physical supercritical fluid deposition technique discussed for polymer films relies on the distinctive properties of the supercritical fluids and the ability to tune their solvation dynamics by changing solvent temperature and pressure. Given the controversy over the terminology of “supercritical fluids”, this section starts with the common description of supercritical fluid, following by the discussion regarding what should be considered a supercritical fluid based on the phase diagram. Subsequently, the discussion goes into whether the van der Waals equation of state is reliable in predicting the phase behavior in mixtures containing polymer and supercritical components.

Traditionally, a supercritical fluid is characterized as a substance above its critical temperature (T_r) and critical pressure (P_r). In the supercritical region, the matter does not exhibit characteristics of either gas or liquid phase and becomes a fluid with liquid-like densities and gas-like viscosities. This behavior was first observed in 1822 by French engineer and physicist, Charles Cagniard de La Tour, in his well-known cannon barrel experiment. He heated different substances, both liquid and vapour, in a sealed canon and continuously shook the container and listened to the sound of a rolling flint ball until at a certain temperature he observed that the sound stopped. Later, he was able to observe this phenomenon in a glass apparatus and witness the single supercritical fluid phase. Afterwards, Irish chemist Thomas Andrews came up with the name “supercritical fluid” for this phenomenan.[186]

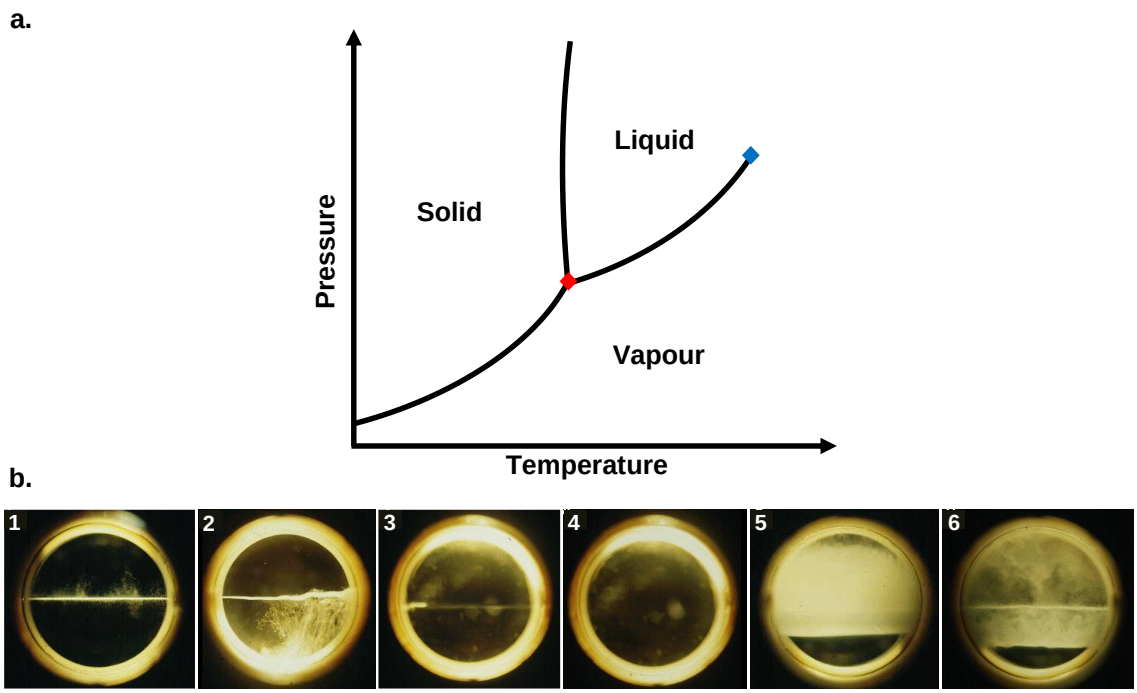

Figure 2.23. (a) The phase diagram for a typical pure substance. The red and blue points correspond to the gas–liquid–solid triple point and critical point repectively. (b) The transition of CO_2 into supercritical phase. 1) Below the critical point with two distinct phases. 2) As the temperature of the system increases, the liquid starts to expand. 3) With further temperature increase, the two phases start to become less distinct. 4) A new supercritical phase forms. 5) As the system is cooled down, the reverse process initiates. 6) With further temperature decrease, the phase separation into liquid and vapor starts to take place.

The state of a substance as a function of temperature and pressure can be displayed using a phase diagram. A general phase diagram for a pure substance is illustrated in Figure 2.23.a, and shows different thermodynamically stable regions, separated by phase boundary lines. The phase boundary lines indicating the conditions under which two phases of matter can coexist at equilibrium. The point on the phase diagram where the phase boundary lines intersect is called the triple point, labeled by a red point on Figure 2.23.a, where all three distinct phases of matter (solid, liquid, gas) coexist. Another distinct point on the phase diagram is the critical point labelled blue on the same figure. Figure 2.23.b displays a series of snapshots capturing the transition of liquid CO_2 into supercritical fluid when heated in a sealed container. If a liquid is heated in a closed container, the vapour pressure increases, thus the vapour density increases as temperature increases. At the same time, the density of the liquid drops due to thermal expansion. This trend continues until the density of the liquid becomes equal to the density

of the vapour and the phase boundary between liquid and vapour phases disappear. The point at which the phase boundary ceases to exist is called the critical point.

Conventionally, the phase diagram is divided into 4 regions separated by the critical isobar and isotherm, shown by dotted blue and red lines respectively on Figure 2.24.a. There is a disagreement in the scientific community regarding the regions (quadrants) considered to be supercritical fluid. For instance, the quadrants II, III, and IV are deemed supercritical fluids, as in neither of them a phase equilibrium is possible.[187] This is in agreement with Younglove's view considering I_L and I_V as liquid and vapour, and calls everything else fluid.[188] On the other hand, Tucker believes only states above the critical temperature, corresponding to quadrants II and III, are supercritical, while Oefelein[189] and Candel et al.[190] refer to quadrant IV as transcritical, and quadrant III as supercritical. Further analysis of this classical four quadrant state plane reveals that the physical justification of these definitions is likely oversimplified. For this reason, a modified diagram capturing the more subtle aspects of the phase behavior in the vicinity of the critical point was proposed by Banuti & Hickey,[191] as shown in Figure 2.24.b. The coexistence line separates the liquid and vapor, and the fluid is in a liquid state for pressures above the coexistence line. At subcritical pressure, the coexistence line divides liquid and vapor; at supercritical pressure, the liquid needs to pass through the pseudoboiling-line before it transforms to a vapor state. At temperatures far above the critical temperature, the vapor acts like an ideal gas. The transformations of the fluid above supercritical pressure occur continuously, without a traditional phase change.

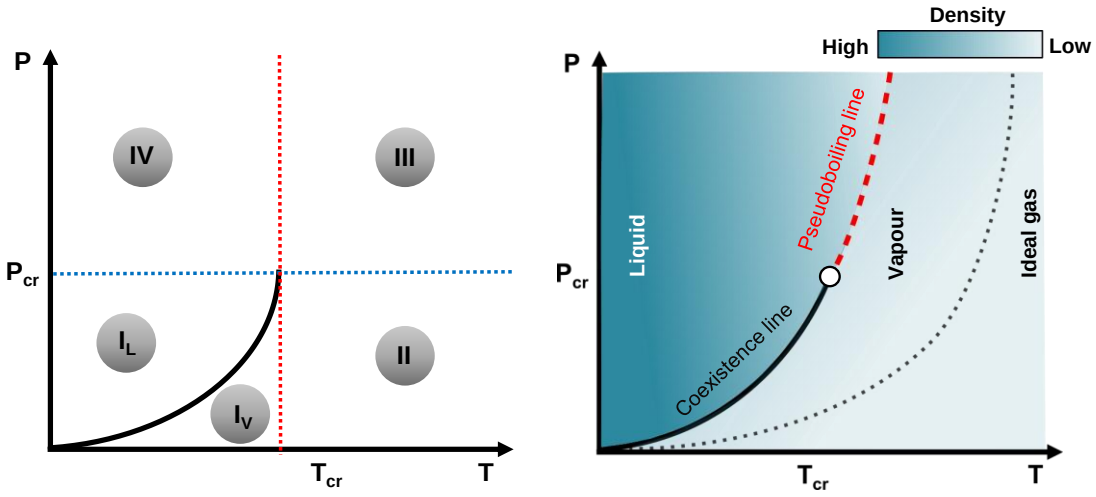

Figure 2.24. Phase diagram. (a) Classical fluid state plane demonstrating different supercritical states structure. The critical isobar and isotherm lines are shown by blue and red dotted lines respectively. (b) Revised fluid state plane with coexistence and pseudoboiling lines. Adapted with permission from reference 191.

As a concrete example, Figure 2.25.a displays the phase diagrams of n-pentane and toluene. As illustrated, the gas-liquid equilibrium curve is interrupted at the critical point, providing a continuum of physicochemical properties. Beyond the critical point, the molecules are not held together as strongly as in the liquid phase via intermolecular forces as the number of them decreases. From the microscopic point of view, the molecules in the liquid phase can be imagined as trapped in each others' potential fields. As the temperature rises, the average kinetic energy of molecules increases and when it reaches a specific temperature, they have enough energy to break free from this potential well. This analogy implies that the critical temperature is approximately proportional to the potential well depth.[192]

The decreased intermolecular forces in supercritical fluids significantly impact the fluid's physical properties. For instance, the density of n-pentane and toluene decreases as temperature increases and significantly drops near the critical region of the fluid (Figure 2.25.b). The solubility of different compounds in supercritical fluids depends on the fluid density, in particular solvent density around the solute. In supercritical fluids, the local solvent density around the solute is higher than the bulk density if the solvent-solute interaction is favorable, leading to higher solvation. Consequently, what makes supercritical fluid an interesting solvent is the ability to easily tailor its solubility power by changing the temperature and pressure, and consequently the fluid density.

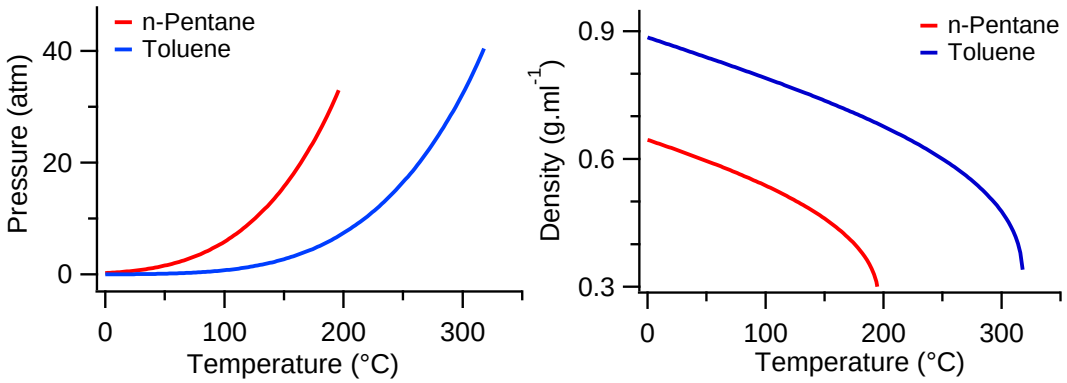

Figure 2.25. (a) Temperature-pressure phase diagrams of n-pentane (T_r : 196.45 °C, P_r : 33.25 atm) and toluene (T_r : 318.64 °C, P_r : 40.72 atm). (b). Density-temperature phase diagrams of n-pentane (ρ_r : 0.273 g.ml^{-1}) and toluene (ρ_r : 0.291 g.ml^{-1}). Data retrieved from NIST Chemistry WebBook on October, 2020.

In general, the liquid-like densities of supercritical fluids combined with their gas-like diffusivities, enable the dissolution and fast transport of species rather easily compared to their liquid state, and make supercritical fluid an excellent candidate as a deposition medium. Moreover, supercritical fluids leave no solvent residue on the substrate surface and have low surface tension. More importantly, supercritical fluids are considered environmentally preferable solvents for not only in deposition and preparation of supported metal nanostructures, but also in the area of polymer processing.[193,194]

2.5.1. The van der Waals Equation of State

The van der Waals equation of state is a simple model that considers the interaction between gas molecules and it is used to develop phase diagrams in addition to understanding the behavior of gases. The van der Waals equation of state has the form

$$P = \frac{RT}{V-b} - \frac{a}{V^2} \tag{2.40}$$

where P is the external pressure and V is the molar volume. In this equation, a and b parameters are normally estimated from the critical point and considered constants (substance specific). However, these parameters can be functions of temperature and

some fluid properties such as acentric factor (ω), critical compressibility factor (Z_c), etc. In fact, certain theoretical and empirical restrictions must be imposed for estimating these parameters.[195]

To examine the extent to which the van der Waals equation of state is reliable in predicting the phase behavior, one can start with the construction of isotherms. As shown in Figure 2.26, the isotherms (line of constant temperature) take different shapes depending on the temperature value. At temperatures that exceed the critical temperature, decreasing the molar volume results in a monotonic increase in pressure, until it reaches the point where molecules are closely packed, and the pressure diverges. The molar volume cannot take values smaller than b, meaning the molecules reached their minimum possible distance. In contrast, for temperatures below the critical temperature, as molar volume is decreased the pressure goes through an initial rise, but then falls, and once more rises (goes through a loop), before reaching molar volume values equal to b. This implies that there is a region where compressing the fluid can cause its pressure to decrease, corresponding to an unstable phase. This instability is interpreted as a liquid-gas phase transition. Based on the isotherm for temperatures below the critical temperature, there are two stable regions corresponding to relatively small and large molar volumes separated with an unstable region.[196] In the region of large molar volume ($v \gg b$), the increase in the pressure is monotonic as expected with a decrease in molar volume. This stable region is the gas state. In the region of relatively small molar volumes ($v \sim b$), molecules are very densely packed, thus small change in the volume requires a great deal of pressure. This state defines a liquid phase. Therefore, the unstable region corresponds to a volume region that liquid and gas are coexisting. To address this anomaly in the isotherm, the Maxwell construction approach connects the high and low molar volume regions by replacing the loop with one isobaric straight line such that the areas cut off above and below this line are equal (Figure 2.26.b).[197] Based on the new constructed isotherm, pressure remains constant as the volume decreases, until all the gas is converted into liquid and afterwards, pressure starts to increase as the liquid volume decreases.[198]

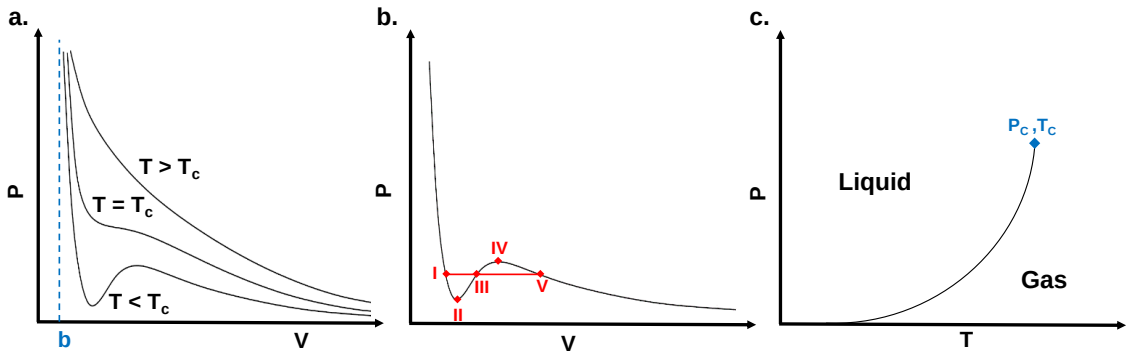

Figure 2.26. Isotherms of the van der Waals equation of state for 3 different temperatures. (b) Maxwell construction for van der Walls isotherm. The isobaric line is constructed such that equal areas are found for I.II.III and III.V.VI. (c) The phase diagram produced based on the Maxwell construction for different temperatures.

The pressure at the phase transition can be established using the isotherms. The phase diagram can be generated by repeating the Maxwell construction for different temperatures and plotting the vapor pressure extracted versus the temperature (Figure 2.26.c). As the temperature approaches the critical temperature, the phase boundary between liquid and gas disappears and they are not distinguishable from each other anymore. There is no more phase transformation above this point and only a single-phase fluid exists.

Mixtures Containing Polymer Components

Similar to the modeling of conventional phase equilibrium, there are several polymer-specific equation of states which can be classified into two broad groups: 1) excess Gibbs free energy (G_{ex}) or activity coefficient models and 2) EoS models.[199] While the activity coefficient models are believed to be more suitable for complex phase behavior, the EoS models have been more successful, especially for high pressure systems. One of the examples of the cubic EoS applicable to large molecules and polymers is Sako, Wu, and Prausnitz (SWP).[200] The SWP equation has been used, with relative success, for mixtures using simple mixing rules. Other EoS and G_{ex} models that have been used with some success are Panagiotopoulos-Reid (PR)[201] and Soave-Redlich-Kwong (SRK)[202] using mainly Wong-Sandler (WS)[203] and Zhong-Masuoka (ZM)[204] mixing rules. Nevertheless, the most promising methods are usually based on the combination of activity coefficient models and EoS for describing mixture phase behavior.

Mixtures Containing Supercritical Components

The virial EoS was the first model used to describe phase behavior of systems with supercritical fluids. However, the most reliable models have been based on the cubic EoS such as Soave-Redlich–Kwong (Eq. 2.41)[202] and Peng-Robinson (Eq. 2.42)[205] equations of state.

$$P = \frac{RT}{V_m - b} - \frac{a}{\sqrt{T} V_m (V_m + b)} \tag{2.41}$$

$$P = \frac{RT}{V_m - b} - \frac{a.\alpha}{V_m^2 + 2bV_m - b^2} \tag{2.42}$$

The SRK EoS is a modified version of the simple RK EoS with a function $\alpha\ (T, \omega)$ involving the temperature and the acentric factor and can be applied to hydrocarbons. On the other hand, the PR EoS model provides reasonable accuracy near the critical point and is a superior model in calculations of the compressibility factors and liquid densities of many materials. There are several combination models based on cubic EoS and mixing rules presented in the literature but lack accurate representation of phase equilibrium in systems containing a supercritical fluid.[206] Nonetheless, it has been proven that the best predictions are the result of using the Gibbs free energy models and nonquadratic mixing rules.

Chapter 3. Methods

This chapter provides a review of relevant concepts and experimental approaches implemented throughout this thesis. The first section provides a detailed description of the supercritical fluid chamber and the complete tabletop setup, following by the procedure detailing the substrate preparation for deposition in the supercritical fluid chamber. Thereafter, a summary of spectroscopic techniques used for establishing the solubility behaviour of polymers and their chemical characterization are described. Subsequently, relevant microscopy tools utilized for the deposited films texture and phase behavior analyses are introduced. Finally, the basic principles and tools employed to successfully develop patterns on the substrate for polymer deposition are outlined.

3.1. High-Pressure System Design

The custom pressure chamber was constructed at the SFU machine shop from beryllium copper (BeCu) by drilling three perpendicular holes into a cube of raw material. In total, the vessel has six ports, including an inlet positioned at the bottom of the chamber (Figure 3.1, Y-Axis) for the introduction of fluids inside the chamber, and an outlet situated at the top port (Figure 3.1, Y-Axis) for the exhaustion of fluids from the chamber. Additionally, there are two sapphire windows positioned to face each other and allow for in-situ transmission UV–vis spectroscopy (Figure 3.1, X-Axis). The port for the introduction of a substrate for deposition is perpendicular to the sapphire windows (Figure 3.1, Z-Axis), allowing to monitor the film growth on the substrate during deposition The chamber was sealed by securing the ports with BeCu flanges using black oxide finished alloy steel bolts (M5-0.8, class 12.9, manufactured by HOLO-KROME®), leaving approximately 27 mL of internal volume. As a safety consideration, the volume of the system was kept low to reduce the total energy of the system. The stored mechanical energy of a filled (27 mL) and pressurized chamber (38 MPa), is equal to dropping a box weighing 5 kg from a 0.13 meters height, or the rupture of mountain bike tire when inflated to a typical pressure. Furthermore, an O-ring made of Kapton® polyimide sheets (0.005" Thick), shown as black O-ring in Figure 3.1, was placed in the groove of each port prior to the attachment of flanges.

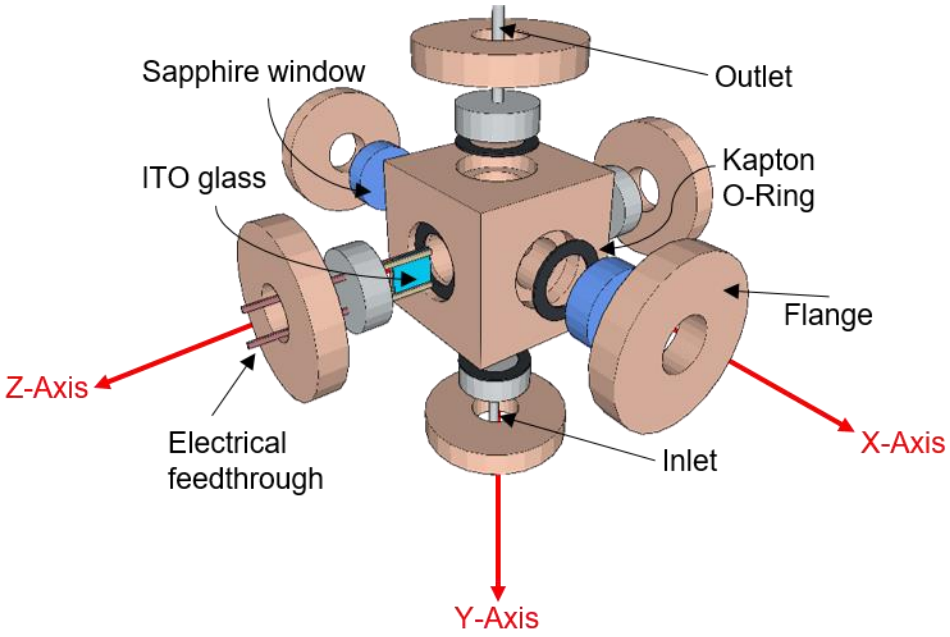

Figure 3.1. Drawing of the high-pressure chamber and some of its components. Bolts, heating elements, and mounting elements are excluded for clarity.

The chamber was pressurized using a manual pressure generator purchased from High Pressure Equipment Co. (HiP 62-6-10). The pressure generator is a manually operated piston designed to compress liquid within a small volume to develop pressure. The pressure was monitored with a transducer (Swagelok PTI series) and is read out with a small LED display.

Figure 3.2 illustrates the complete assembly of supercritical fluid setup including Swagelok fittings and stainless steel tubing. All the wetted parts (beside the sapphire windows) are made of 316 or 17-4PH stainless steel. The commercially purchased system components are rated to 69.0 MPa or greater and were regularly tested up to 24.0 MPa to ensure the integrity of the system at elevated pressures. In addition, there was a 38.0 MPa rupture disc acting as a primary safety measure to prevent over pressurization. As an additional safety consideration, the supercritical chamber was stationed inside a Lexan safety box (labeled 10 in Figure 3.2). Furthermore, it is important to provide an active ventilation of the vessel to rapidly remove any flammable solvent vapors inside the safety box in the event of an unplanned depressurization (vacuum hose is labeled 11 in Figure 3.2).

Materials are introduced into the chamber by placing them into a crucible and placing the crucible at the chamber bottom. The crucible containing the solute (polymer)

was made from glass with a cylindrical shape (diameter = 11.60 mm, height = 6.80 mm, thickness = 0.85 mm). After placing the polymer sample inside the crucible, it was capped with glass wool and wrapped with copper mesh to prevent the uncontrolled dispersion of polymer inside the chamber. The prepared and filled crucible was then placed at the bottom of the chamber prior to sealing the chamber. The scrupulous removal of oxygen is an important safety measure that allows us to work safely with flammable solvents under elevated pressures and temperatures. This was accomplished by purging the chamber with nitrogen via an inlet valve (labeled 7 in Figure 3.2) for minimum 15 minutes to force the air and moisture out of the chamber through the outlet valve (labeled 8 in Figure 3.2). The solvent was also deoxygenated prior to addition to the chamber by nitrogen purging. The purging was achieved via bubbling nitrogen through the solvent for approximately 20 minutes. Both the solvent and chamber were deoxygenated prior to increasing the chamber's temperature.

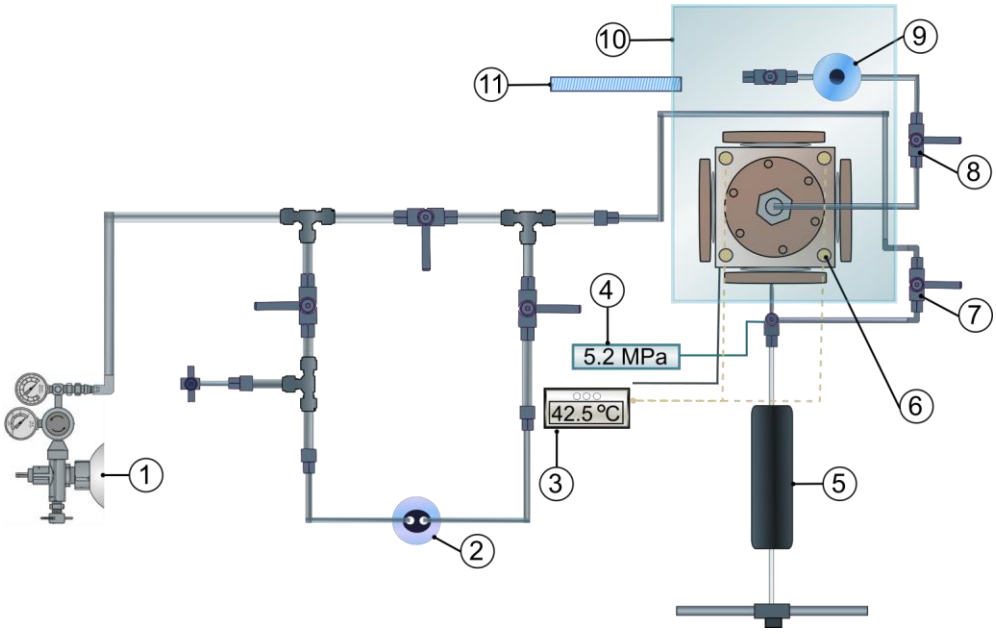

Figure 3.2. Schematic of supercritical tabletop setup (top view) and its components: (1): N_2 cylinder, (2): solvent bottle, (3): Omega benchtop PID controller, (4): pressure display connected to the pressure transducer, (5): manual pressure generator, (6): cartridge heaters x4, (7): inlet valve, (8): outlet valve, (9): cold solvent trap, (10): Lexan safety box, (11): vacuum hose.

In order to set the temperature of the fluid inside the chamber and initiate the polymer dissolution process, the exterior of the chamber was heated by an Omega benchtop PID controller (CSi32 Series with 0.04 °C temperature stability) used to drive

four cartridge heaters connected in parallel and placed symmetrically about the edges of the chamber (labelled 6 in Figure 3.2). A ground-fault circuit interrupter, or GFCI, was also added between the wall power and the power control unit to shut off electrical power in the event of a ground-fault. Concurrently, the chamber's internal pressure was monitored via pressure display (labeled 5 in Figure 3.2), and adjusted, if necessary, using the manual pressure generator (labeled 5 in Figure 3.2).

3.2. In-situ Transmission UV-vis Spectroscopy Setup

The setup for in-situ transmission UV-vis spectroscopy is illustrated in Figure 3.3. The light source and detector were positioned outside the Lexan safety box that houses the supercritical fluid chamber. The optical fibers were fed through small holes that were drilled through the Lexan safety box and securely held in position. Afterwards, they were aligned facing the sapphire windows as portrayed in Figure 3.3. An Ocean Optics USB4000 spectrometer that covers 200−1100 nm ranges with a Toshiba TCD1304AP (3648-element linear silicon CCD array) detector was used. The halogen light source was also purchased from Ocean Optics (HL-2000 with 360−2400 nm wavelength range) and the path length was approximately 15 cm.

The reference spectrum used for the measurements was collected from the solution inside the chamber at room temperature. It was also noted that transmission was slightly higher at increased pressure, thus a different blank was collected for each pressure studied. Additionally, the resolution of the spectra was deliberately decreased to 8 nm to increase the signal-to-noise ratio and thus ensure accurate readings at high absorbance values.

It was imperative for the accuracy of the data collected that the UV-vis spectra collection as a function of temperature was carried out in a successive manner. Thus, UV−vis spectroscopic measurements were performed after the system was given approximately 15 minutes to reach equilibrium and ensuring polymer is dissolved in the supercritical fluid. After UV-vis spectra were collected and the appropriate blank spectrum was subtracted, the data were fitted with two Gaussian peaks using IGOR Pro (Wavemetrics) to establish the solubility behavior as a function of temperature.

At the end of each experiment using in-situ transmission UV-vis spectroscopy, the chamber contents were exhausted through the chamber outlet into a polypropylene vessel with a volume of 500 mL (labelled 9 in Figure 3.2). The vessel has an inlet port to accept the chamber contents and a wide outlet port to prevent over-pressurizing the vessel.

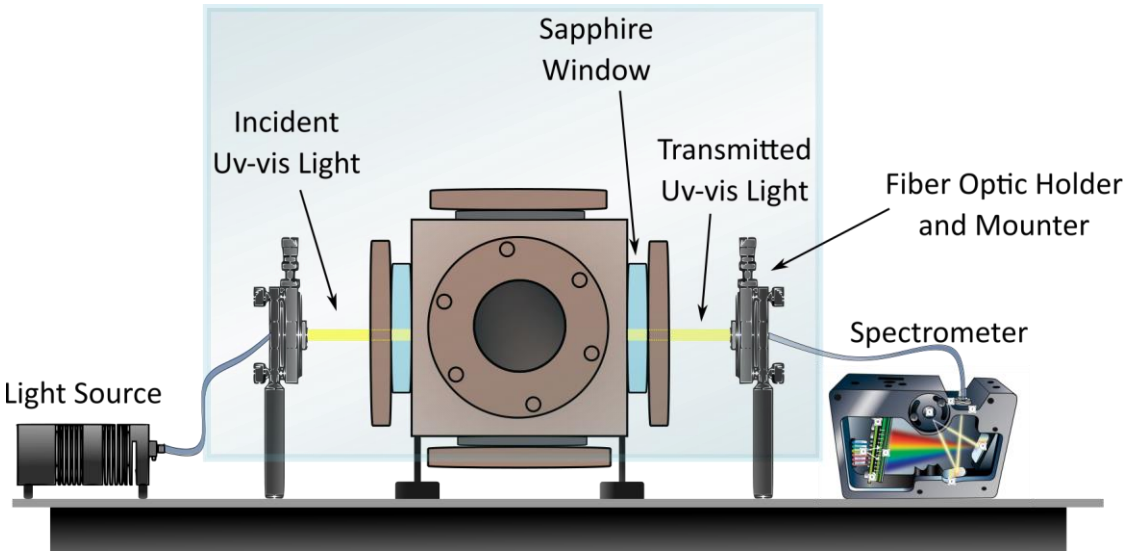

Figure 3.3. Schematic of a section of supercritical tabletop setup (side view) and different components used for the in-situ transmission UV-vis spectroscopy.

3.3. Gravimetric Analysis of Saturated Solutions

In case of the gravimetric analysis, the polymer solubility as a function of temperature was established via direct polymer mass measurement from saturated solutions. To measure the mass of polymer, the chamber contents (saturated solutions) were exhausted through the chamber outlet into a polypropylene vessel with a volume of 500 mL. As a matter of safety, pressure should never be allowed to build inside the collection vessel. It is also important to provide active ventilation of the vessel to rapidly remove any flammable solvent vapors. The rapid expansion of the chamber contents cooled the solution below its boiling point, allowing liquid solvent and polymer to be collected. Afterwards, solvent was removed from the slurry under reduced pressure and the dried polymer mass was weighed.

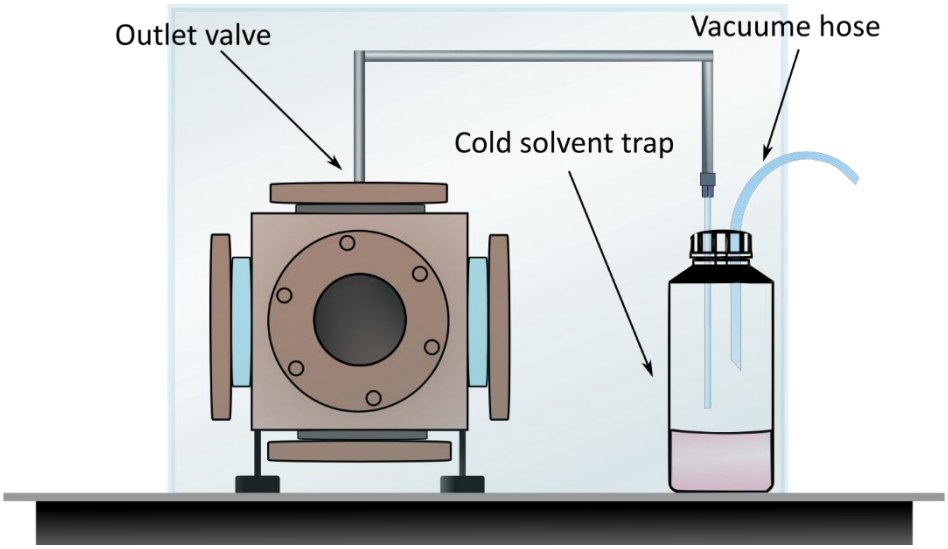

Figure 3.4. Schematic of a section of supercritical tabletop setup (side view) for gravimetric measurements.

3.4. Substrate Preparation for Thin Film Deposition

The substrates used for film deposition were ITO-coated glass slides purchased from Ossila Ltd. The thickness of ITO coating was in the range of 40 to 100 nm with average resistance of 20-60 Ω/sq. ITO glass slides were chosen as substrates because of their optical transparency, electrical conductivity, and ease of use. A thin layer of gold (≈ 50 nm) was deposited near the edges of the substrates by using physical vapor deposition to facilitate a uniform current through the ITO film. The ITO glass slides were cleaned with acetone and isopropyl alcohol consecutively before mounting them on the sample holder and placing the assembly into the chamber. The substrate was placed parallel to the sapphire windows to facilitate the collection of UV-vis spectra during film growth.

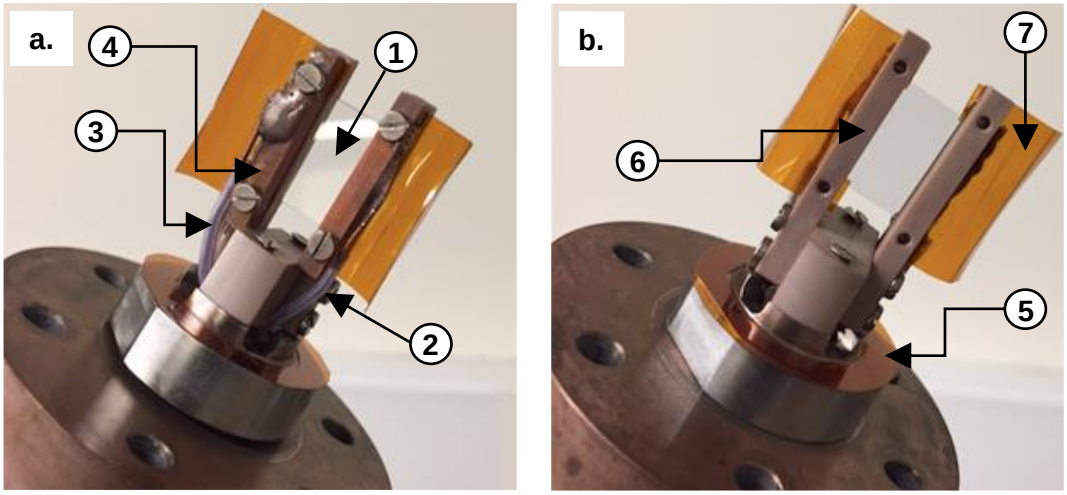

Figure 3.5. The sample holder (a) front view and (b) backside view. The ITO coated glass substrate (labeled 1) is secured between two polyether ether ketone (PEEK) legs (labeled 6) and two copper legs (labeled 4) facing each other. Kapton sheet is used as an O-ring to ensure the proper sealing (labeled 5). Also, Kapton wings were used to prevent short circuit when the chamber is fully closed (labeled 7). The temperature of the substrate surface is monitored using thermocouples (labeled 3) and the voltage is applied to the substrate through copper wires (labeled 2).

3.5. Spectroscopic Techniques

Light interacts with materials in several different ways. During these interactions, light can be transmitted, reflected, or scattered depending on the material's chemical composition and the energy of the incident light. Spectroscopy techniques utilize light-matter interactions to obtain information regarding the structure and properties of the material.[207] As mentioned previously, in-situ UV-vis spectroscopy was used to characterize the concentration of compounds dissolved in supercritical fluids. In addition, Raman spectroscopy was used to characterize polymer films chemical composition. Both of these important techniques will be discussed below.

3.5.1. Transmission Ultraviolet-visible Spectroscopy

The transmission UV-vis spectroscopy was one of the main techniques that helped us to investigate the solubility properties of pressurized polymer solutions at several different temperatures and pressures, identifying the optimized deposition condition. As described in greater detail above, one way this was done was to collect in-situ UV-vis spectra of polymer solutions.

The UV-vis spectroscopy is based on the absorption of ultraviolet or visible light by matter. As the light passes through the matter, electrons are promoted from the ground state to an electronic excited state by absorbing a photon. As a result, the intensity of incident light reduces after absorption, which is directly proportional to the molar concentration of absorbing groups (called chromophores). The Beer-Lambert Law, Equation 3.1, describes how absorption is commonly related to the optical path length (l), molar absorptivity (ε), and the molar concentration of the species (c).[208]

$$A = log\ \frac{I_0}{I} = \varepsilon . l . c \tag{3.1}$$

UV-vis spectroscopy can be used for obtaining information about a compound in solution and in solid state.

3.5.2. Raman Spectroscopy

Raman spectroscopy is a vibrational spectroscopic technique in which the sample is irradiated with narrow band laser light. Interactions with molecular vibrations shift the wavelength of light by an amount equal to the vibrational energy. The scattered light is filtered to remove the main laser line which corresponds to Rayleigh scattering and allows the shift from the main laser line to be more easily detected. This step is important because Raman scattered light constitutes only a small portion of the total signal reaching the detector. In Figure 3.6 different energy states that are involved in Raman spectra are illustrated. Raman scattered light with the same wavelength as the incident light is called Rayleigh scattering. Raman scattered light with shorter wavelength than Rayleigh scattered light is called anti-Stokes, and that with longer wavelength is called Stokes. The change in the energy of the incident photon is directly related to the specific vibrational mode of a molecule and is typically reported in wavenumber (cm^{-1}). Additionally, the surrounding environment of the functional group can result in a change in the peak position. For instance, the presence of hydrogen-bonding interactions can lead to significant frequency shifts of the order of magnitude of hundreds of cm^{-1}.[209] In contrast to IR spectroscopy that probes dipole moment changes, Raman looks at the molecular bond's polarizability providing a complementary probe of intramolecular vibrations.[210]

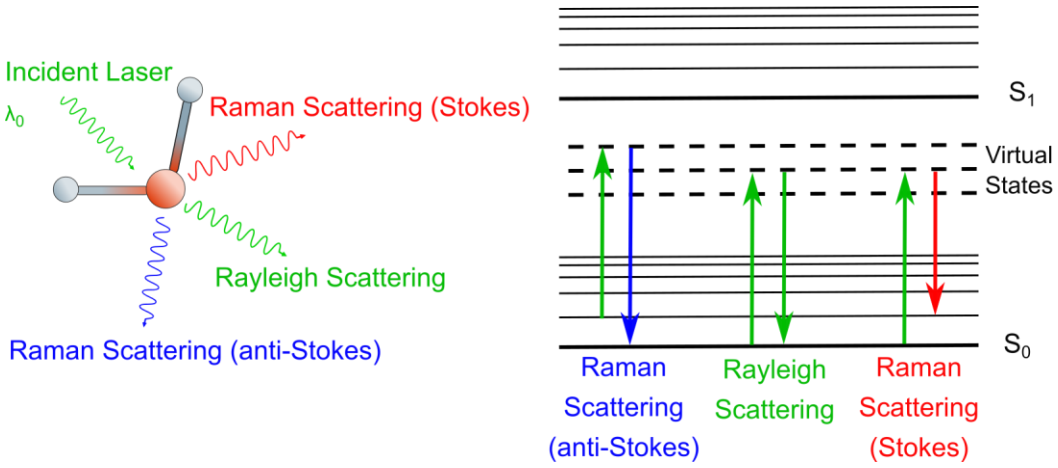

Figure 3.6. The scattering processes that can occur when IR light interacts with a molecule (left) and electronic states diagram of a molecule (right) illustrating the origin of Rayleigh, Stokes and Anti-Stokes Raman Scattering.

3.6. Grazing-Incidence Wide-Angle X-ray Scattering

Grazing-incidence wide-angle x-ray scattering (GIWAXS) is a method developed for studying nanostructures. Following the emergence of synchrotron radiation sources, a collection of surface x-ray scattering and diffraction techniques have emerged to study materials at the surface or interface with small volumes of matter.[211] More importantly, they act as a complementary technique to atomic force microscopy and scanning electron microscopy which typically only measure the surface of the sample.

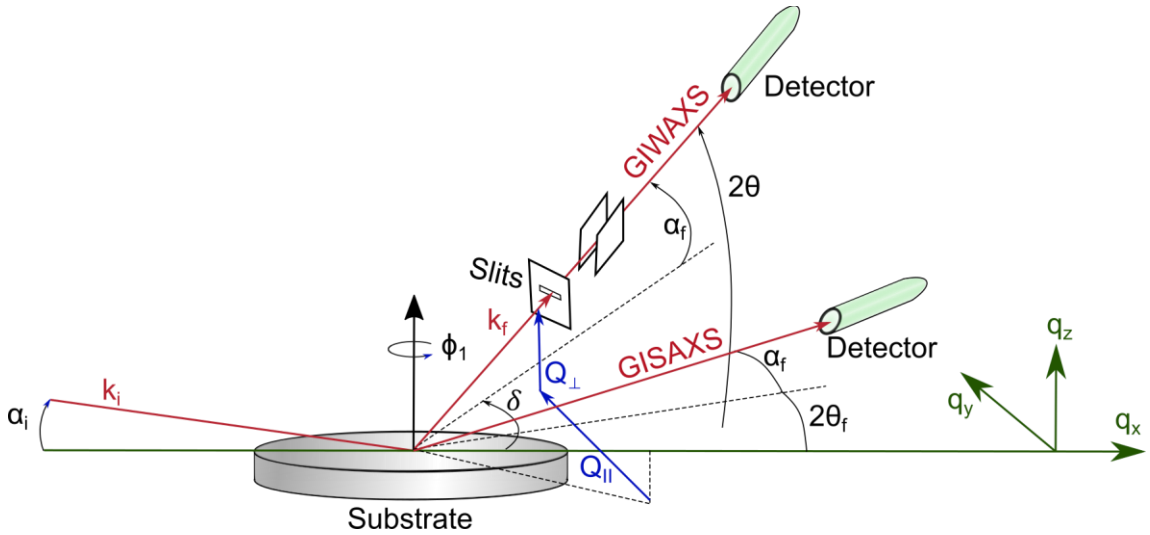

Figure 3.7. Grazing incidence x-ray scattering geometry, at small and large angles (GISAXS and GIWAXS).

Scattering techniques are based on interactions of x-ray beams with sample and analyzing the resulting x-ray scattering pattern. At high frequency regime such as x-rays, the refractive index of all materials is less than one and x-rays with incident angles smaller or equal to the critical angle undergo total external reflection (TER) at an interface and will not penetrate the material's bulk (< few nanometers).[212] Hence, utilizing the technique of x-ray diffraction at very low grazing incidence angles (typically tenths of a degree) with respect to the sample surface helps to maximize the scattering contribution of the investigated material relative to the substrate. Thus, minimizing the unwanted background scattering (both elastic and inelastic) from the bulk.[213] In Figure 3.7, a schematic sketch of the grazing incidence x-ray scattering geometry at different angles is illustrated where the incident angle α_i is close to the angle of total external reflection α_c. GIWAXS corresponds to large values of the scattering angle (2θ) between k_i and k_f, and thus large values of the in-plane ($2\theta_f$) and out-off-plane (α_f) scattering angles. The direction of the scattered wave (k_f) is detected at a direction defined by slits and makes an angle α_f with respect to the sample surface and an in-plane angle $2\theta_f$ with respect to the transmitted beam. The wavevector transfer is defined as $q = k_f - k_i$ and is often broken down into two components: $q_\perp$ perpendicular to the surface and $q_\parallel$ parallel to the surface.[214] In the case of wide-angle x-ray scattering, one can probe the atomic scale order by measuring the scattering intensity and building the intensity distribution in reciprocal space.

Figure 3.8 summarizes the possible 2D GIWAXS patterns observed based on the crystallinity and orientation of the crystals with respect to the substrate surface. As shown in Figure 3.8.a, well-pronounced Bragg peaks are observed in the case of a highly crystalline film with parallel orientation to the substrate surface. In the case of both parallel and perpendicular orientation of crystallites present in the film, Bragg peaks appear along both the vertical and horizontal directions (Figure 3.8.b). The more textured film with randomly orientated domains results in the broadening of the Bragg peaks. For instance, the Bragg peaks along the vertical direction will broaden when domains are oriented with an angular distribution around the horizontal direction (Figure 3.8.c). Figure 3.8.d illustrates the case of disordered film with large degree of crystallites orientation resulting in Bragg peaks smearing out into Debye-Scherrer-like rings.[215]

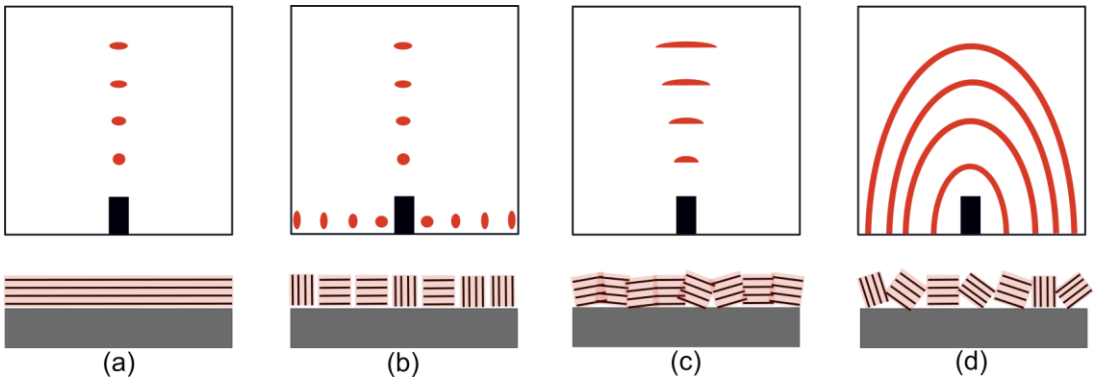

Figure 3.8. Schematic of film crystallinity and corresponding 2D GIWAXS data. (a) vertical lamellar stacking, (b) crystallites with both vertical and horizontal orientation, (c) oriented domains around the horizontal direction and (d) full rotational disorder of crystallites.

GIWAXS has been widely used in polymer science, as the scattering data profile can provide valuable information regarding the polymer chain orientation on the substrate. However, in the case of conjugated polymers, the high degree of paracrystallinity broadens the Bragg peaks and additional analysis is required.[216] For instance, poly(3-hexylthiophene) (P3HT) when cast as a thin film, can crystalize into two major unit cells with distinct chain orientations. As illustrated in Figure 3.9, the polymer chains can adopt either the edge-on or face-on orientation with respect to the substrate. In the edge-on orientation, the side-chains direction (lamellar stacking) is normal to the substrate. In contrast, the face-on orientation involves the aromatic rings (π-π stacking) facing the substrate.

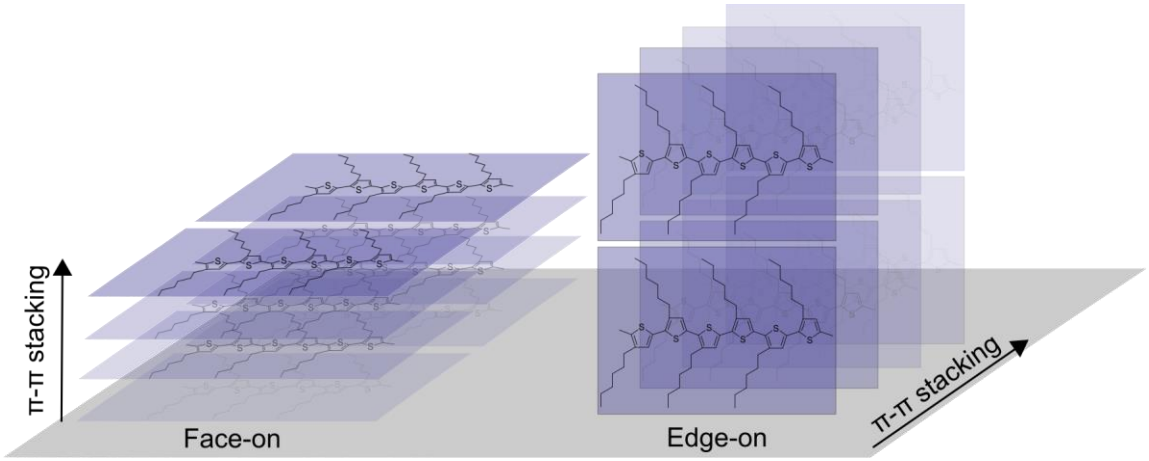

Figure 3.9. Schematic illustration of the face-on and edge-on configurations of P3HT chains.

Figure 3.10 is the corresponding GIWAXS scattering profiles for predominately face-on (a) and edge-on (b) orientations of P3HT. In the predominate face-on orientation, Figure 3.10.a, the lamellae peak appears in the in-plane direction (q_x axis) and the π-π stacking peak in the out-of-plane orientation (q_z axis). In Figure 3.10.b, the lamellar peaks appear along the q_z axis at ~ 0.4 $Å^{-1}$ (in the out-of-plane orientation) with a repeating distance of ~ 1.6 nm corresponding to the parallel lamellae, while the π-π stacking orientation peak is at q_x ~ 1.6 $Å^{-1}$ in the in-plane direction with a spacing of ~ 0.39 nm.

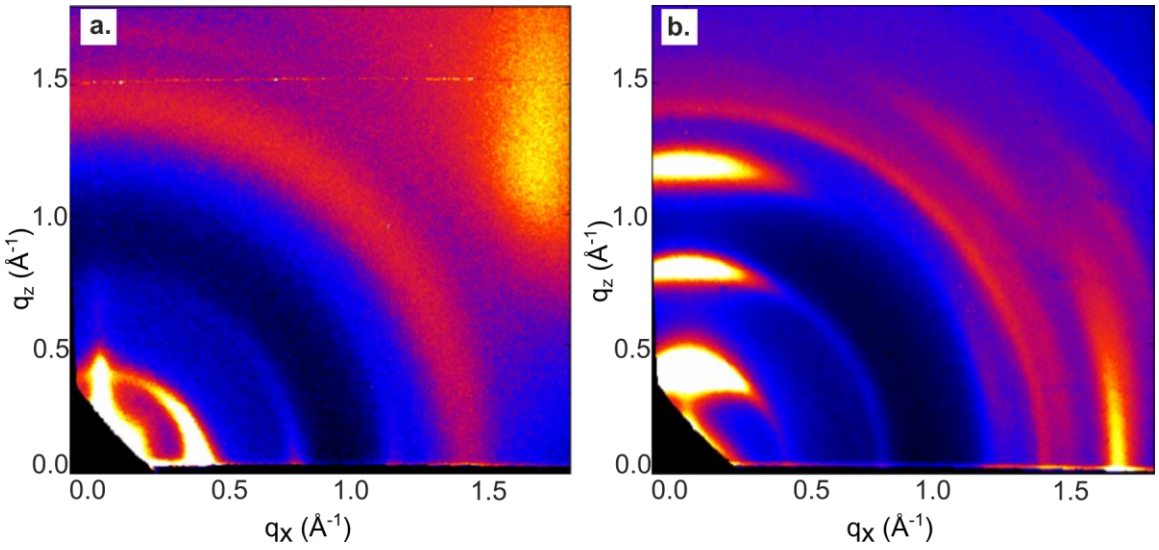

Figure 3.10. GIWAXS patterns of P3HT with predominantly (a) face-on and (b) edge-on orientation. Reprinted with permission from Dr. Kevin G. Yager, Brookhaven National Laboratory, 2020.

3.7. Microscopy Techniques for Morphology Analysis of Deposited Thin Film

Microscopy produces images of samples that are too small to be seen with the naked eye using a variety of techniques. There are three main types of microscopy: optical, scanning probes, and charged particle (electron and ion) each with their set of advantages and limitations. Different types of microscopes have different resolving powers as indicated in Figure 3.11. The resolving power of a microscope can be defined as the inverse of a distance between two points on a specimen that can still be distinguished as distinct entities.

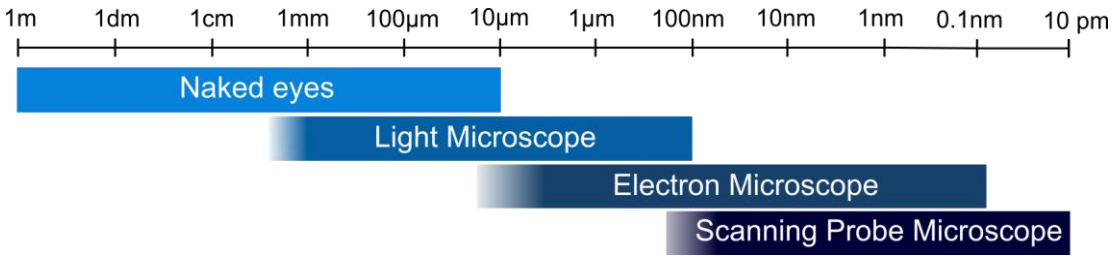

Figure 3.11. Different types of microscopes and their resolving power range.

3.7.1. Optical Microscopy

Optical microscopy refers to any type of microscopy in which visible light is being used to visualize images. Since the visible light is used in this technique, the magnification is limited by the resolving power achieved by the wavelength of the visible light. Abbe's equation can be used to calculate the approximate resolving power of an optical microscope:

$$Resolving\ power = \frac{1}{\Delta d} = \frac{2n.sin\,\theta}{\lambda} \tag{3.2}$$

where n is the refractive index of the medium separating object and aperture and λ is the wavelength of the light illuminating the specimen. As a result, there are two strategies to increase the resolving power: decreasing the wavelength (λ) or increasing the numerical aperture ($2n.\sin\theta$) either through an increase of n or the angle of light coming from the object.

The bright-field microscope is one of the most common and simplest optical microscopes. In bright-field microscopy, a specimen is illuminated from below and the light is collected by an objective lens situated above the specimen. The objective magnifies the light and transmits it to the oculars and/or camera, where the enlarged image of the specimen is displayed. The observed contrast in the bright field image (dark sample on bright background) is due to the light absorbance in dense areas of the specimen.

3.7.2. Polarized Optical Microscopy

The polarized optical microscopy (POM) is a useful microscopy technique that facilitates the observation of birefringent specimens. Although, birefringence is mainly associated with crystals at the microscopic level, it can also be observed at the macroscopic level with polymers and fibers. The intrinsic birefringence is usually related

to the spatial arrangement of atomic groups and molecules, while the form birefringence is based on the spatial arrangement of objects (rods or plates) in a medium of a different refractive index.

Birefringence is the property of crystalline materials that have different indices of refraction in the primary refractive index axes and are defined as optically anisotropic materials.[217]

$$Birefringence = \Delta n = n_{\parallel} - n_{\perp} \tag{3.3}$$

where $n_{\parallel}$ and $n_{\perp}$ are corresponding to the refractive indices of the polarized light parallel and perpendicular to the optical axes.[218]

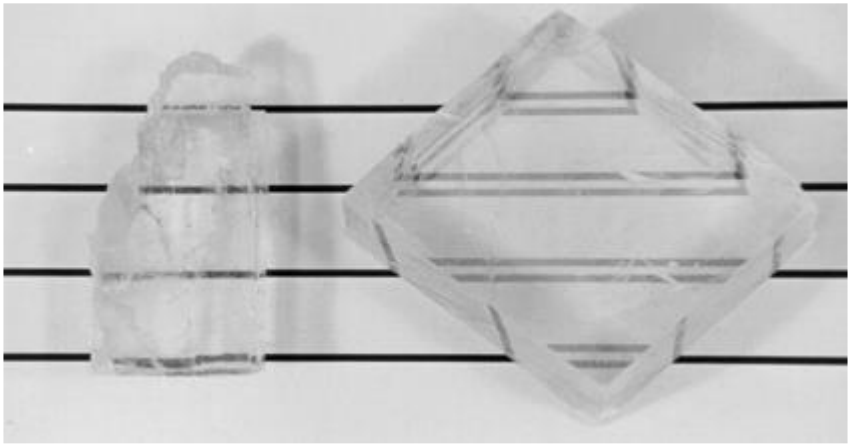

Figure 3.12. Comparison between an isotropic material (left) with only one refractive index for all propagation directions and a birefringent material (right) that has two different refractive indices, allowing two different oscillation directions for the light: a fast and a slow direction, hence a double image. Motic Incorporation Limited Copyright, 2002-2016.

To provide a representation of the refractive indices in different directions, the optical indicatrix is plotted in Figure 3.13.a. An optical indicatrix is an ellipsoid that represents geometrically the variation of three primary refractive indices n_a, n_b, and n_c and the overall refractive index of the material. Isotropic materials, such as cubic crystals, only have one refractive index showing the same optical properties in all directions. In contrast, anisotropic materials like tetragonal, hexagonal, or trigonal crystals, have two unique primary refractive indices. The n_e that is along the c axis is defined as the optical axis as it is the axis for which light experiences no birefringence (parallel to the symmetry axis, so perpendicular to the circular section), and the other primary refractive indices is n_o along

the crystallographic *a* and *b* axes (Figure 3.13.b). The rest of the crystal systems have two optical axes and are named biaxial.

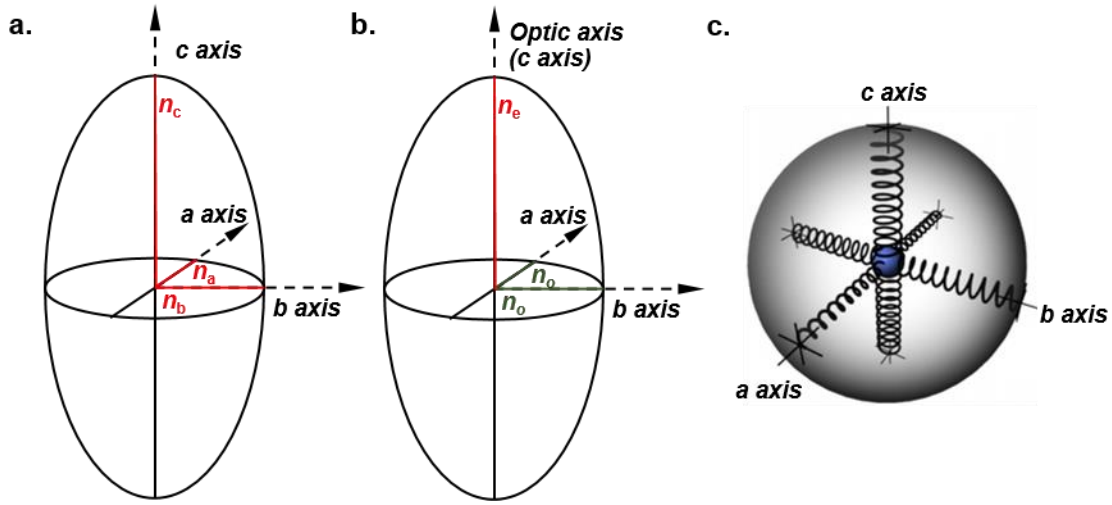

Figure 3.13. (a) A representation of the refractive indices in different directions using the optical indicatrix for a birefringent material. (b) A uniaxial indicatrix where the one optical axis is along the c axis—ellipsoidal indicatrix. (c) A schematic showing an atom feeling different spring strength in different crystalline direction.

Most incoherent light sources generate unpolarized light. The generation of linearly polarized light from such a source requires the use of polarizing optics typically made from natural minerals or synthetic materials consisting of oriented crystallites. Polarized optical microscopes use multiple polarizers to study the birefringence of a specimen. The first polarizer in POM setup is located before the condenser that illuminates the specimen (Figure 3.14), converting unpolarized light into plane-polarized light. The second polarizer in POM, called analyzer, is placed above the objective with the axis perpendicular to the first one (crossed polarizer configuration). In this configuration, the transmitted light will be blocked by the analyzer and a dark background present in the eyepiece. However, if the specimen is an anisotropic material, it changes the state of polarization of light propagating through it and results in bright regions appearing in the dark background.

The birefringent specimen allows the polarized light along the optical axis (called the extraordinary ray, n_e) and the polarized light perpendicular to it (called the ordinary ray, n_o) to travel at different speed. Consequently, these two light components that were in phase when they entered the sample, are retarded at a different speed, and exit the sample out of phase. Later, when passing through the analyzer, the two light components recombine with constructive and destructive interference. The analyzer ensures the same

amplitude at the time of recombination for maximum contrast, while their differential retardation (R) can be measured using a polarized microscope:

$$R = \Delta n \times l \tag{3.4}$$

where Δn is the product of the birefringence and l is the path length through the material.

Birefringent materials are observed as bright objects on a dark background under polarizing optical microscope. The brightness of the images is influenced by many factors, such as intensity of birefringence, thickness of the specimen along the optical pathway, and the alignment of the specimen parallel to one of the two polarizers.[219]

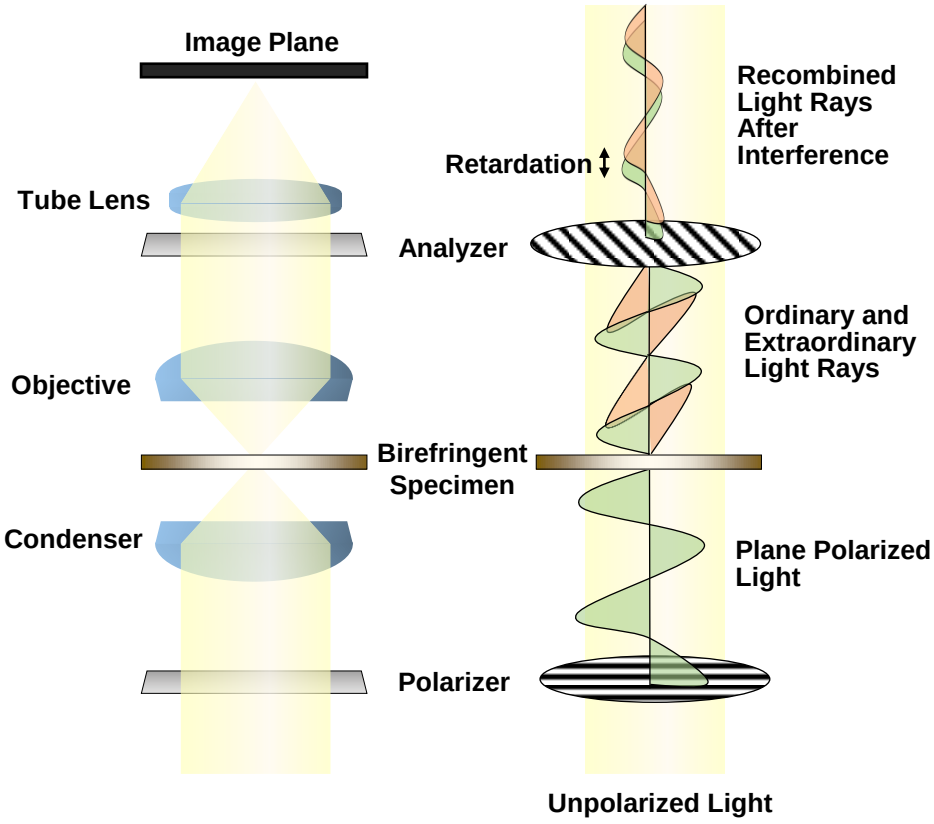

Figure 3.14. The schematic of polarized optical microscope (left) and the corresponding optical path and different light components (right).

3.8. Optical Lithography for Pattern Development

The word "Lithography" originates from a traditional planographic printing technique dating back to the late 18th century which involves printing from a plane surface.

This technique relies on the physicochemical property that oil, and water do not mix. Therefore, the printing elements are soaked with a greasy ink, whereas the nonprinting elements are moistened with water and are ink repellent. The technology for microelectronics fabrication shares similarities with this much older technique and uses light in the process of pattern creation. Thus, it is commonly termed optical lithography or photolithography. In photolithography, a mask is used to create a pattern into a photosensitive emulsion (photoresist) coated onto a surface. All the steps involved in the photolithographic process follow the same principle. A schematic presentation of the photolithography process is shown in Figure 3.15. The procedure starts with chemically cleaning the substrate to remove any traces of impurities. This is vital for promoting the adhesion of a thin uniform layer of photoresist. The photoresist is deposited on the substrate surface using spin coating. There are two types of photoresist: positive photoresist becomes more soluble after exposure to a light source and negative photoresist which becomes less soluble after exposure. Regions of soluble and less soluble material are created by selectively exposing the sample to a light source using a photomask. During the exposure process the pattern on the mask is transferred to the photoresist. Then, the substrate is immersed in a specific solution called “developer” which dissolves away the exposed areas of the positive photoresist or the unexposed areas of the negative photoresist. The substrate is then subjected to subtractive (etching) or additive (deposition) techniques.[220] In the etching process, material is removed from the entire surface, resulting in the removal of material where the substrate is exposed, and removal of layers of photoresist where the substrate is protected. In the deposition process, material is deposited across the entire surface, causing material to be deposited onto the substrate in places where the substrate is exposed.

Etching processes can be characterized as a liquid (wet) or plasma (dry) etching. In microfabrication, there is a variety of wet etchants such as buffered HF used for silicon dioxide (SiO_2) or silicon nitride (Si_3N_4) etching. However, the modern microfabrication technologies are moving away from the wet etching processes due to the dimension control (isotropy), undercutting, and adhesion problems they encounter in these processes. Hence, plasma etching currently plays a significant role in integrated circuit manufacturing owing to its anisotropy, compatibility to automation and vacuum processing technologies, and significantly reduced amount of liquid waste.[221]

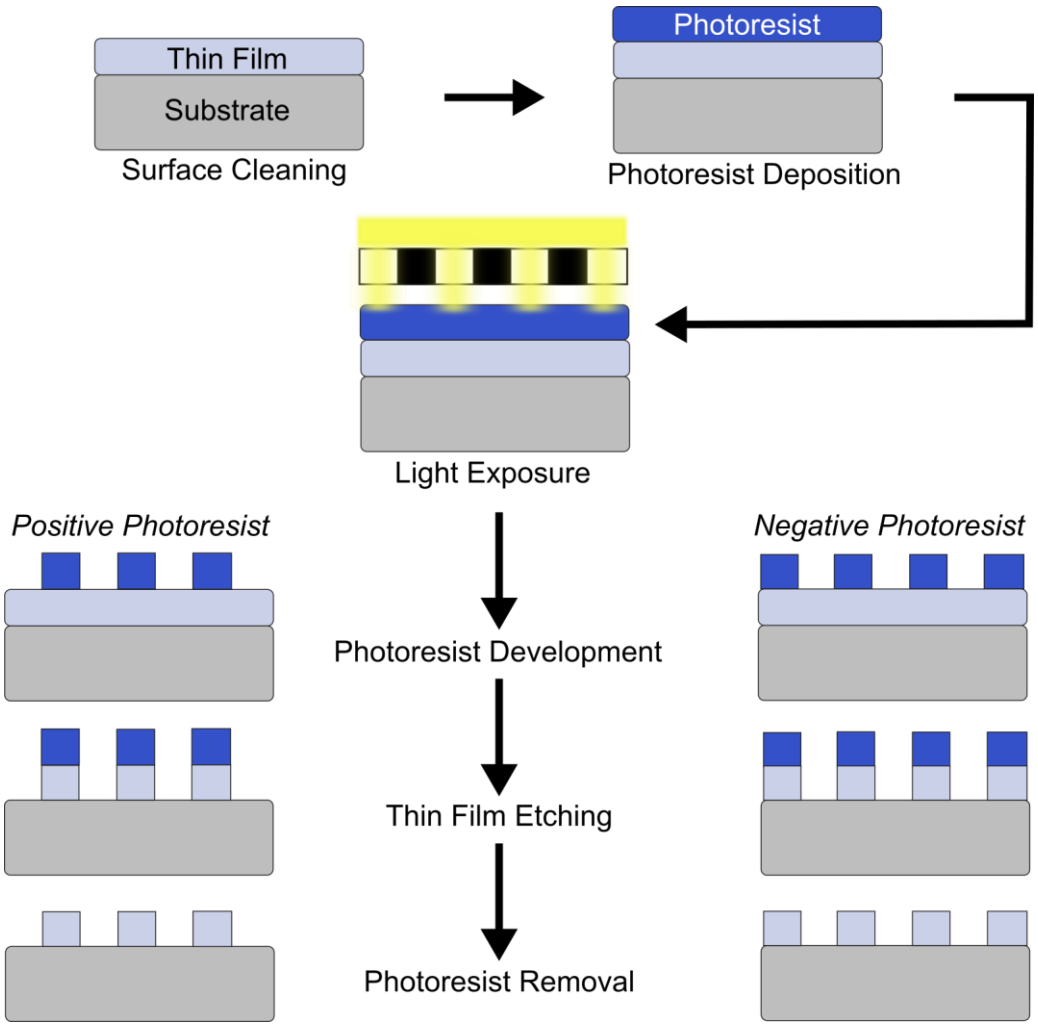

Figure 3.15. Photolithography steps and subtractive pattern transfer.

In plasma etching the material is removed using plasma (a discharge gas) that consists of reactive radicals, ions, electrons, and neutrons. The gas source for plasma usually contains small molecules rich in chlorine or fluorine such as CCl_4. As the active species in plasma gets adsorbed on the surface, they react with the surface material and form volatile products. Afterwards, the volatile products leave the surface and are pumped out with the effluents of the plasma. Figure 3.16 demonstrates different mechanisms during which the surface is etched by plasma active species. In principle, there are three different mechanisms: sputter etching initiated by the bombardments of surface with high energy ions, chemical etching caused by neutral species reacting with the surface materials, and reactive ion etching (RIE) which is a combination of physical sputtering and chemical activity of reactive species with the materials on the surface.[222] The etching

profile in RIE can be tuned by adjusting pressure, gas flow, and the power of the applied radio frequency. Additionally, this can produce an anisotropic etch profile.

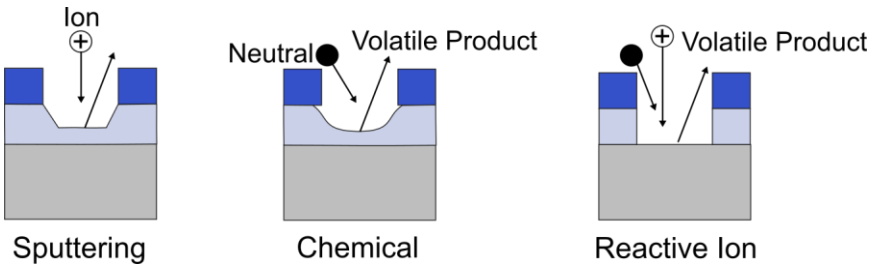

Figure 3.16. Different types of reaction mechanism during plasma etching.

Chapter 4. Physical Supercritical Fluid Deposition of Semiconducting Polymers on Curved and Flexible Surfaces

The results presented in this chapter have been reported in part, see:

Yousefi, N.; Maala, J.J.; Louie, M.; Storback, J.; Kaake, L.G. *ACS Appl. Mater. Interfaces.,* **2020**, 12, 17961-17968.

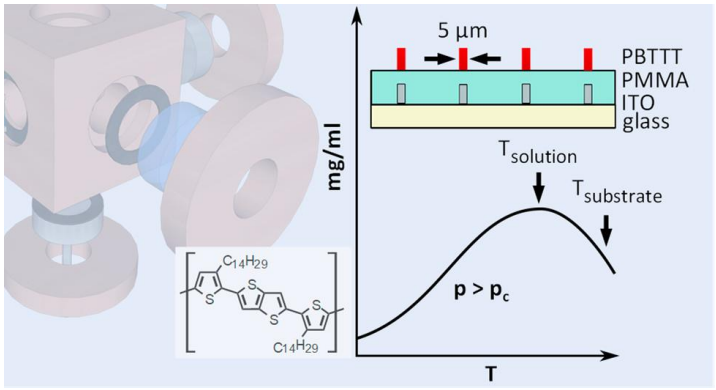

Several people contributed to the work presented in this chapter. We are grateful to Simon Fraser University machine shop staff for machining the chamber components, especially those made from beryllium copper. Undergraduate students, Mikayla Louie, Janneus J. Maala and Jacob Storback who aided in assembly and troubleshooting of the pressure cell and performed important preliminary experiments. Furthermore, Dr. Wen Zhou helped in measuring the Raman spectrum of PBTTT-C_{14}.

4.1. Introduction

Fine control over the deposition of solution-processed materials is a general problem in the science of self-assembly. To fabricate nanoscale structures, two approaches are commonly used. The top-down approach is exemplified by photolithography whereby larger objects are cut into smaller pieces. The bottom-up approach uses intermolecular self-assembly to create larger structures.[223-225] Unfortunately, there is very little overlap between these two approaches, placing limits on both. The molecular level complexity that is available, for example, to biological systems cannot be achieved by using a top-down manufacturing technique. On the other hand, the use of intermolecular forces alone in the placement of nanoscale structures encounters

severe challenges on account of the second law of thermodynamics. Bluntly, a nanomachine is only useful insofar that the work it performs impacts macroscale objects or improves health, and current manufacturing techniques have not yet bridged this gap.

Supercritical fluids provide a unique intermediate between the liquid and vapor phase, and for this reason, we are exploring them as a means of controlling self-assembly. Frequently, supercritical fluids are used in polymer synthesis,[226-231] and the reduction of metal salts can be used to create nanoscale structures.[232,233] In addition, supercritical carbon dioxide ($ScCO_2$) has been used in the processing of organic field effect transistors (OFETs),[234] organic photovoltaics (OPVs),[235,236] metal–organic framework (MOF),[237,238] and aerogels.[239,240] We are interested in a process for material deposition that does not require in situ chemical reactions, which we term physical supercritical fluid deposition to differentiate it from chemical deposition techniques and suggest a comparison with physical vapor deposition. A process that deposits material without in situ chemical reactions is preferable because it allows the compounds of interest to be synthesized, purified, and characterized before deposition. This allows for molecules of significantly higher quality and greater complexity to be employed.

The field of organic semiconductors is one where controlling material self-assembly on many length scales is an important challenge. Most commercial technologies using organic semiconductors employ physical vapor deposition to create thin films. The technique is robust and scalable, and fine shadow masks can be used for micrometer-scale resolution.[241-244] However, the technique requires that the molecules of interest sublime at a temperature lower than their decomposition temperature, limiting the molecular weight of the materials that can be deposited.

Thin films of solution-processable organic semiconductors have excellent properties.[245-248] However, patterned deposition is more technically complicated than using a shadow mask. Printing techniques are common, with each technique offering trade-offs in terms of scalability, ease of ink formulation, and ultimate resolution. For example, direct stamping techniques can deliver superior resolution relative to other techniques but have severe challenges regarding layer-to-layer registry. On the contrary, roll-to-roll printing offers the most scalable method of producing patterned polymer semiconductor films, but ink formulation is difficult and the finest commonly achieved resolution is ~ 100 μm.[249,250] Aerosol jet printing produces the finest resolution at 20-30

μm[251,252] and can deposit material onto convex surfaces, but it requires a print head, making the scalability of the technique unclear. One of the key limitations of all the presented techniques is their inability to work with substrates of negative curvature.

The importance of demonstrating a scalable, high-resolution deposition technique in the field of polymer semiconductors stems from their ever-increasing performance. The charge carrier mobility of polymers has steadily increased for over 30 years, with top performers now on par with polysilicon.[20] Moreover, material quality does not seem to have encountered any fundamental limitations, which argues in favor of optimism regarding further improvements. This seems to suggest that the terms “high performance” and “polymer electronics” need not be at odds with each other. Indeed, the word “cheap” (as representing lower quality than the conventional alternative) need not universally apply to a whole class of materials that have the vast parameter space of organic synthesis at their disposal. However, to begin leveraging this potential, an additive manufacturing technique that delivers control over solution processed materials with an accuracy and fidelity comparable to photolithography must be developed.

We provide the first demonstration that the unique properties of supercritical fluids can be used not only to deposit films of a solution processed material but also to direct its deposition with unprecedented control. The directed self-assembly process uses photolithography, providing a heretofore unexplored connection between top-down and bottom-up self-assembly. The fundamental science underlying self-assembly in supercritical fluids is almost wholly unexplored, and this work provides a unique point of entry to this line of inquiry.

4.2. Results and Discussion

4.2.1. Study of PBTTT-C_{14} Solubility in Supercritical n-pentane

A small glass crucible was filled with poly[2,5-bis(3-tetradecylthiophen-2-yl)thieno[3,2-b]thiophene] (PBTTT-C_{14}).[143] The crucible was capped with glass wool and placed at the bottom of the chamber. The chamber was then filled to the point of overflowing with deoxygenated pentane. The temperature and pressure of the chamber were set by using the manual pressure generator and a temperature control unit. UV-vis spectra of the chamber and its contents were collected 15 min after the chamber had

come to a steady state temperature to ensure saturation of the solution. Spectra collected at room temperature were used as the blank. Figure 4.1 shows absorbance spectra collected at 7.0 MPa as a function of temperature. Because of the high absorbance values involved, the resolution of the spectrometer was decreased, and the spectra were fitted with two Gaussian peaks to capture the behavior as precisely as possible.

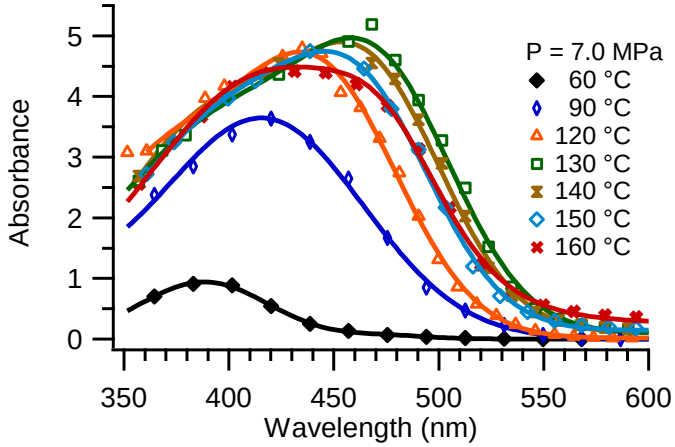

Figure 4.1. UV-vis spectral measurements for the chamber and its contents (solution) for several temperatures and a single pressure. Reprinted with permission from reference 253.

Absorbance spectra displayed in Figure 4.1 show an increase for temperatures up to 130 °C. As the temperature is further increased, the absorbance decreases. To visualize the trends in overall absorbance as a function of temperature and pressure, Figure 4.2.a displays the total integrated intensity obtained from a fit of the data. Absorbance increases with temperature, reaching a maximum value at ≈ 130 °C. Further increases in temperature result in decreasing absorbance.

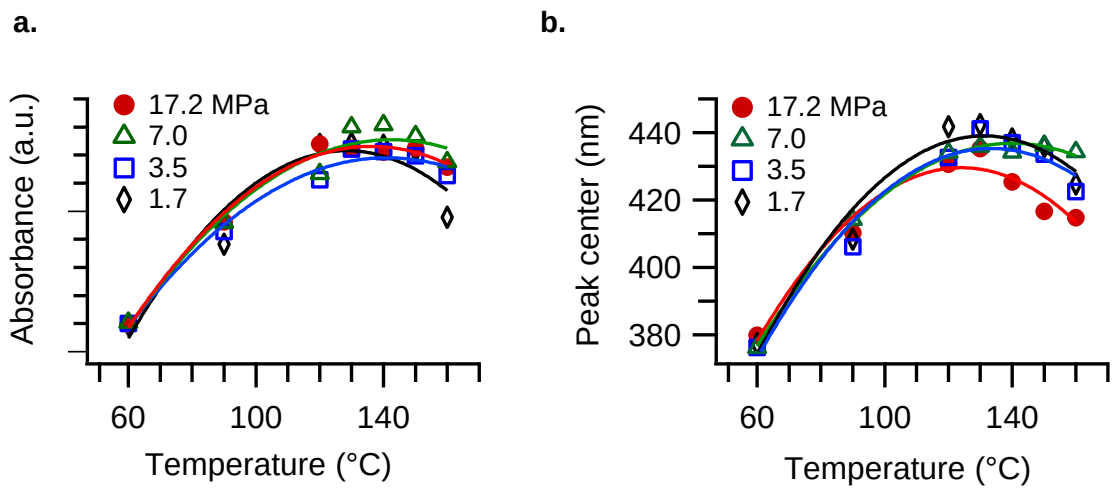

Figure 4.2. (a) Integrated UV-vis absorbance as a function of temperature for several pressures. (b) Estimated center of main absorbance peak as a function of temperature for several pressures. Reprinted with permission from reference 253.

The absorption peak position is also a function of temperature, showing a red-shift in the peak maximum for temperatures up to 130 °C. As the temperature is further increased, a blue-shift is observed. To visualize the trends in peak position as a function of temperature and pressure, Figure 4.2.b displays absorbance peak center as a function of temperature (calculated by the weighted average of the two Gaussian peaks used to fit the data). The peak shifts toward longer wavelengths with increasing temperature up to a maximum, decreasing with further increases in temperature. Very little pressure dependence is observed with respect to the peak position.

The results of Figure 4.1 and Figure 4.2 are best interpreted as demonstrating changes in the amount and type of dissolved material. An alternative hypothesis is that the UV-vis spectra of semiconducting polymers are simply reflecting a known response from temperature and pressure. A monotonic blue-shift with increasing temperature was observed previously,[254] and a monotonic red-shift was observed in response to pressure.[255] Neither effect alters the overall absorbance, in line with spectroscopic sum rules. Instead, the initial increase in absorbance we observe reflects an increase in the amount of dissolved material, and the decrease with further temperature increases indicates a decrease in the amount of dissolved material. This result was also confirmed via gravimetric analysis (see Figure 4.3). The peak shift is reflective of fractionation behavior. As temperature is increased, a red-shift of the spectrum is observed, indicating an increase in the conjugation length of the material.[256] This interpretation is consistent

with the solubility behavior of polymers in supercritical fluids, which favors the solvation of low molecular weight and amorphous material.[227,257-259] As the temperature is further increased, the solubility of the polymer decreases with the longer conjugation length fraction leaving the solution first.

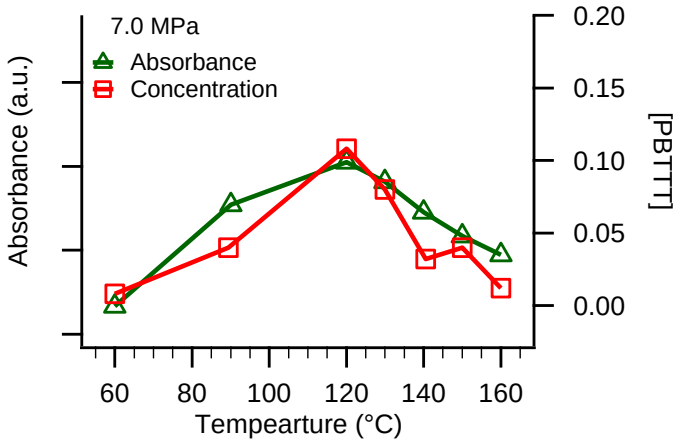

Figure 4.3. Total integrated absorbance (Left axis, a.u.) and concentration (Right axis, mg mL^{-1}) as a function of temperature at 7.0 MPa. Reprinted with permission from reference 253.

The observed nonmonotonic solubility behavior runs counter to the properties of typical polymer solutions at ambient pressure, which tend toward increasing solubility with increasing temperature. However, at pressures above P_C, the solvent transitions continuously from liquid-like to gas-like behavior, and in the limit of pure gas-like behavior the solubility of PBTTT-C_{14} is negligible. Connecting these two regimes with a continuous line suggests strongly that a peak in the solubility will be observed. This behavior is well-known in the supercritical fluid literature and is described as an hourglass-shaped region of immiscibility in temperature-composition space.[260]

Because material becomes less soluble with increased temperature, the entropy of solvation must be negative. This is typically explained by the increasing importance of $\Delta V_{solvation}$ at higher temperatures and lower fluid densities.[194, 261] Microscopically, polymer solvation is accompanied by the formation of a solvent shell. In a liquid nearing its critical temperature, the solvent density of this shell exceeds that of the bulk. Breaking the solvent shell increases the entropy of the solvent, causing the precipitation of the solute.[262] Following McHugh,[194] the problem can be approached quantitatively by using the

Sanchez-Lacombe equation of state, which treats the compressibility of the solvent.[263] A quantitative treatment will be discussed in more detail in Chapter 5.

4.2.2. PBTTT-C_{14} Thin Film Growth in Supercritical n-pentane

The observed maximum in material solubility can be leveraged to grow films on a substrate without the need for chemical reactions. This is the key principle of physical supercritical fluid deposition. To cause material deposition onto a substrate, we hold the temperature of the cell wall at the solubility maximum ($T_{wall} \approx 130$ °C) and resistively heat a substrate immersed in the fluid ($T_{sub} \approx 160$ °C). Because the solubility of the material is lower at the substrate surface, material will precipitate to form a thin film. Figure 4.4 shows optical microscope images of a series of films grown on resistively heated indium tin oxide (ITO) coated glass substrates. The exposure and saturation in these images have been adjusted to better provide visual confirmation of film deposition and allow the film uniformities to be compared.

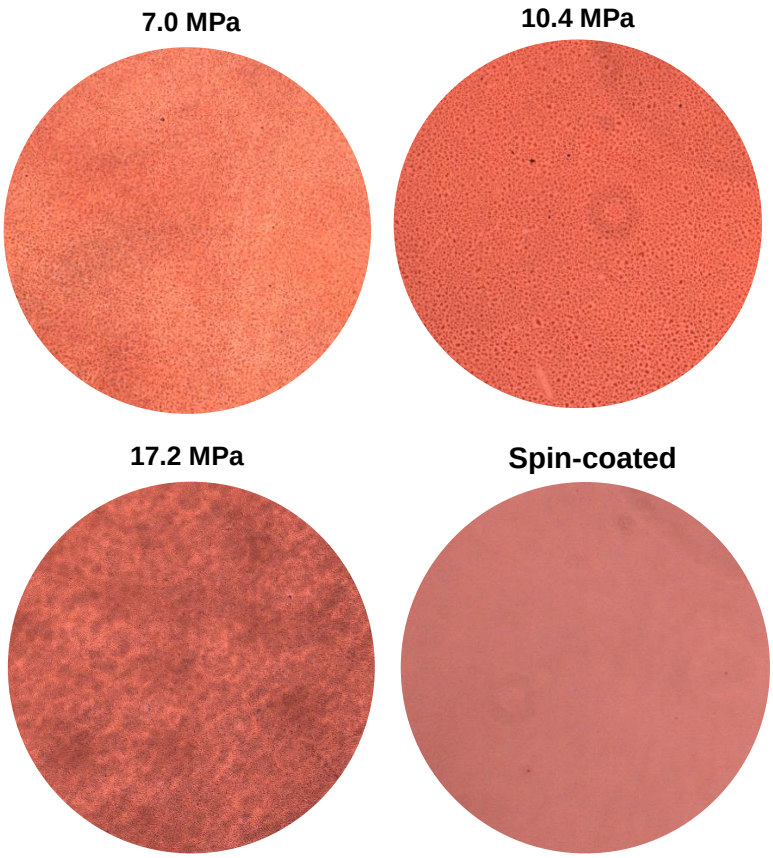

Figure 4.4. Optical microscope images of PBTTT-C_{14} films grown onto ITO substrate with $T_{wall} \approx 130$ °C and $T_{sub} \approx 160$ °C for 90 minutes under several pressure conditions (100x magnification). Adapted with permission from reference 253.

UV-vis spectra of the films grown onto ITO substrates were collected ex situ and are displayed in Figure 4.5. The spectra show a blue-shift in comparison to the spin-coated film of the as-received PBTTT-C_{14}. This is consistent with the observation in Figure 4.1, which suggests polymer fractionation behavior.

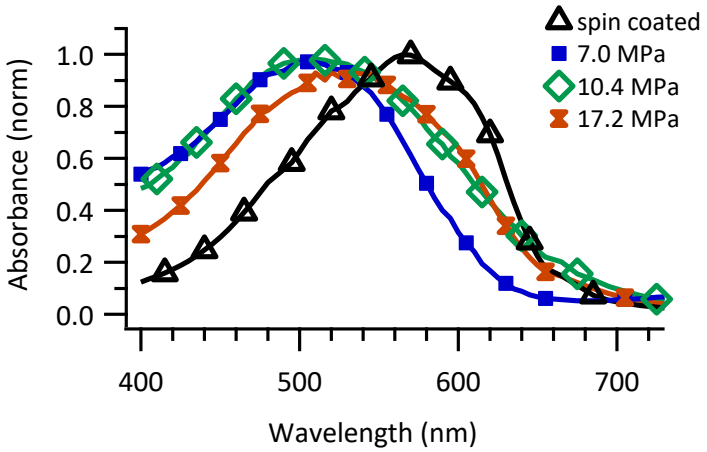

Figure 4.5. Ex situ UV-vis absorbance spectra of the films shown in Figure 4.4. Reprinted with permission from reference 253.

Raman measurements between a deposited film and the as-received material were collected. As illustrated in Figure 4.6, both collected Raman spectra share common features associated with the diagnostic peaks in the range of 1300-1600 cm^{-1}, indicating that the deposited material is chemically unchanged. The thienothiophene core and thiophene rings are known to possess three main modes. According to previous reports, the C-C intra-ring stretching peak position is located at 1380 cm^{-1}, the symmetric C=C stretching peak position is at 1445 cm^{-1}, and the C=C/C-C stretching is at ~ 1488 cm^{-1}. These modes are known to be sensitive to π-electron delocalization (conjugation length) in polythiophene.[264]

For both materials, we observed three main peaks, which are consistent between the two samples. The appearance of our spectra corresponds well with previous reports.[264,265] We observe a strong peak at 1395 cm^{-1} (labeled A), another at 1415 cm^{-1} (labeled B) and the highest energy mode is observed at 1490 cm^{-1} (labeled C). We interpret the consistency between the peak positions of the two samples to demonstrate that the material deposited under supercritical conditions remained chemically unchanged during the deposition process. To better visualize the differences in the peak intensities, the spectra were normalized to the strongest mode, 1390 cm^{-1}. The main difference is attributed to the intensity decrease of C=C/C-C stretching mode for PBTTT-C_{14} thin film at ~ 1488 cm^{-1}. As a result, the height ratio of mode **A** to mode **C** (I_A /I_C) is observed to increase, which has been previously related to the conjugation length.[265,266]

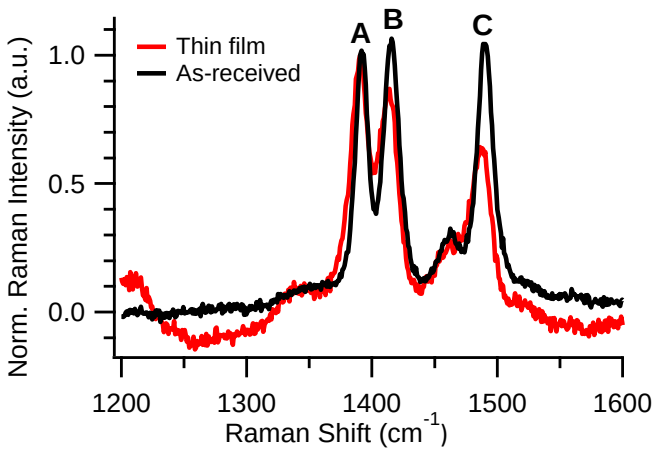

Figure 4.6. Raman spectra of PBTTT-C_{14} as received from the supplier and PBTTT-C_{14} thin film deposited on ITO coated glass after 90 minutes deposition at 17.2 MPa. Reprinted with permission from reference 253.

Some differences in the microscale and nanoscale morphology are observed between the films. For example, nanowires of PBTTT-C_{14} have been precipitated from supercritical hexane,[267] a morphology we observe in some (but not all) of our thin films. Like any other processing technique, film morphology is sensitive to the conditions of film deposition. Because charge carrier mobility is also strongly dependent on film morphology, further studies are necessary to control and optimize charge carrier mobility.

Film deposition was monitored in situ by collecting UV-vis spectra of the ITO coated glass substrates. Figure 4.7 shows the absorbance at 625 nm plotted as a function of time during thin film deposition. This value was chosen because very little light was transmitted at shorter wavelengths. We interpret the increase in absorbance as an increase in film thickness and infer that film thickness increases with respect to time in an approximately linear fashion. This indicates that control over film thickness is relatively straightforward and the technique can be used to create films of arbitrary average thickness.

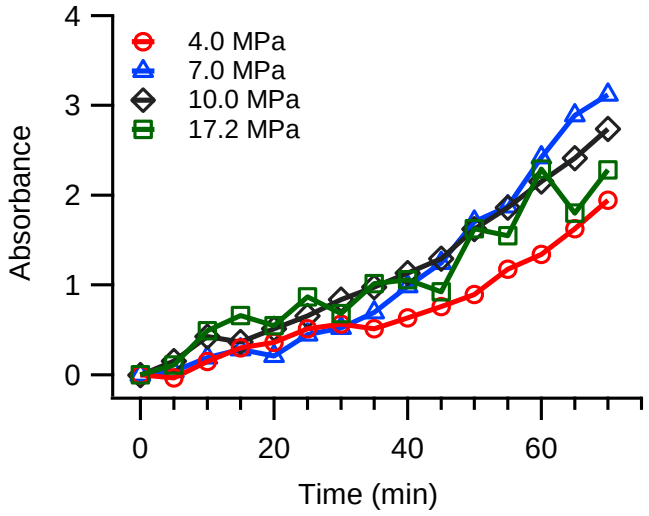

Figure 4.7. In situ UV-vis absorbance at 625 nm collected as a function of time, monitoring film growth (T_{wall} ≈ 130 °C and $T_{substrate}$ ≈ 160 °C). Reprinted with permission from reference 253.

4.2.3. Patterned Deposition of PBTTT-C_{14} on Multifarious Substrates

To demonstrate the wider applicability of this technique, we developed a means of forming patterns of PBTTT-C_{14} on an ITO coated glass substrate. A simple way to produce a pattern in the deposited material is to heat the substrate unevenly, selectively depositing material on the hottest regions of the substrate (Figure 4.8 for a schematic). Thin lines (5 μm) of ITO were created by conventional lithographic techniques, removing the ITO with a reactive ion etcher. Optical microscope images of the results are shown in Figure 4.8.a where the ITO lines can be faintly seen against the glass substrate.

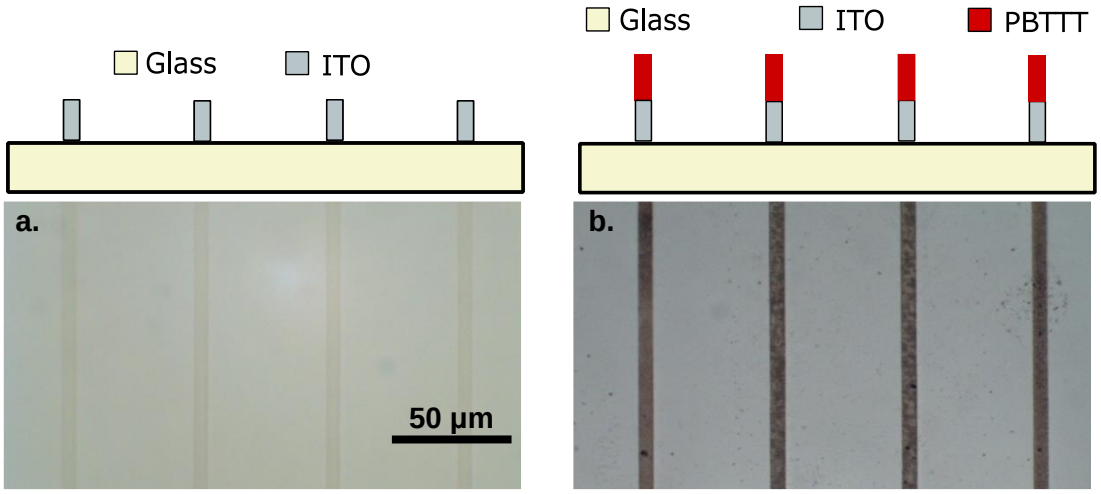

Figure 4.8. Deposition of PBTTT-C_{14} on ITO coated glass after a 3 hrs deposition at 7.0 MPa. The side-view cartoon of patterned substrate is provided at the top of each microscope image (The height scale is ~ 200 nm while the width scale is ~ 200 µm). The corresponding (a) top-view optical microscope image of patterned ITO and (b) deposited PBTTT-C_{14} lines on patterned ITO substrate. Reprinted with permission from reference 253.

The ITO lines were addressed electrically and heated resistively relative to the wall of the supercritical fluid chamber (which was held at 130 °C). Figure 4.8.b displays optical microscope images of the resulting films. Although some amount of overcoating should be expected, the PBTTT-C_{14} lines possess a nearly identical line width relative to the underlying ITO lines. With a line width of 5 µm, this is a 4-fold improvement relative to the line width achievable via aerosol printing techniques.[252] Moreover, the sharpness of the lines indicates that the line width of the technique can likely be improved by a factor of 10, making this demonstration a key step toward using this technique to guide the self-assembly of nanostructured materials. The coffee ring effect,[268] is also absent an important advantage of physical supercritical fluid deposition relative to standard solution processing methods like inkjet printing[269] where drying must be carefully controlled.[270]

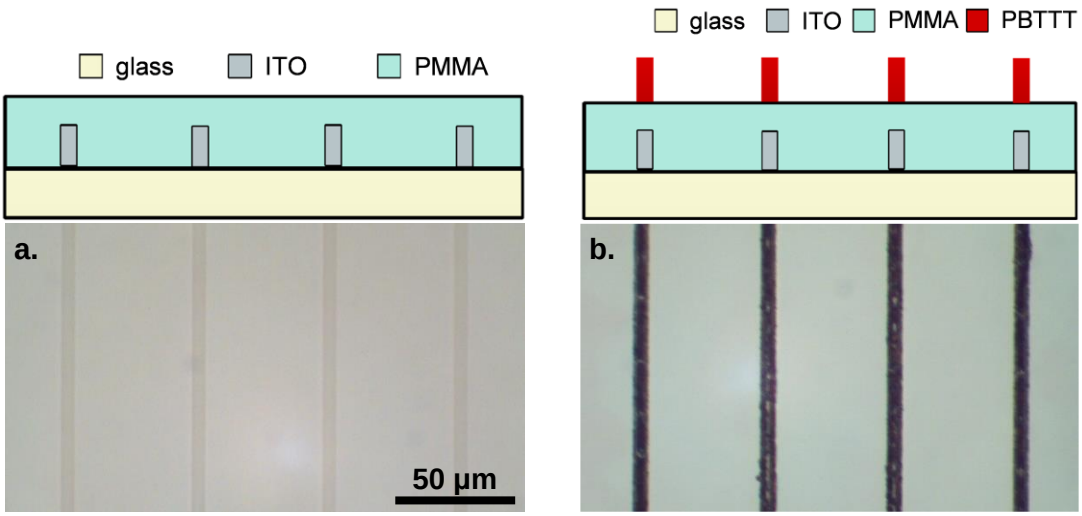

Figure 4.9. Deposition onto PMMA (PMMA film thickness = 165 ± 15 nm). Side-view cartoon is drawn on top of each microscopy image. (a) Top-view optical microscope image of patterned substrate and (b) Deposited PBTTT-C_{14} patterns with deposition condition of: time = 3 hours, *P* = 7.0 MPa. Reprinted with permission from reference 253.

The deposition of semiconducting polymer lines with a line width smaller than conventional printing techniques is an important step toward using it as a manufacturing technique. However, depositing material onto lithographically ITO coated glass does not demonstrate the full potential of the technique. A more commercially applicable deposition mode would be to use the lithographically coated ITO glass as a deposition master, coating it with a substrate that can later be removed, allowing the deposition master to be reused. To demonstrate this, we performed a patterned deposition onto a thin film of cross-linked poly(methyl methacrylate) (PMMA). By depositing a thin and removable layer onto the ITO coated glass, we use the ITO glass as a pattern forming master, allowing us to create patterns on the thin film substrate (PMMA). The thin-film substrate could then be removed from the pattern-forming master and used in, for example, a flexible electronics application. This process could be repeated without the need to replace the pattern-forming master, which could be reused in a manner similar to a photo mask, a shadow mask, or a printing plate. Of course, there is nothing special about ITO coated glass in this context; any pattern-forming master capable of supporting sharp thermal gradients would suffice.

As a first step to demonstrating this process, we coated a patterned ITO substrate with PMMA. The film was crosslinked by heating to 220 °C for at least 30 minutes.[271] Figure 4.9 shows a schematic and optical microscope image of the patterned ITO films

with a PMMA overlayer. The deposition of PBTTT-C_{14} was performed exactly as described in the context of Figure 4.8, with the results being shown in Figure 4.9. No obvious increase in the line width was observed; the PMMA overlayer did not alter the resolution of the finished pattern. In fact, the lower surface energy of PMMA relative to glass seems to have prevented the deposition of small particles on portions of the substrate where deposition was not desired.

As another demonstration of a unique power of this deposition technique, we deposited PBTTT-C_{14} on the concave interior of a poly(dimethylsiloxane) (PDMS) shell. PDMS is a popular silicone elastomer often employed in flexible and stretchable electronics.[272-276] The ability to address concave surfaces is unique to our technique; surfaces of high negative curvature cannot be addressed by a print head, nor can they be deposited on via vapor transport techniques. The ability to deposit material on such a surface not only hints at potential applications in flexible electronics but also illustrates that the technique can be used to deposit patterns on surfaces of any form.

A thin PDMS shell was cast in a die made of a polyimide base and a ball bearing. Before the die was assembled and filled with PDMS, a nichrome wire (AWG = 40, d = 0.0799 mm) was embedded into the die. Figure 4.10 shows a schematic of the object and a microscope image of the object before and after deposition. The object was placed into the supercritical fluid chamber, and deposition was performed in a manner similar to the previous experiments. The nichrome wire was gently removed from the PDMS shell after the deposition, and the resulting object was imaged with a microscope. The results of the deposition are shown in Figure 4.10 (c), demonstrating deposition of PBTTT-C_{14} onto a flexible surface of large negative curvature.

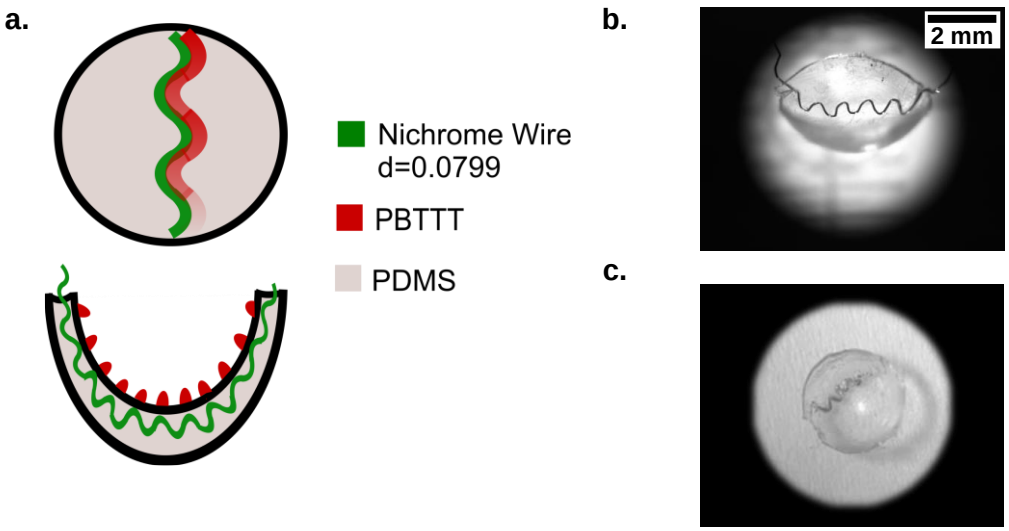

Figure 4.10. Deposition on PDMS hemisphere. (a) Cartoon of top and side view of object. (b) Optical microscope image of PDMS with embedded nichrome wire. The image was taken from an angle looking into the bowl of the hemisphere. (c) Optical microscope image of PDMS hemisphere after deposition and removal of nichrome wire (deposition time = 4 h, P = 7.0 MPa). The image has been taken from the top on the flat surface of the hemisphere. Reprinted with permission from reference 253.

The research performed in connection with Figure 4.10 brings forward two challenges that must be overcome to create high-density circuitry on highly curved and flexible surfaces. The first challenge is to create a deposition master to impart high-density patterns on surfaces of nontrivial curvature (i.e., shapes that cannot be flattened). The second challenge is the difficulty of imaging objects that have microscopic patterns but macroscopic curvature. In other words, conventional microscopy with its limited depth of focus is ill suited to imaging micrometer scale elements on a surface that extends several millimeters vertical to the focal plane. The ability to both create and characterize patterns of this kind is critical to leveraging the full potential of supercritical fluid deposition and stretchable electronics as a whole.

4.3. Conclusion

We presented the initial demonstration of a method that utilizes supercritical fluids and photolithography to direct the self-assembly of a material that can only be processed from solution. The process relies on common properties of solvents above their critical pressure, where solutes can exhibit a maximum in their solubility as a function of temperature. This phenomenon allows films to be formed onto a heated substrate. ITO glass substrates were patterned by using photolithography and, when resistively heated,

directed the formation of polymer lines 5 μm in width. This outperforms the line width of printing techniques like aerosol jet by at least a factor of 4. The pattern forming substrate can be used as a deposition master when overcoated with a flexible and potentially removable thin film substrate. This was demonstrated with a cross-linked PMMA layer. The deposition technique can work with substrates of virtually any shape, as demonstrated by depositing films onto the concave interior of a PDMS hemispherical shell. The pattern forming substrate was created with photolithography, and the patterned films have nearly identical line width, suggesting that much higher resolution patterns can be created. The coupling of photolithography with solution phase self-assembly is the key step to bridge the gap between top-down nanofabrication and bottom-up self-assembly.

4.4. Methods

4.4.1. Transmission UV-vis Spectroscopic Measurements

A custom-built pressure vessel from a block of beryllium copper (BeCu) was utilized for supercritical experiments. The specifications of the high-pressure vessel can be found in section 3.1. As mentioned previously, the pressure vessel has six ports in total, including two sapphire windows to allow in-situ transmission UV-vis spectroscopy. Transmission UV-vis spectroscopic measurements were performed by placing PBTTT-C_{14} into a crucible at the bottom of the chamber before the vessel was sealed and filled with solvent. The chamber exterior was heated by an Omega benchtop PID controller used to drive four cartridge heaters. After the temperature stabilized, the solution was pressurized to 1.7, 3.5, 7.0, and 17.2 MPa by using the manual pressure generator. The system was given ~15 minutes to reach equilibrium before solution absorbance measurements were collected. The in-situ transmission UV-vis spectroscopic measurements details are explained in section 3.2. The reference used for the transmission measurements was the chamber content at room temperature. However, the blank spectra were collected for each pressure as the transmission of the apparatus was slightly higher at increased pressure. This could be attributed to the better refractive index matching between the sapphire windows and the fluid. The resolution of the spectra was decreased to 8 nm to achieve higher signal-to-noise ratio and obtain accurate readings at high absorbance values. The fitting of the data was carried out with two Gaussian peaks using IGOR Pro (Wavemetrics).

4.4.2. Substrate Preparation for Thin Film Deposition

The substrates used for film deposition were ITO-coated glass slides with average resistance of 20-60 Ω/sq. ITO glass slides were chosen as substrates because of their optical transparency, electrical conductivity, and ease of use. A thin layer of gold (≈ 50 nm) was deposited near the edges of the substrates by using physical vapor deposition to facilitate a uniform current through the ITO film. The ITO glass slides were cleaned with acetone and isopropyl alcohol consecutively before mounting them on the sample holder and placing the assembly into the chamber. The substrate was placed parallel to the sapphire windows to facilitate the collection of UV-vis spectra during film growth.

4.4.3. Thin Film Deposition Conditions

The deposition of PBTTT-C_{14} in pressurized n-pentane was performed by first increasing the temperature of the solution to 130 °C. When pressure and temperature had stabilized, the temperature of the ITO glass slide was increased to 160 °C. Increasing the substrate temperature had a subtle impact on the chamber pressure which was addressed accordingly to maintain the desired pressure. In-situ UV-vis measurements were collected during deposition beginning at the 10-minute mark of the deposition process, after the temperature and pressure of the system had stabilized. Spectra were collected every 5 minutes thereafter to monitor the rate of deposition.

4.4.4. Gravimetric Analysis

Gravimetric analysis of PBTTT-C_{14} saturated solutions in n-pentane was perfomred by exhausting the chamber contents through the chamber outlet into a polypropylene vessel with a volume of 500 mL. In more detail, a crucible containing PBTTT-C_{14} was placed at the bottom of the custom pressure cell. The cell was overfilled with deoxygenated pentane before being sealed and pressurized. The vessel had an inlet port to accept the chamber contents and a wide outlet port to avoid over-pressurizing the vessel (the setup assembly can be found in Figure 3.2). The rapid expansion of the chamber contents cooled the solution below its boiling point, allowing liquid n-pentane and (precipitated) PBTTT-C_{14} to be collected. Solvent (n-pentane) was removed from the slurry under reduced pressure, and the dried PBTTT-C_{14} material was weighed.

4.4.5. Pattern Development

The patterned ITO-coated substrates were prepared through photolithography using the OAI Model 800 MBA Mask Aligner in the 4D LABS facility at Simon Fraser University. The photomasks, fused quartz plates covered with patterned microstructures of chromium, were also fabricated at 4D LABS. First, the substrates were placed in Nanostrip2X solution for ~2 hours. Second, the substrates were plasma etched with oxygen for 3 minutes by using a Technics PE-IIA Plasma Etch system. To ensure the adhesion of photoresist to the substrate surface, hexamethyldisilazane (HMDS) vapor was reacted with the surface prior to spin-coating of the photoresist. After the development of the photoresist, the ITO patterns were generated by using a reactive ion etching plasma system from SENTECH (SU 591) located in the 4D LABS user facility at Simon Fraser University. The etch recipe was, 12 mTorr/ 400 W/ 2 sccm Cl_2/ 40 sccm BCl_3/ 40 sccm Ar.[277] Removal of the photoresist yielded ITO lines 5 μm in width with 50 μm of bare glass between the traces.

Films of cross-linked PMMA were created by using a solution of PMMA (Sigma-Aldrich, average $M_W \approx$ 996,000) in butyl acetate (20 mg.mL^{-1}). The film was spin-cast at 1000 rotations per minute for 90 seconds and was crosslinked by heating to 220 °C for at least 30 minutes.[271] The resulting film thickness was 165 ± 15 nm as measured by a Bruker Dektak XT profilometer. The PDMS substrate was fabricated by using premixed and degassed PDMS (Sylgard 184 silicone elastomer kit, base and curing agent mixed at a ratio of 10:1). A thin layer of PDMS was shaped into a plano-convex by using a piece of concave DuPont Vespel Polyimide. A zigzagged shaped nichrome wire (AWG = 40, d = 0.0799 mm) was embedded into the PDMS layer before curing. Afterward, the curing was performed in an oven at 100 °C for an hour.

4.4.6. Characterization of Deposited Thin film

Ex-situ UV-vis spectra of the deposited films, including those prepared by spin-coating, were collected with an Agilent 8453 UV-vis spectrophotometer. Spin-coated films were prepared by using PBTTT-C_{14} in 1,2-dichlorobenzene, (10 mg.mL^{-1}), and the resulting film thickness was ~ 30 nm as measured by a Bruker Dimension Icon atomic force microscope.

Raman spectra were collected using a Reinshaw inVia Raman microscope (50× objective) with an excitation wavelength of (785 nm/50 mW) and acquisition time of 10 seconds. The laser power was set to 1% of its maximum power for as-received PBTTT-C_{14} and 50% for the PBTTT-C_{14} thin film grown in the supercritical fluid chamber at a pressure of 17.2 MPa. All spectra were background-corrected, including the removal of signals from ITO in the case of the film deposited from supercritical fluids. Spectra were normalized to the peak intensity at 1390 cm^{-1}.

Bright-field microscope images were collected with the Axioplan 2 imaging universal microscope from Zeiss, which was coupled with a RETIGA EXi scientific camera from QImaging.

Chapter 5. Physical Supercritical Fluid Deposition of Aliphatic Polymer Films: Controlling the Crystallinity with Pressure

The results presented in this chapter have been reported in part, see:

Yousefi, N.; Saeedi Saghez, B; Pettipas, R. D.; Kelly, T. L.; Kaake, L. G. *Mater. Chem. Front.,* **2021**, 5, 1428-1437.

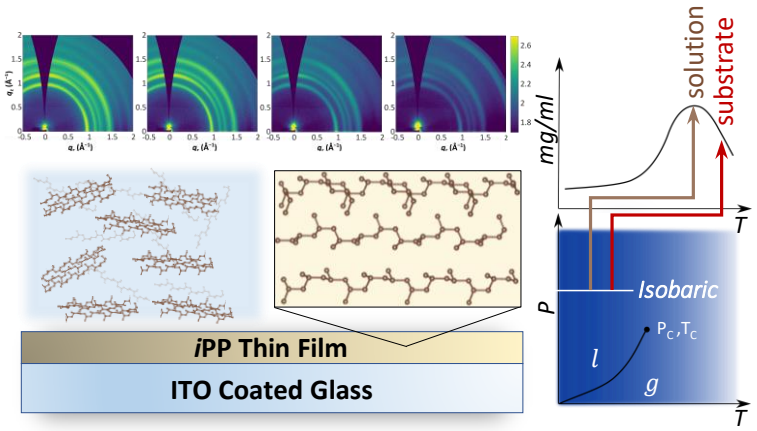

The depositions of isotactic polypropylene in supercritical fluids presented in this chapter were carried out by Nastaran Yousefi and undergraduate student Behrad Saeedi Saghez assisted in performing the depositions. Dr. Timothy Kelly supervised the collection and analysis of GIWAXS data and contributed insightful discussions to this work.

5.1. Introduction

The science of nanofabrication has achieved tremendous success in scaling circuitry via photolithography.[278,279] This top-down approach can be contrasted with the bottom-up approach employed in biology, where larger, more complicated structures are created from molecular building blocks. Synthetic developments along this line have created an incredible diversity of structures, for example molecular machines,[280,281] DNA nano-origami,[282-284] and micellular structures for drug delivery,[285-288] to name but a few. Moreover, a plethora of inorganic structures can be grown from solution, including nanowires,[289-291] colloidal nanocrystals,[292-294] and plasmonic nanostructures.[295-297] To date,

the top-down and bottom-up approaches to self-assembly and nanofabrication exist in largely non-intersecting regions of chemical parameter space. This limits the chemical complexity of materials that can be used in a photolithographic process, and limits the reproducibility, scalability, and control of bottom-up self-assembly.

To address this challenge and better exploit the possibilities afforded by connecting top-down with bottom-up approaches to self-assembly, we introduced a method of film formation that utilizes supercritical fluids (SCFs) in Chapter 4.[253] The technique works by exploiting a maximum in the isobaric solubility of a material to deposit films onto a heated substrate. In the previous work, the substrate was heated resistively by passing current through indium tin oxide (ITO) coated glass substrates. Film deposition was controlled by lithographically patterning the ITO films, producing local resistive heating. Material was found to deposit only where the ITO was present, even when the substrate was coated with a thin film of poly(methylmethacrylate). This demonstration provides a clear path towards controlling solution-phase self-assembly of high molecular weight materials using an additive process that is in turn controlled via photolithography. The additive nature of the pattern formation is critical to providing a clear path towards the unification of top-down and bottom-up approaches to self-assembly and nanofabrication. However, self-assembly in supercritical fluids is not well understood despite a long history of materials-processing using supercritical fluids.

Supercritical fluids exhibit properties intermediate to liquids and gases; these properties can be tuned by varying the temperature and pressure of the system. More generally, a supercritical fluid can be described as a fluid that is pressurized to above or near its critical pressure and held at a temperature near its critical temperature. While this region of the phase diagram cannot be strictly defined in terms of a first-order phase transition, it can be described by several distinct regions. In general, any material in the vicinity of its critical temperature and pressure can be described as a supercritical fluid.[186] The ability of supercritical fluids to exhibit phase behavior intermediate to liquid and vapor has provided many successful applications in areas of polymer synthesis,[226-231,298] and creation of nanoscale structures via reduction of metal salts.[232,233] Moreover, supercritical fluids have been employed in medicine for processing of tissue engineering scaffolds.[299-303]

In order to better understand materials self-assembly in supercritical fluids, we chose to study isotactic polypropylene (*i*PP). It is one of the most widely used plastics because of its thermoprocessability, stability, and good mechanical properties.[304-306] In addition, it is one of the best-understood polymers, and its properties have been further tailored by altering the chain architecture or by means of post-processing techniques.[307-311] These techniques are targeted to modify aspects of the structural hierarchy (crystallite, lamella, and aggregates) that ultimately determine the macroscopic material properties.

Owing to its regioregularity, *i*PP is a highly crystalline polymer with at least 4 different reported structures. The α-form (monoclinic, the most frequent form), β-form (hexagonal), γ-form (triclinic) and one smectic form.[312-315] In addition, the material exhibits diverse self-assembly properties at longer length scales. The most commonly observed structure consists of stacked crystalline lamellae which further assemble to form spherulites and cylindrites.[316] Other observed motifs include dendrites, quadrites, and hedrites. [308,317-321]

The process of crystallization in thin polymer films is different than the polymer melt, resulting in different spherulite morphologies.[322] In a polymer thin film, the spatial restriction causes a preferential orientation of the lamellae that contrasts with the continuous branching and epitaxial growth observed in polymer melts.[323-325] In the case of polymer thin films, pre-aggregation of the polymer happens in the solution state prior to film deposition and solvent chemistry can alter the degree of pre-aggregation.[326,327]

There has been an interest in supercritical fluids or compressible dense fluids over the last few decades due to their ability to tune their solvation power by changing solvent temperature and pressure.[262,328-330] In particular, polymer solubility in SCFs has brought numerous opportunities for physicochemical changes in polymers.[331-334] SCFs have been used to lower polymers' glass transition and induce re-crystallization.[333,335] In addition, crystallization from polymer solutions in dense fluids promotes the formation of different polymorphic states or development of different crystal morphologies such as zigzag or helical chain conformations observed in polystyrene.[336,337]

5.2. Results and Discussion

5.2.1. Isotactic Polypropylene Solubility in Supercritical n-pentane

Before growing films of *i*PP, it is necessary to understand its solubility properties at elevated temperature and pressure. More specifically, the technique relies on a maximum in the isobaric solubility as a function of temperature. The measurement was performed gravimetrically; the solution was exhausted from the chamber and the mass of dissolved *i*PP was measured in the same manner described in section 4.4.4. Figure 5.1 shows the equilibrium concentration of *i*PP in n-pentane as a function of temperature at different pressures. Qualitatively, the concentration increases with temperature up to 418 K, after which further increases in temperature result in a drop in saturation concentration up to 433 K.[338] The observed nonmonotonic solubility behavior for *i*PP agrees with our previous study in which we investigated the solubility of PBTTT-C_{14} in the same solvent (see Chapter 4).[253] It should be mentioned that at higher temperatures, we observed that the upper critical solution temperature (UCST) of *i*PP is reached and the compound becomes miscible in all proportions. This condition was scrupulously avoided in subsequent experiments.

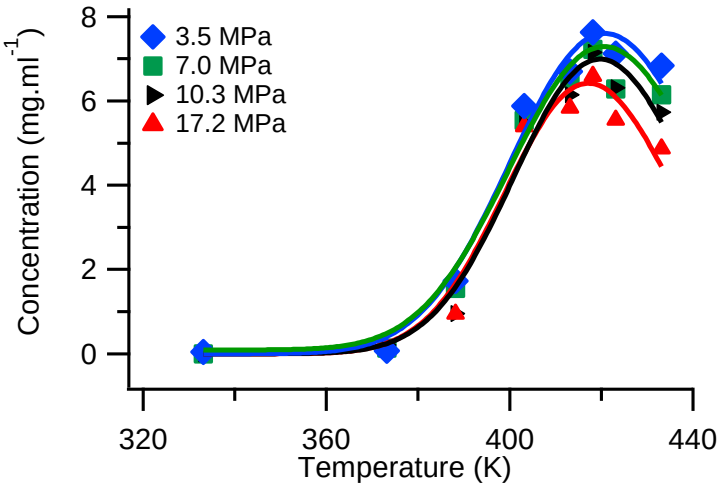

Figure 5.1. Isobaric concentration of *i*PP in n-pentane as a function of temperature. Reprinted with permission from reference 338.

5.2.2. Empirical Model for Polymer Solubility at Elevated Pressures

The nonmonotonic solubility behavior of *i*PP is an important aspect of the film deposition technique presented here and warrants further comment. At ambient pressures, the free energy of solvation is driven by increasing polymer entropy.[194, 261] At higher pressures, decreasing solubility with increasing temperature indicates a negative entropy of solvation as the enthalpy of solvation in hydrocarbon solvents is not strongly temperature dependent. This negative entropy contribution results from the solvent entropy. Specifically, polymer solvation is accomplished by the creation of a solvent shell surrounding the macromolecule. As the temperature approaches the critical temperature from below, the solvent shell becomes higher in density than the surrounding solution. Breaking this shell and releasing the solvent into the bulk increases the overall entropy of the system, causing the polymer to precipitate.[262]

Polymer solution thermodynamics is typically approached from the Flory-Huggins formalism,[339,340] with corrections to the effective interaction parameter being commonly used to describe deviations that lead to a lower critical solution temperature (LCST), for example.[341-343] However, the model is derived under the explicit assumption of an incompressible solution and as such, performs poorly as it is taken further from this original context. To extend the generality of the Flory-Huggins model, a statistical model based on lattice fluids was put forward by Sanchez and Lacombe.[263] However, the price of this generality is that the expression is quite involved and generating a fit to our data is not feasible. Here, we propose an empirically motivated formulation that describes the change in the equilibrium concentration of polymer at elevated pressures and temperatures, where the solvent compressibility plays a dominant role.

We begin by using classical thermodynamics to describe the problem broadly. In particular, the existence of a maximum in the isobaric solubility versus temperature implies that the derivative of free energy with respect to the moles of dissolved polymer (n_2) and temperature is zero.

$$\left(\frac{\partial^2 G}{\partial n_2 \partial T}\right)_P = 0 \tag{5.1}$$

Using the partial derivative relating Gibbs free energy and entropy

$$\left(\frac{\partial G}{\partial T}\right)_P = -S \tag{5.2}$$

It is then clear that at the maximum in solubility, the entropy of solvation is also at a maximum.

$$\left(\frac{\partial S}{\partial n_2}\right)_P = 0 \tag{5.3}$$

Equation 5.3 can be interpreted to mean that the entropy of dissolving additional polymeric material is counterbalanced by a decrease in solvent entropy. As described above, this behavior results from the necessity of forming a solvent shell around the solute. Under these conditions, releasing solvent from the solvent shell increases translational entropy, resulting in a negative entropy of solvation, favoring the precipitation of polymeric material.

We therefore write the Gibbs energy in terms of the enthalpy ΔH, which contains the familiar solubility parameters, the configurational entropy of the solvent and polymer ΔS_C, and the entropy of solvation related to the pure solvent ΔS_P.

$$\Delta G = \Delta H - T\Delta S_C - T\Delta S_P \tag{5.4}$$

Instead of taking derivatives of ΔG, we use it to write the solubility coefficient K, and assume that this coefficient is proportional to the mole fraction of dissolved polymer to within a multiplicative and an additive constant.

$$\Delta G = -RT\ ln\ K = -RT\ ln\left[\frac{\phi_2}{a} - \frac{b}{a}\right] \tag{5.5}$$

Upon rearranging Eq. 5.5 and using Eq. 5.4, we obtain the following:

$$\phi_2 = b + a\ exp\left[-\frac{\Delta H - T\Delta S_C - T\Delta S_p}{RT}\right] \tag{5.6}$$

In the case of our system, the configurational entropy plays only a small role in determining the solubility. This is appropriate given the low concentration regime we are working at and the high molecular weight of the polymer. We will therefore assume this term to be a small contribution that can be accounted for within a and/or b, as it most strongly influences solubility behavior at low temperatures, away from the region of the phase diagram that we are most interested in.

The relationship between the solvent entropy and internal energy is of primary importance in determining the solution properties. The US National Institute of Standards and Technology (NIST) has an extensive database where data regarding the properties of pure fluids is tabulated and accessible. Under the conditions of our experiment, the entropy of pure n-pentane increases linearly as a function of temperature. We therefore write the entropy of solvation as follows:

$$\Delta S_p = -\gamma T \tag{5.7}$$

The sign and temperature dependence of the entropy allows Eq. 5.6 to be rewritten using $T_0 \equiv \sqrt{\Delta H/\gamma}$ as follows:

$$\phi_2(T) = b + a\, exp\left[-\frac{\gamma(T-T_0)^2+2\gamma T\ T_0}{RT}\right] \tag{5.8}$$

Incorporating $2\gamma T_0$ into a yields the final expression which we use to fit our data.

$$\phi_2(T) = b + a\, exp\left[-\frac{\gamma(T-T_0)^2}{RT}\right] \tag{5.9}$$

Figure 5.1 compares the solubility data obtained gravimetrically with a fit of Eq. 5.9. Qualitatively, the fit matches the observations with very little dissolved material at the lowest temperature and a peak in the solubility (T_0) at approximately 417 K. However, to fit the pressure dependent data in Figure 5.1, we describe the change in volume according to the appropriate Maxwell relation,

$$\Delta V \equiv \left(\frac{\partial \Delta G}{\partial P}\right)_T \tag{5.10}$$

and write the pressure dependence of the solubility as follows:

$$\phi_2(P) = b + a\, exp\left[-\frac{P\Delta V}{RT}\right] \tag{5.11}$$

Figure 5.2 compares the solubility of *i*PP in n-pentane at different pressures at constant temperatures as a function of pressure. As shown, the *i*PP solubility drops as a function of the pressure. The decline in solubility seems to be more pronounced at lower pressures and as pressure further increases the effect is of lesser importance.[338] The results and the form of Eq. 5.11 are in good agreement with previous reports on the solubility of *i*PP in n-pentane.[344]

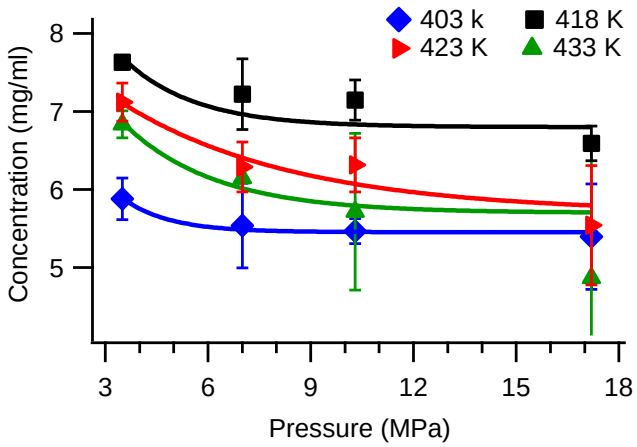

Figure 5.2. Isotherm concentration of *i*PP as a function of pressure. Reprinted with permission from reference 338.

In a similar manner to our previous study on PBTTT-C_{14}, the decrease in the isobaric solubility of *i*PP as a function of temperature can be used to form thin films on a heated substrate. We held the temperature of the cell wall at the solubility maximum (T_{wall} ≈ 418 K) and resistively heated an ITO coated glass substrate that was immersed in the fluid (T_{sub} ≈ 433 K). This procedure causes material to precipitate onto the substrate surface, forming a thin film.

5.2.3. Characterization of Deposited Thin Film

Figure 5.3 shows the deposited films with a series of polarized optical microscope (POM) images. The bright regions in POM micrographs represent the crystalline domains of the *i*PP film. The observation of decreasing brightness with increasing pressure during deposition suggests that the crystallinity of thin film decreases with pressure. Furthermore, samples which do exhibit crystallinity (i.e. films grown at 3.5 MPa) do not resemble the commonly observed spherulitic morphology.[345,346] Instead, we observe a growth process similar to that of diffusion-limited aggregation. In this growth mode, a crystal or aggregate would grow more randomly, which results in fractal-like forms.[345]

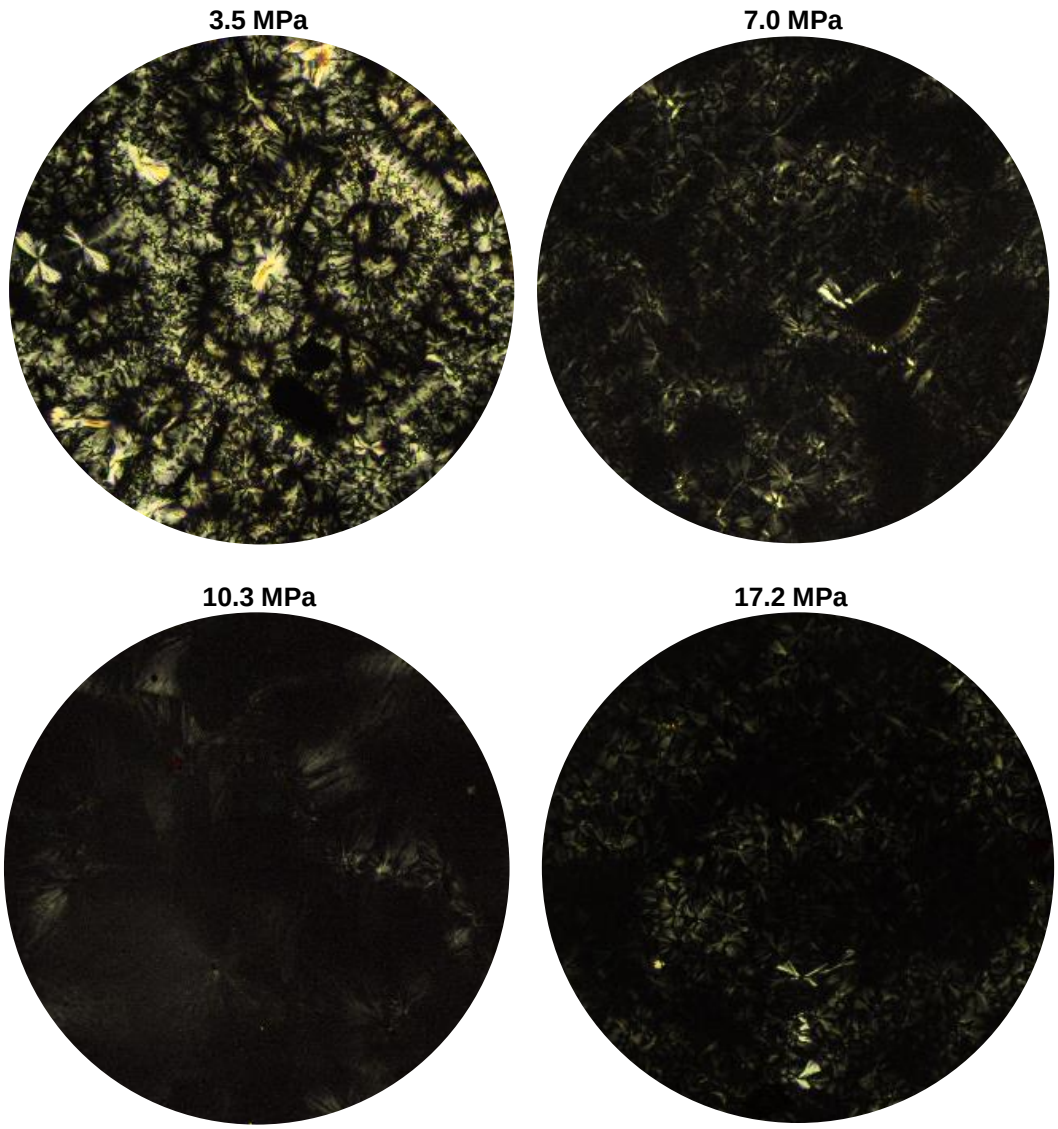

Figure 5.3. Polarized optical microscopy images of *i*PP films grown in supercritical n-pentane (x10) at different pressures. Adapted with permission from reference 338.

To further demonstrate decreasing crystallinity with increasing pressure and to determine the crystal structure of our films, we performed 2D grazing-incidence wide-angle x-ray scattering experiments. Figure 5.4 displays the observed scattering pattern and their corresponding azimuthal integration from films grown at several different pressures. The GIWAXS patterns are consistent with the α-form of *i*PP. In particular, the $(110)_\alpha$, $(130)_\alpha$, $(040)_\alpha$, $(111)_\alpha$, $(131)_\alpha$, and $(041)_\alpha$ peaks, diagnostic of the α-form are observed.[347-349] Moreover, the azimuthally-integrated GIWAXS patterns in Figure 5.4 show scattering intensity as a function of scattering vector (q). The observed scattering pattern is consistent with the *i*PP α-phase,[347,348] with Miller indices of the reflections identified in

red. In addition, a feature attributed to β(300) is observed at 1.09 $Å^{-1}$, indicating a small amount of the β-phase in *i*PP film grown at 3.5 MPa. This feature is not present at higher pressures.

In addition, the intensity of the diagnostic peaks decreases for *i*PP films as pressure increases. This is consistent with our initial interpretation of the POM images, suggesting that the sample crystallinity decreases with increasing deposition pressure.[338] Previous studies of high-molecular-weight *i*PP demonstrate that it adopts the γ-form under high-pressure conditions, with the highest percentage of γ crystallinity found at 200 MPa.[350-353] We have not observed any evidence of γ-phase in our films, consistent with the lower pressure range of our experiment (<35 MPa).

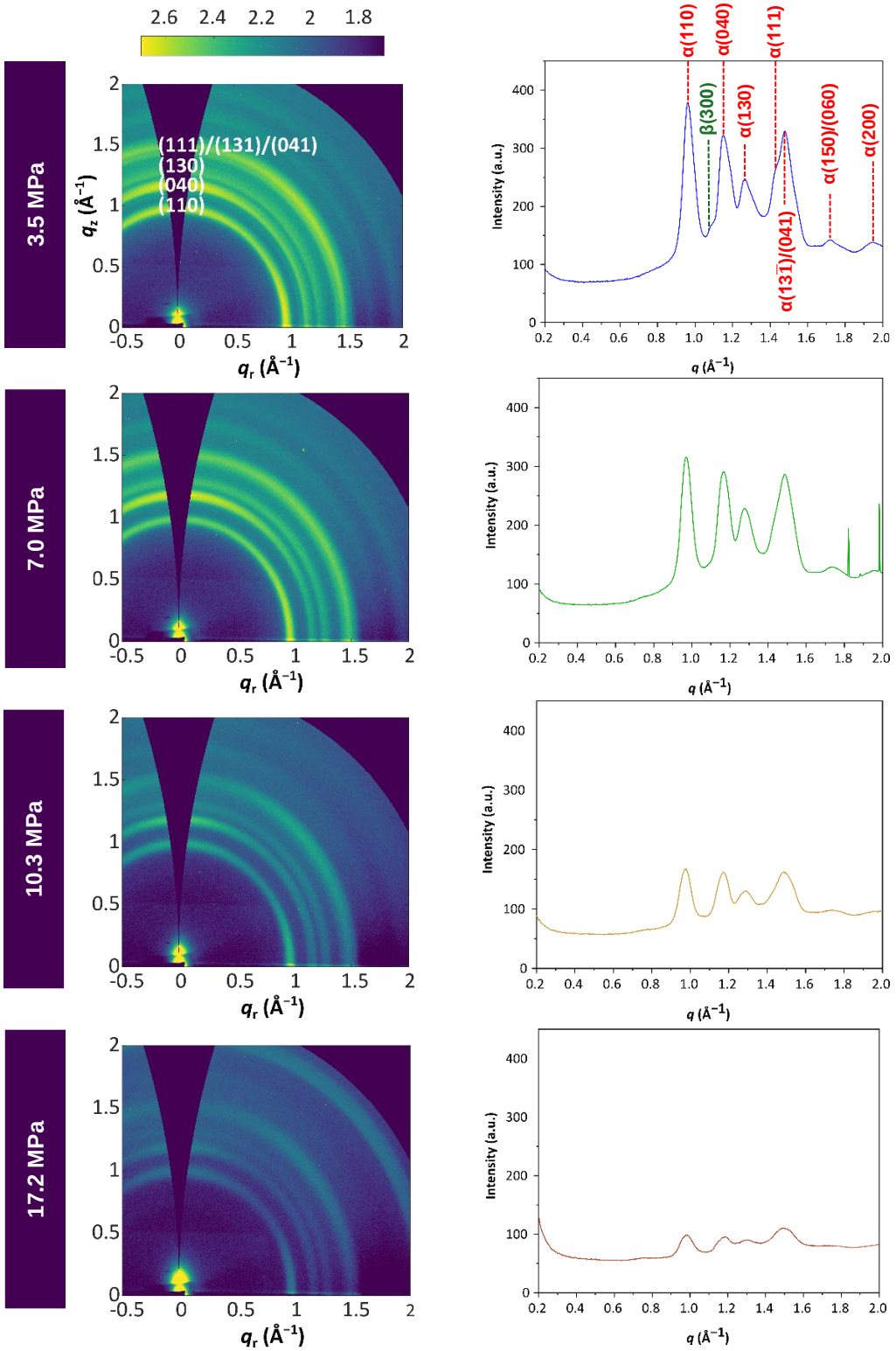

Figure 5.4. GIWAXS patterns of *i*PP films grown in pressurized n-pentane at different pressures (log scale) and their Azimuthally-integrated GIWAXS patterns. Adapted with permission from reference 338.

The GIWAXS patterns also provide information regarding the preferred orientation of the *i*PP chains relative to the substrate. This can be more easily shown with partial pole figures in Figure 5.5.a, constructed from the data in Figure 5.4. The data show that the (110) reflection has two distinct preferred orientations, both out-of-plane (along q_z) and in-plane (along q_r). The (040) reflection is preferentially oriented along q_z, which is consistent with the observed in-plane (110) scattering. This suggests two preferred orientations for the *i*PP crystallites, shown in Figure 5.5.b, with either $q_{(110)}$ or $q_{(040)}$ normal to the substrate. In both orientations, the *i*PP chains lie parallel to the substrate.[338]

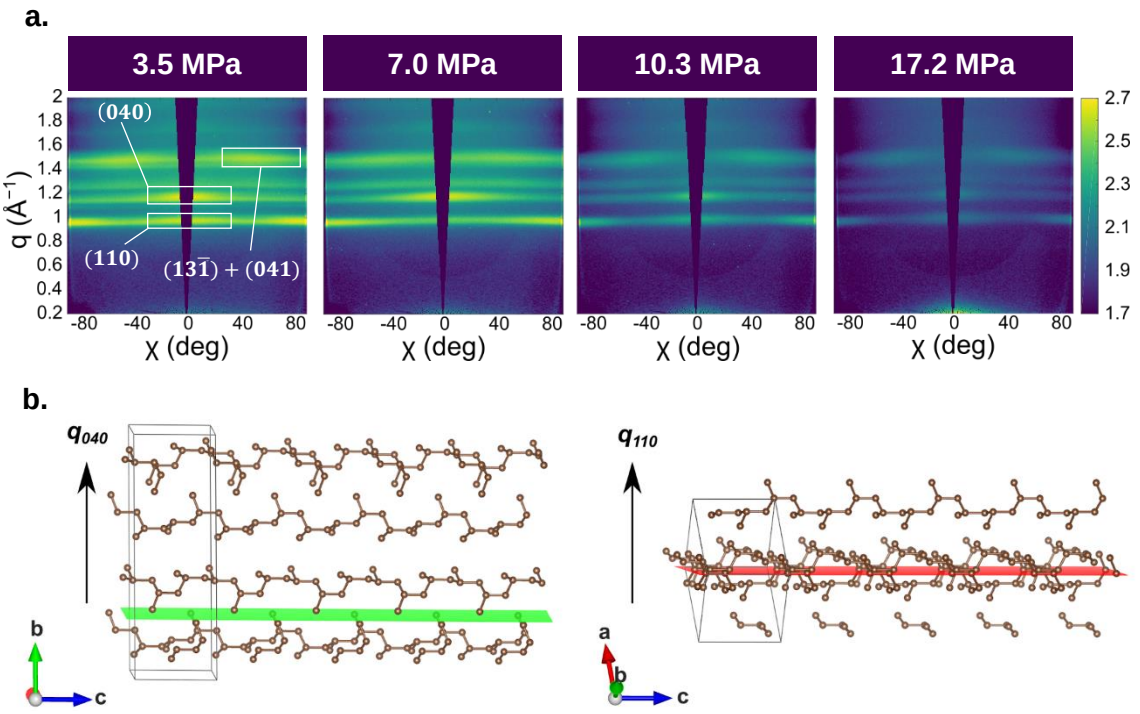

Figure 5.5. (a) GIWAXS partial pole figures of the *i*PP films grown in n-pentane at different pressures. (b) Proposed model for the two preferred orientations of *i*PP chains. Reprinted with permission from reference 338.

As mentioned earlier, the non-spherulitic morphologies of the *i*PP films grown under supercritical conditions suggests that diffusion-limited aggregation is the primary growth mechanism. This rationalizes the more chaotic assembly of *i*PP than would be inferred from large scale spherulitic morphologies. As a result of the diffusion-limited aggregation mechanism, aggregation in solution (a.k.a pre-aggregation) is most likely responsible for the pressure dependence of the crystallinity.

If polymer chains aggregate prior to deposition, fluid properties must be used to explain the decrease in crystallinity at elevated pressures. Because the chamber is sealed and does not contain a free surface, the Rayleigh number (Ra) can be used to distinguish between possible flow regimes.[354] This quantity can be expressed in terms of the isothermal compressibility (β), the magnitude of the thermal gradient (ΔT), density (ρ), dynamic viscosity (μ), thermal diffusivity (α), and the length scale relevant to the problem (x), presumably the distance between the chamber wall and the substrate in this experiment, which is approximately 2 cm.

$$Ra = \frac{\beta \Delta T \rho g x^3}{\mu \alpha} \tag{5.12}$$

Three regimes of fluid flow can be distinguished. At low Rayleigh number, $(Ra < 10^3)$ the fluid does not flow. In this case, mass and thermal transport are driven by diffusion. At higher Rayleigh number, turbulence develops, and flow is driven by density fluctuations arising from thermal gradients. In this flow regime, most of the temperature drop occurs in a thin fluid layer near the boundary where flow can be thought to be laminar.[355] At very high Rayleigh number $(Ra > 10^{13})$ the turbulence disrupts even the boundary layer, entering what is called "ultimate" flow.[356] We visually observe light scattering at the substrate surface during deposition which suggests that flow is in the turbulent regime. This is confirmed by an estimate of the Rayleigh number (Ra) on pure n-pentane from data tabulated by NIST which places $Ra \approx 10^{11}$. For completeness, we also estimate the Prandtl number (Pr) to be approximately $Pr = 3.5$.

The flow regime appropriate for our experimental conditions and our observations suggest that during film deposition, the temperature drops rapidly in a thin boundary layer near the ITO surface. This is depicted in Figure 5.6, a cartoon which describes our proposed mechanism of film formation.

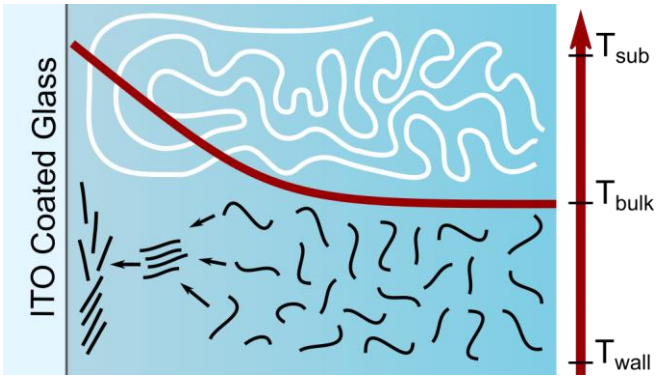

Figure 5.6. Cartoon representing the change in the fluid temperature and flow during the deposition process. Black lines indicate *i*PP chains, white lines describe turbulent flow. Reprinted with permission from reference 338.

The presence of polymer in solution affects solution viscosity, with higher concentrations of polymer being associated with lower Ra and less chaotic flows. We therefore hypothesize that the lower concentration of polymer at higher pressures increases Ra making the flow more turbulent, inhibiting the self-assembly of crystallites. Given the limited diffusion of polymers once they have impacted the surface, smaller and less ordered material would result in more amorphous films. This explanation is in accord with the pressure dependence of our POM and GIWAXS results.

5.3. Conclusion

We measured the solubility of isotactic polypropylene in supercritical n-pentane as a function of temperature and pressure by means of gravimetric analysis. The isobaric solubility exhibits a clear peak versus temperature, while the isothermal solubility exhibits a decrease with pressure for the lowest pressures and is largely pressure independent thereafter. We described our observations with a simple model based on classical thermodynamics. Thin films were formed by resistively heating an ITO coated glass slide immersed in a saturated solution. Films were grown at several pressures and their morphology was studied using polarized optical microscopy and grazing incidence wide angle x-ray scattering. Both the microscopy and the x-ray scattering were consistent with an overall decrease in crystallinity. The α-phase of the material was the predominant crystalline form with the dominant chain orientation parallel to the substrate.

During deposition, we observe light scattering near the substrate surface, indicative of solution turbulence. In addition, pure n-pentane exhibits high Rayleigh

number under these conditions, also pointing towards a turbulent flow regime. We presented a mechanistic description of film formation. First, material precipitates from solution in a pre-aggregation step forming crystallites if not disrupted by solution turbulence. Second, material is deposited onto the substrate where it has limited ability to reorganize to form larger scale structures. These findings provide us with basic principles governing the self-assembly in supercritical fluids and highlight the importance of engineering low Rayleigh number flows to achieve more controlled self-assembly.

5.4. Methods

5.4.1. Solubility Measurement via Gravimetric Analysis

Solubility measurements were performed by placing isotactic polypropylene (Sigma Aldrich, average M_W ~ 250,000) into a crucible at the bottom of the chamber before the vessel was sealed and filled with deoxygenated solvent. The chamber exterior was heated using an Omega benchtop PID controller. After the temperature stabilized, the solution was pressurized to 3.5, 7.0, 10.3, and 17.2 MPa using the manual pressure generator and given approximately four hours to reach saturation. Afterward, gravimetric analysis of saturated solutions of isotactic polypropylene in n-pentane were carried out by exhausting the chamber contents through the chamber outlet into a polypropylene vessel. The gravimetric analysis was carried out similar to PBTTT-C_{14} analysis discussed in section 4.4.4.

5.4.2. Substrate Preparation for Thin Film Deposition and Deposition Condition

The substrates used for deposition were the same ITO coated glass slides used for the deposition of PBTTT-C_{14}. The substrate specification and preparation steps can be found in section 4.4.2. The deposition of isotactic polypropylene in pressurized n-pentane was carried out by first increasing the temperature of the solution to 418 K. When pressure and temperature had stabilized, the temperature of the ITO glass slide was increased to 433 K. Increasing the substrate temperature had a subtle effect on the chamber pressure which was adjusted to maintain the desired pressure.

5.4.3. Characterization of Deposited Thin Film

Texture and phase behavior analyses were carried out using polarized optical microscopy (POM) on an Olympus BS50 microscope equipped with cross polarizers.

GIWAXS measurements were performed at the Hard x-ray MicroAnalysis (HXMA) beamline of the Canadian Light Source. An energy of 12.688 keV was selected using a Si(111) monochromator. The beam size was defined by slits having a 0.2 mm vertical gap and a 0.3 mm horizontal gap, and the angle of incidence was set to 0.1°. The diffraction patterns were collected on a Rayonix SX165 CCD camera (80 µm pixel size; 16.3 cm diameter) using an acquisition time of 30 s. The sample-to-detector distance (224 mm) was calibrated using a silver behenate powder standard. The GIWAXS data were processed using the GIXSGUI software package in MATLAB.[357] The patterns were calibrated, solid angle and polarization corrections applied, and the data was reshaped to account for the missing wedge along q_z.

Chapter 6. Physical Supercritical Fluid Deposition of Aliphatic Polymer Films: Controlling the Crystallinity with Solvent Additive

The results presented in this chapter have been reported in part, see:

Yousefi, N.; Saeedi Saghez, B; Pettipas, R. D.; Kelly, T. L.; Kaake, L. G. *New J. Chem.,* Submitted for publication, **2021.**

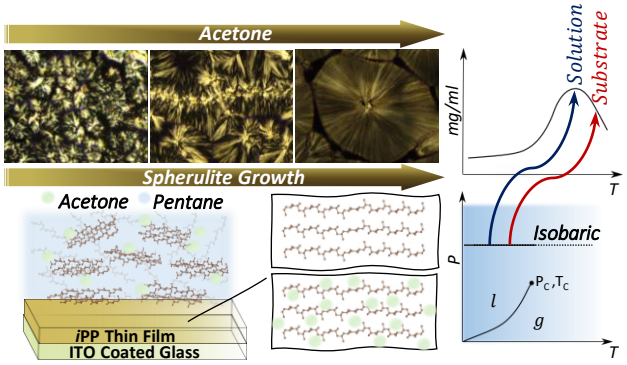

The depositions of isotactic polypropylene in supercritical fluids presented in this chapter were carried out by Nastaran Yousefi and undergraduate student, Behrad Saeedi Saghez assisted in performing the depositions. Dr. Timothy Kelly supervised the collection and analysis of GIWAXS data and contributed insightful discussions to this work.

6.1. Introduction

Photolithography, the prime example of top-down nanomanufacturing methods is ubiquitous in the microelectronics industry.[278,279,358] In contrast, bottom-up processes create more complex structures from the self-assembly of molecular and atomic components.[359] The bottom-up approach has resulted in diverse set of novel structures such as molecular machines,[280,281] DNA nano-origami,[282-284] and micellular structures for drug delivery,[285-288] amongst many others. Furthermore, a plethora of inorganic structures can be created including nanowires,[289-291] nanotubes,[360] colloidal nanocrystals,[292-294] and plasmonically active nanostructures.[295-297] The central challenge in nanotechnology is that these approaches are still largely non-overlapping. This limits the chemical complexity of materials that can be assembled using top-down lithography, and limits the reproducibility

and hence, the scalability of manufacturing processes that use bottom-up self-assembly to position nanoscale structures on surfaces.

In an effort to address this challenge, we have introduced a film formation technique using supercritical fluids (SCFs).[253] The technique relies on a maximum in the isobaric solubility of a material to deposit films onto a heated substrate. Resistive heating provides the most straightforward means of increasing substrate temperature. This approach to self-assembly provides an entirely new path towards well-controlled self-assembly of high molecular weight materials in the solution phase using an additive process that is in turn controlled via photolithography. The successful coupling of solution phase self-assembly and lithography bridges the gap between bottom-up and top-down self-assembly. However, the mechanism by which the self-assembly takes place in supercritical fluids is not well understood despite a long history of materials processing using supercritical fluids.

The SCF is a state intermediate between gas and liquid and its properties, for example, solvation power can be easily tuned by changing temperature and/or pressure of the system.[262,328-330] The unique combination of liquid-like density, and gas-like diffusivity and solvating properties of SCFs have resulted in a variety of successful applications in the field of polymer science. For example, SCF's can be used as a solvent for synthesis,[226-231,298] or imparting chemical and morphological changes.[331-334] Other studies have used supercritical fluids to lower polymers' glass transition and induce re-crystallization.[333,335] Additionally, significant morphological changes are induced by the crystallization from polymer solutions at high pressures such as decrease in the crystal lamellae thickness in polycaprolactone[332] and zigzag or helical chain conformations observed in polystyrene.[336,337]

In order to gain a better insight into polymer self-assembly in supercritical fluids, we selected isotactic polypropylene (*i*PP) since it is one of the most well-understood crystalline polymers.[304-306] This polymer has properties that can be further tailored by altering the chain architecture or by means of post-processing techniques.[307-311] These techniques are designed to alter structural hierarchy (crystallite, lamellae, and aggregates) that ultimately determine the macroscopic material properties.

The crystallization of *i*PP proceeds by the known two-step process of nucleation, followed by crystal growth.[361,362] The crystalline phase may adopt different structures and morphologies based on the crystallization conditions.[363,364] For instance, thin polymer films and materials formed from the melt have different spherulite morphologies.[322] The difference is mainly due to the spatial restriction that lamellae experience in polymer thin film, inhibiting the primarily epitaxial growth seen in polymer melts.[323-325]

To gain better control of self-assembly in supercritical fluids, we investigated solvent additives and/or mixed solvents. The use of additives in polymer processing is common, especially in the context of nucleation agents and plasticizers.[365,366] The use of solvent additives, intended to evaporate during thin film formation, has been extensively investigated in the organic electronics community,[34,35,157,367] and has been shown to profoundly influence solar cell efficiencies by altering nanoscale self-assembly.[153,154,368-370] In the case of polymer thin films, the polymer pre-aggregation in the solution state and the solvent chemistry play pivotal roles in the formation of different morphologies in the deposited films.[326,327] The solvent additive approach has been demonstrated as a promising method to alter polymer aggregations and obtain different thin film morphologies.[371-375]

6.2. Results and Discussions

6.2.1. Solubility of Isotactic Polypropylene in a Binary Solvent System

In order to study the *i*PP solubility and its self-assembly in supercritical n-pentane:acetone, we established the equilibrium concentration of *i*PP in n-pentane:acetone solutions at different temperatures and pressures using gravimetric analysis. Figure 6.1 displays the concentration of *i*PP as a function of temperature at a pressure of 10.3 MPa for each solvent system. Initially, the concentration of *i*PP increases with temperature before reaching a maximum and decreasing with further temperature increases. This nonmonotonic behavior was observed previously with PBTTT-C_{14} (refer to section 4.2.1). It should be pointed out that we observe an upper critical solution temperature (UCST) of 448 K and have deliberately conducted our experiments below this temperature. We note that the UCST we observe is higher than a previously reported LCST for this system.[376] We interpret the previous work as demonstrating nonmonotonic solubility behavior rather than a true transition from miscibility to phase-separated

behavior. Increasing the volume fraction of acetone causes the temperature of the concentration maximum to shift towards higher temperatures. In addition, the peak appears to sharpen.

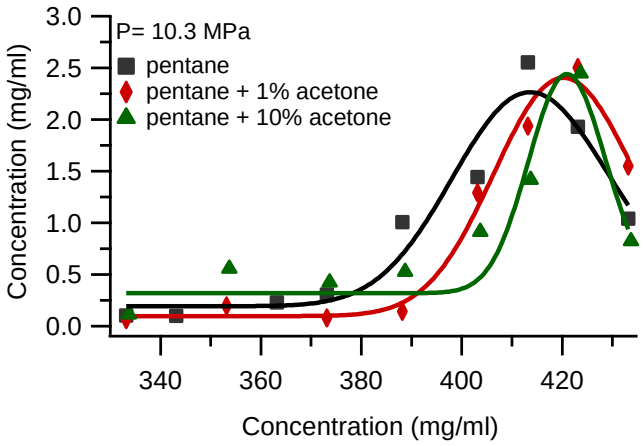

Figure 6.1. Isobaric concentration of *i*PP in n-pentane:acetone as a function of temperature at P = 10.3MPa.

The observation of a solubility maximum at temperatures lower than a UCST is not easily explained using the standard Flory-Huggins approach to solution thermodynamics. In this approach, increasing polymer entropy promotes solvation while mismatched solubility parameters inhibit solvation. The relative contribution of mismatched solubility parameters to the free energy of mixing decreases monotonically with temperature, eventually leading to a UCST, beyond which the polymer is miscible with the solvent. Conversely, decreasing solubility with increasing temperature requires a negative entropy of solvation in the absence of specific intermolecular forces which can be broken (e.g. hydrogen bonds).

A negative entropy of solvation points towards the importance of the solvent entropy in the solvation process. As the critical temperature of the solvent is approached, the density of the solvent decreases substantially, and a chemical equilibrium can be thought to exist between the solvent shell and the bulk solvent. Releasing solvent molecules from the shell and precipitating the polymer increases the overall entropy, leading to a negative entropy of solvation.

6.2.2. Polymer Solubility Model for a Binary Solvent System

A few quantitative models predicting polymer solubility in supercritical fluids exist including those of Sanchez-Lacombe, Simha-Somcynsky, the Statistical Associating Fluid Theory (SAFT) and the perturbed chain (PC)-SAFT.[263, 335, 377, 378] However, these models are too complex to fit our data set and, in their generality, lack intuitive transparency. To address this, we developed a simple model based on classical thermodynamics to describe polymer solubility for the more limited case in which we are primarily interested (refer to section 5.2.2.)

We describe the free energy, ΔG, of the system in terms of the enthalpy ΔH, which includes the intermolecular forces and is typically given in terms of solubility parameters. Equation 6.1 also contains the configurational entropy of the solvent and polymer ΔS_C, and the entropy of solvation related to the pure solvent ΔS_P.

$$\Delta G = \Delta H - T\Delta S_C - T\Delta S_P \tag{6.1}$$

Focusing only on the interplay between ΔH and ΔS_P, we can derive an expression for the concentration of *i*PP versus temperature as follows:

$$\phi_2 = b + a\, exp\left[-\frac{\gamma(T-T_0)^2}{RT}\right] \tag{6.2}$$

Where $T_0 \equiv \sqrt{\Delta H/\gamma}$ with γ describing the slope of a linear increase in ΔS_{P} with respect to temperature. This assumption is consistent with the behavior of solvent entropy with respect to temperature.

Figure 6.1 shows the fit with respect to the collected data. The peak in the concentration versus temperature can be fit with an approximately Gaussian lineshape. In addition, Eq. 6.2 makes specific predictions about the position of the peak with respect to changing solvent composition. We expect that acetone, an antisolvent for *i*PP, should have a larger ΔH of solvation, and exhibit a higher temperature peak in the isobaric solubility. This is consistent with our observations, demonstrating the validity of Eq. 6.2 in qualitatively describing this system. The peak also appears to narrow, but noise in the data prevents more specific conclusions being drawn. Gravimetric analysis is a robust technique, but not exceptionally precise and has very poor throughput.

6.2.3. Characterization of *i*PP Thin Film

Using the solubility data in Figure 6.1, we devised the deposition conditions that would produce thin films of *i*PP from supercritical n-pentane:acetone solutions. The temperature of the chamber wall was set to 418 K (423 K in case of n-pentane:acetone). And, an ITO coated glass substrate was resistively heated to 433 K to initiate the deposition. These conditions were reproduced for several pressures, allowing us to examine effect of pressure and changing solvent composition.

Figure 6.2 presents a series of polarized optical microscope images of the deposited *i*PP films. Bright regions are typically interpreted to indicate the presence of birefringent crystallites. We observe a decrease in brightness of POM micrographs with an increase in pressure across all solvent systems, indicating reduced crystallinity of thin films with pressure. In addition, the films grown in n-pentane with crystalline domains (i.e. films grown at 3.5 MPa) do not show similar features to the commonly observed spherulites in *i*PP films. The lack of order in crystalline regions resembles the diffusion limited aggregation growth process in which the mechanism of growth is more random and results in fractal structures.[345]

On the other hand, the addition of acetone to n-pentane not only enhances spherulite formation in *i*PP films but also increases spherulite diameter. The influence of solvent additive is more pronounced at low pressures especially at 3.5 MPa with the largest spherulites being formed with the highest concentration of acetone. We postulate that the acetone remains in the film for a short time following material deposition, increasing chain mobility following deposition. As a side note, we observe dendritic ß-*i*PP lamellae in case of 1% acetone addition at 7.0 MPa. The crystallization of ß-*i*PP in thin films requires α-form crystals to act as nucleation sites for ß-*i*PP crystals switching the direction of lamellar growth.

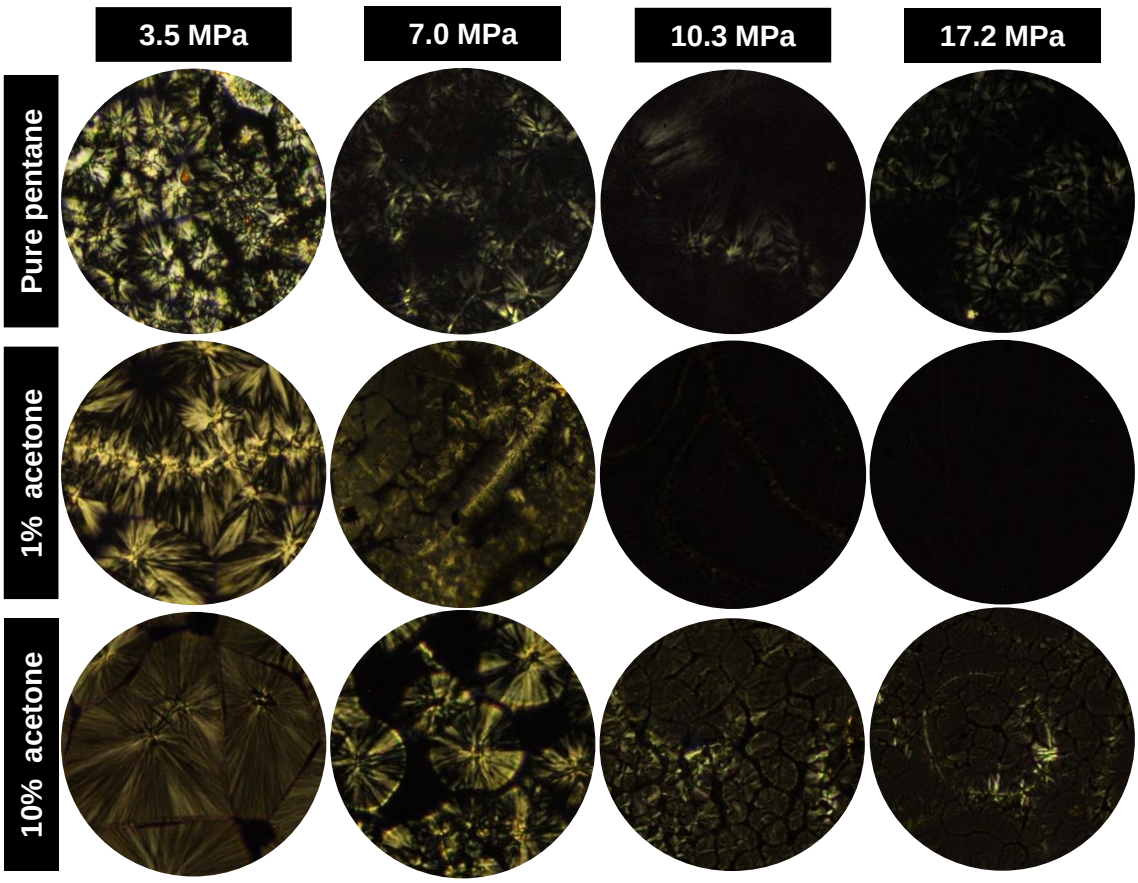

Figure 6.2. Polarized optical microscopy images of *i*PP films grown in supercritical n-pentane and n-pentane:acetone (x10) at different pressures.

The description emerging from the POM analysis is that crystallinity decreases as pressure increases and increases as acetone concentration increases. To further study the effect of pressure and solvent additive on the morphology of deposited films, we performed 2D grazing-incidence wide-angle x-ray scattering experiments. Figure 6.3 displays the observed scattering pattern from films grown at several different pressures from n-pentane:acetone solutions. The GIWAXS patterns are consistent with the α-form of *i*PP for all samples. Specifically, the diagnostic peaks of the α-form, $(110)_{\alpha}$, $(130)_{\alpha}$, $(040)_{\alpha}$, $(111)_{\alpha}$, $(131)_{\alpha}$, and $(041)_{\alpha}$ are observed.[347,348] Moreover, the intensity of the diagnostic peaks decreases for all *i*PP films as the pressure is increased.

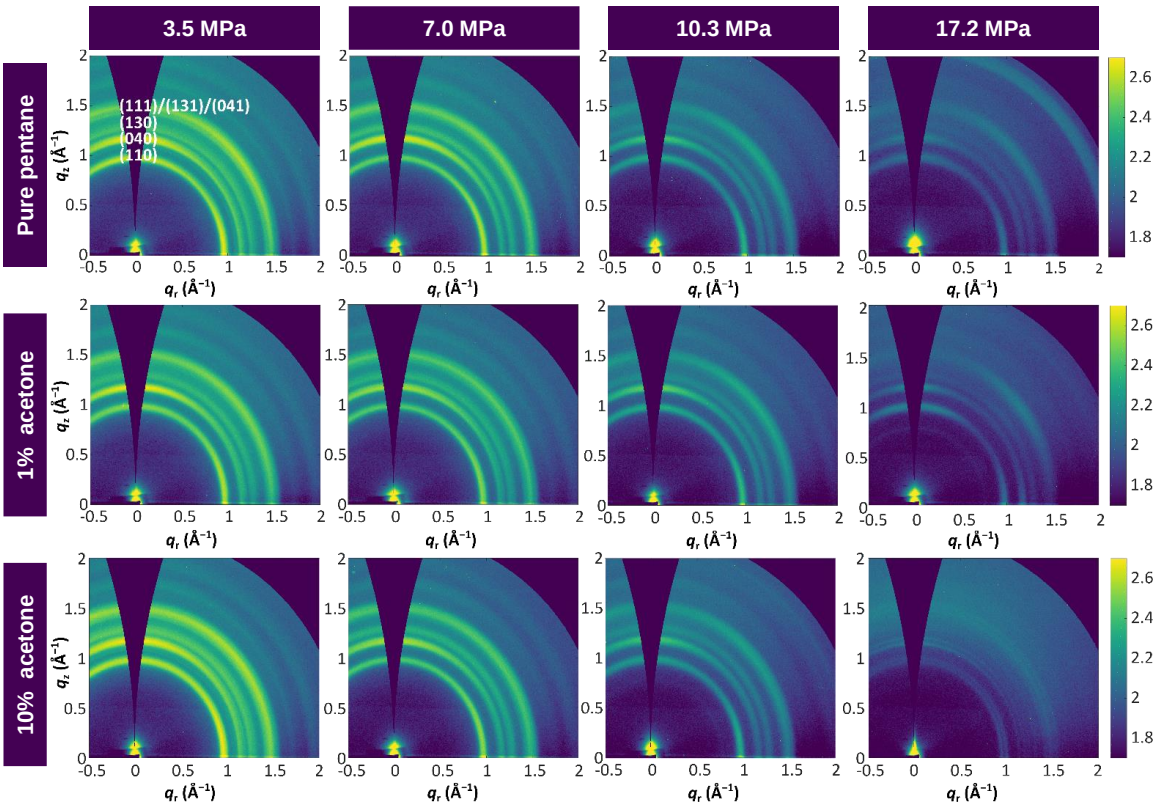

Figure 6.3. GIWAXS patterns of *i*PP films grown in pressurized n-pentane:acetone solutions at different pressures. Intensity is plotted on a log scale.

Figure 6.4 displays azimuthally integrated linecuts of the GIWAXS data for films grown in pure n-pentane and n-pentane:acetone at several different pressures. The azimuthal integrations show a scattering pattern similar to that of the α-*i*PP previously reported.[313,347,349] In addition, there is a decrease in the intensity of the peaks for *i*PP films with increasing pressure. This is consistent with our analysis of POM images suggesting that an increase in deposition pressure results in a reduced crystallinity in *i*PP films. Apart from the α-*i*PP features, there is also a $(300)_{\beta}$ peak indicating the formation of a small amount of ß-*i*PP at 3.5 MPa. However, this feature does not appear at pressures higher than 3.5 MPa. Additionally, ɣ-*i*PP is reported to be formed only at significantly elevated pressures with the maximum fraction of ɣ-*i*PP occurring at 200 MPa. .[350-353] However, we observed feature corresponding to ɣ-*i*PP in the film deposited at 17.2 MPa in the presence of 10% acetone, namely $(111)_{\gamma}$ and $(117)_{\gamma}$ reflections.

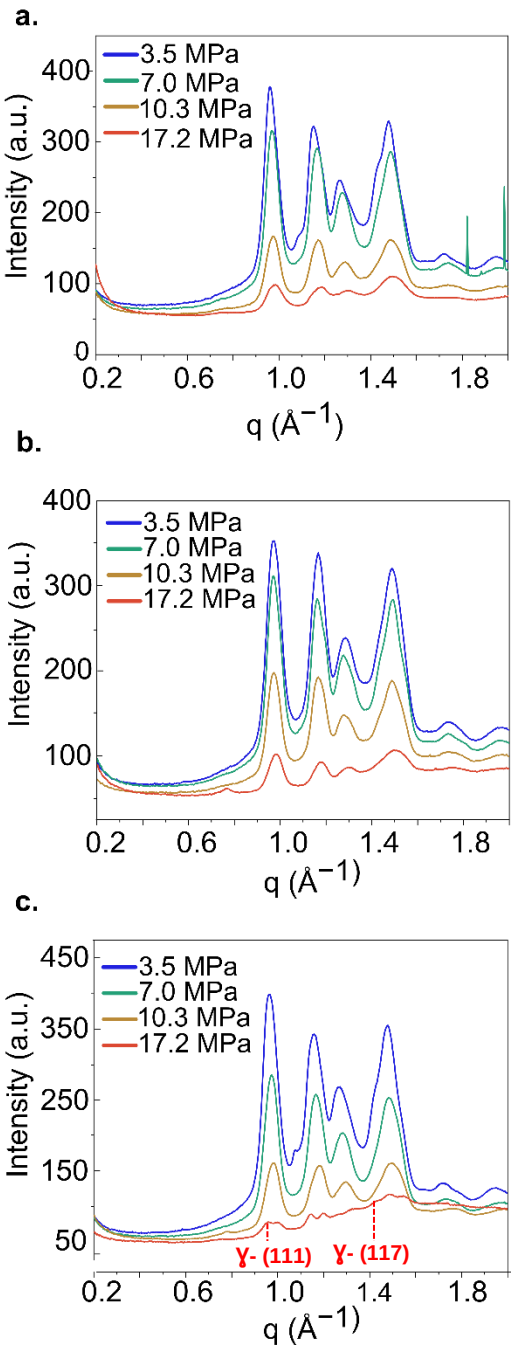

Figure 6.4. Azimuthally-integrated linecuts of the GIWAXS data for *i*PP films grown at different pressures. (a) pure n-pentane. (b) n-pentane + 1% acetone. (c) n-pentane + 10% acetone.

Furthermore, the number average molecular weight (M_n), weight average molecular weight (M_w), and polydispersity index (PDI) of as-received *i*PP sample was compared with *i*PP samples collected via gravimetric analysis from supercritical n-pentane:acetone solutions. This investigation was carried out as there is a possibility of polymer fractionation in supercritical fluids with respect to molecular weight via

isothermally increasing pressure profile above the melting temperature of the polymer.[379] The molecular weight measurements were performed via size exclusion chromatography (SEC) and the results are provided in Table 6.1. Based on the results, there is no consistent trend that can correlate the crystallinity degree observed in *i*PP films to the polymer molecular weight. Hence, fluid properties must be primarily responsible for the observed reduced crystallinity in *i*PP films as a function of deposition pressure.

Table 6.1. The number average molecular weight (M_n), weight average molecular weight (M_w), and polydispersity index (PDI) of as-received *i*PP sample and *i*PP samples collected via gravimetric analysis from supercritical n-pentane:acetone solutions at 418 K (423 K in case of n-pentane:acetone) at different pressures via size exclusion chromatography.

Sample	M_n	M_W	PDI
***i*PP, as received**	120,094	4,729,300	39.380
***i*PP in n-pentane, 3.5 MPa**	129,828	6,407,432	49.353
***i*PP in n-pentane, 7.0 MPa**	136,908	7,607,899	55.570
***i*PP in n-pentane, 10.3 MPa**	131,275	7,001,019	53.331
***i*PP in n-pentane, 17.2 MPa**	134,660	6,092,031	45.240
***i*PP in n-pentane + 1% acetone, 10.3 MPa**	127,078	5,306,952	41.761
***i*PP in n-pentane + 10% acetone, 10.3 MPa**	140,478	4,952,082	35.252

To synthesize our findings, a schematic drawing of the deposition mechanism is provided in Figure 6.5. In this figure, the change in solvent density is represented by false color gradient, with lower solvent density nearer the substrate. We propose that the drop in solvent density in this region is correlated with the precipitation of material from n-pentane, where the entropy of the system favors disruption of the solvent shell.

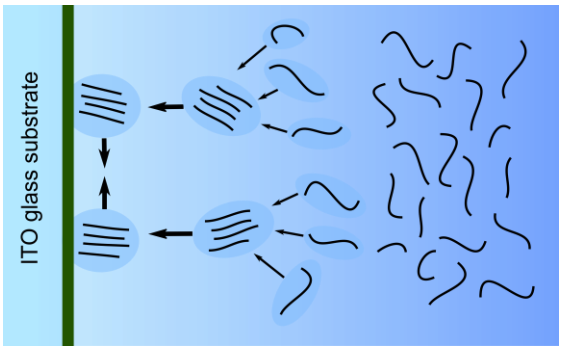

Figure 6.5. Cartoon representing the deposition mechanism in n-pentane:acetone. Black lines indicate polymer chains, blue ovals indicate acetone solvent shell, false color gradient represents local density of n-pentane.

Additionally, it is anticipated that the flow regime is turbulent, exhibiting high Rayleigh number. This was indeed confirmed by the observed light scattering near the substrate surface during the deposition process. Moreover, ring-like structures are observed in several POM images at high pressures (see Figure 6.6) which we interpret as indicative of Rayleigh-Bénard convection cells.

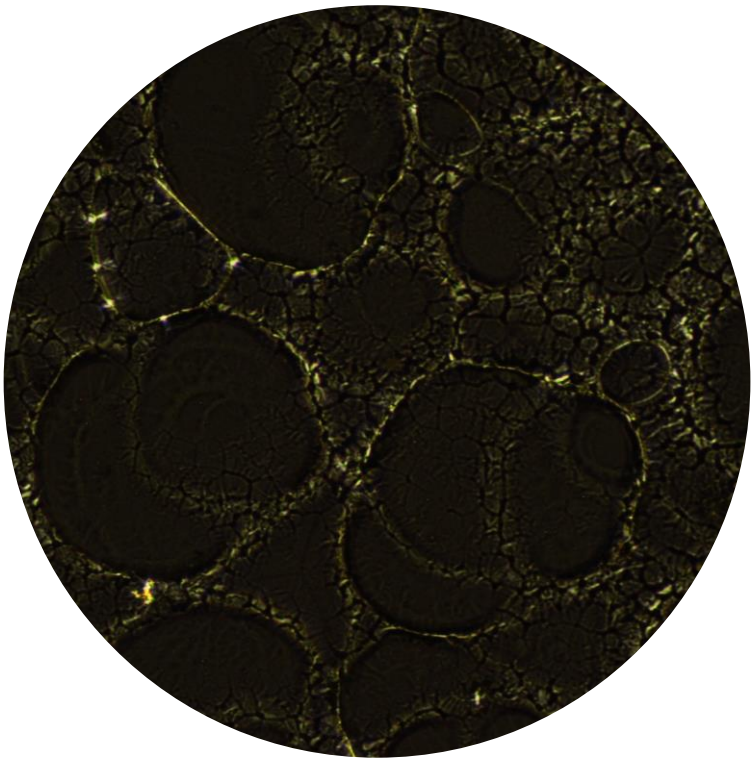

Figure 6.6. Polarized optical microscopy image (x10) of *i*PP film grown in supercritical n-pentane at 10.3 MPa in the presence of 10% acetone.

The presence of acetone has two complementary effects on the deposition. First, it acts as a viscosity modifier, decreasing the Rayleigh number of the system. This leads to a decrease in bulk solution turbulence and an increase in the thickness of the laminar boundary layer at the heated surface. Both effects lead to a more controlled polymer aggregation in the boundary layer. The second effect of acetone is that it remains with the polymer as it is deposited onto the surface, allowing for greater chain mobility, further increasing crystallinity.

6.3. Conclusion

We investigated the solubility of isotactic polypropylene in supercritical *n*-pentane as a function of temperature via gravimetric analysis. The isobaric solubility displayed a peak with temperature which can be described by an empirically motivated model. Furthermore, the influence of a solvent additive was studied by adding acetone to *n*-pentane. A peak shift and a peak narrowing were observed, both of which are predicted by lower overall solvent entropy. Based on the solubility behavior, deposition conditions were established and *i*PP thin films were grown by resistively heating a substrate in the saturated solution. The morphology of the thin films grown at different pressures were studied using polarized optical microscopy and grazing incidence wide angle x-ray scattering. The results confirmed the decrease in crystallinity with pressure due to an increased turbulence near the substrate surface. The addition of acetone enhanced larger scale self-assembly, evidenced by spherulite formation as seen in the POM images. Our findings are consistent with a two-step film formation model in which the initial step involves pre-aggregation in solution that establishes the local crystalline order. The second step involves chain mobility on the surface, that increases in the presence of acetone, with acetone presumably being slower to leave the film. In conclusion, the results presented here demonstrate the key principles of self-assembly in supercritical fluids which may be applicable to a wide range of materials and deposition conditions.

6.4. Methods

6.4.1. Solubility Measurement via Gravimetric Analysis

The solubility measurements were carried out for all the studied solvent systems via gravimetric analysis discussed in detail in section 5.4.1.

6.4.2. Substrate Preparation for Thin Film Deposition and Deposition Condition

ITO coated glass slides were used as the substrate for deposition of i*PP* (for specifications refer to section 4.4.2). The deposition of isotactic polypropylene in pressurized n-pentane was performed by first increasing the temperature of the solution to 418 K (423 K in case of *n*-pentane:acetone). When pressure and temperature had stabilized, the temperature of the ITO glass slide was increased to 433 K to initiate the deposition.

6.4.3. Characterization of Deposited Thin Film

The *i*PP deposited films were analyzed using POM and GIWAXS. Detailed information is available in section 5.4.3.

6.4.4. High-temperature Size Exclusion Chromatography

Number average molecular weight (M_n), weight average molecular weight (M_w), and polydispersity index (PDI) were evaluated by high-temperature size exclusion chromatography (SEC) using 1,2,4-trichlorobenzene and performed on a EcoSEC HLC-8321GPC/HT (Tosoh Bioscience) equipped with a single TSKgel GPC column (GMHHR-H; 300 mm × 7.8 mm) calibrated with monodisperse polystyrene standards. The samples were prepared using 1 mg/mL of sample in trichlorobenzene (TCB), which were allowed to stir at 80 °C for 12 h prior to injection. The analysis of the samples was performed at 180 °C with a flow rate of 1.0 mL/min with injection quantities of 300 µL. The data was collected and integrated using EcoSEC 8321GPC HT software suite.

Chapter 7. Conclusions and Future Directions

7.1. Conclusions

This thesis has outlined a novel solution-based deposition technique for growing polymer thin films based on the distinctive properties of supercritical fluids. The primary goal of the project is to establish a solution-phase analog of physical vapour deposition method that does not require any in-situ chemical reactions, and more importantly offers superior pattern resolution than printing techniques like aerosol jet. To achieve this goal, the initial step involved investigating the solubility behaviour of a selected semiconducting polymer, PBTTT-C_{14}, in pentane at different temperatures and pressures. The deposition in supercritical fluid was established based on a somewhat common property of a solute-solvent system, a maximum in their solubility as a function of temperature. This phenomenon allows films to be formed onto a heated substrate. Taking advantage of this unique property of supercritical fluids, ITO glass substrates were resistively heated and thin films of PBTTT-C_{14} were grown in supercritical pentane. Subsequently, ITO glass substrates were patterned by using photolithography and directed the formation of polymer lines 5 μm in width, exceeding the line width of printing techniques like aerosol jet by a least a factor of 4. Afterwards, we demonstrated the deposition of PBTTT-C_{14} on finely patterned features onto a cross-linked PMMA layer and a PDMS hemispherical shell. The patterned films had nearly identical line width, suggesting that much higher resolution patterns can be created. The ability to deposit materials on flexible polymer films and curved surfaces is particularly important as it highlights the potential use of this deposition technique in the industrial manufacturing of flexible electronics. However, what makes the physical supercritical fluid deposition noteworthy is that it provides an unprecedented opportunity to couple photolithography with solution phase self-assembly. This removes the barrier of the chemical complexity of materials that can be used in a photolithographic process and the potential scalability of the technique for industrial applications.

Despite a long history of using supercritical fluids as a processing media for materials, the mechanism for self-assembly in supercritical fluids is still not fully understood. Therefore, the natural next step was to study polymer self-assembly in supercritical fluids. To achieve this goal, the self-assembly of isotactic polypropylene films

from supercritical n-pentane was investigated. The deposited thin film morphology was studied using POM and GIWAXS, and the findings were summarized with a proposed two-step model describing the film formation in supercritical fluids. The initial step of self-assembly occurs in solution, enabling pre-aggregation in solution phase and the formation of local crystallites. The second step involves the longer length scale organization on the substrate surface. Given that pre-aggregation takes place in solution, the fluid mechanics is an important consideration for controlling the polymer assembly. Indeed, our findings provided evidence supporting that an increase in solution turbulence disrupts the solution-phase self-assembly and results in reduced crystallinity of deposited films. Apart from this, the second step to film formation is strongly dependent on the chain mobility on the surface, accommodating polymer chain reorganization to form larger scale structures. To further explore what impacts the chain mobility on the surface, acetone was added as an additive to n-pentane and isotactic polypropylene films were deposited. The presence of acetone significantly changed the morphology of the deposited film. It was inferred based on our findings that acetone primary acts as a viscosity modifier and decreases the bulk fluid turbulence leading to a more controlled pre-aggregation in solution. Moreover, acetone remains with the polymer as it deposits on the surface and facilitate higher polymer chain mobility, which in turn allows for higher length order and increased crystallinity. These findings highlight the significant impact solvent engineering can play in controlling the self-assembly of polymers in supercritical fluids and achieving more controlled self-assembly.

Additionally, we were able to develop a simple thermodynamic model to predict both the temperature and pressure dependence of the polymer solubility in supercritical fluids based on the interplay of intermolecular interactions and solvent entropy. To validate the model, the equilibrium concentrations of isotactic polypropylene polymer predicted by the model were compared with the experimental data collected at elevated pressures and temperatures. The model results qualitatively match the experimental results, both manifesting very little dissolved materials at the lowest temperature and the existence of a maximum in the isobaric solubility versus temperature. Furthermore, the isothermal solubility of iPP was investigated experimentally and compared with the proposed thermodynamic model. The isothermal solubility exhibits a decrease with pressure for the lowest pressures and is largely pressure independent thereafter. These results were in

good agreement with the proposed thermodynamic model predictions and with previous reports on the solubility of iPP in n-pentane.

7.2. Future Directions

The development of a unique deposition technique that allows thin films of polymer to be grown in supercritical fluids is very promising, primarily because there is no need for in-situ chemical reactions, and it can be easily adapted for deposition of a variety of materials. But more importantly, the morphology of the deposited films using supercritical fluids can be altered by means of both pressure and solvent additive. Nonetheless, the technique is still in its infancy and its further growth will be highly dependent on the efforts to investigate the transport properties of organic semiconductor films grown from supercritical fluids and subsequently compare the results to films deposited using other available techniques. As discussed in Chapter 2, the charge transport in organic semiconductors depends largely on the structural order at different levels and as a result the processing techniques is of paramount importance. Based on our preliminary results, the morphology of the PBTTT-C_{14} films deposited via physical supercritical fluid deposition technique is significantly different than those deposited through other techniques. The AFM images of the PBTTT films grown via spin-coating, slow-drying, drop-casting and physical supercritical fluid deposition are presented in Figure 7.1 for comparison.

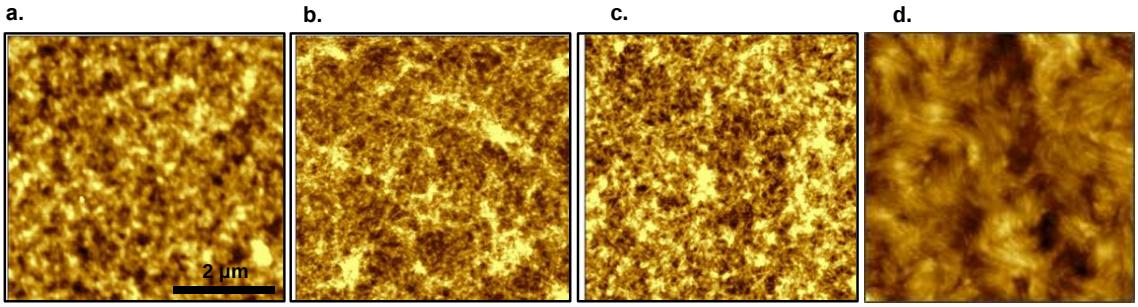

Figure 7.1. AFM height images of pure PBTTT films deposited using spin-coating (a), slow-drying (b), drop-casting (c), and physical supercritical fluid deposition at 3.5 MPa (d). None of the PBTTT films presented here were thermally annealed. The scale bar is the same for all the images. Images a, b, and c were reprinted with permission from reference 380.

There is a clear morphological difference among the four deposited films, which points out that the polymer self-assembly can be varied significantly by changing the processing technique. For instance, the spin-coated film looks unstructured compared to

slow-dried and drop-casted films where fibril-like aggregates are more distinctively visible due to an increased film solidification time. On the other hand, the PBTTT film grown in supercritical fluids reveals fibrillar aggregates that reach lengths in the order of micrometers. This observation is in accordance with the deposition mechanism offered previously in this thesis. The two-step polymer self-assembly in supercritical fluids, accommodate the timeframe and the freedom necessary for the polymer chains to assemble in a more ordered aggregates, hence enhancing the structural order to a higher degree in the deposited films. Indeed, such morphology modification will impact the transport properties, which demonstrates how crucial it is that future works involve the study of transport properties of films grown from supercritical fluids.

In this thesis I reported how solvent additive can control the crystallinity of isotactic polypropylene thin films and based on the observations a deposition mechanism was proposed. I propose a separate set of experiments to assess the influence of solvent additive on organic semiconductor films nanostructure and investigate the structure-property relationship governing charge transport. Preliminary experiments demonstrate the role that solvent additive plays in altering the morphologies of deposited thin films in *i*PP, suggesting that similar strategies can be employed with PBTTT-C_{14}. Figure 7.2 presents the AFM images of PBTTT-C_{14} thin films deposited in supercritical n-pentane (Figure 7.2.a) and n-pentane + 0.5% mol toluene (Figure 7.2.b) at 3.5 MPa. The findings highlighted that in the presence of toluene, the fibrillar aggregates observed in pure n-pentane start to disappear and the morphology shifts towards the formation of longer fibers reaching lengths of 4-5 micrometers. Concurrently, it appears that the reduced number of aggregates in the presence of toluene can result in reduced interconnectivity between them. How this modification in morphology translates to the electronic properties of polymer semiconductor films is the question that needs further investigation in the future.

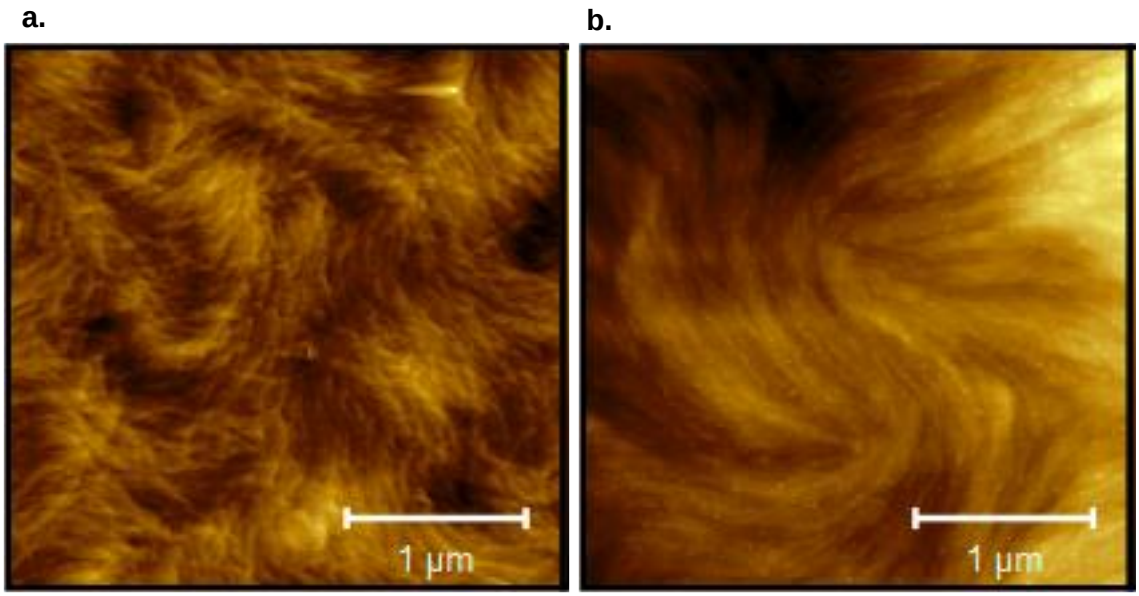

Figure 7.2. AFM height images of PBTTT-C_{14} films deposited in (a) supercritical n-pentane and (b) n-pentane + 0.5% mol toluene at 3.5 MPa.

As discussed in Chapter 5, the degree of crystallinity in deposited thin films was pressure dependent, which is due to the change of fluid turbulence near the substrate surface as a function of pressure. Given the impact of fluid mechanics on the final morphology of thin films, one of the approaches to regulate the fluid turbulence can be achieved by incorporating some changes in the current substrate holder design to modify the boundary layer thickness. This approach is based on the $Ra \propto l^3$ relationship between Rayleigh number (Ra) and characteristic length of the fluid domain (l). In order to decrease the turbulence where self-assembly of polymer crystallites take place, the thickness of the boundary layer must be decreased. One possible approach to achieve this would be to add a layer of fine mesh in close distance from the ITO substrate, thus creating an array of cells in the boundary layer where fluid can flow through mesh openings. This proposed strategy can lead to the reduction of characteristic length to that of the mesh opening sizes and as a result reducing the Ra number.

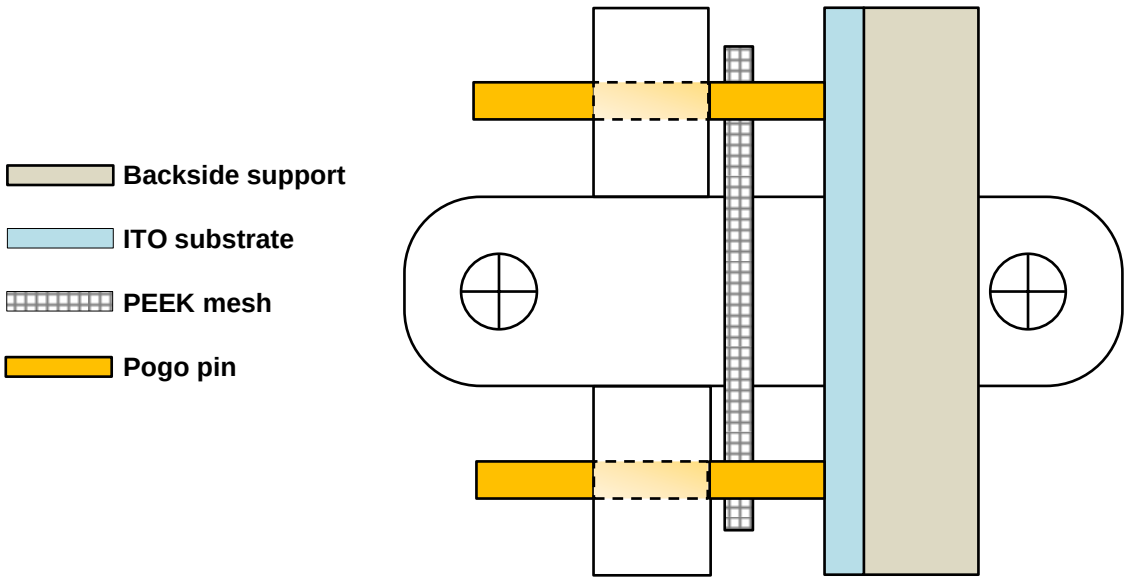

Figure 7.3. Schematic of a proposed sample holder design with an incorporation of a PEEK mesh in front of the ITO substrate to reduce the fluid turbulence near the substrate.

Another possible direction of future work could involve the expansion of the physical supercritical fluid deposition technique to other classes of materials, extending its application beyond semiconducting and aliphatic polymers. For instance, the physical supercritical fluid deposition of organic small molecules, nanoparticles, metals, and metal oxides. This avenue is particularly critical in justifying the physical supercritical fluid deposition technique as a compelling processing technology that provides advantages over the existing techniques based on its application diversity and economic, and technical considerations.

References

1. Silinš, E., *Organic molecular crystals : their electronic states / E. A. Silinsh*. Berlin ; New York : Springer-Verlag: 1980.
2. Pope, M., *Electronic processes in organic crystals and polymers / Martin Pope and Charles E. Swenberg*. 2nd ed.; New York : Oxford University Press: 1999.
3. Guo, X.; Facchetti, A., The journey of conducting polymers from discovery to application. *Nat. Mater.* **2020,** *19* (9), 922-928.
4. Caironi, M.; Muller, C.; von Hauff, E.; Sommer, M., New Materials for Organic Electronics: Improved Properties to Tackle Application Challenges. *Adv. Electron. Mater.* **2018,** *4* (10), 1800621.
5. Skotheim, T. A.; Reynolds, J. R., *Handbook of Conducting Polymers*. Baton Rouge: CRC Press LLC: Baton Rouge, 2007.
6. Borsenberger, P. M., *Organic photoreceptors for imaging systems / Paul M. Borsenberger, David S. Weiss*. New York : M. Dekker: New York, 1993.
7. Fratini, S.; Nikolka, M.; Salleo, A.; Schweicher, G.; Sirringhaus, H., Charge transport in high-mobility conjugated polymers and molecular semiconductors. *Nat. Mater.* **2020,** *19* (5), 491-502.
8. Tang, C. W., Two-layer organic photovoltaic cell. *Appl. Phys. Lett.* **1986,** *48* (2), 183-185.
9. Tsumura, A.; Koezuka, H.; Ando, T., Polythiophene Field-Effect Transistor - Its Characteristics and Operation Mechanism. *Synth. Met.* **1988,** *25* (1), 11-23.
10. Burroughes, J. H.; Jones, C. A.; Friend, R. H., New Semiconductor-Device Physics in Polymer Diodes and Transistors. *Nature* **1988,** *335* (6186), 137-141.

11. Horowitz, G.; Fichou, D.; Peng, X. Z.; Xu, Z. G.; Garnier, F., A Field-Effect Transistor Based on Conjugated Alpha-Sexithienyl. *Solid State Commun.* **1989,** *72* (4), 381-384.

12. Tang, C. W.; Vanslyke, S. A., Organic Electroluminescent Diodes. *Appl. Phys. Lett.* **1987,** *51* (12), 913-915.

13. Burroughes, J. H.; Bradley, D. D. C.; Brown, A. R.; Marks, R. N.; Mackay, K.; Friend, R. H.; Burn, P. L.; Holmes, A. B., Light-Emitting-Diodes Based on Conjugated Polymers. *Nature* **1990,** *347* (6293), 539-541.

14. Yun, H. J.; Kang, S. J.; Xu, Y.; Kim, S. O.; Kim, Y. H.; Noh, Y. Y.; Kwon, S. K., Dramatic Inversion of Charge Polarity in Diketopyrrolopyrrole-Based Organic Field-Effect Transistors via a Simple Nitrile Group Substitution. *Adv. Mater.* **2014,** *26* (43), 7300-7307.

15. Kim, G.; Kang, S. J.; Dutta, G. K.; Han, Y. K.; Shin, T. J.; Noh, Y. Y.; Yang, C., A Thienoisoindigo-Naphthalene Polymer with Ultrahigh Mobility of 14.4 $cm^2/V.s$ That Substantially Exceeds Benchmark Values for Amorphous Silicon Semiconductors. *J. Am. Chem. Soc.* **2014,** *136* (26), 9477-9483.

16. Kang, I.; Yun, H. J.; Chung, D. S.; Kwon, S. K.; Kim, Y. H., Record High Hole Mobility in Polymer Semiconductors via Side-Chain Engineering. *J. Am. Chem. Soc.* **2013,** *135* (40), 14896-14899.

17. Lee, J.; Han, A. R.; Yu, H.; Shin, T. J.; Yang, C.; Oh, J. H., Boosting the Ambipolar Performance of Solution-Processable Polymer Semiconductors via Hybrid Side-Chain Engineering. *J. Am. Chem. Soc.* **2013,** *135* (25), 9540-9547.

18. Li, J.; Zhao, Y.; Tan, H. S.; Guo, Y. L.; Di, C. A.; Yu, G.; Liu, Y. Q.; Lin, M.; Lim, S. H.; Zhou, Y. H.; Su, H. B.; Ong, B. S., A stable solution-processed polymer semiconductor with record high-mobility for printed transistors. *Sci. Rep.* **2012,** *2*, 9.

19. Luo, C.; Kyaw, A. K. K.; Perez, L. A.; Patel, S.; Wang, M.; Grimm, B.; Bazan, G. C.; Kramer, E. J.; Heeger, A. J., General Strategy for Self-Assembly of Highly Oriented Nanocrystalline Semiconducting Polymers with High Mobility. *Nano Lett.* **2014,** *14* (5), 2764-2771.

20. Himmelberger, S.; Salleo, A., Engineering Semiconducting Polymers for Efficient Charge Transport. *MRS Commun.* **2015,** *5* (3), 383-395.

21. Xiao, M. F.; Kang, B. S.; Lee, S. B.; Perdigao, L. M. A.; Luci, A.; Warr, D. A.; Senanayak, S. P.; Nikolka, M.; Statz, M.; Wu, Y. T.; Sadhanala, A.; Schott, S.; Carey, R.; Wang, Q. J.; Lee, M. J.; Kim, C.; Onwubiko, A.; Jellett, C.; Liao, H. L.; Yue, W.; Cho, K. W.; Costantini, G.; McCulloch, I.; Sirringhaus, H., Anisotropy of Charge Transport in a Uniaxially Aligned Fused Electron-Deficient Polymer Processed by Solution Shear Coating. *Adv. Mater.* **2020,** *32* (23), 8.

22. Boutry, C. M.; Kaizawa, Y.; Schroeder, B. C.; Chortos, A.; Legrand, A.; Wang, Z.; Chang, J.; Fox, P.; Bao, Z. N., A stretchable and biodegradable strain and pressure sensor for orthopaedic application. *Nat. Electron.* **2018,** *1* (5), 314-321.

23. Ramirez, J.; Rodriquez, D.; Urbina, A. D.; Cardenas, A. M.; Lipomi, D. J., Combining High Sensitivity and Dynamic Range: Wearable Thin-Film Composite Strain Sensors of Graphene, Ultrathin Palladium, and PEDOT:PSS. *ACS Appl. Nano Mater.* **2019,** *2* (4), 2222-2229.

24. Gerasimov, J. Y.; Gabrielsson, R.; Forchheimer, R.; Stavrinidou, E.; Simon, D. T.; Berggren, M.; Fabiano, S., An Evolvable Organic Electrochemical Transistor for Neuromorphic Applications. *Adv. Sci.* **2019,** *6* (7), 8.

25. Uguz, I.; Proctor, C. M.; Curto, V. F.; Pappa, A. M.; Donahue, M. J.; Ferro, M.; Owens, R. M.; Khodagholy, D.; Inal, S.; Malliaras, G. G., A Microfluidic Ion Pump for In Vivo Drug Delivery. *Adv. Mater.* **2017,** *29* (27), 6.

26. Ghezzi, D.; Antognazza, M. R.; Maccarone, R.; Bellani, S.; Lanzarini, E.; Martino, N.; Mete, M.; Pertile, G.; Bisti, S.; Lanzani, G.; Benfenati, F., A polymer optoelectronic interface restores light sensitivity in blind rat retinas. *Nature Photonics* **2013,** *7* (5), 400-406.

27. Ghezzi, D.; Antognazza, M. R.; Dal Maschio, M.; Lanzarini, E.; Benfenati, F.; Lanzani, G., A hybrid bioorganic interface for neuronal photoactivation. *Nat. Commun.* **2011,** *2*, 7.

28. Rand, D.; Jakesova, M.; Lubin, G.; Vebraite, I.; David-Pur, M.; Derek, V.; Cramer, T.; Sariciftci, N. S.; Hanein, Y.; Glowacki, E. D., Direct Electrical Neurostimulation with Organic Pigment Photocapacitors. *Adv. Mater.* **2018,** *30* (25), 11.

29. Macchia, E.; Manoli, K.; Holzer, B.; Di Franco, C.; Ghittorelli, M.; Torricelli, F.; Alberga, D.; Mangiatordi, G. F.; Palazzo, G.; Scamarcio, G.; Torsi, L., Single-molecule detection with a millimetre-sized transistor. *Nat. Commun.* **2018,** *9*, 10.

30. Dijk, G.; Rutz, A. L.; Malliaras, G. G., Stability of PEDOT:PSS-Coated Gold Electrodes in Cell Culture Conditions. *Adv. Mater. Technol.* **2020,** *5* (3), 6.

31. Wang, G. M.; Swensen, J.; Moses, D.; Heeger, A. J., Increased mobility from regioregular poly(3-hexylthiophene) field-effect transistors. *J. Appl. Phys.* **2003,** *93* (10), 6137-6141.

32. Cho, S.; Lee, K.; Yuen, J.; Wang, G. M.; Moses, D.; Heeger, A. J.; Surin, M.; Lazzaroni, R., Thermal annealing-induced enhancement of the field-effect mobility of regioregular poly(3-hexylthiophene) films. *J. Appl. Phys.* **2006,** *100* (11), 6.

33. Li, G.; Shrotriya, V.; Yao, Y.; Yang, Y., Investigation of annealing effects and film thickness dependence of polymer solar cells based on poly(3-hexylthiophene). *J. Appl. Phys.* **2005,** *98* (4), 5.

34. Keum, J. K.; Xiao, K.; Ivanov, I. N.; Hong, K. L.; Browning, J. F.; Smith, G. S.; Shao, M.; Littrell, K. C.; Rondinone, A. J.; Payzant, E. A.; Chen, J. H.; Hensley, D. K., Solvent Quality-Induced Nucleation and Growth of Parallelepiped Nanorods in Dilute Poly(3-Hexylthiophene) (P3HT) Solution and the Impact on the Crystalline Morphology of Solution-Cast Thin Film. *Crystengcomm* **2013,** *15* (6), 1114-1124.

35. Zhao, K.; Khan, H. U.; Li, R. P.; Su, Y. S.; Amassian, A., Entanglement of Conjugated Polymer Chains Influences Molecular Self-Assembly and Carrier Transport. *Adv. Funct. Mater.* **2013,** *23* (48), 6024-6035.

36. O'Connor, B.; Kline, R. J.; Conrad, B. R.; Richter, L. J.; Gundlach, D.; Toney, M. F.; DeLongchamp, D. M., Anisotropic Structure and Charge Transport in Highly Strain-Aligned Regioregular Poly(3-hexylthiophene). *Adv. Funct. Mater.* **2011,** *21* (19), 3697-3705.

37. Brinkmann, M.; Wittmann, J. C., Orientation of regioregular poly(3-hexylthiophene) by directional solidification: A simple method to reveal the semicrystalline structure of a conjugated polymer. *Adv. Mater.* **2006,** *18* (7), 860-863.

38. Sirringhaus, H.; Tessler, N.; Friend, R. H., Integrated optoelectronic devices based on conjugated polymers. *Science* **1998,** *280* (5370), 1741-1744.

39. Salleo, A.; Chabinyc, M. L.; Yang, M. S.; Street, R. A., Polymer thin-film transistors with chemically modified dielectric interfaces. *Appl. Phys. Lett.* **2002,** *81* (23), 4383-4385.

40. Salleo, A.; Chen, T. W.; Volkel, A. R.; Wu, Y.; Liu, P.; Ong, B. S.; Street, R. A., Intrinsic hole mobility and trapping in a regioregular poly(thiophene). *Phys. Rev. B* **2004,** *70* (11), 10.

41. Baude, P. F.; Ender, D. A.; Haase, M. A.; Kelley, T. W.; Muyres, D. V.; Theiss, S. D., Pentacene-based radio-frequency identification circuitry. *Appl. Phys. Lett.* **2003,** *82* (22), 3964-3966.

42. Viola, F. A.; Brigante, B.; Colpani, P.; Dell'Erba, G.; Mattoli, V.; Natali, D.; Caironi, M., A 13.56 MHz Rectifier Based on Fully Inkjet Printed Organic Diodes. *Adv. Mater. Commun.* **2020,** *32* (33), 2002329.

43. Soeren, S.; Kris, M.; Vladimir, A.; Carsten, D.; Stijn De, V.; Jan, G.; Paul, H., 50 MHz rectifier based on an organic diode. *Nat. Mater.* **2005,** *4* (8), 597.

44. Gelinck, G. H.; Huitema, H. E. A.; Van Veenendaal, E.; Cantatore, E.; Schrijnemakers, L.; Van der Putten, J.; Geuns, T. C. T.; Beenhakkers, M.; Giesbers, J. B.; Huisman, B. H.; Meijer, E. J.; Benito, E. M.; Touwslager, F. J.; Marsman, A. W.; Van Rens, B. J. E.; De Leeuw, D. M., Flexible active-matrix displays and shift registers based on solution-processed organic transistors. *Nat. Mater.* **2004,** *3* (2), 106-110.

45. Zhou, L. S.; Wanga, A.; Wu, S. C.; Sun, J.; Park, S.; Jackson, T. N., All-organic active matrix flexible display. *Appl. Phys. Lett.* **2006,** *88* (8), 3.

46. Kymissis, I., The physics of organic semiconductors. Boston, MA: Springer US: Boston, MA, 2008; pp 1-12.

47. Alcácer, L., *Electronic structure of organic semiconductors : polymers and small molecules / Luís Alcácer*. San Rafael California 40 Oak Drive, San Rafael, CA, 94903, USA : Morgan & Claypool Publishers: 2018.

48. Rockett, A.; Rockett, A., *Materials Science of Semiconductors*. Boston: Springer: Boston, 2008.

49. Mei, J. G.; Bao, Z. N., Side Chain Engineering in Solution-Processable Conjugated Polymers. *Chem. Mater.* **2014,** *26* (1), 604-615.

50. Szarko, J. M.; Guo, J. C.; Liang, Y. Y.; Lee, B.; Rolczynski, B. S.; Strzalka, J.; Xu, T.; Loser, S.; Marks, T. J.; Yu, L. P.; Chen, L. X., When Function Follows Form: Effects of Donor Copolymer Side Chains on Film Morphology and BHJ Solar Cell Performance. *Adv. Mater.* **2010,** *22* (48), 5468-5472.

51. Lan, S. C.; Chang, C. K.; Lu, Y. H.; Lin, S. W.; Jen, A. K. Y.; Wei, K. H., Side chain structure affects the molecular packing and photovoltaic performance of oligothiophene-based solution-processable small molecules. *Rsc Advances* **2015,** *5* (83), 67718-67726.

52. Ko, S. W.; Hoke, E. T.; Pandey, L.; Hong, S. H.; Mondal, R.; Risko, C.; Yi, Y. P.; Noriega, R.; McGehee, M. D.; Bredas, J. L.; Salleo, A.; Bao, Z. A., Controlled Conjugated Backbone Twisting for an Increased Open-Circuit Voltage while Having a High Short-Circuit Current in Poly(hexylthiophene) Derivatives. *J. Am. Chem. Soc.* **2012,** *134* (11), 5222-5232.

53. Heeger, A. J., *Semiconducting and metallic polymers / by Alan J. Heeger, N. Serdar Sariciftci, Ebinazar B. Namdas*. Oxford : Oxford University Press: 2010.

54. Heeger, A. J., Semiconducting and metallic polymers: The fourth generation of polymeric materials (Nobel lecture). *Angewandte Chemie-International Edition* **2001,** *40* (14), 2591-2611.

55. Shirakawa, H.; Louis, E. J.; Macdiarmid, A. G.; Chiang, C. K.; Heeger, A. J., Synthesis of Electrically Conducting Organic Polymers - Halogen Derivatives of Polyacetylene, $(CH)_X$. *J. Chem. Soc. Chem. Comm.* **1977,** (16), 578-580.

56. Chiang, C. K.; Fincher, C. R.; Park, Y. W.; Heeger, A. J.; Shirakawa, H.; Louis, E. J.; Gau, S. C.; MacDiarmid, A. G., Electrical Conductivity in Doped Polyacetylene. *Physical Review Letters* **1977,** *39* (17), 1098-1101.

57. Chiang, C. K.; Gau, S. C.; Fincher, C. R.; Park, Y. W.; Macdiarmid, A. G.; Heeger, A. J., Polyacetylene, $(CH)_X$ - N-Type and P-type Doping and Compensation. *Appl. Phys. Lett.* **1978,** *33* (1), 18-20.

58. Tomozawa, H.; Braun, D.; Phillips, S.; Heeger, A. J.; Kroemer, H., Metal-Polymer Schottky Barriers on Cast Films of Soluble Poly(3-Alkylthiophenes). *Synth. Met.* **1987,** *22* (1), 63-69.

59. Garnier, F.; Hajlaoui, R.; Yassar, A.; Srivastava, P., All-Polymer Field-Effect Transistor Realized by Printing Techniques. *Science* **1994,** *265* (5179), 1684-1686.

60. Drury, C. J.; Mutsaers, C. M. J.; Hart, C. M.; Matters, M.; de Leeuw, D. M., Low-cost all-polymer integrated circuits. *Applied Physics Letters* **1998,** *73* (1), 108-110.

61. Parker, I. D., Carrier Tunneling and Device Characteristics in Polymer Light-Emitting-Diodes. *J. Appl. Phys.* **1994,** *75* (3), 1656-1666.

62. Gersten, J. I., *The physics and chemistry of materials / Joel I. Gersten, Frederick W. Smith*. New York : Wiley: 2001.

63. Kittel, C., *Introduction to solid state physics / Charles Kittel*. 8th ed. ed.; Hoboken, NJ : Wiley: 2005.

64. Sze, S. M., *Physics of semiconductor devices / S.M. Sze and Kwok K. Ng*. 3rd ed. ed.; Hoboken, NJ : Wiley-Interscience: 2007.

65. Simon, S. H., *The Oxford Solid State Basics*. Oxford: Oxford University Press, Incorporated: Oxford, 2013.

66. Ashcroft, N. W., *Solid state physics / by Neil W. Ashcroft and N. David Mermin*. New York : Holt, Rinehart and Winston: 1976.

67. Walsh, D.; Solymar, L., Semiconductors. 8th Edition ed.; Oxford University Press: 2010; pp 1-1.

68. Silinš, E., *Organic molecular crystals : their electronic states*. Berlin ; New York : Springer-Verlag: 1980.

69. Reese, C.; Chung, W. J.; Ling, M. M.; Roberts, M.; Bao, Z. N., High-performance microscale single-crystal transistors by lithography on an elastomer dielectric. *J. Appl. Phys.* **2006,** *89* (20), 3.

70. Takeya, J.; Yamagishi, M.; Tominari, Y.; Hirahara, R.; Nakazawa, Y.; Nishikawa, T.; Kawase, T.; Shimoda, T.; Ogawa, S., Very high-mobility organic single-crystal

transistors with in-crystal conduction channels. *J. Appl. Phys.* **2007,** *90* (10), 102120-102120-3.

71. Vollmer, A.; Ovsyannikov, R.; Gorgoi, M.; Krause, S.; Oehzelt, M.; Lindblad, A.; Mårtensson, N.; Svensson, S.; Karlsson, P.; Lundvuist, M.; Schmeiler, T.; Pflaum, J.; Koch, N., Two dimensional band structure mapping of organic single crystals using the new generation electron energy analyzer ARTOF. *J. Electron. Spectros. Relat. Phenomena.* **2012,** *185* (3-4), 55-60.

72. Takeya, J.; Tsukagoshi, K.; Aoyagi, Y.; Takenobu, T.; Iwasa, Y., Hall Effect of Quasi-Hole Gas in Organic Single-Crystal Transistors. *Jpn. J. Appl. Phys.* **2005,** *44* (No. 46), L1393-L1396.

73. Nakayama, Y.; Uragami, Y.; Machida, S. i.; Koswattage, K. R.; Yoshimura, D.; Setoyama, H.; Okajima, T.; Mase, K.; Ishii, H., Full Picture of Valence Band Structure of Rubrene Single Crystals Probed by Angle-Resolved and Excitation-Energy-Dependent Photoelectron Spectroscopy. *Appl. Phys. Express.* **2012,** *5* (11), 111601-111601-3.

74. Obata, S.; Miura, T.; Shimoi, Y., Theoretical prediction of crystal structures of rubrene. *Jpn. J. Appl. Phys.* **2014,** *53* (1S), 1.

75. Sutton, C.; Sears, J. S.; Coropceanu, V.; Brédas, J. L., Understanding the Density Functional Dependence of DFT-Calculated Electronic Couplings in Organic Semiconductors. *J. Phys. Chem. Lett.* **2013,** *4* (6), 919-924.

76. Wang, C.; Dong, H.; Jiang, L.; Hu, W., Organic semiconductor crystals. *Chem. Soc. Rev.* **2018,** *47* (2), 422-5.

77. Podzorov, V.; Menard, E.; Rogers, J. A.; Gershenson, M. E., Hall effect in the accumulation layers on the surface of organic semiconductors. *Phys. Rev. Lett.* **2005,** *95* (22), 4.

78. Liu, C. A.; Minari, T.; Lu, X. B.; Kumatani, A.; Takimiya, K.; Tsukagoshi, K., Solution-Processable Organic Single Crystals with Bandlike Transport in Field-Effect Transistors. *Adv. Mater.* **2011,** *23* (4), 523-526.

79. Sakanoue, T.; Sirringhaus, H., Band-like temperature dependence of mobility in a solution-processed organic semiconductor. *Nat. Mater.* **2010,** *9* (9), 736-740.

80. Anderson, P. W., Absence of Diffusion in Certain Random Lattices. *Phys. Rev.* **1958,** *109* (5), 1492-1505.

81. Minder, N. A.; Ono, S.; Chen, Z. H.; Facchetti, A.; Morpurgo, A. F., Band-Like Electron Transport in Organic Transistors and Implication of the Molecular Structure for Performance Optimization. *Adv. Mater.* **2012,** *24* (4), 503-508.

82. Gershenson, M. E.; Podzorov, V.; Morpurgo, A. F., Colloquium: Electronic transport in single-crystal organic transistors. *Rev. Mod. Phys.* **2006,** *78* (3), 973-989.

83. Cheng, Y. C.; Silbey, R. J., A unified theory for charge-carrier transport in organic crystals. *J. Chem. Phys.* **2008,** *128* (11).

84. Bredas, J. L.; Calbert, J. P.; da Silva, D. A.; Cornil, J., Organic semiconductors: A theoretical characterization of the basic parameters governing charge transport. *Proceedings of the National Academy of Sciences of the United States of America* **2002,** *99* (9), 5804-5809.

85. Deng, W. Q.; Goddard, W. A., Predictions of hole mobilities in oligoacene organic semiconductors from quantum mechanical calculations. *J. Phys. Chem. B.* **2004,** *108* (25), 8614-8621.

86. Jurchescu, O. D.; Popinciuc, M.; van Wees, B. J.; Palstra, T. T. M., Interface-controlled, high-mobility organic transistors. *Adv. Mater.* **2007,** *19* (5), 688-692.

87. Landau, L. D., Über die Bewegung der Elektronen in Kristallgitter. *Phys. Z. Sowjetunion.* **1933,** *3*, 644–645.

88. Hultell, M.; Stafström, S., Polaron dynamics in highly ordered molecular crystals. *Chem. Phys. Lett.* **2006,** *428* (4), 446-450.

89. Feynman, R. P., Slow Electrons in a Polar Crystal. *Phys. Rev.* **1955,** *97* (3), 660-665.

90. Holstein, T., Studies of polaron motion: Part I. The molecular-crystal model. *Ann. Phys.* **1959,** *8* (3), 325-342.

91. Schein, L. B.; Glatz, D.; Scott, J. C., Observation of the transition from adiabatic to nonadiabatic small polaron hopping in a molecularly doped polymer. *Phys. Rev. Lett.* **1990,** *65* (4), 472-475.

92. Parris, R. E.; Kenkre, V. M.; Dunlap, D. H., Nature of charge carriers in disordered molecular solids: Are polarons compatible with observations? *Phys. Rev. Lett.* **2001,** *87* (12), 4.

93. Asadi, K.; Kronemeijer, A. J.; Cramer, T.; Koster, L. J. A.; Blom, P. W. M.; de Leeuw, D. M., Polaron hopping mediated by nuclear tunnelling in semiconducting polymers at high carrier density. *Nat. Commun.* **2013,** *4*, 8.

94. Troisi, A., Charge transport in high mobility molecular semiconductors: classical models and new theories. *Chem. Soc. Rev.* **2011,** *40* (5), 2347-2358.

95. Aleshin, A. N.; Lee, J. Y.; Chu, S. W.; Lee, S. W.; Kim, B.; Ahn, S. J.; Park, Y. W., Hopping conduction in polydiacetylene single crystals. *Phys. Rev. B. Condens. Matter Mater. Phys.* **2004,** *69* (21).

96. Dhoot, A. S.; Wang, G. M.; Moses, D.; Heeger, A. J., Voltage-induced metal-insulator transition in polythiophene field-effect transistors. *Phys. Rev. Lett.* **2006,** *96* (24), 246403-246403.

97. Bozdag, K. D.; Chiou, N. R.; Prigodin, V. N.; Epstein, A. J., Magnetic field, temperature and electric field dependence of magneto-transport for polyaniline nanofiber networks. *Syn. Met.* **2010,** *160* (3), 271-274.

98. Mott, N. F.; Davis, E. A., *Electronic Processes in Non-Crystalline Materials*. Oxford: Oxford University Press, Incorporated: Oxford, 2012.

99. Efros, A. L.; Shklovskii, B. I., Coulomb gap and low temperature conductivity of disordered systems. *J. Phys. C.* **1975,** *8* (4), L49-L51.

100. Prigodin, V. N.; Epstein, A. J., Comment on "voltage-induced metal-insulator transition in polythiophene field-effect transistors". *Phys. Rev. Lett.* **2007,** *98* (25), 259703-259703.

101. Ling, L.; Nianduan, L.; Ming, L., Physical origin of nonlinear transport in organic semiconductor at high carrier densities. *J. Appl. Phys.* **2014,** *116* (16), 164504.

102. Kim, K. H.; Lara-Avila, S.; Kang, H.; He, H.; Eklöf, J.; Hong, S. J.; Park, M.; Moth-Poulsen, K.; Matsushita, S.; Akagi, K.; Kubatkin, S.; Park, Y. W., Apparent Power Law Scaling of Variable Range Hopping Conduction in Carbonized Polymer Nanofibers. *Sci. Rep.* **2016,** *6* (1), 37783-37783.

103. Shklovskii, B. I., Hopping Conduction in Semiconductors Subjected to a Strong Electric-field. *Soviet Physics Semiconductors-Ussr* **1973,** *6* (12), 1964-1967.

104. Horowitz, G.; Lang, P.; Mottaghi, M.; Aubin, H., Extracting parameters from the current-voltage characteristics of field-effect transistors. *Adv. Func. Mater.* **2004,** *14* (11), 1069-1074.

105. Horowitz, G.; Delannoy, P., An Analytical Model for Organic-Based Thin-Film Transistors. *J. Appl. Phys.* **1991,** *70* (1), 469-475.

106. Horowitz, G.; Hajlaoui, M. E., Mobility in polycrystalline oligothiophene field-effect transistors dependent on grain size. *Adv. Mater.* **2000,** *12* (14), 1046-1050.

107. Chesterfield, R. J.; McKeen, J. C.; Newman, C. R.; Ewbank, P. C.; da Silva, D. A.; Bredas, J. L.; Miller, L. L.; Mann, K. R.; Frisbie, C. D., Organic thin film transistors based on N-alkyl perylene diimides: Charge transport kinetics as a

function of gate voltage and temperature. *J. Phys. Chem. B.* **2004,** *108* (50), 19281-19292.

108. Horowitz, G.; Hajlaoui, R.; Delannoy, P., Temperature-Dependence of the Field-Effect Mobility of Sexithiophene - Determination of the Density of Traps. *Journal De Physique Iii* **1995,** *5* (4), 355-371.

109. Liu, C.; Huang, K. R.; Park, W. T.; Li, M. M.; Yang, T. Z.; Liu, X. Y.; Liang, L. J.; Minari, T.; Noh, Y. Y., A unified understanding of charge transport in organic semiconductors: the importance of attenuated delocalization for the carriers. *Mater. Horiz.* **2017,** *4* (4), 608-618.

110. Tsao, H. N.; Mullen, K., Improving polymer transistor performance via morphology control. *Chem. Soc. Rev.* **2010,** *39* (7), 2372-2386.

111. McMahon, D. P.; Troisi, A., Organic Semiconductors: Impact of Disorder at Different Timescales. *Chemphyschem* **2010,** *11* (10), 2067-2074.

112. Bredas, J. L.; Beljonne, D.; Coropceanu, V.; Cornil, J., Charge-transfer and energy-transfer processes in pi-conjugated oligomers and polymers: A molecular picture. *Chem. Rev.* **2004,** *104* (11), 4971-5003.

113. Sirringhaus, H.; Brown, P. J.; Friend, R. H.; Nielsen, M. M.; Bechgaard, K.; Langeveld-Voss, B. M. W.; Spiering, A. J. H.; Janssen, R. A. J.; Meijer, E. W.; Herwig, P.; de Leeuw, D. M., Two-dimensional charge transport in self-organized, high-mobility conjugated polymers. *Nature* **1999,** *401* (6754), 685-688.

114. Segatta, F.; Lattanzi, G.; Faccioli, P., Predicting Charge Mobility of Organic Semiconductors with Complex Morphology. *Macromolecules* **2018,** *51* (21), 9060-9068.

115. Zhang, X. R.; Bronstein, H.; Kronemeijer, A. J.; Smith, J.; Kim, Y.; Kline, R. J.; Richter, L. J.; Anthopoulos, T. D.; Sirringhaus, H.; Song, K.; Heeney, M.; Zhang, W. M.; McCulloch, I.; DeLongchamp, D. M., Molecular origin of high field-effect

mobility in an indacenodithiophene-benzothiadiazole copolymer. *Nat. Commun.* **2013,** *4*, 9.

116. Noriega, R.; Rivnay, J.; Vandewal, K.; Koch, F. P. V.; Stingelin, N.; Smith, P.; Toney, M. F.; Salleo, A., A general relationship between disorder, aggregation and charge transport in conjugated polymers. *Nat. Mater.* **2013,** *12* (11), 1038-1044.

117. Duong, D. T.; Ho, V.; Shang, Z. R.; Mollinger, S.; Mannsfeld, S. C. B.; Dacuna, J.; Toney, M. F.; Segalman, R.; Salleo, A., Mechanism of Crystallization and Implications for Charge Transport in Poly(3-ethylhexylthiophene) Thin Films. *Adv. Func. Mater.* **2014,** *24* (28), 4515-4521.

118. Mollinger, S. A.; Krajina, B. A.; Noriega, R.; Salleo, A.; Spakowitz, A. J., Percolation, Tie-Molecules, and the Microstructural Determinants of Charge Transport in Semicrystalline Conjugated Polymers. *ACS Macro. Lett.* **2015,** *4* (7), 708-712.

119. Hoofman, R.; de Haas, M. P.; Siebbeles, L. D. A.; Warman, J. M., Highly mobile electrons and holes on isolated chains of the semiconducting polymer poly(phenylenevinylene). *Nature* **1998,** *392* (6671), 54-56.

120. Prins, P.; Grozema, F. C.; Schins, J. M.; Savenije, T. J.; Patil, S.; Scherf, U.; Siebbeles, L. D. A., Effect of intermolecular disorder on the intrachain charge transport in ladder-type poly(p-phenylenes). *Phys. Rev. B.* **2006,** *73* (4), 10.

121. Salleo, A.; Kline, R. J.; DeLongchamp, D. M.; Chabinyc, M. L., Microstructural Characterization and Charge Transport in Thin Films of Conjugated Polymers. *Adv. Mater.* **2010,** *22* (34), 3812-3838.

122. Kline, R. J.; McGehee, M. D.; Toney, M. F., Highly oriented crystals at the buried interface in polythiophene thin-film transistors. *Nat. Mater.* **2006,** *5* (3), 222-228.

123. Redecker, M.; Bradley, D. D. C.; Inbasekaran, M.; Woo, E. P., Mobility enhancement through homogeneous nematic alignment of a liquid-crystalline polyfluorene. *Appl. Phys. Lett.* **1999,** *74* (10), 1400-1402.

124. Martens, H. C. F.; Blom, P. W. M.; Schoo, H. F. M., Comparative study of hole transport in poly(p-phenylene vinylene) derivatives. *Phys. Rev. B.* **2000,** *61* (11), 7489-7493.

125. McCullough, R. D., The chemistry of conducting polythiophenes. *Adv. Mater.* **1998,** *10* (2), 93-116.

126. McCullough, R. D.; Lowe, R. D., Enhanced Electrical-Conductivity in Regioselectively Synthesized poly(3-Alkylthiophenes). *J. Chem. Soc. Chem. Comm.* **1992,** 1, 70-72.

127. Ong, B. S.; Wu, Y. L.; Li, Y. N.; Liu, P.; Pan, H. L., Thiophene polymer semiconductors for organic thin-film transistors. *Chem. Euro. J.* **2008,** *14* (16), 4766-4778.

128. Katz, H. E.; Bao, Z. N.; Gilat, S. L., Synthetic chemistry for ultrapure, processable, and high-mobility organic transistor semiconductors. *Acc. Chem. Res.* **2001,** *34* (5), 359-369.

129. Bao, Z.; Dodabalapur, A.; Lovinger, A. J., Soluble and processable regioregular poly(3-hexylthiophene) for thin film field-effect transistor applications with high mobility. *Appl. Phys. Lett.* **1996,** *69* (26), 4108-4110.

130. Osterbacka, R.; An, C. P.; Jiang, X. M.; Vardeny, Z. V., Two-dimensional electronic excitations in self-assembled conjugated polymer nanocrystals. *Science* **2000,** *287* (5454), 839-842.

131. Verilhac, J. M.; Pokrop, R.; LeBlevennec, G.; Kulszewicz-Bajer, I.; Buga, K.; Zagorska, M.; Sadki, S.; Pron, A., Molecular weight dependent charge carrier

mobility in poly(3,3 ''-dioctyl-2,2 ' : 5 ',2 ''-terthiophene). *J. Phys. Chem. B.* **2006,** *110* (27), 13305-13309.

132. Tsao, H. N.; Cho, D. M.; Park, I.; Hansen, M. R.; Mavrinskiy, A.; Yoon, D. Y.; Graf, R.; Pisula, W.; Spiess, H. W.; Mullen, K., Ultrahigh Mobility in Polymer Field-Effect Transistors by Design. *J. Am. Chem. Soc.* **2011,** *133* (8), 2605-2612.

133. Gasperini, A.; Sivula, K., Effects of Molecular Weight on Microstructure and Carrier Transport in a Semicrystalline Poly(thieno)thiophene. *Macromolecules* **2013,** *46* (23), 9349-9358.

134. Kline, R. J.; McGehee, M. D.; Kadnikova, E. N.; Liu, J. S.; Frechet, J. M. J., Controlling the field-effect mobility of regioregular polythiophene by changing the molecular weight. *Adv. Mater.* **2003,** *15* (18), 1519-1522.

135. Kline, R. J.; McGehee, M. D.; Kadnikova, E. N.; Liu, J. S.; Frechet, J. M. J.; Toney, M. F., Dependence of regioregular poly(3-hexylthiophene) film morphology and field-effect mobility on molecular weight. *Macromolecules* **2005,** *38* (8), 3312-3319.

136. Koch, F. P. V.; Rivnay, J.; Foster, S.; Muller, C.; Downing, J. M.; Buchaca-Domingo, E.; Westacott, P.; Yu, L. Y.; Yuan, M. J.; Baklar, M.; Fei, Z. P.; Luscombe, C.; McLachlan, M. A.; Heeney, M.; Rumbles, G.; Silva, C.; Salleo, A.; Nelson, J.; Smith, P.; Stingelin, N., The impact of molecular weight on microstructure and charge transport in semicrystalline polymer Semiconductors poly(3-hexylthiophene), a model study. *Prog. Poly. Sci.* **2013,** *38* (12), 1978-1989.

137. Beljonne, D.; Cornil, J.; Sirringhaus, H.; Brown, P. J.; Shkunov, M.; Friend, R. H.; Bredas, J. L., Optical signature of delocalized polarons in conjugated polymers. *Adv. Func. Mater.* **2001,** *11* (3), 229-234.

138. Jiang, X. M.; Osterbacka, R.; Korovyanko, O.; An, C. P.; Horovitz, B.; Janssen, R. A. J.; Vardeny, Z. V., Spectroscopic studies of photoexcitations in regioregular and regiorandom polythiophene films. *Adv. Funct. Mater.* **2002,** *12* (9), 587-597.

139. Rubinstein, M., *Polymer physics / Michael Rubinstein and Ralph H. Colby*. Oxford ; New York : Oxford University Press: 2003.

140. Zhang, W.; Gomez, E. D.; Milner, S. T., Predicting Chain Dimensions of Semiflexible Polymers from Dihedral Potentials. *Macromolecules* **2014,** *47* (18), 6453-6461.

141. Donald, A. M., *Liquid crystalline polymers / A.M. Donald, A.H. Windle, S. Hanna*. 2nd ed. ed.; Cambridge : Cambridge University Press: 2006.

142. Knaapila, M.; Stepanyan, R.; Lyons, B. P.; Torkkeli, M.; Monkman, A. P., Towards General Guidelines for Aligned, Nanoscale Assemblies of Hairy-Rod Polyfluorene. *Adv. Func. Mater.* **2006,** *16* (5), 599-609.

143. McCulloch, I.; Heeney, M.; Bailey, C.; Genevicius, K.; Macdonald, I.; Shkunov, M.; Sparrowe, D.; Tierney, S.; Wagner, R.; Zhang, W. M.; Chabinyc, M. L.; Kline, R. J.; McGehee, M. D.; Toney, M. F., Liquid-crystalline Semiconducting Polymers with High Charge-carrier Mobility. *Nat. Mater.* **2006,** *5* (4), 328-333.

144. Kuei, B.; Gomez, E. D., Chain conformations and phase behavior of conjugated polymers. *Soft Matter* **2017,** *13* (1), 49-67.

145. Venkateshvaran, D.; Nikolka, M.; Sadhanala, A.; Lemaur, V.; Zelazny, M.; Kepa, M.; Hurhangee, M.; Kronemeijer, A. J.; Pecunia, V.; Nasrallah, I.; Romanov, I.; Broch, K.; McCulloch, I.; Emin, D.; Olivier, Y.; Cornil, J.; Beljonne, D.; Sirringhaus, H., Approaching disorder-free transport in high-mobility conjugated polymers. *Nature* **2014,** *515* (7527), 384-388.

146. Gu, K.; Snyder, C. R.; Onorato, J.; Luscombe, C. K.; Bosse, A. W.; Loo, Y.-L., Assessing the Huang–Brown Description of Tie Chains for Charge Transport in Conjugated Polymers. *ACS Macro. Lett.* **2018,** *7* (11), 1333-1338.

147. McCulloch, B.; Ho, V.; Hoarfrost, M.; Stanley, C.; Do, C.; Heller, W. T.; Segalman, R. A., Polymer Chain Shape of Poly(3-alkylthiophenes) in Solution Using Small-Angle Neutron Scattering. *Macromolecules* **2013,** *46* (5), 1899-1907.

148. Kline, R. J.; McGehee, M. D., Morphology and Charge Transport in Conjugated Polymers. *J. Macromol. Sci. Rev. chem. Phys.* **2006,** *46* (1), 27-45.

149. Rieger, R.; Beckmann, D.; Pisula, W.; Steffen, W.; Kastler, M.; Müllen, K., Rational Optimization of Benzo[2,1-b;3,4-b′]dithiophene-Containing Polymers for Organic Field-Effect Transistors. *Adv. Mater.* **2010,** *22* (1), 83-86.

150. Guo, X.; Puniredd, S. R.; Baumgarten, M.; Pisula, W.; Müllen, K., Rational Design of Benzotrithiophene-Diketopyrrolopyrrole-Containing Donor-Acceptor Polymers for Improved Charge Carrier Transport. *Adv. Mater.* **2013,** *25* (38), 5467-5472.

151. Bridges, C. R.; Ford, M. J.; Thomas, E. M.; Gomez, C.; Bazan, G. C.; Segalman, R. A., Effects of Side Chain Branch Point on Self Assembly, Structure, and Electronic Properties of High Mobility Semiconducting Polymers. *Macromolecules* **2018,** *51* (21), 8597-8604.

152. Kim, J. H.; Park, J. H.; Lee, J. H.; Kim, J. S.; Sim, M.; Shim, C.; Cho, K., Bulk heterojunction solar cells based on preformed polythiophene nanowires via solubility-induced crystallization. *J. Mater. Chem.* **2010,** *20* (35), 7398-7405.

153. Lee, J. K.; Ma, W. L.; Brabec, C. J.; Yuen, J.; Moon, J. S.; Kim, J. Y.; Lee, K.; Bazan, G. C.; Heeger, A. J., Processing additives for improved efficiency from bulk heterojunction solar cells. *J. Am. Chem. Soc.* **2008,** *130* (11), 3619-3623.

154. Zheng, Y. F.; Wang, G.; Huang, D.; Kong, J.; Goh, T.; Huang, W.; Yu, J. S.; Taylor, A. D., Binary Solvent Additives Treatment Boosts the Efficiency of PTB7:PCBM Polymer Solar Cells to Over 9.5%. *Sol. RRL.* **2018,** *2* (4), 8.

155. Verilhac, J. M.; LeBlevennec, G.; Djurado, D.; Rieutord, F.; Chouiki, M.; Travers, J. P.; Pron, A., Effect of macromolecular parameters and processing conditions on supramolecular organisation, morphology and electrical transport properties in thin layers of regioregular poly(3-hexylthiophene). *Syn. Met.* **2006,** *156* (11-13), 815-823.

156. Beaujuge, P. M.; Frechet, J. M. J., Molecular Design and Ordering Effects in pi-Functional Materials for Transistor and Solar Cell Applications. *J. Am. Chem. Soc.* **2011,** *133* (50), 20009-20029.

157. Na, J. Y.; Kim, M.; Park, Y. D., Solution Processing with a Good Solvent Additive for Highly Reliable Organic Thin-Film Transistors. *J. Phys. Chem. C.* **2017,** *121* (25), 13930-13937.

158. Yang, H. C.; Shin, T. J.; Yang, L.; Cho, K.; Ryu, C. Y.; Bao, Z. N., Effect of mesoscale crystalline structure on the field-effect mobility of regioregular poly(3-hexyl thiophene) in thin-film transistors. *Adv. Funct. Mater.* **2005,** *15* (4), 671-676.

159. Chang, J. F.; Sun, B. Q.; Breiby, D. W.; Nielsen, M. M.; Solling, T. I.; Giles, M.; McCulloch, I.; Sirringhaus, H., Enhanced mobility of poly(3-hexylthiophene) transistors by spin-coating from high-boiling-point solvents. *Chem. Mater.* **2004,** *16* (23), 4772-4776.

160. Zhang, F. L.; Jespersen, K. G.; Bjorstrom, C.; Svensson, M.; Andersson, M. R.; Sundstrom, V.; Magnusson, K.; Moons, E.; Yartsev, A.; Inganas, O., Influence of solvent mixing on the morphology and performance of solar cells based on polyfluorene copolymer/fullerene blends. *Adv. Funct. Mater.* **2006,** *16* (5), 667-674.

161. Hoven, C. V.; Dang, X. D.; Coffin, R. C.; Peet, J.; Nguyen, T. Q.; Bazan, G. C., Improved Performance of Polymer Bulk Heterojunction Solar Cells Through the Reduction of Phase Separation via Solvent Additives. *Adv. Mater.* **2010,** *22* (8), E63-66.

162. Peet, J.; Kim, J. Y.; Coates, N. E.; Ma, W. L.; Moses, D.; Heeger, A. J.; Bazan, G. C., Efficiency enhancement in low-bandgap polymer solar cells by processing with alkane dithiols. *Nat. Mater.* **2007,** *6* (7), 497-500.

163. Soeda, J.; Matsui, H.; Okamoto, T.; Osaka, I.; Takimiya, K.; Takeya, J., Highly Oriented Polymer Semiconductor Films Compressed at the Surface of Ionic Liquids for High-Performance Polymeric Organic Field-Effect Transistors. *Adv. Mater.* **2014,** *26* (37), 6430-6435.

164. Tseng, H. R.; Ying, L.; Hsu, B. B. Y.; Perez, L. A.; Takacs, C. J.; Bazan, G. C.; Heeger, A. J., High Mobility Field Effect Transistors Based on Macroscopically Oriented Regioregular Copolymers. *Nano Lett.* **2012,** *12* (12), 6353-6357.

165. Lee, M. J.; Gupta, D.; Zhao, N.; Heeney, M.; McCulloch, I.; Sirringhaus, H., Anisotropy of Charge Transport in a Uniaxially Aligned and Chain-Extended, High-Mobility, Conjugated Polymer Semiconductor. *Adv. Funct. Mater.* **2011,** *21* (5), 932-940.

166. Li, G.; Yao, Y.; Yang, H.; Shrotriya, V.; Yang, G.; Yang, Y., "Solvent annealing" effect in polymer solar cells based on poly(3-hexylthiophene) and methanofullerenes. *Adv. Funct. Mater.* **2007,** *17* (10), 1636-1644.

167. Ong, B. S.; Wu, Y. L.; Liu, P.; Gardner, S., High-performance semiconducting polythiophenes for organic thin-film transistors. *J. Am. Chem. Soc.* **2004,** *126* (11), 3378-3379.

168. Padinger, F.; Rittberger, R. S.; Sariciftci, N. S., Effects of postproduction treatment on plastic solar cells. *Adv. Funct. Mater.* **2003,** *13* (1), 85-88.

169. Kline, R. J.; DeLongchamp, D. M.; Fischer, D. A.; Lin, E. K.; Heeney, M.; McCulloch, I.; Toney, M. F., Significant dependence of morphology and charge carrier mobility on substrate surface chemistry in high performance polythiophene semiconductor films. *Appl. Phys. Lett.* **2007,** *90* (6).

170. Umeda, T.; Kumaki, D.; Tokito, S., Surface-energy-dependent field-effect mobilities up to 1 cm^2/Vs for polymer thin-film transistor. *J. Appl. Phys.* **2009,** *105* (2).

171. Crossland, E. J. W.; Rahimi, K.; Reiter, G.; Steiner, U.; Ludwigs, S., Systematic Control of Nucleation Density in Poly(3-Hexylthiophene) Thin Films. *Adv. Funct. Mater.* **2011,** *21* (3), 518-524.

172. Schulz, G. L.; Ludwigs, S., Controlled Crystallization of Conjugated Polymer Films from Solution and Solvent Vapor for Polymer Electronics. *Adv. Funct. Mater.* **2017,** *27* (1), 16.

173. Steyrleuthner, R.; Schubert, M.; Howard, I.; Klaumunzer, B.; Schilling, K.; Chen, Z. H.; Saalfrank, P.; Laquai, F.; Facchetti, A.; Neher, D., Aggregation in a High-Mobility n-Type Low-Bandgap Copolymer with Implications on Semicrystalline Morphology. *J. Am. Chem. Soc.* **2012,** *134* (44), 18303-18317.

174. Takacs, C. J.; Treat, N. D.; Kramer, S.; Chen, Z. H.; Facchetti, A.; Chabinyc, M. L.; Heeger, A. J., Remarkable Order of a High-Performance Polymer. *Nano Lett.* **2013,** *13* (6), 2522-2527.

175. Luzio, A.; Criante, L.; D'Innocenzo, V.; Caironi, M., Control of charge transport in a semiconducting copolymer by solvent-induced long-range order. *Sci. Rep.* **2013,** *3*, 6.

176. Kim, Y.; Cook, S.; Tuladhar, S. M.; Choulis, S. A.; Nelson, J.; Durrant, J. R.; Bradley, D. D. C.; Giles, M.; McCulloch, I.; Ha, C. S.; Ree, M., A strong

regioregularity effect in self-organizing conjugated polymer films and high-efficiency polythiophene: fullerene solar cells. *Nat. Mater.* **2006,** *5* (3), 197-203.

177. DeLongchamp, D. M.; Vogel, B. M.; Jung, Y.; Gurau, M. C.; Richter, C. A.; Kirillov, O. A.; Obrzut, J.; Fischer, D. A.; Sambasivan, S.; Richter, L. J.; Lin, E. K., Variations in semiconducting polymer microstructure and hole mobility with spin-coating speed. *Chem. Mater.* **2005,** *17* (23), 5610-5612.

178. Osaka, I.; Takimiya, K., Backbone orientation in semiconducting polymers. *Polymer* **2015,** *59*, A1-A15.

179. Joshi, S.; Grigorian, S.; Pietsch, U.; Pingel, P.; Zen, A.; Neher, D.; Scherf, U., Thickness dependence of the crystalline structure and hole mobility in thin films of low molecular weight poly(3-hexylthiophene). *Macromolecules* **2008,** *41* (18), 6800-6808.

180. Kim, D. H.; Jang, Y.; Park, Y. D.; Cho, K., Surface-induced conformational changes in poly(3-hexylthiophene) monolayer films. *Langmuir* **2005,** *21* (8), 3203-3206.

181. Kim, D. H.; Park, Y. D.; Jang, Y. S.; Yang, H. C.; Kim, Y. H.; Han, J. I.; Moon, D. G.; Park, S. J.; Chang, T. Y.; Chang, C. W.; Joo, M. K.; Ryu, C. Y.; Cho, K. W., Enhancement of field-effect mobility due to surface-mediated molecular ordering in regioregular polythiophene thin film transistors. *Adv. Funct. Mater.* **2005,** *15* (1), 77-82.

182. Davidson, P. A., *Turbulence: An Introduction for Scientists and Engineers*. Oxford: Oxford University Press: Oxford, 2004.

183. Rayleigh, L., LIX. On convection currents in a horizontal layer of fluid, when the higher temperature is on the under side. *The London, Edinburgh, and Dublin Philosophical Magazine and Journal of Science* **1916,** *32* (192), 529-546.

184. Benard, H., Les tourbillons cellulaires dans une nappe liquide. *Rev. Gen. Sci. Pures Appl.* **1900,** *11*, 1261-1271.

185. Kadanoff, L. P., Turbulent Heat Flow: Structures and Scaling. *Phys. Today* **2001,** *54* (8), 34-39.

186. Clifford, T., *Fundamentals of supercritical fluids / Tony Clifford*. New York : Oxford University Press: 2002.

187. Bellan, J., Theory, Modeling and Analysis of Turbulent Supercritical Mixing. *Combust. Sci. Technol.* **2006,** *178* (1-3), 253-281.

188. Younglove, B. A., Erratum: Thermophysical Properties of Fluids. I. Argon, Ethylene, Parahydrogen, Nitrogen, Nitrogen Trifluoride, and Oxygen. *J. Phys. Chem. Ref. Data.* **1985,** *14* (2), 619-619.

189. Oefelein, J. C., Mixing and Combustion of Cryogenic Oxygen-Hydrogen Shear-Coaxial Jet Flames at Supercritical Pressure. *Combust. Sci. Technol.* **2006,** *178* (1-3), 229-252.

190. Candel, S.; Juniper†, M.; Singla, G.; Scouflaire, P.; Rolon, C., Structure and Dynamics of Cryogenic Flames at Supercritical Pressure. *Combust. Sci. Technol.* **2006,** *178* (1-3), 161-192.

191. Banuti, D. T.; Raju, M.; Ma, P. C.; Hickey, J. P., Seven Questions about Supercritical Fluids - Towards a New Fluid State Diagram. American Institute of Aeronautics and Astronautics: Grapevine, Texas, 2017.

192. Giovangigli, V.; Matuszewski, L.; Dupoirieux, F., Detailed modeling of planar transcritical H_2-O_2-N_2 flames. *Combust. Theor. Model.* **2011,** *15* (2), 141-182.

193. Bozbağ, S. E.; Erkey, C., Supercritical deposition: Current status and perspectives for the preparation of supported metal nanostructures. *J. Supercrit. Fluids.* **2015,** *96*, 298-312.

194. Kirby, C. F.; McHugh, M. A., Phase Behavior of Polymers in Supercritical Fluid Solvents. *Chem. Rev.* **1999,** *99* (2), 565-602.

195. Martin, J. J., Cubic Equations of State - Which. *Ind. Eng. Chem. Process. Des. Dev.* **1979,** *18* (2), 81-97.

196. Johnston, D. C., *Advances in thermodynamics of the van der Waals fluid / David C Johnston*. San Rafael California 40 Oak Drive, San Rafael, CA, 94903, USA : Morgan & Claypool Publishers: 2014.

197. Clerk-Maxwell, J., On the Dynamical Evidence of the Molecular Constitution of Bodies. *Nature* **1875,** *11* (279), 357-359.

198. Stanley, H. E., *Introduction to phase transitions and critical phenomena / by H. Eugene Stanley*. New York : Oxford University Press: 1971.

199. Orbey, H.; Bokis, C. P.; Chen, C. C., Equation of state modeling of phase equilibrium in the low-density polyethylene process: The Sanchez-Lacombe, statistical associating fluid theory, and polymer-Soave-Redlich-Kwong equations of state. *Ind. Eng. Chem. Res.* **1998,** *37* (11), 4481-4491.

200. Sako, T.; Wu, A. H.; Prausnitz, J. M., A Cubic Equation of State for High-Pressure Phase-Equilibria of Mixtures Containing Polymers and Volatile Fluids. *J. Appl. Polym. Sci.* **1989,** *38* (10), 1839-1858.

201. Panagiotopoulos, A. Z.; Reid, R. C., New Mixing Rule for Cubic Equations of State for Highly Polar, Asymmetric Systems. In *Equations of State*, American Chemical Society: 1986; Vol. 300, pp 571-582.

202. Soave, G., Equilibrium constants from a modified Redlich-Kwong equation of state. *Chem. Eng. Sci.* **1972,** *27* (6), 1197-1203.

203. Yang, T.; Chen, G. J.; Yan, W.; Guo, T. M., Extension of the Wong-Sandler mixing rule to the three-parameter Patel-Teja equation of state: Application up to the near-critical region. *Chem. Eng. J. (Lausanne, Switzerland : 1996)* **1997,** *67* (1), 27-36.

204. Zhong, C.; Masuoka, H., A new mixing rule for cubic equations of state and its application to vapor-liquid equilibria of polymer solutions. *Fluid Ph. Equilibria.* **1996,** *123* (1), 59-69.

205. Peng, D. Y.; Robinson, D. B., A New Two-Constant Equation of State. *Ind. Eng. Chem. Fundamen.* **1976,** *15* (1), 59-64.

206. Valderrama, J. O., The State of the Cubic Equations of State. *Ind. Eng. Chem. Res.* **2003,** *42* (8), 1603-1618.

207. Vitha, M. F., *Spectroscopy: Principles and Instrumentation*. Newark: John Wiley & Sons, Incorporated: Newark, 2018.

208. Anderson Rosaleen, J.; Bendell David, J.; Groundwater Paul, W., Ultraviolet-Visible (UV-Vis) Spectroscopy. Royal Society of Chemistry: 2004; pp 1-1.

209. Schrader, B., *Infrared and Raman spectroscopy : methods and applications / edited by Bernhard Schrader*. Weinheim ; New York : VCH: 1995.

210. Larkin, P., *Infrared and Raman Spectroscopy: Principles and Spectral Interpretation*. Second edition; US: Elsevier: US, 2011.

211. Feidenhans; apos; l, R., Surface structure determination by X-ray diffraction. *Surf. Sci. Rep.* **1989,** *10* (3), 105-188.

212. Als-Nielsen, J.; McMorrow, D., *Elements of Modern X-ray Physics*. 2. Aufl. ed.; New York: Wiley: New York, 2011.

213. Renaud, G.; Lazzari, R.; Leroy, F., Probing surface and interface morphology with Grazing Incidence Small Angle X-Ray Scattering. *Surf. Sci. Rep.* **2009,** *64* (8), 255-380.

214. Giannini, C.; Ladisa, M.; Altamura, D.; Siliqi, D.; Sibillano, T.; De Caro, L., X-ray Diffraction: A Powerful Technique for the Multiple-Length-Scale Structural Analysis of Nanomaterials. *Crystals (Basel)* **2016,** *6* (8), 87.

215. Muller-Buschbaum, P., The Active Layer Morphology of Organic Solar Cells Probed with Grazing Incidence Scattering Techniques. *Adv. Mater.* **2014,** *26* (46), 7692-7709.

216. Rivnay, J.; Mannsfeld, S. C. B.; Miller, C. E.; Salleo, A.; Toney, M. F., Quantitative Determination of Organic Semiconductor Microstructure from the Molecular to Device Scale. *Chem. Rev.* **2012,** *112* (10), 5488-5519.

217. Tilley, R. J. D., *Colour and the optical properties of materials : an exploration of the relationship between light, the optical properties of materials and colour / Richard J.D. Tilley*. 2nd ed.; Chichester, West Sussex, U.K. : Wiley: 2011.

218. Oldenbourg, R., Polarized light microscopy: principles and practice. *Cold Spring Harb Protoc* **2013,** *2013* (11).

219. Wolman, M., Polarized light microscopy as a tool of diagnostic pathology. *J. Histochem. Cytochem.* **1975,** *23* (1), 21-50.

220. Mack, C. A., *Fundamental principles of optical lithography : the science of microfabrication / Chris Mack*. Chichester, West Sussex, England ; Hoboken, NJ, USA : Wiley: 2007.

221. Madou, M. J., *Fundamentals of microfabrication and nanotechnology*. CRC Press: 2018.

222. Cuomo, J. J.; Rossnagel, S. M.; Westwood, W. D., Reactive Ion Etching. William Andrew Publishing/Noyes: 1990; pp 1-1.

223. Anelli, P. L.; Spencer, N.; Stoddart, J. F., A Molecular Shuttle. *J. Am. Chem. Soc.* **1991,** *113* (13), 5131-5133.

224. Dietrich-Buchecker, C. O.; Sauvage, J. P.; Kintzinger, J. P., Une Nouvelle Famille de Molecules : Les Metallo-catenanes. *Tetrahedron Lett.* **1983,** *24* (46), 5095-5098.

225. Koumura, N.; Zijlstra, R. W. J.; van Delden, R. A.; Harada, N.; Feringa, B. L., Light-driven Monodirectional Molecular Rotor. *Nature* **1999,** *401*, 152.

226. McCluskey, G. E.; Lee, J. K.; Sha, J.; Ober, C. K.; Watkins, S. E.; Holmes, A. B., Synthesis and Processing of Organic Materials in Supercritical Carbon Dioxide. *Mrs Bulletin* **2009,** *34* (2), 108-115.

227. Cooper, A. I., Polymer Synthesis and Processing Using Supercritical Carbon Dioxide. *J. Mater. Chem.* **2000,** *10* (2), 207-234.

228. Desimone, J. M.; Guan, Z.; Elsbernd, C. S., Synthesis of Fluoropolymers in Supercritical Carbon Dioxide. *Science* **1992,** *257* (5072), 945-947.

229. M. Kerton, F.; A. Lawless, G.; P. Armes, S., First example of a conducting polymer synthesised in supercritical fluids. *J. Mater. Chem.* **1997,** *7* (10), 1965-1966.

230. Anderson, P. E.; Badlani, R. N.; Mayer, J.; Mabrouk, P. A., Electrochemical synthesis and characterization of conducting polymers in supercritical carbon dioxide. *J. Am. Chem. Soc.* **2002,** *124* (35), 10284-10285.

231. Li, L.; Counts, K. E.; Kurosawa, S.; Teja, A. S.; Collard, D. M., Tuning the Electronic Structure and Solubility of Conjugated Polymers with Perfluoroalkyl Substituents: Poly(3-perfluorooctylthiophene), The First supercritical-CO_2-soluble conjugated polymer. *Adv. Mater.* **2004,** *16* (2), 180-183.

232. Blackburn, J. M.; Long, D. P.; Cabanas, A.; Watkins, J. J., Deposition of Conformal Copper and Nickel Films from Supercritical Carbon Dioxide. *Science* **2001,** *294* (5540), 141-145.

233. Cabanas, A.; Long, D. P.; Watkins, J. J., Deposition of Gold Films and Nanostructures from Supercritical Carbon Dioxide. *Chem. Mater.* **2004,** *16* (10), 2028-2033.

234. Dong, B. X.; Amonoo, J. A.; Purdum, G. E.; Loo, Y. L.; Green, P. F., Enhancing Carrier Mobilities in Organic Thin-Film Transistors Through Morphological

Changes at the Semiconductor/Dielectric Interface Using Supercritical Carbon Dioxide Processing. *ACS Appl. Mater. Interfaces.* **2016,** *8* (45), 31144.

235. Amonoo, J. A.; Glynos, E.; Chen, X. C.; Green, P. F., An Alternative Processing Strategy for Organic Photovoltaic Devices Using a Supercritical Fluid. *J. Phys. Chem. C.* **2012,** *116* (39).

236. Ambuken, P. V.; Stretz, H. A.; Dadmun, M.; Michael Kilbey, S., Gas Expanded Polymer Process to Anneal Nanoparticle Dispersion in Thin Films. *Sol. Energy Mater Sol. Cells.* **2015,** *140*, 101-107.

237. Nelson, A. P.; Farha, O. K.; Mulfort, K. L.; Hupp, J. T., Supercritical Processing as a Route to High Internal Surface Areas and Permanent Microporosity in Metal-Organic Framework Materials. *J. Am. Chem. Soc.* **2009,** *131* (2), 458.

238. Farha, O.; Hupp, J., Rational Design, Synthesis, Purification, and Activation of Metal-Organic Framework Materials. *Accounts Chem. Res.* **2010,** *43* (8), 1166-1175.

239. Kistler, S. S., Coherent Expanded Aerogels and Jellies. *Nature* **1931,** *127* (3211), 741.

240. Kistler, S. S., Coherent Expanded-Aerogels. *J. Phys. Chem.* **1931,** *36* (1), 52-64.

241. Forrest, S. R., Ultrathin Organic Films Grown by Organic Molecular Beam Deposition and Related Techniques. *Chem. Rev.* **1997,** *97* (6), 1793-1896.

242. Bahlke, M. E.; Mendoza, H. A.; Ashall, D. T.; Yin, A. S.; Baldo, M. A., Dry Lithography of Large-area, Thin-film Organic Semiconductors Using Frozen CO_2 Resists. *Adv. Mater.* **2012,** *24* (46), 6136.

243. Jean, J.; Wang, A.; Bulović, V., In Situ Vapor-deposited Parylene Substrates for Ultra-thin, Lightweight Organic Solar Cells. *Org. Electron.* **2016,** *31*, 120-126.

244. Biswas, S.; Shalev, O.; Pipe, K. P.; Shtein, M., Chemical Vapor Jet Deposition of Parylene Polymer Films in Air. *Macromolecules* **2015,** *48* (16), 5550-5556.

245. Fan, B. B.; Du, X. Y.; Liu, F.; Zhong, W. K.; Ying, L.; Xie, R. H.; Tang, X. F.; An, K.; Xin, J. M.; Li, N.; Ma, W.; Brabec, C. J.; Huang, F.; Cao, Y., Fine-tuning of the Chemical Structure of Photoactive Materials for Highly Efficient Organic Photovoltaics. *Nat. Energy* **2018,** *3* (12), 1051-1058.

246. Cui, Y.; Yao, H. F.; Zhang, J. Q.; Zhang, T.; Wang, Y. M.; Hong, L.; Xian, K. H.; Xu, B. W.; Zhang, S. Q.; Peng, J.; Wei, Z. X.; Gao, F.; Hou, J. H., Over 16% Efficiency Organic Photovoltaic Cells Enabled by a Chlorinated Acceptor with Increased Open-Circuit Voltages. *Nat. Commun.* **2019,** *10*, 8.

247. Ni, Z. J.; Dong, H. L.; Wang, H. L.; Ding, S.; Zou, Y.; Zhao, Q.; Zhen, Y. G.; Liu, F.; Jiang, L.; Hu, W. P., Quinoline-Flanked Diketopyrrolopyrrole Copolymers Breaking through Electron Mobility over 6 cm^2/V.s in Flexible Thin Film Devices. *Adv. Mater.* **2018,** *30* (10), 7.

248. Yuan, J.; Zhang, Y.; Zhou, L.; Zhang, C.; Lau, T.-K.; Zhang, G.; Lu, X.; Yip, H. L.; So, S. K.; Beaupré, S.; Mainville, M.; Johnson, P. A.; Leclerc, M.; Chen, H.; Peng, H.; Li, Y.; Zou, Y., Fused Benzothiadiazole: A Building Block for n-Type Organic Acceptor to Achieve High-Performance Organic Solar Cells. *Adv. Mater.* **2019,** *31* (17), 1807577.

249. Sondergaard, R. R.; Hosel, M.; Krebs, F. C., Roll-to-Roll Fabrication of Large Area Functional Organic Materials. *J. Poly. Sci. Poly. Phys.* **2013,** *51* (1), 16-34.

250. Baeg, K. J.; Caironi, M.; Noh, Y. Y., Toward Printed Integrated Circuits based on Unipolar or Ambipolar Polymer Semiconductors. *Adv. Mater.* **2013,** *25* (31), 4210-4244.

251. Cho, J. H.; Lee, J.; Xia, Y.; Kim, B.; He, Y. Y.; Renn, M. J.; Lodge, T. P.; Frisbie, C. D., Printable Ion-gel Gate Dielectrics for Low-Voltage Polymer Thin-Film Transistors on Plastic. *Nat. Mater.* **2008,** *7* (11), 900-906.

252. Tait, J. G.; Witkowska, E.; Hirade, M.; Ke, T. H.; Malinowski, P. E.; Steudel, S.; Adachi, C.; Heremans, P., Uniform Aerosol Jet Printed Polymer Lines with 30 μm Width for 140 ppi Resolution RGB Organic Light Emitting Diodes. *Org. Electron.* **2015,** *22*, 40-43.

253. Yousefi, N.; Maala, J. J.; Louie, M.; Storback, J.; Kaake, L. G., Physical Supercritical Fluid Deposition: Patterning Solution Processable Materials on Curved and Flexible Surfaces. *ACS Appl. Mater. Interfaces.* **2020,** *12* (15), 17961-17968.

254. Yang, C.; Orfino, F. P.; Holdcroft, S., A Phenomenological Model for Predicting Thermochromism of Regioregular and Nonregioregular poly(3-alkylthiophenes). *Macromolecules* **1996,** *29* (20), 6510-6517.

255. Schmidtke, J. P.; Kim, J. S.; Gierschner, J.; Silva, C.; Friend, R. H., Optical Spectroscopy of a Polyfluorene Copolymer at High Pressure: Intra- and Intermolecular Interactions. *Phys. Rev. Lett.* **2007,** *99* (16), 167401.

256. Yamagata, H.; Spano, F. C., Strong Photophysical Similarities between Conjugated Polymers and J-aggregates. *J. Phys. Chem. Lett.* **2014,** *5* (3), 622-632.

257. Shieh, Y. T.; Su, J. H.; Manivannan, G.; Lee, P. H. C.; Sawan, S. P.; Spall, W. D., Interaction of Supercritical Carbon Dioxide with Polymers. 1. Crystalline Polymers. *J. Appl. Polym. Sci.* **1996,** *59* (4), 695-705.

258. Shieh, Y. T.; Su, J. H.; Manivannan, G.; Lee, P. H. C.; Sawan, S. P.; Spall, W. D., Interaction of Supercritical Carbon Dioxide with Polymers. 2. Amorphous Polymers. *J. Appl. Polym. Sci.* **1996,** *59* (4), 707-717.

259. Hunter, E.; Richards, R. B. Fractionation of Polymeric Ethylene. 1948.

260. Kiran, E., Polymer Miscibility and Kinetics of Pressure — Induced Phase Separation in Near-Critical and Supercritical Fluids. In *Supercritical Fluids.*, Kiran E., D. P. G., Peters C.J., Ed. Springer: Dordrecht, 2000; Vol. 366, pp 167-192.

261. Patterson, D., Polymer compatibility with and without a solvent. *Polym. Eng. Sci.* **1982,** *22* (2), 64-73.

262. Eckert, C. A.; Knutson, B. L.; Debenedetti, P. G., Supercritical fluids as solvents for chemical and materials processing. *Nature* **1996,** *383* (6598), 313-318.

263. Sanchez, I. C.; Lacombe, R. H., Statistical Thermodynamics of Polymer Solutions. *Macromolecules* **1978,** *11* (6), 1145-1156.

264. Paternò, G. M.; Robbiano, V.; Fraser, K. J.; Frost, C.; García Sakai, V.; Cacialli, F., Neutron Radiation Tolerance of Two Benchmark Thiophene-Based Conjugated Polymers: the Importance of Crystallinity for Organic Avionics. *Sci. Rep.* **2017,** *7* (1), 41013.

265. Francis, C.; Fazzi, D.; Grimm, S. B.; Paulus, F.; Beck, S.; Hillebrandt, S.; Pucci, A.; Zaumseil, J., Raman Spectroscopy and Microscopy of Electrochemically and Chemically Doped High-mobility Semiconducting Polymers. *J. Mater. Chem. C.* **2017,** *5* (25), 6176-6184.

266. Castiglioni, C.; Gussoni, M.; Zerbi, G., Understanding of Vibrational Spectra of Polyconjugated Molecules by Means of the “Effective Conjugation Coordinate”. *Syn. Met.* **1991,** *43* (1-2), 3407-3412.

267. Colella, N. S.; Labastide, J. A.; Cherniawski, B. P.; Thompson, H. B.; Marques, S. R.; Zhang, L.; Usluer, Ö.; Watkins, J. J.; Briseno, A. L.; Barnes, M. D., Poly[2,5-bis(3-dodecylthiophen-2-yl)thieno[3,2-b]thiophene] Oligomer Single-Crystal Nanowires from Supercritical Solution and Their Anisotropic Exciton Dynamics. *J. Phys. Chem. Lett.* **2017,** *8* (13), 2984-2989.

268. Deegan, R. D.; Bakajin, O.; Dupont, T. F.; Huber, G.; Nagel, S. R.; Witten, T. A., Capillary Flow as the Cause of Ring Stains from Dried Liquid Drops. *Nature* **1997,** *389* (6653), 827-829.

269. Kawase, T.; Shimoda, T.; Newsome, C.; Sirringhaus, H.; Friend, R. H., Inkjet Printing of Polymer Thin Film Transistors. *Thin Solid Films* **2003,** *438*, 279-287.

270. Soltman, D.; Subramanian, V., Inkjet-printed Line Morphologies and Temperature Control of the Coffee Ring Effect. *Langmuir* **2008,** *24* (5), 2224-2231.

271. Hsu, B. B. Y.; Duan, C. H.; Namdas, E. B.; Gutacker, A.; Yuen, J. D.; Huang, F.; Cao, Y.; Bazan, G. C.; Samuel, I. D. W.; Heeger, A. J., Control of Efficiency, Brightness, and Recombination Zone in Light-Emitting Field Effect Transistors. *Adv. Mater.* **2012,** *24* (9), 1171-1175.

272. Rogers, J. A.; Someya, T.; Huang, Y. G., Materials and Mechanics for Stretchable Electronics. *Science* **2010,** *327* (5973), 1603-1607.

273. Sekitani, T.; Someya, T., Stretchable, Large-area Organic Electronics. *Adv. Mater.* **2010,** *22* (20), 2228-2246.

274. Bauer, S.; Bauer-Gogonea, S.; Graz, I.; Kaltenbrunner, M.; Keplinger, C.; Schwodiauer, R., 25th Anniversary Article: A Soft Future: From Robots and Sensor Skin to Energy Harvesters. *Adv. Mater.* **2014,** *26* (1), 149-162.

275. Filiatrault, H. L.; Porteous, G. C.; Carmichael, R. S.; Davidson, G. J. E.; Carmichael, T. B., Stretchable Light-Emitting Electrochemical Cells Using an Elastomeric Emissive Material. *Adv. Mater.* **2012,** *24* (20), 2673-2678.

276. Lipomi, D. J.; Bao, Z., Stretchable and Ultraflexible Organic Electronics. *MRS Bulletin* **2017,** *42* (2), 93-97.

277. Vitale, S. A.; Berry, S., Etching Selectivity of Indium Tin Oxide to Photoresist in High Density Chlorine- and Ethylene-containing Plasmas. *J. Vac. Sci. Technol. B.* **2013,** *31* (2), 3.

278. Liddle, J. A.; Gallatin, G. M., Nanomanufacturing: A Perspective. *ACS Nano* **2016,** *10* (3), 2995-3014.

279. Cooper, K., Scalable Nanomanufacturing-A Review. *Micromachines* **2017,** *8* (1), 8.

280. Kay, E. R.; Leigh, D. A.; Zerbetto, F., Synthetic Molecular Motors and Mechanical Machines. *Angew. Chem. Int. Edit.* **2007,** *46* (1-2), 72-191.

281. Balzani, V.; Credi, A.; Raymo, F. M.; Stoddart, J. F., Artificial Molecular Machines. *Angew. Chem. Int. Edit.* **2000,** *39* (19), 3348-3391.

282. Shih, W. M.; Quispe, J. D.; Joyce, G. F., A 1.7-kilobase Single-stranded DNA that Folds into a Nanoscale Octahedron. *Nature* **2004,** *427* (6975), 618-621.

283. Douglas, S. M.; Dietz, H.; Liedl, T.; Hogberg, B.; Graf, F.; Shih, W. M., Self-assembly of DNA into Nanoscale Three-dimensional Shapes. *Nature* **2009,** *459* (7245), 414-418.

284. Rothemund, P. W. K., Folding DNA to Create Nanoscale Shapes and Patterns. *Nature* **2006,** *440* (7082), 297-302.

285. Cho, K. J.; Wang, X.; Nie, S. M.; Chen, Z.; Shin, D. M., Therapeutic Nanoparticles for Drug Delivery in Cancer. *Clin. Cancer Res.* **2008,** *14* (5), 1310-1316.

286. Kreuter, J., Drug Targeting with Nanoparticles. *Eur. J. Drug Metabol. Pharmacokinet.* **1994,** *19* (3), 253-256.

287. Kataoka, K.; Harada, A.; Nagasaki, Y., Block Copolymer Micelles for Drug Delivery: Design, Characterization and Biological Significance. *Adv. Drug Deliv. Rev.* **2001,** *47* (1), 113-131.

288. Allen, C.; Maysinger, D.; Eisenberg, A., Nano-engineering Block Copolymer Aggregates for Drug Delivery. *Colloid Surf. B-Biointerfaces* **1999,** *16* (1-4), 3-27.

289. Cho, K. S.; Talapin, D. V.; Gaschler, W.; Murray, C. B., Designing PbSe Nanowires and Nanorings Through Oriented Attachment of Nanoparticles. *J. Am. Chem. Soc.* **2005,** *127* (19), 7140-7147.

290. Javey, A.; Nam, S.; Friedman, R. S.; Yan, H.; Lieber, C. M., Layer-by-layer Assembly of Nanowires for Three-dimensional, Multifunctional Electronics. *Nano Lett.* **2007,** *7* (3), 773-777.

291. Baca, A. J.; Ahn, J. H.; Sun, Y. G.; Meitl, M. A.; Menard, E.; Kim, H. S.; Choi, W. M.; Kim, D. H.; Huang, Y.; Rogers, J. A., Semiconductor Wires and Ribbons for High-performance Flexible Electronics. *Angew. Chem. Int. Edit.* **2008,** *47* (30), 5524-5542.

292. Yin, Y.; Alivisatos, A. P., Colloidal Nanocrystal Synthesis and the Organic-inorganic Interface. *Nature* **2005,** *437* (7059), 664-670.

293. Milliron, D. J.; Hughes, S. M.; Cui, Y.; Manna, L.; Li, J. B.; Wang, L. W.; Alivisatos, A. P., Colloidal Nanocrystal Heterostructures with Linear and Branched Topology. *Nature* **2004,** *430* (6996), 190-195.

294. Lee, J. H.; Wu, Q.; Park, W., Metal Nanocluster Metamaterial Fabricated by the Colloidal Self-assembly. *Opt. Lett.* **2009,** *34* (4), 443-445.

295. Shevchenko, E. V.; Bodnarchuk, M. I.; Kovalenko, M. V.; Talapin, D. V.; Smith, R. K.; Aloni, S.; Heiss, W.; Alivisatos, A. P., Gold/Iron Oxide Core/Hollow-Shell Nanoparticles. *Adv. Mater.* **2008,** *20* (22), 4323-4329.

296. Fan, J. A.; Wu, C. H.; Bao, K.; Bao, J. M.; Bardhan, R.; Halas, N. J.; Manoharan, V. N.; Nordlander, P.; Shvets, G.; Capasso, F., Self-Assembled Plasmonic Nanoparticle Clusters. *Science* **2010,** *328* (5982), 1135-1138.

297. Jones, M. R.; Osberg, K. D.; Macfarlane, R. J.; Langille, M. R.; Mirkin, C. A., Templated Techniques for the Synthesis and Assembly of Plasmonic Nanostructures. *Chem. Rev.* **2011,** *111* (6), 3736-3827.

298. Woods, H. M.; Silva, M.; Nouvel, C.; Shakesheff, K. M.; Howdle, S. M., Materials Processing in Supercritical Carbon Dioxide: Surfactants, Polymers and Biomaterials. *J. Mater. Chem.* **2004,** *14* (11), 1663-1678.

299. Reverchon, E.; Adami, R.; Cardea, S.; Della Porta, G., Supercritical Fluids Processing of Polymers for Pharmaceutical and Medical Applications. *J. Supercrit. Fluids.* **2009,** *47* (3), 484-492.

300. Davies, O. R.; Lewis, A. L.; Whitaker, M. J.; Tai, H. Y.; Shakesheff, K. M.; Howdle, S. M., Applications of Supercritical CO_2 in the Fabrication of Polymer Systems for Drug Delivery and Tissue Engineering. *Adv. Drug Deliv. Rev.* **2008,** *60* (3), 373-387.

301. Annabi, N.; Nichol, J. W.; Zhong, X.; Ji, C.; Koshy, S.; Khademhosseini, A.; Dehghani, F., Controlling the Porosity and Microarchitecture of Hydrogels for Tissue Engineering. *Tissue engineering. Part B, Reviews* **2010,** *16* (4), 371.

302. Tai, H. Y.; Mather, M. L.; Howard, D.; Wang, W. X.; White, L. J.; Crowe, J. A.; Morgan, S. P.; Chandra, A.; Williams, D. J.; Howdle, S. M.; Shakesheff, K. M., Control of Pore Size and Structure of Tissue Engineering Scaffolds Produced by Supercritical Fluid Processing. *Eur. Cells Mater.* **2007,** *14*, 64-76.

303. Tai, H.; Popov, V. K.; Shakesheff, K. M.; Howdle, S. M., Putting the Fizz into Chemistry: Applications of Supercritical Carbon Dioxide in Tissue Engineering, Drug delivery and Synthesis of Novel Block Copolymers. *Biochem. Soc. Trans.* **2007,** *35*, 516-521.

304. De Rosa, C.; Auriemma, F.; Di Girolamo, R.; de Ballesteros, O. R., Crystallization of the Mesomorphic Form and Control of the Molecular Structure for Tailoring the Mechanical Properties of Isotactic Polypropylene. *J. Polym. Sci. Pt. B-Polym. Phys.* **2014,** *52* (10), 677-699.

305. Zia, Q.; Radusch, H. J.; Androsch, R., Deformation Behavior of Isotactic Polypropylene Crystallized via a Mesophase. *Polym. Bull.* **2009,** *63* (5), 755-771.

306. Pasquini, N., *Polypropylene handbook*. Hanser: Munich, 2005.

307. Lopez-Manchado, M. A.; Valentini, L.; Biagiotti, J.; Kenny, J. M., Thermal and Mechanical Properties of Single-walled Carbon Nano tubes-polypropylene Composites Prepared by Melt Processing. *Carbon* **2005,** *43* (7), 1499-1505.

308. Varga, J., Beta-modification of Isotactic Polypropylene: Preparation, Structure, Processing, Properties, and Application. *J. Macromol. Sci. Phys.* **2002,** *B41* (4-6), 1121-1171.

309. Liu, Q.; Sun, X. L.; Li, H. H.; Yan, S. K., Orientation-induced Crystallization of Isotactic Polypropylene. *Polymer* **2013,** *54* (17), 4404-4421.

310. Cocca, M.; Androsch, R.; Righetti, M. C.; Malinconico, M.; Di Lorenzo, M. L., Conformationally Disordered Crystals and Their Influence on Material Properties: The Cases of Isotactic Polypropylene, Isotactic Poly(1-butene), and Poly(L-lactic acid). *J. Mol. Struct.* **2014,** *1078*, 114-132.

311. De Rosa, C.; Auriemma, F.; Di Girolamo, R.; de Ballesteros, O. R.; Pepe, M.; Tarallo, O.; Malafronte, A., Morphology and Mechanical Properties of the Mesomorphic Form of Isotactic Polypropylene in Stereodefective Polypropylene. *Macromolecules* **2013,** *46* (13), 5202-5214.

312. Beintema, J.; Addink, E. J., Polymorphism of Crystalline Polypropylene. *Polymer* **1961,** *2* (2), 185-193.

313. Natta, G.; Corradini, P., Structure and Properties of Isotactic Polypropylene. *Il Nuovo Cimento (1955-1965)* **1960,** *15* (1), 40-51.

314. Li, L. B.; de Jeu, W. H., Shear-induced Smectic Ordering and Crystallisation of Isotactic Polypropylene. *Faraday Discuss.* **2005,** *128*, 299-319.

315. Lotz, B.; Wittmann, J. C.; Lovinger, A. J., Structure and morphology of poly(propylenes): A molecular analysis. *Polymer* **1996,** *37* (22), 4979-4992.

316. Padden, F. J.; Keith, H. D., Spherulitic Crystallization in Polypropylene. *J. Appl. Phys.* **1959,** *30* (10), 1479-1484.

317. Varga, J.; Ehrenstein, G. W., High-temperature Hedritic Crystallization of the Beta-modification of Isotactic Polypropylene. *Colloid Polym. Sci.* **1997,** *275* (6), 511-519.

318. Trifonova-Van Haeringen, D.; Varga, J.; Ehrenstein, G. W.; Vancso, G. J., Features of the Hedritic Morphology of Beta-isotactic Polypropylene Studied by Atomic Force Microscopy. *J. Polym. Sci. Pt. B-Polym. Phys.* **2000,** *38* (5), 672-681.

319. Padden, F. J.; Keith, H. D., Crystallization in Thin Films of Isotactic Polypropylene. *J. Appl. Phys.* **1966,** *37* (11), 4013-4020.

320. Zhang, B.; Chen, J. J.; Liu, B. C.; Wang, B. H.; Shen, C. Y.; Reiter, R.; Chen, J. B.; Reiter, G., Morphological Changes of Isotactic Polypropylene Crystals Grown in Thin Films. *Macromolecules* **2017,** *50* (16), 6210-6217.

321. Zhang, B.; Wang, B. H.; Chen, J. J.; Shen, C. Y.; Reiter, R.; Chen, J. B.; Reiter, G., Flow-Induced Dendritic beta-Form Isotactic Polypropylene Crystals in Thin Films. *Macromolecules* **2016,** *49* (14), 5145-5151.

322. Prud'homme, R. E., Crystallization and Morphology of Ultrathin Films of Homopolymers and Polymer Blends. *Prog. Polym. Sci.* **2016,** *54-55*, 214-231.

323. Michell, R. M.; Muller, A. J., Confined Crystallization of Polymeric Materials. *Prog. Polym. Sci.* **2016,** *54-55*, 183-213.

324. Liu, Y. X.; Chen, E. Q., Polymer Crystallization of Ultrathin Films on Solid Substrates. *Coord. Chem. Rev.* **2010,** *254* (9-10), 1011-1037.

325. Yu, C. T.; Xie, Q.; Bao, Y. Z.; Shan, G. R.; Pan, P. J., Crystalline and Spherulitic Morphology of Polymers Crystallized in Confined Systems. *Crystals* **2017,** *7* (5), 20.

326. Nguyen, T. Q.; Doan, V.; Schwartz, B. J., Conjugated Polymer Aggregates in Solution: Control of Interchain Interactions. *J. Chem. Phys.* **1999,** *110* (8), 4068-4078.

327. Wenz, G.; Muller, M. A.; Schmidt, M.; Wegner, G., Structure of Poly(Diacetylenes) in Solution. *Macromolecules* **1984,** *17* (4), 837-850.

328. Tomasko, D. L.; Li, H. B.; Liu, D. H.; Han, X. M.; Wingert, M. J.; Lee, L. J.; Koelling, K. W., A Review of CO_2 Applications in the Processing of Polymers. *Ind. Eng. Chem. Res.* **2003,** *42* (25), 6431-6456.

329. Nalawade, S. P.; Picchioni, F.; Janssen, L., Supercritical Carbon Dioxide as a Green Solvent for Processing Polymer Melts: Processing Aspects and Applications. *Prog. Polym. Sci.* **2006,** *31* (1), 19-43.

330. Ely, J. F., *A Review of Supercritical Fluid Extraction*. Forgotten Books: London, 1983.

331. Zhou, H.; Fang, H.; Yang, J. C.; Xie, X. M., Effect of the supercritical CO2 on surface structure of PMMA/PS blend thin films. *J. Supercrit. Fluids* **2003,** *26* (2), 137-145.

332. Shieh, Y. T.; Yang, H. S., Morphological Changes of Polycaprolactone with High-pressure CO_2 Treatment. *J. Supercrit. Fluids* **2005,** *33* (2), 183-192.

333. Kiran, E.; Liu, K.; Ramsdell, K., Morphological Changes in Poly(epsilon-caprolactone) in Dense Carbon Dioxide. *Polymer* **2008,** *49* (7), 1853-1859.

334. Kiran, E., Polymer miscibility, phase separation, morphological modifications and polymorphic transformations in dense fluids. *J. Supercrit. Fluids* **2009,** *47* (3), 466-483.

335. Di Maio, E.; Iannace, S.; Mensitieri, G.; Nicolais, L., A Predictive Approach Based on the Simha-Somcynsky Free-volume Theory for the Effect of Dissolved Gas on

Viscosity and Glass Transition Temperature of Polymeric Mixtures. *J. Polym. Sci. Pt. B-Polym. Phys.* **2006,** *44* (13), 1863-1873.

336. Ma, W. M.; Yu, J.; He, J. S., Competitive Influence of Atactic Polystyrene and Supercritical Carbon Dioxide on the Conformation of Syndiotactic Polystyrene. *J. Polym. Sci. Pt. B-Polym. Phys.* **2007,** *45* (14), 1755-1764.

337. Ma, W. M.; Yu, J.; He, J. S., Direct Formation of Gamma Form Crystal of Syndiotactic Polystyrene from Amorphous State in Supercritical CO_2. *Macromolecules* **2004,** *37* (18), 6912-6917.

338. Yousefi, N.; Saeedi Saghez, B.; Pettipas, R. D.; Kelly, T. L.; Kaake, L. G., Physical supercritical fluid deposition of polymer films: controlling the crystallinity with pressure. *Mater. Chem. Front.* **2021,** 5, 1428-1437.

339. Flory, P. J., Thermodynamics of high polymer solutions. *J. Chem. Phys.* **1942,** *10* (1), 51-61.

340. Huggins, M. L., Solutions of long chain compounds. *J. Chem. Phys.* **1941,** *9* (5), 440-440.

341. Panayiotou, C.; Vera, J. H., Thermodynamics of Polymer-Polymer-Solvent and Block Copolymer-solvent Systems .1. Experimental Measurements. *Polym. J.* **1984,** *16* (2), 89-102.

342. Orofino, T. A.; Flory, P. J., Relationship of the Second Virial Coefficient to Polymer Chain Dimensions and Interaction Parameters. *J. Chem. Phys.* **1957,** *26* (5), 1067-1076.

343. Schweizer, K. S.; Singh, C., Microscopic solubility-parameter theory of polymer blends: General predictions. *Macromolecules* **1995,** *28* (6).

344. Kiran, E.; Xiong, Y., Miscibility of Isotactic Polypropylene in n-pentane and n-pentane plus Carbon Dioxide Mixtures at High Pressures. *J. Supercrit. Fluids* **1998,** *11* (3), 173-177.

345. P. C. Hiemenz , T. P. L., *Polymer Chemistry*. 2nd ed.; Taylor & Francis Inc , CRC Press Inc: 2007; p 608.

346. Varga, J., Supermolecular Structure of Isotactic Polypropylene. *J. Mater. Sci.* **1992,** *27* (10), 2557-2579.

347. Jones, A. T.; Aizlewood, J. M.; Beckett, D. R., Crystalline Forms of Isotactic Polypropylene. *Die Makromolekulare Chemie* **1964,** *75* (1), 134-158.

348. Natta, G.; Corradini, P., *Structure and Properties of Isotactic Polypropylene*. Pergamon: 1967; Vol. 2, p 743-746.

349. Burgt, F. P. T. J. v. d. Crystallization of Isotactic Polypropylene : The Influence of Stereo-defects. Technische Universiteit Eindhoven, Eindhoven, 2002.

350. Thomann, R.; Wang, C.; Kressler, J.; Mulhaupt, R., On the Gamma-Phase of Isotactic Polypropylene. *Macromolecules* **1996,** *29* (26), 8425-8434.

351. Sauer, J. A.; Pae, K. D., Structure and Thermal Behavior of Pressure-Crystallized Polypropylene. *J. Appl. Phys.* **1968,** *39* (11), 4959-4968.

352. Alamo, R. G.; Kim, M. H.; Galante, M. J.; Isasi, J. R.; Mandelkern, L., Structural and Kinetic Factors Governing the Formation of the Gamma Polymorph of Isotactic Polypropylene. *Macromolecules* **1999,** *32* (12), 4050-4064.

353. Campbell, R. A.; Phillips, P. J.; Lin, J. S., The Gamma-Phase of High-Molecular-Weight Polypropylene .1. Morphological Aspects. *Polymer* **1993,** *34* (23), 4809-4816.

354. Kundu, P. K.; Cohen, I. M.; Hu, H., *Fluid Mechanics*. Elsevier Science: 2001.

355. Belmonte, A.; Tilgner, A.; Libchaber, A., Boundary layer length scales in thermal turbulence. *Phys. Rev. Lett.* **1993,** *70* (26), 4067-4070.

356. Ahlers, G.; Bodenschatz, E.; Funfschilling, D.; Grossmann, S.; He, X.; Lohse, D.; Stevens, R. J. A. M.; Verzicco, R., Logarithmic Temperature Profiles in Turbulent Rayleigh-Bénard Convection. *Phys. Rev. Lett.* **2012,** *109* (11), 114501.

357. Jiang, Z., GIXSGUI : a MATLAB Toolbox for Grazing-Incidence X-Ray Scattering Data Visualization and Reduction, and Indexing of Buried Three-Dimensional Periodic Nanostructured Films. *J. Appl. Crystallogr.* **2015,** *48* (3), 917-926.

358. Fang, F. Z.; Zhang, X. D.; Gao, W.; Guo, Y. B.; Byrne, G.; Hansen, H. N., Nanomanufacturing-Perspective and Applications. *CIRP Ann-Manuf. Technol.* **2017,** *66* (2), 683-705.

359. Biswas, A.; Bayer, I. S.; Biris, A. S.; Wang, T.; Dervishi, E.; Faupel, F., Advances in Top-Down and Bottom-Up Surface Nanofabrication: Techniques, Applications & Future Prospects. *Adv. Colloid Interface Sci.* **2012,** *170* (1-2), 2-27.

360. Maune, H. T.; Han, S. P.; Barish, R. D.; Bockrath, M.; Goddard, W. A.; Rothemund, P. W. K.; Winfree, E., Self-Assembly of Carbon Nanotubes into Two-Dimensional Geometries Using DNA Origami Templates. *Nat. Nanotechnol.* **2010,** *5* (1), 61-66.

361. Wunderlich, B., *Macromolecular physics*. New York : Academic Press: 1973.

362. Long, Y.; Shanks, R. A.; Stachurski, Z. H., Kinetics of Polymer Crystallization. *Prog. Polym. Sci.* **1995,** *20* (4), 651-701.

363. Reiter, G.; Strobl, G. R.; Reiter, G.; SpringerLink, *Progress in Understanding of Polymer Crystallization edited by Günter Reiter, Gert R. Strobl*. 1st ed. 2007. ed.; Berlin, Heidelberg : Springer Berlin Heidelberg : Imprint: Springer: 2007.

364. Pawlak, A.; Galeski, A., Crystallization of Polypropylene. In *Polypropylene Handbook: Morphology, Blends and Composites*, Karger-Kocsis, J.; Bárány, T., Eds. Springer International Publishing: Cham, 2019; pp 185-242.

365. Bolgar, M., *Handbook for the Chemical Analysis of Plastic and Polymer Additives*. Second edition. ed.; Boca Raton, Florida : CRC Press, Taylor & Francis Group: 2016.

366. Nair, R. R.; Blake, P.; Grigorenko, A. N.; Novoselov, K. S.; Booth, T. J.; Stauber, T.; Peres, N. M. R.; Geim, A. K., Fine Structure Constant Defines Visual Transparency of Graphene. *Science* **2008,** *320* (5881), 1308-.

367. Bubnova, O.; Khan, Z. U.; Wang, H.; Braun, S.; Evans, D. R.; Fabretto, M.; Hojati-Talemi, P.; Dagnelund, D.; Arlin, J. B.; Geerts, Y. H.; Desbief, S.; Breiby, D. W.; Andreasen, J. W.; Lazzaroni, R.; Chen, W. M. M.; Zozoulenko, I.; Fahlman, M.; Murphy, P. J.; Berggren, M.; Crispin, X., Semi-metallic polymers. *Nat. Mater.* **2014,** *13* (2), 190-194.

368. Perez, L. A.; Rogers, J. T.; Brady, M. A.; Sun, Y. M.; Welch, G. C.; Schmidt, K.; Toney, M. F.; Jinnai, H.; Heeger, A. J.; Chabinyc, M. L.; Bazan, G. C.; Kramer, E. J., The Role of Solvent Additive Processing in High Performance Small Molecule Solar Cells. *Chem. Mater.* **2014,** *26* (22), 6531-6541.

369. Liang, Y. Y.; Xu, Z.; Xia, J. B.; Tsai, S. T.; Wu, Y.; Li, G.; Ray, C.; Yu, L. P., For the Bright Future-Bulk Heterojunction Polymer Solar Cells with Power Conversion Efficiency of 7.4%. *Adv. Mater.* **2010,** *22* (20), E135-138.

370. Aich, B. R.; Lu, J. P.; Beaupre, S.; Leclerc, M.; Tao, Y., Control of the Active Layer Nanomorphology by Using Co-Additives towards High-Performance Bulk Heterojunction Solar Cells. *Org. Electron.* **2012,** *13* (9), 1736-1741.

371. Gao, J.; Duan, L. Y.; Yang, G. H.; Zhang, Q.; Yang, M. B.; Fu, Q., Manipulating Poly(lactic acid) Surface Morphology by Solvent-Induced Crystallization. *Appl. Surf. Sci.* **2012,** *261*, 528-535.

372. Vittoria, V.; Riva, F., Solvent-Induced Crystallization of Quenched Isotactic Polypropylene in Different Liquids. *Macromolecules* **1986,** *19* (7), 1975-1979.

373. Cornelis, H.; Kander, R. G.; Martin, J. P., Solvent-Induced Crystallization of Amorphous Poly(ether ether ketone) by Acetone. *Polymer* **1996,** *37* (20), 4573-4578.

374. Wang, J.; Dibenedetto, A. T.; Johnson, J. F.; Huang, S. J.; Cercena, J. L., Solvent-Induced Crystallization of Aromatic Polyimide. *Polymer* **1989,** *30* (4), 718-721.

375. Lin, S. B.; Koenig, J. L., Spectroscopic Characterization of Solvent-Induced Crystallization of PET. *J. Polym. Sci. Pt. B-Polym. Phys.* **1983,** *21* (8), 1539-1558.

376. Charlet, G.; Delmas, G., Thermodynamic Properties of polyolefin Solutions at High Temperature: 1. Lower Critical Solubility Temperatures of polyethylene, polypropylene and ethylene-propylene copolymers in Hydrocarbon Solvents. *Polymer* **1981,** *22* (9), 1181-1189.

377. Huang, S. H.; Radosz, M., Equation of State for Small, Large, Polydisperse, and Associating Molecules. *Ind. Eng. Chem. Res.* **1990,** *29* (11), 2284-2294.

378. Gross, J.; Sadowski, G., Perturbed-chain SAFT: An Equation of State Based on a Perturbation Theory for Chain Molecules. *Ind. Eng. Chem. Res.* **2001,** *40* (4), 1244-1260.

379. Watkins, J. J.; Krukonis, V. J.; Condo, P. D.; Pradhan, D.; Ehrlich, P. Fractionation of High Density Polyethylene in Propane by Isothermal Pressure Profiling and Isobaric Temperature Profiling. *J. Supercrit. Fluids.* **1991**, *4* (10), 24-31.

380. Paternò, G. M.; Skoda, M. W. A.; Dalgliesh, R.; Cacialli, F.; Sakai, V. G., Tuning Fullerene Intercalation in a Poly (thiophene) derivative by Controlling the Polymer Degree of Self-Organisation. *Sci. Rep.* **2016,** *6* (1), 34609-34609.